Clouded by molecules

An unparalleled view of the molecular interstellar medium in M51

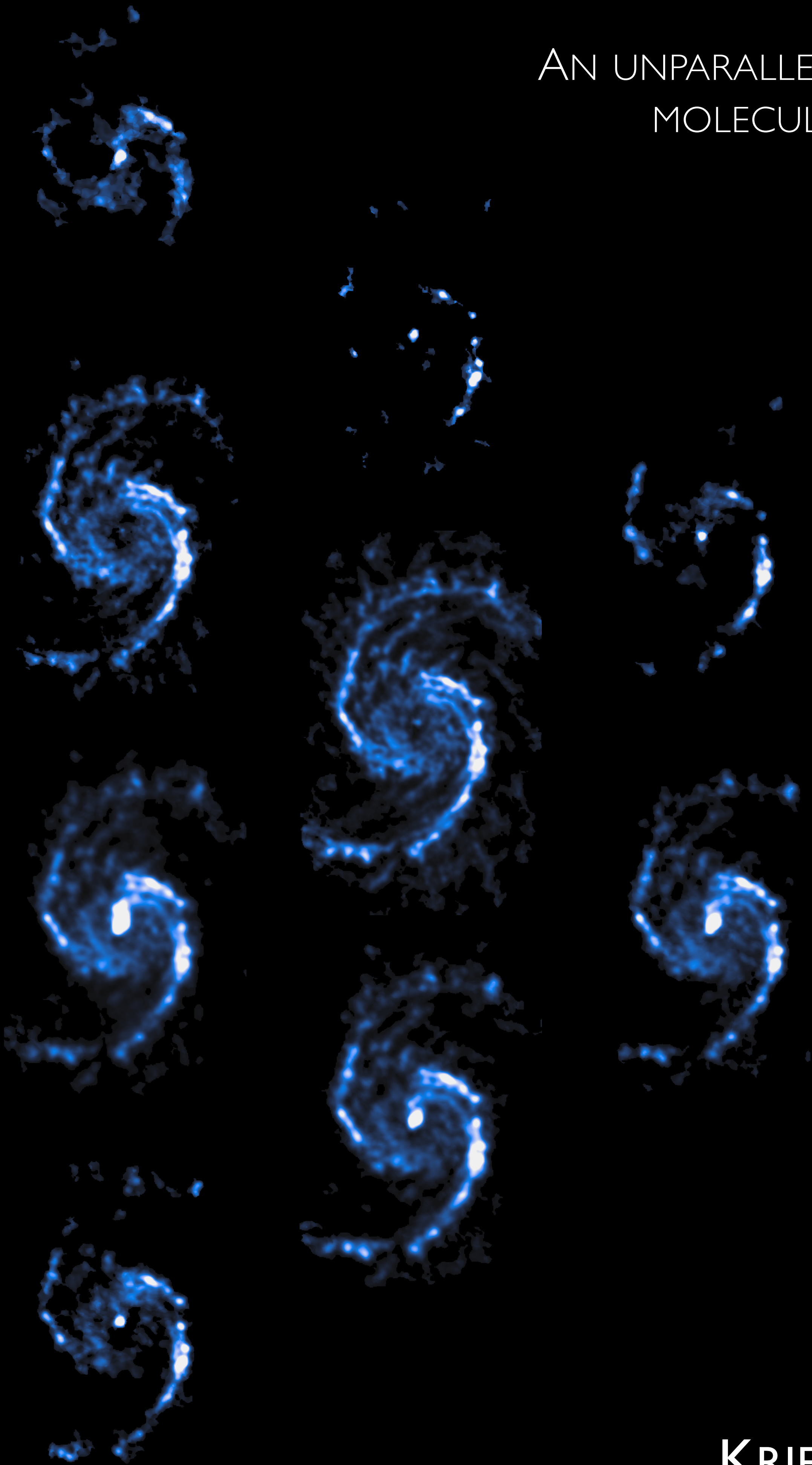

Sophia
Katharina
Krieger (Stuber)

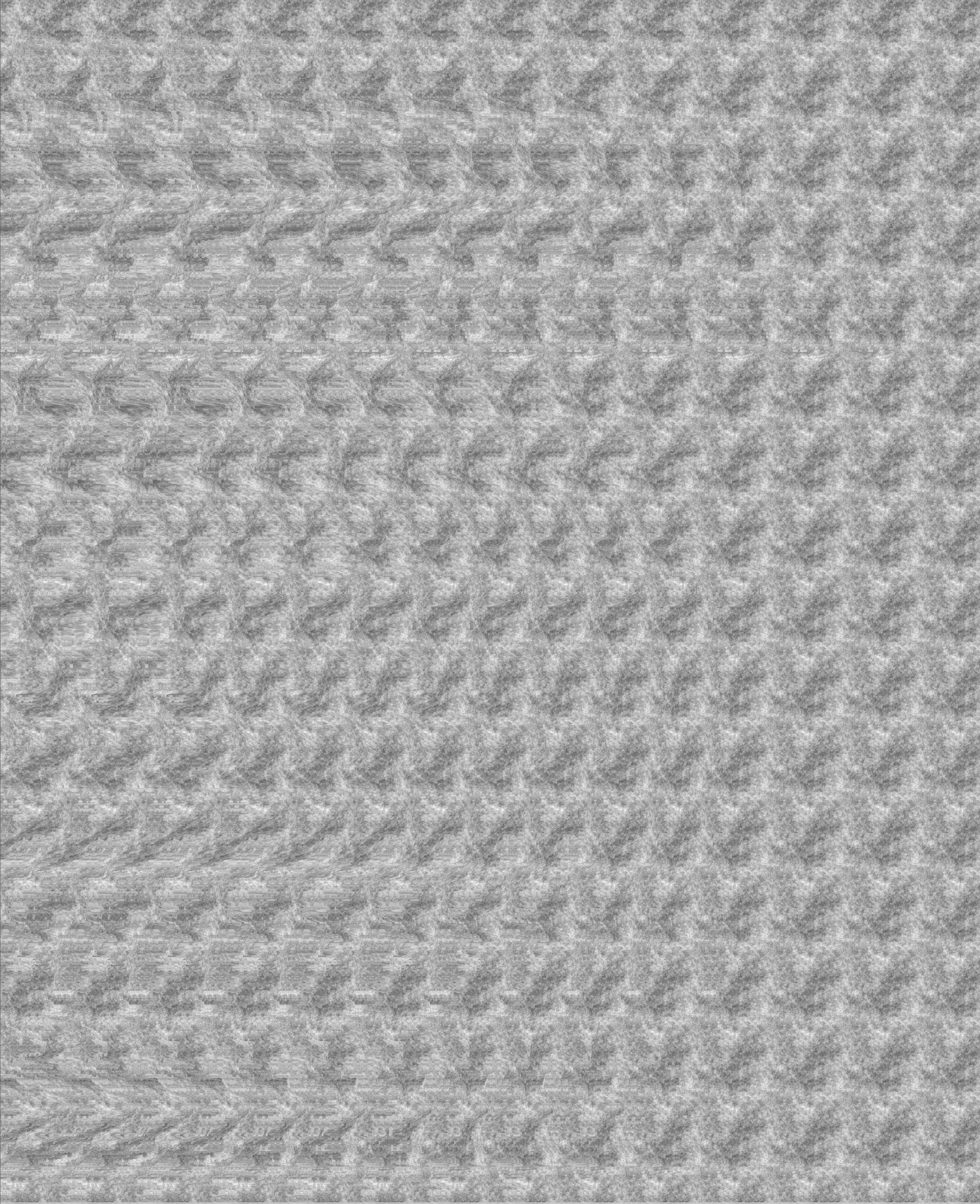

Front cover: Integrated intensity maps (mom-0) from the SWAN survey & schematic of M51 with the SWAN field of view highlighted. *Credit*: S.K.Krieger

Section numbers: All galaxy schematics in this thesis are hand-drawn by S.K.Krieger. This includes the galaxy schematics used as Section numbers, as well as the M51 schematic.

This page: Autostereogram of HCN mom-0 map made with *https://yx.stereogram-maker.com/*. Focusing on a point behind the image will let you experience the HCN mom-0 map in '3D'.

Dissertation

submitted to the

Combined Faculty of Mathematics, Engineering and Natural Sciences

of Heidelberg University, Germany

for the degree of

Doctor of Natural Sciences

Put forward by

Sophia Katharina Krieger (née Stuber)

born in: Öhringen

Oral examination: July 14, 2025

CLOUDED BY MOLECULES

An unparalleled view of the molecular interstellar medium in M51

Sophia Katharina Krieger
née Stuber

Referees: Prof. Dr. Hans-Walter Rix, Dr. Dominika Wylezalek
Supervisor: Dr. Eva Schinnerer
Advisers: Prof. Dr. Hans-Walter Rix, Prof. Dr. Ralf Klessen

ABSTRACT

Star formation is fueled by dense molecular gas residing in the dense and cold interiors of molecular clouds. For decades, the emission of selected molecules, such as HCN and HCO^+, has been used to trace this dense molecular gas phase within the Milky Way and external galaxies. Studies have revealed a tight link between star formation rate and the emission of these molecules, observed on both sub-cloud scales in the Milky Way and at kiloparsec scales in other galaxies. However, it has been recently established that the properties of molecular clouds significantly depend on the galactic environment they are residing in. Yet, observations of particularly the dense molecular phase – the direct fuel of star formation that resides within those clouds – are often limited to kiloparsec-scale resolution insufficient to access cloud properties or resolved studies of molecular clouds in a single environment only. To understand how exactly the large-scale galactic environments within galaxies are able to regulate the properties of star formation within molecular clouds, it is essential to gain a cloud-scale view of dense gas across a range of galactic environments.

This thesis provides the first piece in understanding this link, with the most comprehensive analysis of common dense gas tracers on cloud-scales across a diverse set of galactic environments. "Surveying the Whirlpool galaxy at Arcseconds with NOEMA" (SWAN), is the largest cloud-scale mapping of 3-4 mm emission in an external galaxy to date and the focus of this thesis.

The detailed view provided by SWAN shows that dense gas is not only confined to spiral arms, but that its tracers emit brightly in the interarm region and galaxy center, suggesting future star formation across the disk. The first time in-depth comparison between common extragalactic dense gas tracers and the Galactic 'gold standard' tracer N_2H^+ reveals significant variations with both large-scale environment and local cloud-scale regions, which are undetected at coarser kiloparsec-scale resolution. Particularly, the center of M51 emerges as an extreme environment in which the relation between these dense gas tracers varies strongly. The utility of HCN emission in tracing gas density, breaks down when tested in M51's (extreme) environments and HCO^+ presents itself as a more robust dense gas tracer. While studies from Milky Way clouds have questioned the use of HCN in tracing high gas density regions, this is the first time it has been tested at cloud-scales for entire cloud populations and the first time this could be placed into the context of galactic environments. Our new insights on the physical conditions that drive the dense gas emission reveal that gas density is not the sole driver of their emission. This implies that second order dependencies on other physical parameters like dynamical equilibrium pressure, star-formation rate and stellar mass surface density have a pronounced effect and cannot be neglected in further analysis. This thesis demonstrates the importance to place the star formation laws into an environmental context.

ZUSAMMENFASSUNG

Die Sternentstehung wird durch dichtes molekulares Gas gespeist, das sich im dichten und kalten Inneren von Molekülwolken befindet. Seit Jahrzehnten wird die Emission ausgewählter Moleküle, wie HCN und HCO^+, genutzt, um dieses dichte molekulare Gas in der Milchstraße und anderen Galaxien zu detektieren. Studien zeigen einen engen Zusammenhang zwischen der Sternentstehungsrate und Emission dieser Moleküle – sowohl auf kleinen Skalen innerhalb von Molekülwolken in der Milchstraße, als auch auf Kiloparsec-Skalen in anderen Galaxien. Neuste Ergebnise haben gezeigt, dass die Eigenschaften von Molekülwolken erheblich von der galaktischen Umgebung abhängen, in der sie sich befinden. Dennoch sind Beobachtungen, insbesondere des dichten molekularen Gases - des direkten Treibstoffs der Sternentstehung, welcher sich innerhalb dieser Wolken befindet - oft unzureichend: Entweder sind es Kiloparsec-Beobachtungen, zu groß um die Eigenschaften von Wolken zu untersuchen, oder höher-auflösende Beobachtungen, welche auf eine einzelne Umgebung beschränkt sind. Um zu verstehen, wie genau galaktische Umgebungen die Eigenschaften der Sternentstehung in Molekülwolken regulieren können, ist es entscheidend, das dichte molekulare Gas auf Wolkenskalen in verschiedenen galaktischen Umgebungen zu erfassen.

Diese Arbeit liefert den ersten Baustein zum Verständnis dieses Zusammenhangs und präsentiert die bislang umfassendste Analyse gängiger Indikatoren für dichtes Gas auf Wolkenskalen in einer Vielzahl von galaktischen Umgebungen. Das Projekt "Surveying the Whirlpool galaxy at Arcseconds with NOEMA" (SWAN) ist die bisher umfangreichste wolkenskalige Kartierung von Emission im 3-4 mm Bereich in einer externen Galaxie und bildet den Kern dieser Arbeit.

Der detaillierte Blick auf das dichte Gas zeigt, dass es nicht nur in den Spiralarmen vorkommt, sondern auch zwischen den Spiralarmen und im Zentrum der Galaxie hell strahlt. Dies deutet zukünftige Sternbildung in der gesamten Scheibe an. Der erstmalige ausführliche Vergleich zwischen den gängigen extragalaktischen und dem galaktischen "Goldstandard" Indikator für dichtes Gas, N_2H^+, zeigt signifikante Variationen in Abhängigkeit von sowohl galaktischer Umgebung, als auch lokalen Wolkenskalen. Diese Variationen sind auf Kiloparsec-Beobachtungen undetektiert. Insbesondere das Zentrum von M51 erweist sich als extreme Umgebung, in der die Emission der dichten Gasindikatoren deutlich variiert. Die Aussagekraft von HCN-Emission als Indikator für die Gasdichte bricht in den (extremen) Umgebungen von M51 zusammen, während sich HCO^+ als robusterer Indikator für dichtes Gas erweist. Während bereits Studien in der Milchstraße Zweifel an der Eignung von HCN als Dichteindikator aufgeworfen haben, ist dies die erste Untersuchung auf Wolkenskalen über ganze Wolkenpopulationen hinweg – und zugleich die erste, die in den Kontext galaktischer Umgebungen eingebettet ist. Unsere neuen Erkenntnisse zu den physikalischen Bedingungen, die die dichte Gasemission antreiben, zeigen, dass die Gasdichte nicht der alleinige Einflussfaktor ist. Bedeutende sekundäre Abhängigkeiten von weiteren physikalischen Parametern, wie dem dynamischen Gleichgewichtsdruck, der Sternentstehungsrate und der stellaren Massendichte, dürfen in zukünftigen Analysen nicht vernachlässigt werden. Diese Arbeit unterstreicht die Notwendigkeit, Sternentstehungsgesetze im Kontext ihrer galaktischen Umgebung zu betrachten.

ACKNOWLEDGEMENTS

My thanks goes to my supervisor Eva Schinnerer, without whom my PhD would not have been possible. Thanks for your guidance in both scientific questions as well as the jungle of political nuances within collaborations. I thank many members of the PHANGS collaboration, who helped me tackle all different problems encountered during my PhD, to mention a few of them, I thank Miguel Querejeta, Antonio Usero and Maria Jimenez-Donaire for their very welcoming support during my visit at OAN and beyond. I thank the colleagues and friends at MPIA, who joined me weekly in my tea obsession. I thank my thesis committee members Hans-Walter Rix and Ralf Klessen for their advise throughout the years, and thank Dominika Wylezalek and André Butz for kindly agreeing to being part of my thesis defense committee.

Outside of MPIA there are many people I want to thank for their support during my PhD: Thank you Nico, for always having chocolate when I needed, for saying “let’s do it” when asked if we could celebrate our wedding as a galaxy merger and for always being by my side. You introduced me to MPIA and the astronomical world. I thank my friends, who would constantly *rotate, translate and boost* my motivation and view on life, and spend many hours dealing with my characters in dungeons and dragons. Sport was another vital way of dealing with stressful situations, and I thank the friends from the TSG 78 Heidelberg for introducing me to discus throwing. Lastly, I want to thank my parents for their support throughout the years.

♡

Man, he took his time in the sun
Had a dream to understand
A single grain of sand

Nightwish,
Greatest Show on Earth

CONTENTS

LIST OF FIGURES

LIST OF TABLES

PHYSICAL BACKGROUND

1 MOTIVATION

Just about hundred years ago, in 1920, the "Great Debate" shaped the astronomical community. Astronomers Heber Curtis and Harlow Shapley discussed the nature of so-called spiral nebulae, whether those features are small parts belonging to a gigantic Milky Way, or whether those objects are independent islands of their own. This discussion is the foundation of extragalactic astronomy as we know it today. By now, deep observations with various telescopes have revealed the vast amount of galaxies in our universe, differing in shape, size and color, and each filled with millions to billions of stars. A galaxy's stellar growth and evolution depends on the formation of those stars, and even further, the life on earth is only possible due to ancient star formation and the atoms forged in this process.

Star formation is a universal process that happens even in the most isolated galaxies within voids (Verley et al., 2007). Yet, even today, we have not fully understood the full star formation cycle within galaxies. In the modern picture of star formation (Section 2.1), it is fueled by molecular gas (Section 2.1.1) and closely linked with molecular cloud evolution (Section 2.1.2). Dense clumps of molecular gas inside the clouds collapse to then spark nuclear fusion. However, studies observing individual clouds within our Milky Way find variances in cloud properties and in the efficiency at which stars are formed from cloud to cloud. While the central molecular zone hosts large quantities of molecular gas, the star formation per unit gas is low compared to other regions in the Milky Way (e.g., Henshaw et al., 2023). Extragalactic observations reveal changes in dense gas fractions with different environments within galaxies, such as galaxy centers (e.g., review by Schinnerer and Leroy, 2024). In other words, the host

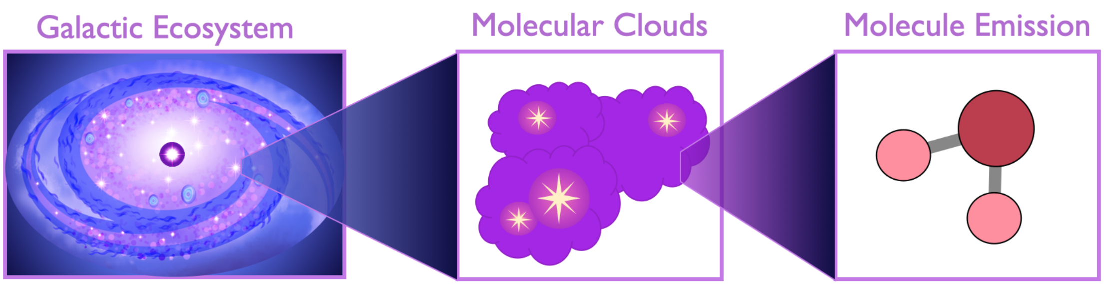

Figure 1: Schematic of the methodology used throughout this thesis: Galactic ecosystems and environments within them shape molecular clouds and the star formation fueled by those clouds. Emission lines of different molecules allow us to study the conditions of and within such clouds.

galaxy seems to be able to set the initial conditions for star formation. These findings raise even further questions:

How are galaxies able to impact molecular clouds? And what sets the even denser molecular clumps residing within clouds? How is the rate at which gas is converted into stars affected?

These questions can not be solved without a thorough analysis of the astrochemical conditions within galaxies (see schematic Figure 1): The galactic environment changes the properties of and within molecular clouds. These properties can be accessed via the emission of different molecular species sensitive to different conditions.

While the high spatial resolution achievable within our Milky Way not only allows us to resolve molecular clouds, but filaments, clumps and cores, the connection with the larger-scale structure present within our Galaxy is difficult, as our location within our own Galaxy's disk impedes the view. Nearly face-on observations of extragalactic targets provide excellent view of the large-scale structures such as spiral arms and bars that shape the gravitational potential of galaxies, yet, high-resolution observations are time-intensive and most often do not resolve clumps or smaller molecular clouds. In this thesis, I study the conditions of the dense phase of the molecular gas in an exemplary galaxy, M51, as captured by the emission of several molecules across an area never probed at this resolution.

2 INTRODUCTION

2.1 STAR FORMATION IN THE INTERSTELLAR MEDIUM

A large fraction of the baryonic matter in the universe is distributed in the interstellar medium (ISM) residing within a galaxy's gravitational potential. A constant interplay of dynamics driven by the galaxy's potential, interactions with other galaxies, radiation from objects within the galaxy, and material in- and outflows shape the ISM. To first order, local universe galaxies can be considered ecosystems that maintain their stable non-equilibrium state by self-regulating their energy and material flows. The compulsion of those galaxy systems to evolve to states of lowest energy possible gives rise to a flat rotating disks. In those disks, external and internal perturbations allow for the emergence of non-axisymmetric stellar structures such as spiral arms or stellar bars (Binney and Tremaine, 2008; Kormendy and Ho, 2013). Star formation is thought to preferentially occur in features such as spiral arms, and to be less pronounced along stellar bars. This makes these structures within galaxy disks and their interplay with the ISM key aspects for understanding the secular evolution of galaxies.

2.1.1 The different phases of the ISM

The baryonic material within galaxies that is not part of stars is commonly divided into different phases based on temperature and density. About 70% of the ISM by mass (and $\sim 91\%$ by number) is attributed to hydrogen, $\sim 28\%$ to helium and the remaining few percent to heavier elements, also referred to as "metals" (Ferrière, 2001; Carroll and Ostlie, 2017). Ionized hot and warm gas (temperatures $T \gtrsim 10^4$K), while very voluminous, is very low in density. Photo-ionized by ultra-violet (UV) photons from young O/B stars, the typical scale height of this gas phase reaches up to several kiloparsecs. At temperatures below 5000 K, the neutral warm and cold medium enables atoms to remain neutral and reach densities of $\sim 1-30$ particles per cm^{-3}. The even colder (T$\sim$ 100 K) neutral medium, with scale heights of a few 100 parsecs, provides efficient shielding for the even denser gas, allowing molecules to form (e.g., Draine, 2011). The emergence of a molecular gas layer is governed by rivaling processes of molecule formation out of atomic hydrogen gas and destruction via the interstellar radiation field or radiation of nearby hot stars. As reactions between hydrogen atoms in the gas phase are mostly inefficient, molecular hydrogen is dominantly formed via reactions that happen on the surface of dust grains (Tielens, 2021). These molecules only exist in larger quantities in regions with high enough column densities or shielding by dust to

Figure 2: JWST observations of star-forming region NGC 3324 in the Carina nebula. Stellar radiation and stellar winds from young, massive stars located north outside the field of view have eroded the cloud in the upper half of the image (blue colors). In the lower half, infrared emission stemming from dust (orange colors) reveals a cloud of gas and dust in which newly formed stars start to create bubbles and cavities in their surroundings. *Image credit:* NASA/ESA/CSA/STScI

oppose the efficient photodissociation of molecular hydrogen via far-UV photons from the stellar radiation field (Krumholz, 2014). While only about $\sim 0.1\%$ in interstellar volume of a spiral galaxy is filled by molecular gas, the processes of star formation are tightly linked with this gas phase (e.g., Ferrière, 2001). Since the molecules efficiently cool compared to other gas phases, they accumulate in a thin layer with a scale height of only ~ 100 pc. Further, tracers of the bulk molecular distribution respond well to the underlying gravitational potential and the emerging kinematics (Lang et al., 2020; Stuber et al., 2023b). Large complex molecules and solid particles based on silicates and carbonaceous materials make up the dust component of the ISM. A famous example of such complex particles are polycyclic aromatic particles (PAH), which – due to their key role in cooling the ISM, tracing the star formation rate (SFR) and the impact of feedback – have been a key focus of studies by the recent observations with the James Web Space telescope (JWST, see reviews by Carroll and Ostlie, 2017; Schinnerer and Leroy, 2024, see Figure 2).

Within galaxies there is a constant mixing and conversion from one gas phase to the other, driven by turbulence due to thermal instability, supernovae feedback and gas accretion onto the disk. The "baryon life cycle" describes the conversion of different gas phases within galaxies. Shielded by diffuse atomic gas and dust, molecules can form, cool and molecular clumps reach densities high enough for star formation to ignite. Those very stars ionize their surrounding gas, eject their envelopes. The hotter gas, once able to cool down again will repeat the cycle all over again. Within this cycle, of particular interest is the molecular gas phase, which fuels the formation of future stars.

2.1.2 Modern molecular cloud evolution picture

High-resolution observations of different phases of the ISM over the last decade have resulted in an emerging picture of the evolution of molecular clouds (Figure 3, Schinnerer and Leroy, 2024). We note that molecular clouds are neither spherical, nor do they have clear boundaries or sizes, but can often be resolved into smaller filamentary

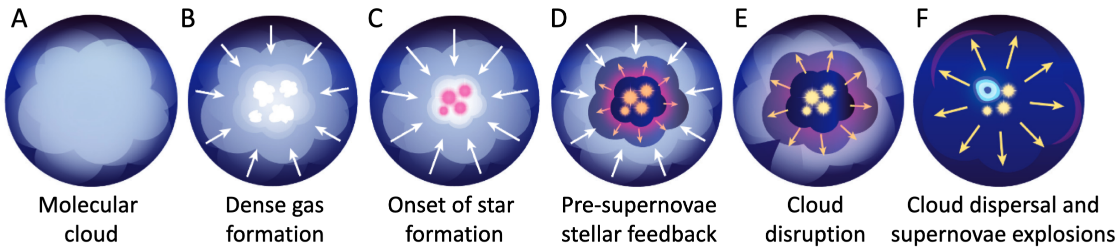

Figure 3: Molecular cloud evolution from Schinnerer and Leroy (2024), displaying schematically the different stages of a star forming molecular cloud (A-F). Blue to white colors indicate increase in gas density, stellar light attenuation is decreased from red to yellow, and light red color indicates ionized gas. Some of the evolutionary phases described here can be seen in the star-forming region in the Carina nebula (Figure 2).

structures of a sponge-like structure (e.g., review by Beuther et al., 2025). Yet, for visual and observational purposes, the assumption of spherical independent features called clouds has proven useful. With typical sizes of $\sim 50-100\,\mathrm{pc}$ (Tielens, 2021; Schinnerer and Leroy, 2024) and masses $M \gtrsim 10^5\,M_\odot$, those so-called "Giant-molecular clouds" (GMCs) are frequently studied in both the Milky Way and extragalactic targets (e.g., Dobbs and Pringle, 2013; Colombo et al., 2014a; Lada and Dame, 2020; Schinnerer and Leroy, 2024). Within the typical life time of a GMC of $\sim 5-30\,\mathrm{Myr}$ (Schinnerer and Leroy, 2024), the following evolutionary processes can be identified:

A) MOLECULAR CLOUDS, OVERDENSITIES OF COLD, PREDOMINANTLY MOLECULAR GAS: As the stellar radiation field penetrates the outer layers of the cloud, its surface mostly consist of a mixture of atomic hydrogen, ionized carbon, followed by neutral carbon and molecular hydrogen (H_2), and towards the center of the cloud we find a mixture of H_2, neutral carbon and carbon monoxide. While the far-UV radiation is likely not able to penetrate the boundaries of the molecular cloud, cosmic rays are thought to be the main heating mechanisms in cloud interiors (Krumholz, 2014). Carbon monoxide, CO, is the second most abundant molecule in the ISM (e.g., review by Bolatto et al., 2013). It is predominantly formed via gas-phase reactions and its ability to cool via its rotational transitions balances the cosmic ray heating to an equilibrium temperature of about $\sim 10\,\mathrm{K}$ (Krumholz, 2014), which matches the typical gas temperature of a GMC ($\sim 10-50\,\mathrm{K}$, e.g., Dobbs et al., 2014; Klessen and Glover, 2015). GMCs typically have surface densities of $\Sigma_{\mathrm{GMC}} \sim 40-100\,M_\odot\,\mathrm{pc}^{-2}$ (Lada and Dame, 2020; Leroy et al., 2017a; Schinnerer and Leroy, 2024) and volume densities of $\rho_{\mathrm{GMC}} \sim 1-10\,M_\odot\,\mathrm{pc}^{-3}$ (Colombo et al., 2014a; Leroy et al., 2017a), with a balance between their kinetic and potential energy due to self-gravity. The typical observed life time of a molecular cloud ranges between $5-30\,\mathrm{Myr}$ with longer life times found in higher mass galaxies (see review by Schinnerer and Leroy, 2024). A closer look at the properties, chemistry and observational results will be provided in Section 2.2 & 2.3 .

B) DENSE MOLECULAR GAS FORMATION: A subset of the gas within the cloud is able to reach higher densities (Figure 3B). High-resolution observations of individual clouds in the Milky Way have resolved molecular clouds into substructures, so-called "clumps" of (sub-)pc size with densities of $\sim 10^4-10^5\,\mathrm{cm}^{-3}$ and even denser "cores" within those clumps of sizes of $\lesssim 0.1\,\mathrm{pc}$ and densities of $\sim 10^5-10^7\,\mathrm{cm}^{-3}$. We refer to gas that resides in these clumps and cores as "dense (molecular) gas" from here on. A tighter correlation between higher column density gas (i.e., $n > 10^4\,\mathrm{cm}^{-3}$) and

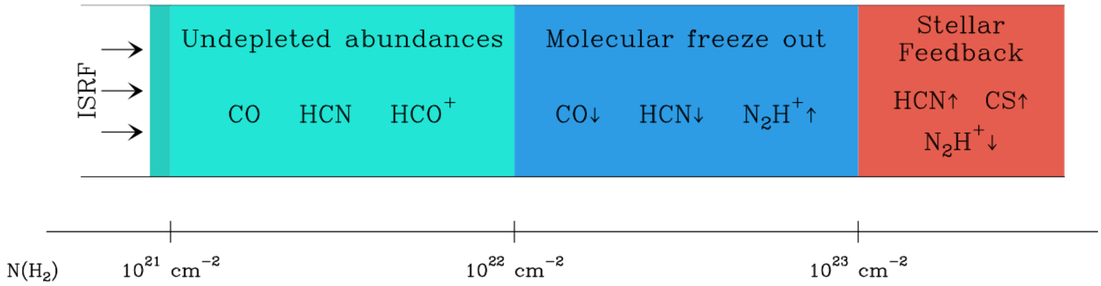

Figure 4: Schematic from Tafalla et al. (2023) based on sub-pc scale observations of several Milky Way molecular clouds. The penetration of the interstellar radiation field (ISRF) into the cloud interior decreases with increasing column density (N(H_2), allowing for cold and dense regions to exist. Within those cold and dense regions, molecules such as CO freeze onto dust grains, allowing other molecules such as N_2H^+ to increase in abundance, as their main destruction path is via reactions with CO. At even higher column densities (N(H_2)$\gtrsim 10^{23}\,\mathrm{cm}^{-2}$) high mass star formation occurs, and stellar feedback elevates the gas temperatures ($T > 30\,\mathrm{K}$), reversing the molecular freeze out and enhancing the abundance of temperature sensitive molecular species such as CS and HCN.

star formation rates (SFRs) (Lada et al., 2010) suggests that the denser molecular gas is fueling the star formation processes in contrast to lower column density gas. Column density, which describes the number of particles per unit area along the line of sight, is often used as reasonable proxy for the actual volume density of the gas (Leroy et al., 2017a). Many studies suggest a density threshold for core and thus star formation (Klessen and Glover, 2015, and references within), above which the gas fragments and becomes gravitationally unstable. The higher column density gas provides efficient shielding from the interstellar radiation field so that more complex molecules can form. With increased density, gas temperature decreases, and some molecules freeze onto dust grains, allowing other molecules to exist in larger quantities (Figure 4). How to reliably detect dense molecular gas, particularly in external galaxies is debated in the literature (see Section 2.3). Most of the lifetime of a cloud is dedicated to this stage of dense gas formation until the onset of star formation, also known as "ramp-up" time, of about $\tau \sim 4-20\,\mathrm{Myr}$ (Schinnerer and Leroy, 2024).

c) ONSET OF STAR FORMATION: The dense cores residing within dense clumps within molecular clouds are the regions in which stars form (Figure 3c). Well embedded within the cloud, these newly formed stars provide a new source of radiation and heating, changing the chemical composition of the gas surrounding the star (Figure 4). This can lead to the development of ionized hydrogen regions (HII regions) while infall is still occurring (MacKay et al., 2023). This stage in the cloud evolution is speculated to only last $1-3\,\mathrm{Myr}$ (Schinnerer and Leroy, 2024). Star formation out of molecular gas is generally inefficient, with low star formation efficiencies (SFE, the star formation rate per gas mass[1]) of $\sim 0.5-5\%$ (Tielens, 2021; Schinnerer and Leroy, 2024). Even when only considering the denser gas ($n_{H_2}^{\mathrm{dense}} \sim 10^4\,\mathrm{cm}^{-3}$), the efficiency at which dense gas is converted into stars is of the same order of $\sim 0.3\%$ (Schinnerer and Leroy, 2024). Gravity-dominated models alone struggle to explain such low star formation efficiencies, and the influence of turbulence has been suggested as main driving mech-

1 SFE is a measure of the fraction of molecular gas that is converted into stars under the assumption of a constant star formation rate over time. Usually, SFE is calculated per fiducial timescale such as the free-fall time τ_{eff}. τ_{eff} is the time it takes a spherical cloud to collapse based on solely self-gravity.

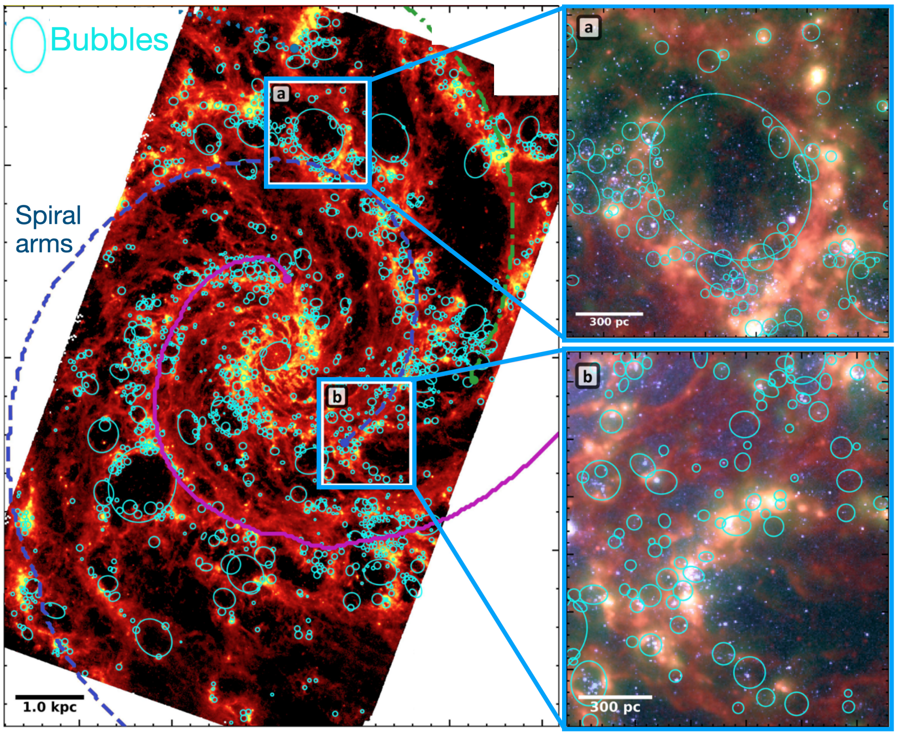

Figure 5: Bubbles in the disk of NGC 0628 (blue circles) identified by Watkins et al. (2023) based on high-resolution JWST observations. *Left:* MIRI F770W. *Right:* zoom in into selected regions with MIRI F770W (red), MUSE Hα (green) and HST B-band (blue). Many of those bubbles stem from stellar feedback mechanisms.

anism that prevents large quantities of the molecular gas from collapsing (Krumholz, 2014; Tielens, 2021).

The role of galaxy environment (i.e. top down picture) in shaping the dense gas star-forming regions in contrast to a rather independent small-scale process (bottom up view) is under discussion (Krumholz, 2014; Klessen and Glover, 2015, and references within). A tight relation between low-resolution dense gas observations and infrared luminosity indicative of star formation across galaxies (Gao and Solomon, 2004), aka the "Gao-Solomon-relation" might point to a universal density threshold for star formation, which I will present in more detail in Section 2.3. The observational challenges in detecting dense molecular gas across large-scale environments within galaxies to tackle these questions will be a major focus of this thesis.

D) STELLAR FEEDBACK AND CLOUD DISRUPTION: Over time, the continued input of energy and momentum from massive stars formed within the cloud are able to disrupt (photoionization) or destroy (displacement) the molecular cloud until it is fully dispersed (Figure 3d-f). The timescale between the onset of stellar feedback and the cloud dispersion is estimated to last $\sim 1-6$ Myrs (Schinnerer and Leroy, 2024). The effect of the stellar feedback creates cavities, often called "bubbles" in the interstellar medium (Watkins et al., 2023, Figure 5). Recent studies find increased star formation at the rims of those bubbles that indicate shock driven star formation and are associated with the spiral arms (Watkins et al., 2023; Barnes et al., 2023).

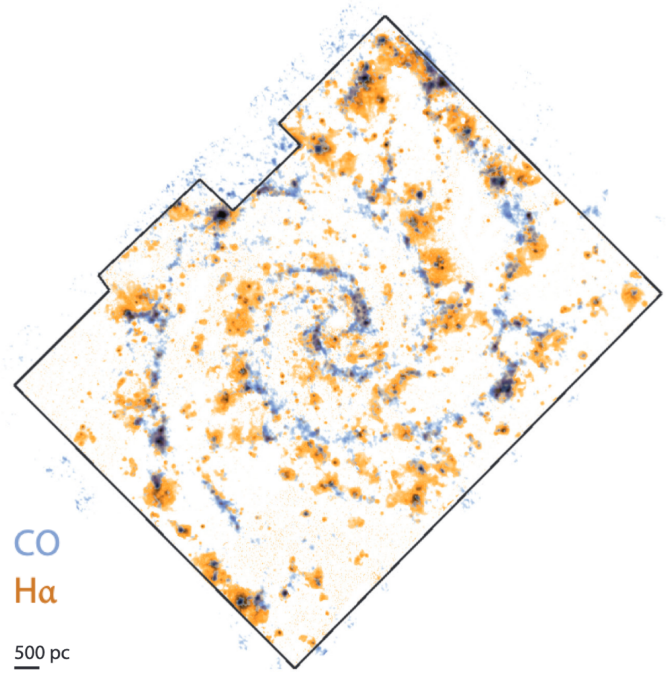

Figure 6: Tracers of recent star formation and molecular gas by Kreckel et al. (2018) in NGC 0628 at ~ 50 pc resolution show a clear distinct separation between the gas phases across the spiral arms of this nearby galaxy. Young star formation (gold) is traced by Hα emission observed with VLT/MUSE, molecular gas (blue) is traced by CO(2-1) emission observed with ALMA as part of the PHANGS survey.

2.1.3 Molecular cloud evolution viewed at extragalactic resolutions

In sub-pc scale resolution studies of molecular clouds in the Milky Way, the individual evolutionary stages of molecular clouds can be spatially separated (i.e., see Figure 2). However, in our own Galaxy, our position within the disk impedes a clear view of the morphological structures present and the bright galaxy center obscures clouds that may lay behind it. Other nearby galaxies, observed face-on, can provide a detailed view on those morphological structures, but their distances of several megaparsec make observations at high physical resolution very time intensive or even impossible. Yet, the morphology of a galaxy is one of the backbones of modern astronomy (e.g., Kormendy and Kennicutt, 2004; Buta, 2013), capturing not only the apparent structural geometry, but provides direct access to the underlying gravitational potential. Due to the dissipative nature of molecular gas it responds tightly to the underlying potential (Stuber et al., 2023b) and gas density and star formation processes are linked to and shaped by morphological structures.

As an example, spiral arms are known to host abundant star formation. In galaxies with two dominant spiral arms (also known as "grand-design"), the increased star formation is often explained by their commonly observed density wave nature (Buta, 2013): These dynamical features of increased gas density promote the accumulation of molecular material which eventually leads to increased star formation close to the spiral arms (e.g., Meidt et al., 2015; Pour-Imani et al., 2016; Querejeta et al., 2024). Efforts in the last years have achieved resolutions at which a separation between tracers of recent star formation and the bulk molecular gas can be seen across the spiral arms in extragalactic targets (Figure 6, Kreckel et al., 2018). The typical resolution at which star forming sites or HII regions and bulk molecular gas peaks can be separated in nearby galaxies occurs at scales of $\sim 100\,\mathrm{pc}$ (i.e., Kruijssen et al., 2018; Kim et al., 2023). This is a direct result of the natural separation of these processes via spiral arm density waves and has been measured in many galaxies (Roberts, 1969; Egusa et al., 2009, 2017). While not all spiral arms seem to be of density wave nature, the frequency of other spiral arm types (i.e. material arms, or transient dynamical spirals) in contrast to density wave spiral arms is still debated (e.g., Foyle et al., 2011; Ferreras et al., 2012; Martínez-García and González-Lópezlira, 2013, Querejeta et al., in prep.).

Another example of morphological structures important for star formation are stellar bars. Stellar bars are dynamical features that shock molecular gas and funnel it to galaxy centers while generally inhibiting star formation across large parts of their structure (e.g., Buta, 2013; Fraser-McKelvie et al., 2020; Sormani et al., 2023). Lastly, rings such as dynamical resonance rings are stable sites where large quantities of gas can efficiently accumulate, promoting star formation (e.g., Buta, 2013; Stuber et al., 2023b; Schinnerer et al., 2023, Gleis et al in prep.). The Central Molecular Zone (CMZ) in our Milky Way is assumed to have a ring-like structure as well (e.g., Henshaw et al., 2023), and the star formation in this ring compared to its gas content an open puzzle (Longmore et al., 2013).

How exactly this interplay between morphological features and molecular cloud properties happens is still under debate. Physical properties induced by such features that are found to be linked to the molecular gas include surface densities of molecular gas, stellar mass and SFR, but also internal cloud pressure or dynamical equilibrium pressure (recent examples by Sun et al., 2018, 2020, 2022). The centers of galaxies are established examples of high pressure and high stellar mass surface density and star formation conditions are thought to be more extreme in galaxy centers compared to their disks (Schinnerer and Leroy, 2024).

In summary, star formation can not be understood without the larger-scale galactic environment it resides in and is influenced by. Yet, the above mentioned results highlight the link between galactic environment and the *bulk* molecular gas distribution. To gain a proper understanding of the molecular cloud evolution in galaxies, observations of the **dense** phase of molecular gas are essential.

2.2 STUDYING MOLECULAR GAS

Molecular gas is the foundation of future star formation. Yet, many studies find variations in both the bulk and the dense gas to SFR relation, from individual clouds to our own galactic Central Molecular Zone (Longmore et al., 2013) up to environments within galaxies (i.e., Usero et al., 2015; Schinnerer and Leroy, 2024; Tanaka et al., 2024). Many of these variations are related to the question on how to reliably detect dense gas, which has proven challenging over the last years. This section will outline the properties and astrochemical conditions of molecules and promising dense gas tracers, as well as the challenges that arise when observing those tracers.

2.2.1 Molecular emission lines

In the interstellar medium, the frequent interaction of molecules with electromagnetic radiation and other matter results in radiation at various wavelengths, which can be used to obtain physical properties of the gas, such as gas temperature, density and ionization state. For molecules, we can, in general, distinguish three different types of excitation (see Bolatto et al., 2013; Tielens, 2021):

a) Electronic transitions - one or more electrons of the molecule get excited. Typical emission due to electronic transitions occurs at visual or ultraviolet wavelengths (few $\sim$eV energies)

b) Vibrational transitions - the vibrational energy states of the molecule get excited, the movement has no net angular momentum, but the lengths of the bonds between the molecule's atoms are changed. The oscillation of the atoms' positions around their equilibrium position results in quantized vibrational energy levels. This gives typical energies of $\sim 0.1 - 0.01$ eV , which correspond to infrared emission.

c) Rotational transitions - the state of the atoms around the center of mass gets excited, a movement with a non-zero angular momentum occurs, while the lengths of the bonds between the atoms are unchanged. Typical energies of rotational transitions are $\sim 10^{-3}$ eV, which corresponds to emission in the mm and sub-mm regime.

Once the higher energy levels of a molecule are populated, it can be de-excited and a photon of particular energy and wavelength is emitted. This can happen via radiative de-excitation or spontaneous decay (e.g., Draine, 2011; Tielens, 2021). Excitation of molecular energy levels can happen by absorption of radiation or collisions with other particles, such as hydrogen (atomic or molecular), electrons, or other molecular species. In dense regions, collisions also de-excite molecules without the emission of a photon. As the typical temperature of molecular gas is around 10-20 K, the conditions are not sufficient to populate the higher vibrational and electronic levels in most parts of the ISM (Bolatto et al., 2013; Draine, 2011). Such temperatures are, however, enough to allow for rotational transitions to happen, making the lower rotational transitions (i.e. transition from rotational quantum number $J = 1 \rightarrow 0$, or $J = 2 \rightarrow 1$) of various molecules the dominant probe used to observe molecular gas. Table 1 lists a few commonly observed spectral lines caused by these molecular rotational transitions and their respective frequencies.

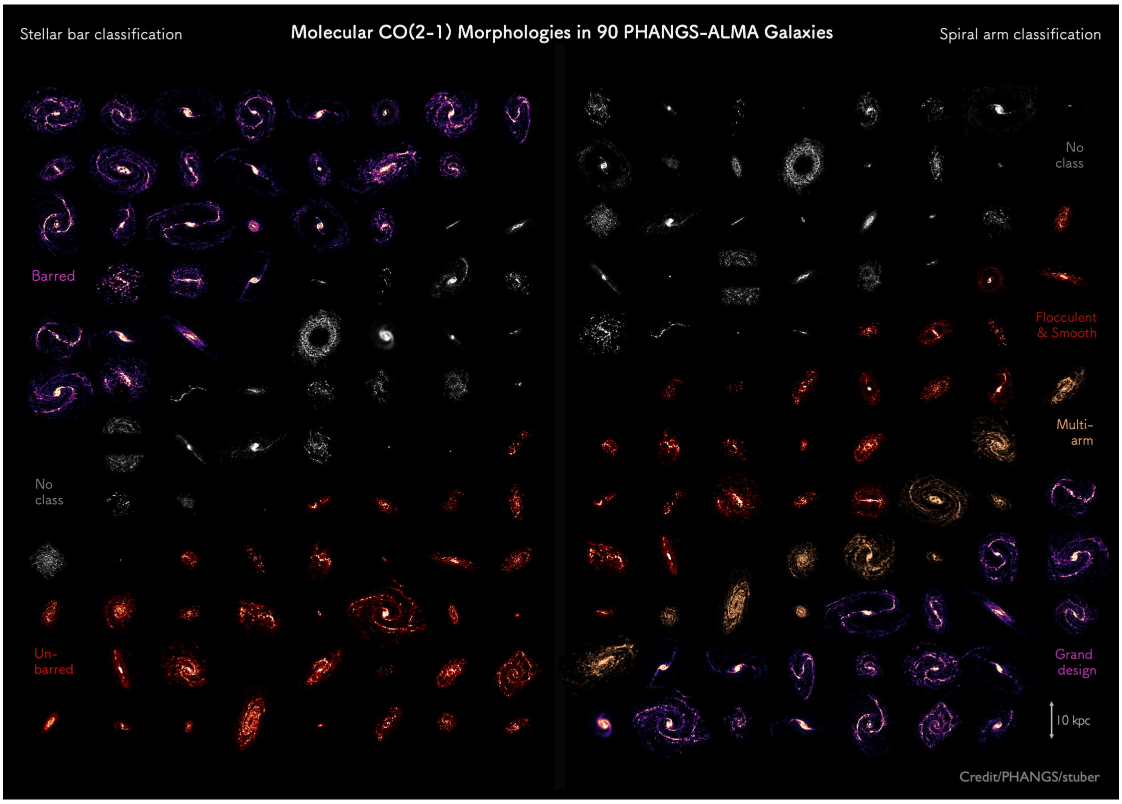

Figure 7: CO(2-1) observations in ~ 90 nearby star-forming galaxies from the PHANGS-ALMA survey at approximately cloud scale resolutions of $\sim 1'' \approx 100\,\mathrm{pc}$. From Stuber et al. (2023b). The dissipative nature of the molecular gas allows it to neatly trace morphological structures set by the underlying gravitational potential. The 90 galaxies are colored by their molecular-gas based bar classification (*left half*) and spiral arm classification (*right half*).

2.2.2 Bulk molecular gas

The most abundant molecule in the ISM, H_2, is challenging to observe. As a diatomic homo-nuclear molecule, it lacks a permanent dipole moment and thus the corresponding dipolar rotational transitions (Draine, 2011). Allowed rotational transitions include quadrupole transitions in the far-infrared and shorter wavelengths but the according spontaneous decay lifetimes are of order $\sim 100\,\mathrm{yrs}$ and the lowest possible transitions correspond to energies above ground state of $E/k_b \gtrsim 500\,\mathrm{K}$ (Bolatto et al., 2013), where k_B refers to the Boltzman constant. Therefore, its excitation is rare in the mostly cold ISM ($\sim 10-50\,\mathrm{K}$). Vibrational transitions of H_2 are at even higher energy levels and therefore temperatures and can mostly be found in shocked regions (Bolatto et al., 2013). Electronic transitions of H_2 are found in the far-UV range and often stem from the diffuse ISM. To reliably trace the molecular gas distribution, the second most abundant molecule, CO, has been proven reliable:

CARBON MONOXIDE – A PROXY FOR H_2: In contrast to H_2, rotational transitions of the second most abundant molecule, carbon monoxide ($^{12}C^{16}O$, CO hereafter), can be observed in the mm and sub-mm range. This molecule is excited (and de-excited) by collisions, and is an efficient coolant of the interstellar medium that radiates away kinematic energy of molecular gas (MacKay et al., 2023). The lowest rotational transition corresponds to temperatures of $E/k_b \approx 5.53\,\mathrm{K}$. Therefore, CO is easily excited in the cold ISM (Bolatto et al., 2013). These transitions further correspond to a wavelength regime (~ 3 – 4 mm, Table 1) in which the atmosphere is fairly transparent, which allows for ground-based observations with telescopes such as the ALMA and NOEMA interferometers (see Section 2.2.4). CO has been used as tracer of molecular gas from nearby to high-redshift galaxies (e.g., Helfer et al., 2003; Walter et al., 2016; Saintonge et al., 2017; Bolatto et al., 2017; Hodge et al., 2019; Leroy et al., 2021b, see also Figure 7).

Under the assumption that CO and H_2 are well mixed, one can convert the observed emission of CO into estimates of the H_2 masses via a constant so-called CO-to-H_2 conversion factor, α_{CO}. In reality, α_{CO} varies between and within galaxies (Bolatto et al., 2013) and so-called "CO-dark clouds", regions with plenty of H_2 but without or little CO emission have been found. Many prescriptions for an accurate calculation of α_{CO} have been developed, such as estimates that take into account metallicity, stellar mass surface density, velocity dispersion or CO isotopologues (e.g., Bolatto et al., 2013; Sun et al., 2022; Chiang et al., 2024; Teng et al., 2024).

ALTERNATIVE TRACERS OF BULK MOLECULAR GAS: To estimate the bulk molecular gas distribution, mainly H_2 column densities, alternative approaches are provided by dust emission, i.e., as observed by Herschel (Draine, 2011), or ionized carbon (C[II], Pineda et al., 2013). None of these alternative methods are without challenges and uncertainties, and thus, emission from CO remains the most commonly used bulk molecular gas tracer.

2.2.3 Tracing physical conditions within the molecular gas:

While CO emission is a fairly reliable tracer of the bulk molecular gas distribution, it does not differentiate well between diffuser molecular gas and the denser, colder or hotter gas clumps related to the actual formation of stars. To probe the physical conditions present within the molecular gas, the emission of other molecules can be used. To access denser gas regions, molecules are selected based on their high critical densities (see Section 2.3.1) or due to different chemical processes (see Section 2.3.3). A particular focus on denser gas is provided in Section 2.3. Some molecules are found to be abundant in shocked regions, such as HNCO (Martín et al., 2008; Kelly et al., 2017; Harada et al., 2024a), while others thrive in photo-dissociation regions, such as C_2H (e.g., Cuadrado et al., 2015; Kirsanova et al., 2021). Line ratios among molecular transitions are assumed to be in close connection with many physical gas conditions: gas temperature, ionization rate, density distribution.

Astronomical observations are often limited by the 2D projection along the line-of-sight and are not able to recover the actual 3D distribution of the gas. As ^{12}CO is abundant, its spectral lines are bright and radiation emitted within the interiors of a cloud can be reabsorbed immediately. In such a situation, the observable emission is no longer proportional to the column density in the upper level of the emission transition observed (Draine, 2011; MacKay et al., 2023). One example are the low-J transitions of ^{12}CO, which are found to be optically thick in many nearby galaxy observations (Draine, 2011; Sandstrom et al., 2013; den Brok et al., 2025, and references within). In contrast to that, the lower-J transitions of CO isotopologues ^{13}CO and C^{18}O are expected to remain optically thinner, providing insights into optical depth (Langer and Penzias, 1990; Cormier et al., 2018).

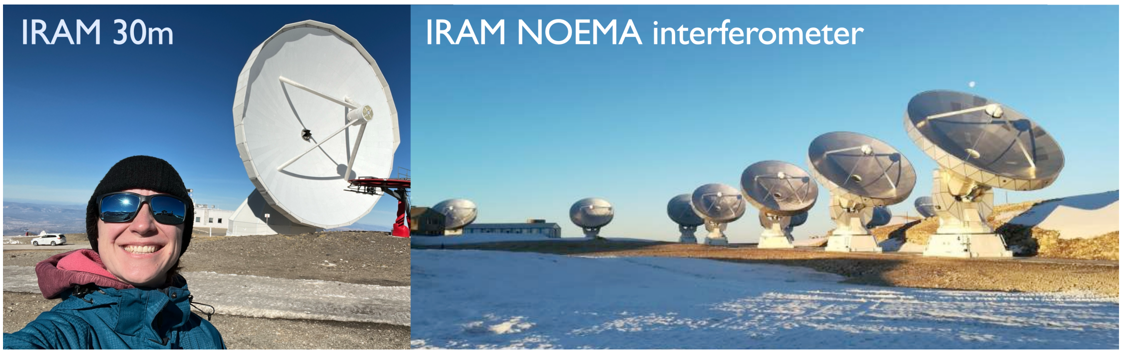

Figure 8: IRAM 30m single-dish telescope (left) located at ~ 3000 m elevation at the Pico Veleta in southern Spain, and the IRAM "NOrthern Extended Millimeter Array" (NOEMA) interferometer located on the Plateau de Bure at ~ 2500 m elevation in the French Alps. *Image credit:* Stuber *(left panel)*, IRAM *(right panel)*

2.2.4 Observing molecular gas in the (sub-) millimeter

Molecular rotational transition lines have wavelengths of a few mm to sub-mm. The observational techniques used for these wavelengths are the same as used for radio wavelengths and thus often referred to as "radio astronomy" or "radio interferometry". As the angular resolution of a telescope is defined as $\theta \sim \lambda/D$, it becomes non-trivial to resolve emission at these frequencies at scales of individual GMCs in local galaxies with a single telescope. Still, it can be achieved via interferometers by combining the collecting area of several telescopes separated by baseline b to achieve a resolution $\theta \sim \lambda/b$. Observations in the range from millimeter to radio wavelengths commonly make use of this technique, with baselines ranging from few meters to several kilometers with ALMA, NOEMA (Figure 8), SMA, up to ~ 8000 km with the VLBA.

A single radio dish of parabolic shape has a non-uniform reception pattern, which is best described as the Fourier transform of the aperture. The antenna response is maximized towards the center of the dish, in the form of the main-lobe. The half power beam width (Θ) of the main-lobe power describes the resolution of the radio telescope via $\theta \propto \lambda/\Theta$. Under the assumption of black body radiation with Rayleigh-Jeans approximation, the flux density B_ν of a source is linearly dependent on the temperature T (Draine, 2011; Maoz, 2016):

$$B_\nu = \frac{2\nu^2 k_B}{c^2} T \tag{1}$$

with speed of light c, frequency ν and Boltzman constant k_B. The signal measured via radio telescopes is therefore often described as "brightness temperature" where the detected signal is the sum of the source temperature and the sum of thermal noise temperatures. After the signal is received by the antenna, it is amplified and mixed to an intermediate frequency processable by modern electronics. Lastly, the analog signal is converted into a digital signal that can be analyzed by computers.

To obtain higher resolution, the signals of several radio antennas can be combined. The geometric differences in the location of two antennas with respect to the source creates a delay in the signal in one antenna compared to the other (Figure 9). Correcting the phase difference in this signal and combining the corrected signals of two antennas results in a point in the so-called "uv-plane" which is the Fourier transform of the sky-plane (the observable distribution of emission on the sky). Technically, this is achieved

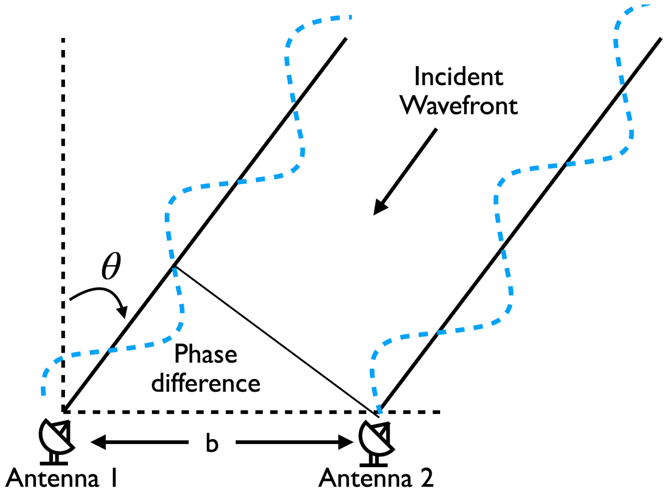

Figure 9: Schematic of interferometry between two antennas 1 and 2. The reception of the incident wavefront is delayed in Antenna 1 due to the geometrical differences in antenna location, creating a difference in the signal phase. *Image adjusted, based on:* `https://en.wikipedia.org/wiki/File:PhaseInterferometry.png`

by pairwise correlating the phase corrected signals of all available antennas. Due to the pairwise combination, n antennas produce $n(n-1)/2$ different uv-points, and interferometers, such as NOEMA, usually use $9-12$ antennas at a time. The amount and distribution of uv-points determines which structures of the source emission the interferometer can recover. For example, the longest baselines determines the smallest recoverable spatial scale. To maximize the coverage of the uv-plane with uv-points, earth's rotation can be used, as it changes the projected baseline towards the source.

These interferometers can collect emission stemming from small-scale structures, but filter out emission that stems from more spatially extended regions as the shortest baseline can never be zero (due to the size of the dish). This can lead to a significant underestimation of the total flux in nearby galaxies (e.g., Pety et al., 2013). To obtain a more reliable estimate of the total emission, it is common practice to combine interferometric with single dish observations. For NOEMA, this means adding in observations taken with the IRAM-30m telescope (Figure 8).

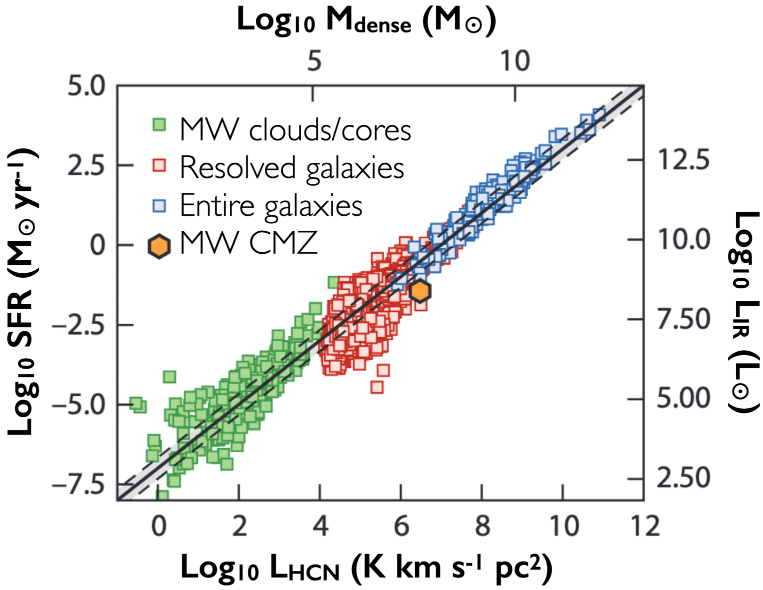

Figure 10: Gao-Solomon relation from Schinnerer and Leroy (2024), relating SFR, commonly obtained from infrared luminosity L_{IR}, and dense gas mass (M_{dense}), which can be estimated based on the emission of HCN (L_{HCN}). Observations from clouds and cores from the Milky Way (green squares) overall follow the same relation as observations from cloud-scales to kpc-scales in nearby galaxies (resolved galaxies, red squares) and from unresolved galaxies (blue squares). The Milky Way CMZ is underproducing stars based on the dense gas mass as obtained from L_{HCN}. Within galaxies, higher resolution increases the scatter of the relation (i.e. red squares compared to blue ones), suggesting that individual environments within galaxies impact the Gao-Solomon relation.

2.3 THE DENSE PHASE OF MOLECULAR GAS

Historically, observations have long found a relation between the gas mass of the ISM and tracers of recent star formation. One example is the "Schmidt-Kennicutt relation" (Schmidt, 1959; Kennicutt, 1998), which relates surface densities of gas (atomic and molecular hydrogen, HI and H_2, combined) with those of star formation rate (in external galaxies):

$$\Sigma_{SFR} \propto \Sigma_{Gas}^{N} \tag{2}$$

N is a positive usually larger-than-unity power-law index. However, many surveys over the past have shown three regimes within this relation with varying power law index from low to high values of Σ_{gas}: the HI dominated regime, the intermediate regime and the H_2 dominated regime. Observations of the bulk molecular gas show a tighter and nearly linear correlation with star formation rates, than when combining molecular and atomic gas phase, (e.g., Schruba et al., 2011; Leroy et al., 2013), and observations of denser molecular gas, such as traced by HCN emission, correlate even more tightly with tracers of star formation rate (e.g., Gao and Solomon, 2004; Bigiel et al., 2016; Neumann et al., 2025). The latter is also known as "Gao-Solomon relation" and shown in Figure 10, which connects observations of individual clouds in the Milky Way with observations of resolved and unresolved galaxies.

Observations like these led to the development of the modern picture of cloud evolution introduced in Section 2.1.2. While this seemingly universal law spans more than ten orders of magnitude in HCN luminosity, resolved galaxy observations show

Line (1)	ν_{rest} [GHz] (2)	n_{crit} [cm^{-3}] (3)	I_{CO}/I_{Line} (4)
HNCO(4–3)	87.93	1.0×10^4 a	~ 127 c
HCN(1–0)	88.63	3.0×10^5 b	~ 42 b
HCO^+(1–0)	89.19	4.5×10^4 b	~ 123 b
HNC(1–0)	90.66	1.1×10^5 b	~ 91 a
N_2H^+(1–0)	93.17	4.1×10^4 b	~ 278 d
$C^{18}O$(1–0)	109.78	4.8×10^2 b	~ 67 b
HNCO(5–4)	109.90	1.0×10^7 a	~ 173 c
^{13}CO(1–0)	110.20	4.8×10^2 b	~ 11 b
^{12}CO(1–0)	115.27	5.7×10^2 b	
^{12}CO(2–1)	230.54	4.4×10^3 b	~ 1.5 b

Table 1: Properties of molecular emission lines commonly observed in extragalactic targets. This table lists their rest frequency (2), critical density n_{crit} (3) obtained from either a: Jiménez-Donaire et al. (2019) or b: Schinnerer and Leroy (2024, and references within) and the typical line ratio with CO(1-0) (4) from a, b and the following additional sources: c: average value from Takano et al. (2019), Watanabe et al. (2014), and Chen et al. (2017). d: Jiménez-Donaire et al. (2023). Critical densities and typical line ratios are collected by source a based on various sources. Further details can be found in their table 4.

a larger scatter than observations of unresolved galaxies. Those resolved observations further show trends with galaxy environments within galaxies: Centers of galaxies and other high stellar surface density, high-pressure parts of galaxies show an increase in dense gas fractions (estimated via HCN/CO) (Usero et al., 2015; Gallagher et al., 2018a; Jiménez-Donaire et al., 2019), but many centers host little star formation given their vast dense gas reservoir (Schinnerer and Leroy, 2024). Our own Milky Way's central molecular zone (CMZ) is no exception and has little star formation despite hosting large quantities of dense gas (Longmore et al., 2013). In addition, radiation by active galactic nuclei (AGN), or their commonly found galactic molecular outflows (Stuber et al., 2021) are additional features that seemingly impact the gas conditions and star formation: Outflows are suggested to both enhance or quench star-formation via shocks that trigger (Silk, 2013; van Breugel and Dey, 1993) or destroy molecular gas (Sturm et al., 2011; Fabian, 2012). Extreme conditions similar to galaxy centers are found in starburst galaxies and galaxy mergers (that sometimes lead to starbursts), or in (Ultra-) luminous infrared galaxies (U/LIRGS), which frequently host outflows as well (e.g., Pereira-Santaella et al., 2018). Those galaxies typically depict very high ratios of HCN/CO in their centers (Schinnerer and Leroy, 2024). These observations suggest the impact of external factors on star formation processes instead of a fixed density threshold for star formation.

2.3.1 Critical densities

While historically, HCN has been the mostly used tracer of dense gas in galactic and extragalactic studies, recent Galactic observations question the ability of HCN to trace actual dense gas. In this Section, I introduce some of the common criteria used to select dense gas tracing molecular emission lines, as well as their limitations and alternatives.

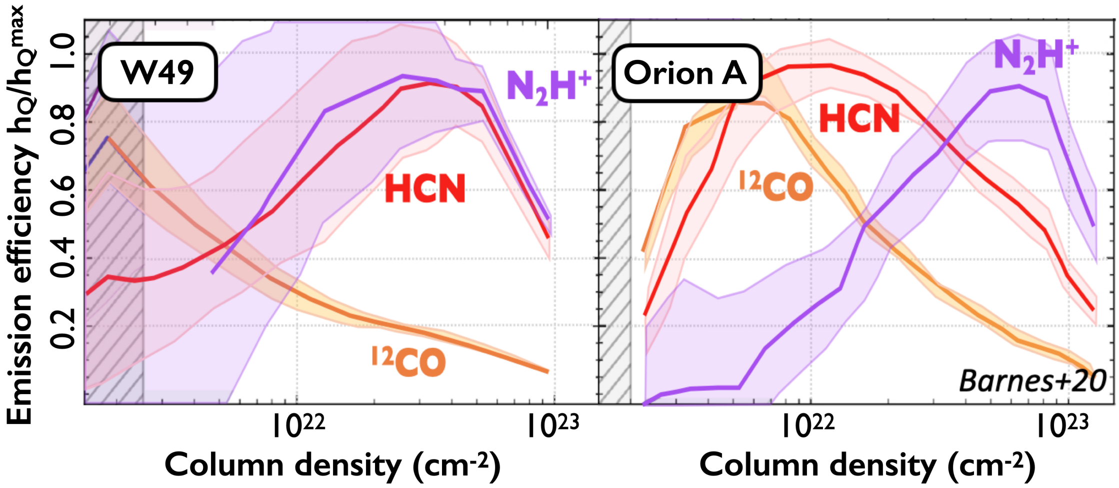

Figure 11: Emission efficiency $h_Q/h_{Q,max}$ for different molecules as a function of column density in two Milky Way clouds, adapted from Barnes et al. (2020). h_Q is defined as ratio of integrated intensity of the different molecules and the molecular hydrogen column density. The massive star forming region W49 spans an area of $\sim 100 \times 100$ pc and is observed at ~ 3 pc. Orion A is larger in area, but observed at ~ 0.05 pc scales.

The physical conditions of molecular clouds are dominated by temperature, density, radiation field and cosmic ray flux. While radiative de-excitation dominates the emission process at lower densities, de-excitation via collisions with other particles dominate the emission in higher density regions (MacKay et al., 2023). To better describe the relation between excitation, radiative decay and de-excitation, and the dependency on gas density, one can refer to a molecule's "critical density". This density varies for each molecule and depends on the kinetic temperature of the gas. At densities below the critical density, on average, each exciting collision is followed by radiative de-excitation. At densities above the critical one, collisional de-excitation becomes the dominant mechanism. Under ideal conditions, the maximum emission efficiency thus happens close to critical density (MacKay et al., 2023). Molecules with comparably high critical densities are therefore suggested as "dense gas tracers", with the expectation of brighter emission originating from higher density regions. We list some of the commonly observed molecular lines and their critical densities in Table 1. Historically the so-called "critical density" has been one major selection criteria for dense gas tracing molecular emission lines. Hydrogen cyanide, HCN, has a comparably high critical density of $n_{crit} \sim 10^5\,\mathrm{cm}^{-3}$ and is – in contrast to many other molecules – comparably bright (HCN(1-0) is $\sim 5-10$ times fainter than CO(1-0) in LIRGS and ULIRGS and ~ 30 times fainter than ^{12}CO (1-0) in normal galaxies).

In reality, conditions are not ideal and many molecules are able to emit brightly below their critical densities due to radiative trapping or collisions with electrons (Schinnerer and Leroy, 2024). This had led to the development of the temperature dependent "effective excitation density" n_{eff} (Shirley, 2015), that takes into account radiative trapping and is typically $1-2$ orders of magnitude lower than n_{crit}. Figure 11 shows variations in the emission efficiency of HCN, CO and N_2H^+ in two Milky Way clouds as function of column density. The emissivity describes how efficient a molecule emits as a function of gas density and is often defined as ratio between line intensity and gas column density (Leroy et al., 2017b; Schinnerer and Leroy, 2024).

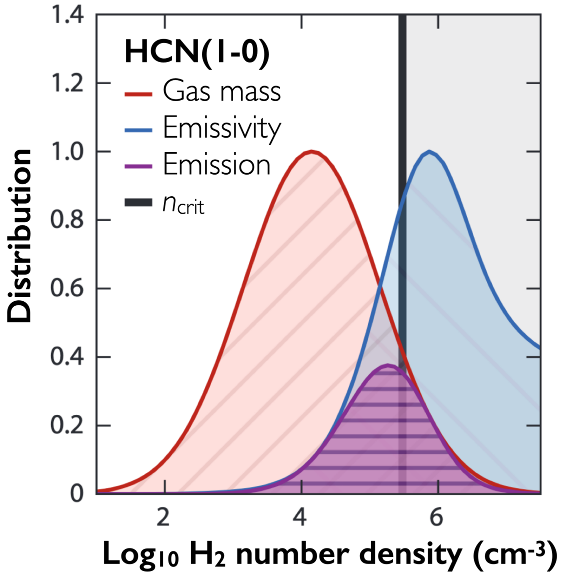

Figure 12: The molecular line emission of a parcel of gas (purple) is the convolution of the emissivity (blue) and mass distribution (red) of said gas. A molecular transition such as HCN(1-0) has a comparably high critical density (black solid line) above which the emissivity peaks. Yet, if the mass distribution peaks at lower densities, then a significant fraction of the actual emission can still stem from densities lower than critical.

2.3.2 Emission vs Emissivity

Gas at densities below the critical one still emits – it simply does not emit at its maximum efficiency. If most of the gas has densities lower than critical in contrast to densities being above critical, then the observed integrated emission of such a region can be dominated by the lower density gas. The observed emission is the convolution of the gas mass distribution and the emissivity of a molecular transition line as illustrated for HCN(1-0) in Figure 12.

However, it is for this exact reason – that the emissivity of dense gas tracers depends on densities below n_{crit} – that line ratios with bulk molecular gas, i.e., HCN/CO are thought to be sensitive to the physical density distribution within one beam (Leroy et al., 2017b; Schinnerer and Leroy, 2024). Observations find the HCN/CO ratio tightly linked with estimates of gas mass surface density Σ_{mol} across many nearby star-forming galaxies (see most recent overview by Neumann et al., 2025), suggesting that this ratio is a first-order tracer of the average gas density.

2.3.3 Astrochemistry of common dense gas tracers

Based on critical density, effective critical density and its brightness, the lower-J transitions of HCN, but also HNC and HCO^+ are commonly used to access dense gas – often as line ratios with ^{12}CO (e.g., review by Schinnerer and Leroy, 2024). In addition to density, temperature and radiation might change the abundance and excitation of those molecules (e.g., Harada et al., 2019; Hacar et al., 2020; Tielens, 2021). The term "astrochemistry" describes the chemical processes leading to the formation and destruction of various molecules inferred from both observations in laboratories on Earth as well as in space. For extragalactic observations these laboratories are often regions of several pc to kpc in size, and astrochemistry requires, i.e., temperature and radiation field to stay reasonably constant.

The list below is far from complete and other molecules (i.e., CN) are proposed as dense gas tracers "as we speak". Below I focus on the dense gas tracers that are most commonly used and that are part of the observations that are the foundation of this thesis.

HCN AND HNC: In cold molecular clouds, hydrogen cyanide, HCN, and its isomer hydrogen isocyanide, HNC, are primarily formed via dissociative recombination of HCNH+ via: $\mathrm{HCNH^+ + e^- \longrightarrow A + H}$ (Loison et al., 2014) where A corresponds to both HCN and HNC which are produced in equal quantities in cold dense regions, at temperatures $\lesssim 200\,\mathrm{K}$ (Hacar et al., 2020). Both molecules are found in dense clouds (Loison et al., 2014), diffuse clouds (Liszt and Lucas, 2001), translucent molecular clouds (e.g., Turner et al., 1997) and star-forming regions (Jørgensen et al., 2004).

At warmer temperatures, neutral-neutral reactions are proposed to off-balance the abundance ratio of both molecules towards HCN: $\mathrm{HNC + H \longrightarrow HCN + H}$ and $\mathrm{HNC + O \longrightarrow NH + CO}$. The energy barrier of these reactions is disputed, with estimates ranging from a few 100 K up to $\Delta E \sim 2000\,\mathrm{K}$. Hacar et al. (2020) find the HCN/HNC ratio being a reasonable indicator of gas temperature in colder gas ($\sim 10 - 40\,\mathrm{K}$) in the Orion nebula at sub-pc resolution, but the usage in lower-resolution extragalactic results remains questionable (e.g., Eibensteiner et al., 2022). Other extragalactic studies suggest HCN/HNC as indicator of FUV radiation (Santa-Maria et al., 2023; Harada et al., 2024b) or cosmic ray ionization rate (CRIR) (Behrens et al., 2022).

N_2H^+: The molecular ion diazenylium, N_2H^+, is nowadays the preferred dense gas tracer in many Milky Way studies (e.g., Pirogov et al., 2003; Kirk et al., 2007; Bergin and Tafalla, 2007; Pety et al., 2017). Instead of very high critical densities, this molecules chemically exists in dense and cold regions. Its main destruction mechanism is the reaction with CO. N_2H^+ therefore thrives in cold regions where ^{12}CO is depleted by freezing to dust grains. Further, CO reacts with H_3^+, which is necessary for the formation of N_2H^+. Removing CO leads to a decreased N_2H^+ destruction and increased formation (Bergin and Tafalla, 2007). These dense and cold regions are small in spatial size, which – in addition to N_2H^+ being less abundant – makes it challenging to observe in galaxies, as the low resolution will dilute the already weak emission.

N_2H^+ is mainly formed by protonation of N_2: $\mathrm{N_2 + H_3{}^+ \longrightarrow N_2H^+ + H_2}$.
In addition to the destruction via CO molecules, an increased cosmic ray ionization rate is found to convert N_2H^+ into HCO^+ via: $\mathrm{N_2H^+ + CO \longrightarrow HCO^+}$ (Harada et al., 2019).

HCO^+: Another commonly observed molecular ion is HCO^+ due to its brightness and moderate critical density. As its frequencies are very similar to HCN and HNC, it is fairly easy to observe all three molecules in a single observation. HCO^+ is formed out of H_3^+ in colder and denser regions similar to N_2H^+, but via the reaction with CO: $\mathrm{H_3{}^+ + CO \longrightarrow HCO^+ + H_2}$ (Indriolo and McCall, 2012; Bisbas et al., 2015; Luo et al., 2024b, e.g.,). In regions where CO is frozen to dust grains, H_3^+ is mainly reacting to form N_2H^+ instead of HCO^+. Electron recombination can reverse the process to form CO out of HCO^+: $\mathrm{HCO^+ + e^- \longleftrightarrow CO + H}$. In dense and warmer clouds the number density of free electrons should equal the number density of the most abundant ions which include N_2H^+ and HCO^+ as well as H_3^+ and H_3O^+ (Luo et al., 2024a): $\mathsf{n(e\text{-})} = \mathsf{n(HCO^+)} + \mathsf{n(N_2H^+)} + \mathsf{n(H_3{}^+)} + \mathsf{n(H_3O^+)}$.

3 THE WHIRLPOOL GALAXY

3.1 A UNIQUE LABORATORY FOR STAR FORMATION

The Whirlpool galaxy, also known as NGC 5194 or M51a (Figure 13) is one of the most iconic nearby spiral galaxies in the northern hemisphere. Its proximity ($D \sim 8.58\,\mathrm{Mpc}$, McQuinn et al., 2016; systemic velocity $v_{sys} \sim 471.7 \pm 0.3\,\mathrm{km/s}$, Shetty et al., 2007) and high surface brightness have made it the target of many studies for decades, and their combined results have led to a significant improvement of our understanding of star formation (Section 3.1.1). While its interaction with dwarf companion galaxy M51b (Figure 13) causes slightly more complex dynamics, its high surface brightness and nearly face-on orientation (inclination $i \sim 22 \pm 5°$, Colombo et al., 2014b) make M51a (hereafter referred to as M51) uniquely suited to study the interplay between its galactic environment and star formation.

M51 is a fairly normal local star-forming galaxy (Figure 14) with a stellar mass of $M_\odot \sim 10^{10.5}$ and a total galaxy star formation rate of $\sim 3.4\,M_\odot\,\mathrm{yr}^{-1}$ (Calzetti et al., 2005). The total molecular gas reservoir has a mass of $\sim 2 \times 10^9\,M_\odot$ (Schuster et al., 2007) and is comparable to other typical nearby star-forming galaxies (Figure 14).

3.1.1 Morphology of M51

M51 is most famous for its two "grand-design" spiral arms that give it its whirlpool-like appearance and are likely shaped by the interaction with dwarf companion M51b. In addition to those spiral arms, M51 offers additional environments such as a molecular ring, nuclear bar and AGN.

Spiral arms: The two spiral arms in M51 are called a "grand-design" spiral structure. The inner part of the spiral arms in M51 are usually considered classical density waves (at radii $R \lesssim 80'' \lesssim 3.4\,\mathrm{kpc}$), which are patterns of increased surface density that are self-regulated, long-lasting and slowly rotating with a single angular speed (Lin and Shu, 1964; Bertin et al., 1989a,b; Meidt et al., 2013, see Section 2.1.3). Within the radius of co-rotation ($\sim 100''$ for M51, Querejeta et al., 2016a) the gas and stars rotate at a faster angular speed than the density wave, which means that gas and stars can overtake the spiral arm. As the density wave is expected to promote the accumulation of molecular gas and dense gas formation, this leads in theory to an evolutionary offset across the spiral arms (e.g., Roberts, 1969; Egusa et al., 2009). The molecular clouds (traced by CO) are located close to the potential well, while star formation (traced by e.g., $H\alpha$)

Figure 13: The Whirlpool galaxy (NGC 5194, Messier 51a) is interacting with its dwarf companion galaxy (NGC 5195, M51b) about ~ 10 kpc north of the center of M51a as seen by the HST rgb image. *Image credit:* NASA, ESA, S. Beckwith (STScI), and The Hubble Heritage Team (STScI/AURA)

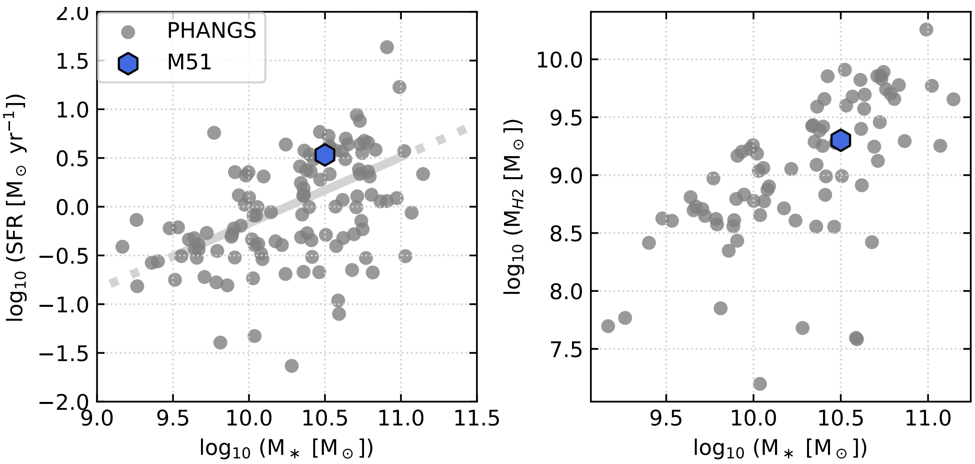

Figure 14: Left panel: Global SFR as function of stellar mass (M_*) for ~ 100 galaxies from the PHANGS survey (Leroy et al., 2021b), which is a sample of nearby galaxies representative of typical nearby star-forming galaxies. We add the main sequence of star-forming galaxies (SFMS) from Leroy et al. (2019, grey line) and interpolate towards higher and lower stellar masses (grey dotted line). M51 (blue hexagon) is a representative star-forming galaxy. The SFMS describes the average relation between stellar mass and SFR that the majority of local star-forming galaxies follow. Galaxies with higher SFRs (above the SFMS) are called starbursts. Elliptical galaxies are usually found well below the main sequence, often referred to as "red-sequence".
Right panel: Molecular gas mass (M_{H2}) as function of stellar mass for the same set of galaxies. In the so-called "molecular gas main sequence" (Lin et al., 2019) M51 is also fairly normal compared to the PHANGS galaxies (Leroy et al., 2021b).

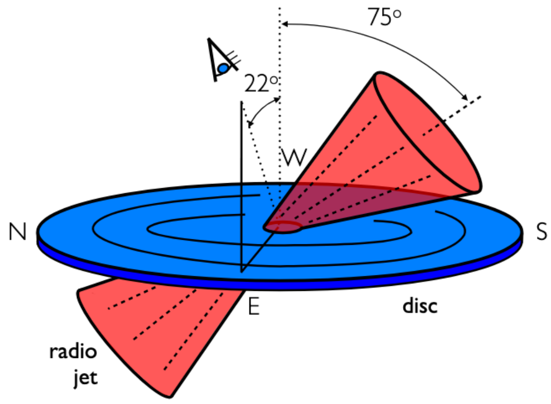

Figure 15: Approximate orientation of the radio jet compared to M51's disk. Schematic from Querejeta et al. (2016b) based on the kinematic disk orientation from Colombo et al. (2014b) and the jet inclination from Cecil (1988).

is offset to the leading (convex) side of the spiral within those inner radii (e.g., Egusa et al., 2009, 2017, Querejeta et al. in prep.).

At larger radii ($R \gtrsim 90''$) the spiral arms are usually considered features of material moving at series of distinct speeds, often referred to as "material arms" (Meidt et al., 2013; Colombo et al., 2014b). While gas and stars can overtake or be overtaken by the spiral arm in a density wave scenario, the material arms are made of stars and gas that move together over time.

Molecular ring: The two spiral arms converge in the inner disk to form a (pseudo-) ring at $r \sim 1.3\,\mathrm{kpc}$, at which molecular gas accumulates. Due to the abundant star formation found in this ring, it is sometimes considered a starburst ring (Calzetti et al., 2005).

Inner bar: Within the molecular ring, at radii $r \lesssim 1.2\,\mathrm{kpc}$, a nuclear stellar bar funnels gas to the very center of M51 (e.g., Querejeta et al., 2016a). This nuclear bar is thought to drive another dynamical mode (m=3 mode) with co-rotation radius at $r \sim 1.3\,\mathrm{kpc}$ (Colombo et al., 2014b). Within the molecular ring ($r \lesssim 20'' \approx 0.8\,\mathrm{kpc}$), there is little to no star formation (Meidt et al., 2013), but X-ray emission is bright (Zhang et al., 2025).

AGN and outflow: At the very center of M51, a Seyfert type 2 AGN is located, which drives a large-scale radio jet that is inclined $\sim 15°$ to the disk (Querejeta et al., 2016b, see Figure 15) and removes more molecular gas (depending on the geometry of the outflow up to $\sim 10-90\,\mathrm{M_\odot\,yr^{-1}}$) than there is secularly inflowing to the center (inflow $\sim 1\,\mathrm{M_\odot\,yr^{-1}}$ Querejeta et al., 2017).

Overall, the morphology and properties of M51 are complex, but well studied. The multitude of galactic environments make M51 the perfect laboratory to test star-formation laws under different conditions.

3.2 OVERVIEW OF MOLECULAR GAS OBSERVATIONS IN M51

The Whirlpool galaxy is well observed across the full electromagnetic spectrum, including many observations of its molecular gas reservoir. The bulk molecular gas, as

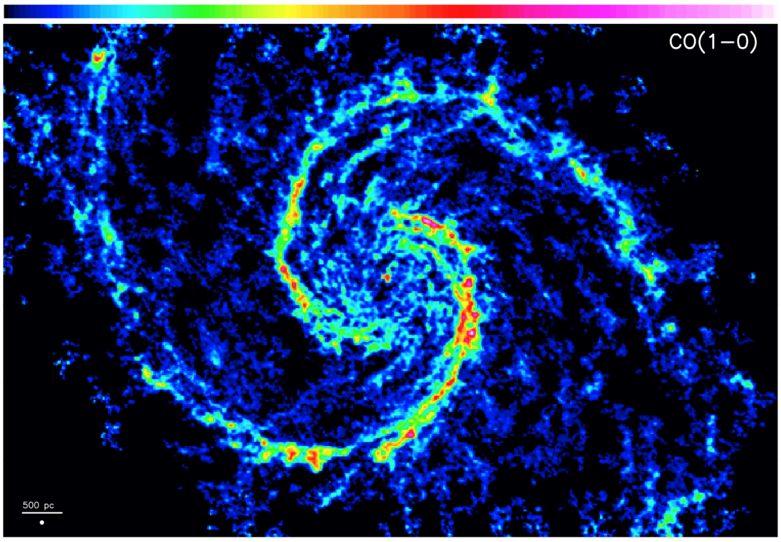

Figure 16: CO(1-0) at $1'' \sim 40\,\mathrm{pc}$ resolution in the central disk of M51 from PdBI Arcsecond Whirlpool Survey (PAWS, Schinnerer et al., 2013).

traced by CO(1-0) has been observed since Scoville and Young (1983) with the Five College Radio Astronomy Observatory telescope, followed by various other lower-resolution observations (an illustrative, yet incomplete list: Rydbeck et al., 1985; Vogel et al., 1988; Lord and Young, 1990; Garcia-Burillo et al., 1993; Nakai et al., 1994; Aalto et al., 1998, and many more). Continuous efforts have revealed both cloud-scale observations of individual regions within M51 (e.g., $\sim 2''$ in the center or $0.7''$ in one spiral arm; Scoville et al., 1998; Egusa et al., 2011) or large-scale maps of M51 at lower resolutions (e.g., 12″and 4″resolution maps Schuster et al., 2007; Koda et al., 2009). One of the most recent efforts by Schinnerer et al. (2013) led to a 1″resolution ($\sim 40\,\mathrm{pc}$) high-sensitivity mapping of M51 (Figure 16, PAWS survey). These deep observations have led to a superb understanding of the bulk molecular gas distribution (Schinnerer et al., 2013; Pety et al., 2013), its gas kinematics (e.g., Meidt et al., 2013; Colombo et al., 2014b) and molecular cloud population (e.g., Hughes et al., 2013; Colombo et al., 2014a; Meidt et al., 2015).

The bulk molecular gas distribution is one key property of the ISM, but improving our understanding of star formation requires insights from other molecular lines as well, particularly the dense molecular tracers (compare Section 2.3): ß At kiloparsec-scales, Watanabe et al. (2014) detected 13 different molecular species, including N_2H^+ and HNCO in two pointings in the southern spiral arms. The EMPIRE survey (Jiménez-Donaire et al., 2019) observed dense gas tracers HCN, HNC and HCO^+ across M51's entire disk with the IRAM 30m telescope and the CLAWS survey (den Brok et al., 2022) added CO isotopologues, ^{13}CO, $C^{18}O$, and dense gas tracing molecule N_2H^+ (1-0) at similar (kiloparsec) resolution across M51's entire disk (see Section 4.4.4 for a comparison). At higher resolutions, individual regions within M51 have been targeted: Matsushita et al. (2015) observed HCN(1-0) at $\sim 30\,\mathrm{pc}$ resolution in the very center to study the AGN and outflow, and Querejeta et al. (2019) observed the same molecular line at $\sim 150\,\mathrm{pc}$ in three pointings within M51 (see Section 4.4.4). At the same resolution, Chen et al. (2017) observed HCN, HNC and HCO^+ (1-0) in one pointing in the outer spiral arm $\gtrsim 120''$ north of the center.

The combination of high-resolution observations of the bulk molecular gas, and individual regions within M51 and the low resolution observations across the entire disk have revealed significant variations in the molecular cloud composition with the environments present in M51. The natural next step is to combine the advantages of both kinds of data - obtaining a high-resolution high-sensitivity multi-molecular species map across multiple environments. This is what the "Surveying the Whirlpool at Arcseconds with NOEMA" (SWAN) survey – the core of this thesis – provides.

3.3 SCIENTIFIC GOALS AND OUTLINE OF THIS THESIS

The key open questions on the star formation process include the following: What is the impact of galactic environment on star formation? Is star formation driven by local gas density thresholds set by its immediate surroundings, or are the larger-scale dynamics within galaxies fundamentally shaping the molecular clouds and dense gas star formation that resides in it? The work presented in this thesis is motivated by these questions. More specifically:

- **Where do we detect emission from molecules sensitive to different gas conditions? How much does it vary with galactic environment?** In Chapter 4, I will present the observations, data reduction and quality assurance of the IRAM 200h NOEMA+30m SWAN survey. I will qualitatively compare the emission of the nine detected lines within the disk and analyze how their emission compares between the center and the disk.

- **How robust are common dense gas tracers at cloud-scales?** I will test the usage of the commonly used dense gas tracer HCN by comparing its emission with the fainter "gold-standard" dense gas tracer N_2H^+ in Chapter 5. In Chapter 6 this analysis will be expanded to include HNC and HCO^+.

- **What are the environmental conditions that set the dense gas fraction within M51?** In Chapter 6, I will explore the connection between the larger-scale galactic environments present in M51 and the emission of all detected dense gas tracers from the SWAN survey. I will test the physical conditions the dense gas responds to and how they vary with galactic environments.

SURVEYING THE WHIRLPOOL AT ARCSECONDS WITH NOEMA (SWAN)

4 SURVEY DESIGN AND OBSERVATIONS

This chapter including Appendix A comprises the article published in the Astronomy & Astrophysics journal volume 696 in 2025 under the title "Surveying the Whirlpool at Arcseconds with NOEMA (SWAN) - II Survey design and observations". The paper has been reformatted to match the style of this thesis.

Stuber, S.K., Pety, J., Usero, A., Schinnerer, E., Bigiel, F., Jiménez-Donaire, M.,
den Brok, J., Leroy, A.K., Galić, I., Hughes, A., Thorp, M.,
and the PHANGS team

Contributions from co-authors: *The following significant contributions are performed from authors other than the first author and are not explicitly mentioned in the text:*

- *Quality analysis: The error beam analysis presented in Appendix A.1, mentioned in Section 4.3.2 is performed by co-author J. den Brok based on his work on the CLAWS survey (den Brok et al., 2022, their Appendix A). The CLAWS data is partially incorporated in the SWAN survey presented in this work.*
- *Quality analysis: The comparison between the newly obtained and archival 30m observations used in this work (Appendix A.2, mentioned in Section 4.3.2) is performed by co-author M. Jiménez-Donaire based on their expertise on the archival data set obtained from the EMPIRE survey (Jiménez-Donaire et al., 2019).*

Abstract

We present Surveying the Whirlpool at Arcseconds with NOEMA (SWAN), a high-resolution, high-sensitivity survey to map molecular lines in the 3mm band in M51 (the Whirlpool galaxy). SWAN has obtained the largest high-sensitivity map ($\sim 5 \times 7\,\mathrm{kpc}^2$) of N_2H^+ emission at ~cloud-scale resolution ($3'' \sim 125\,\mathrm{pc}$) in an external galaxy to date. Here, we describe the observations and data reduction of ~ 214 hours of interferometric data from the Northern Extended Millimetre Array (NOEMA) and ~ 55 hours of tailored new observations with the 30m telescope of the Institut de radioastronomie

millimétrique (IRAM), as well as the combination of these NOEMA and new IRAM-30m observations with ∼ 14 hours of archival IRAM-30m observations. We detect widespread emission from nine molecular transition lines. The J=1-0 transitions of the CO isotopologs ^{13}CO and C^{18}O are detected at high significance across the full observed field of view (FoV). HCN(1-0), HNC(1-0), HCO$^+$(1-0), and N$_2$H$^+$(1-0) are detected in the center, molecular ring, and spiral arms of the galaxy, while the shock tracer HNCO(4-3) and (5-4) and PDR tracer C$_2$H(1-0) are detected in the central ∼1 kpc and molecular ring only. For most of the lines that we detect, average line ratios with respect to ^{12}CO are increased by up to a factor of ∼ 3 in the central 1 kpc, where an active galactic nucleus and its low-inclination outflow are present, compared to the disk. Line ratios between CO isotopologs show less variation across the SWAN FoV. Across the full SWAN FoV, ^{13}CO, C^{18}O, HCN, HNC, HCO$^+$ and N$_2$H$^+$ are $8\pm^{2}_{2}$, $29\pm^{7}_{6}$, $17\pm^{3}_{5}$, $37\pm^{5}_{10}$, $26\pm^{5}_{3}$ and $63\pm^{38}_{10}$ times fainter than ^{12}CO, respectively, in pixels where each line is significantly detected. Although we observe variations in line ratios between larger-scale environments like the center and disk of M51, the scatter within each environment also indicates the influence of smaller-scale processes. The ability to measure these effects is only possible thanks to the high resolution and high sensitivity of the SWAN dataset across multiple environments. This provides the sharpest view of these molecular transitions over the largest physical area ever captured in an external galaxy.

4.1 INTRODUCTION

Star formation is a fundamental process for mass growth of galaxies, and thus their evolution. While the rate of star formation is closely tied to the amount of molecular gas present on scales ranging from individual cores inside molecular clouds to entire galaxies (e.g., Bigiel et al., 2008; Kennicutt and Evans, 2012), (massive) star formation occurs only in the densest regions of molecular clouds (Gao and Solomon, 2004; Wu et al., 2005; Lada et al., 2012; Evans et al., 2014). These dense regions within molecular clouds are generally too small to be resolved at extragalactic distances. Therefore, to study molecular gas at different densities, especially in external galaxies, astronomers combine emission lines that span a wide range of critical or effective excitation densities (e.g., Shirley, 2015).

The high-dipole moment molecules HCN, its isomer HNC, and HCO$^+$ all have high critical densities and relatively bright rotational transitions in the $\lambda = 3$ mm window. As a result, these emission lines have often been considered as "dense gas tracers" and have been observed in extragalactic targets for decades (Helfer and Blitz, 1993; Aalto et al., 1997, 2002; Gao and Solomon, 2004; Brouillet et al., 2005; Aalto et al., 2012; Buchbender et al., 2013; Usero et al., 2015; Bigiel et al., 2016; Jiménez-Donaire et al., 2019; Krieger et al., 2020; Bešlić et al., 2021; Eibensteiner et al., 2022; Rybak et al., 2022; Imanishi et al., 2023; Neumann et al., 2023b). Many of these surveys reveal systematic variations in line ratios like HCN/CO as a function of the environment (see references above and review by Schinnerer and Leroy, 2024), suggesting that the host galaxy sets the initial conditions for star formation. Even further, the efficiency with which stars are formed out of dense gas seems to vary drastically within larger-scale structures, such as larger-scale bars (Bešlić et al., 2021; Eibensteiner et al., 2022; Neumann et al., 2024) or even our own Milky Way's central molecular zone (CMZ, Longmore et al., 2013).

Unfortunately, these emission lines are also typically $\gtrsim 20$ times fainter than ^{12}CO (Usero et al., 2015; Jiménez-Donaire et al., 2019, 2023; Schinnerer and Leroy, 2024). As a result, recent observations of those dense gas tracers attempting to link galaxy environment and molecular gas conditions either focus on mapping larger regions of galaxy disks at low resolution ($\sim 500-1000$pc; Bigiel et al., 2016; Gallagher et al., 2018a; Jiménez-Donaire et al., 2019; Heyer et al., 2022; Neumann et al., 2023b) or focus on higher-resolution (i.e., ~ 100 pc) observations of individual regions within galaxies (e.g., galaxy centers, spiral arms; Chen et al., 2017; Bešlić et al., 2021, 2024; Neumann et al., 2024). While the former is insufficient to isolate individual star-forming regions of molecular clouds, the latter does not capture changes across different environments.

Clearly, a major next step in dense gas tracer studies is to observe these tracers at both much higher physical resolution and across larger areas in galaxy disks. This paper presents the IRAM Large Program "Surveying the Whirlpool at Arcseconds with NOEMA" (SWAN), which aims to take this natural next step. SWAN used the NOrthern Extended Millimetre Array (NOEMA) and IRAM 30m single-dish telescope to map the emission from dense gas tracers (HCN(1-0), HNC(1-0), HCO^+ (1-0), N_2H^+ (1-0)) in the 3mm band across a large $5 \times 7\,\mathrm{kpc}^2$ portion of the prototypical grand-design spiral M51, one of the closest ($D \approx 8.5$ Mpc; McQuinn et al., 2016) northern, face-on, star-forming galaxies. Additionally, we observe CO isotopologs $C^{18}O$, ^{13}CO(1-0), shock-tracing emission lines (HNCO(4-3), HNCO(5-4)), and tracers of photo-dissociation regions (PDR, C_2H(1-0)). We achieve 125 pc resolution, which is sufficient to resolve the population of giant molecular clouds (GMCs) and approaches the size scale of individual massive GMCs or star-forming complexes.

Of particular interest is the first high-resolution, high-sensitivity wide-field extragalactic map of N_2H^+ from SWAN (Stuber et al., 2023a). Galactic studies, which detect a much larger suite of molecular emission lines due to the proximity of their targets, prefer the use of this molecular ion, N_2H^+, over HCN, HNC, and HCO^+ to identify regions of dense ($n \sim 10^5\,\mathrm{cm}^{-3}$) molecular gas. Based on Galactic studies, there is an active ongoing discussion in the literature about how the observed intensity of HCN, HNC, and HCO^+ depends on the gas density distribution, chemical abundances, and other factors (Shirley, 2015; Pety et al., 2017; Kauffmann et al., 2017; Leroy et al., 2017b; Gallagher et al., 2018b; Heyer et al., 2022; Santa-Maria et al., 2023; Neumann et al., 2023b; Tafalla et al., 2023). N_2H^+, in contrast, not only has a high critical density, but chemical reactions in the molecular phase of the interstellar medium (ISM) ensure that N_2H^+ is a selective tracer of dense gas. One of the main destruction mechanisms of N_2H^+ is the reaction with ^{12}CO to form HCO^+ and other molecules. N_2H^+ therefore exclusively survives in the densest, coldest parts of molecular clouds, where ^{12}CO is frozen out onto dust grains (column densities above 10^{22} cm^{-2}; see Pety et al., 2017; Kauffmann et al., 2017; Tafalla et al., 2021). Since N_2H^+ emission is more than ~ 70 times fainter than ^{12}CO emission (e.g., Jiménez-Donaire et al., 2023; Stuber et al., 2023a), it has been challenging to observe in extragalactic targets. Previous observations of N_2H^+ in targets beyond the Local Group include a handful of single-target single-dish studies with kiloparsec-scale resolution (e.g., den Brok et al., 2022; Jiménez-Donaire et al., 2023) and a few dedicated higher-resolution studies of bright galaxy centers (e.g., Meier and Turner, 2005; Martín et al., 2021; Eibensteiner et al., 2022). In light of the importance of mapping this tracer across a galaxy disk, preliminary maps of N_2H^+ and HCN from the SWAN survey have already been presented in Stuber et al. (2023a, hereafter: S23).

SWAN builds on the high-quality view of the molecular ISM from CO (1-0) mapping by PAWS (Schinnerer et al., 2013; Meidt et al., 2013; Colombo et al., 2014a) as well as overlapping coverage by VLA radio continuum mapping (including free-free emission), JWST, and HST recombination line and infrared mapping (e.g., Kennicutt et al., 2007; Dumas et al., 2011; Querejeta et al., 2019; Kessler et al., 2020). These means that the bulk molecular ISM and recent star formation are uniquely well constrained in this galaxy. The ISM and dynamical environment across the galaxy are also well understood from extensive previous multiwavelength analysis (e.g., Walter et al., 2008; Meidt et al., 2013; Colombo et al., 2014b; den Brok et al., 2022). M51 was targeted by several previous lower-resolution dense gas tracer mapping studies that detected strong environmental variations in, for example, the HCN/CO ratio across the galaxy (at 500-1000pc resolution; Usero et al., 2015; Bigiel et al., 2016; Heyer et al., 2022). At $\sim$ 100pc resolution, individual regions within M51 were targeted (i.e., Chen et al., 2017; Querejeta et al., 2019). This makes M51 an ideal target to investigate the physical origin of the environmental variations in HCN/CO, SFR/HCN, and similar quantities observed at much larger spatial scales.

This paper presents the full suite of 3 mm lines observed as part of the SWAN IRAM Large Program, and is structured as follows. In Sect. 4.2, we describe the SWAN observations. The data reduction, imaging, and data quality assessment are presented in Sect. 4.3. In Sect. 4.4, we compare the spatial distribution of all the nine 3 mm lines detected in the SWAN dataset, and compare their relative intensity to ^{12}CO and previous literature observations. An interpretation of these findings is provided in Sect. 4.5. We summarize our main conclusions in Sect. 4.6.

The richness of the SWAN data allows for more detailed studies of, for example, the variations in ^{12}CO isotopologs (Galic et al, submitted) and also, in combination with SMA observations in den Brok et al. (2025), a direct comparison of the dense gas tracing lines across different environments (for a first comparison of HCN and N_2H^+, see Stuber et al., 2023a, with an extensive comparison including HNC and HCO^+ underway, Stuber et al. in prep.) and with cloud properties (e.g., gas mass surface density, line width, virial parameter; Bigiel et al., in prep.). Further dedicated studies of the central molecular outflow are under way (Thorp et al. in prep., Usero et al., in prep.).

4.2 OBSERVATIONS

SWAN utilizes observations from the IRAM Large Program LP003 (PIs: E. Schinnerer & F. Bigiel), which mapped emission lines in the $\sim$ 3 mm band across the central 5×7 kpc^2 of the nearby galaxy M51 with both the NOEMA and the IRAM 30m single-dish telescope.

4.2.1 NOEMA observations

Observations with NOEMA were taken between January 2020 and December 2021, with the antenna configuration split between the C (59%; 126h) and D (41%; 88h) configurations. In total, we used 17 pointings to map the central $\sim 5 \times 7$ kpc^2 of M51's disk (Fig. 17). The mosaic uses hexagonal spacing.

For the SWAN observations, the receiver was tuned to a sky frequency of 88.49177 GHz, which corresponds to the frequency of HCN(1-0) redshifted by the systemic velocity of M51 ($v_{sys} \sim 471.7\,\mathrm{km\,s^{-1}}$). We covered the ~ 15.5 GHz ($\times 2$ polarizations) instantaneous bandwidth at the default Polyfix 2 MHz resolution. The setup was selected to cover the main target lines ^{13}CO, C^{18}O (1-0) in the upper side band, as well as HCN, HCO$^+$, HNC and N_2H^+ (1-0) in the lower side band (Table 3). As the configuration of Polyfix permits up to 16 high-resolution (62.5 kHz) windows per 4 GHz, we placed between three and five such windows around the rest frequency of each of our target lines.

We evaluated the quality of the SWAN observations based on the automatic calibration reports obtained with the standard `GILDAS/CLIC` calibration pipeline. The automatic quality assessment tool was used to filter out poor data (see `GILDAS/CLIC` manual[1]). Out of a total of $\sim$ 246h of observations, $\sim$ 214h were taken under average to excellent observing conditions (i.e., low water vapor, minimum cloud coverage, minimum antenna tracking errors without systematic variations, good phase and amplitude stability). The average water vapor during these 214h was ~ 4 mm.

We used the quasars J1259+516 and J1332+473 as our main phase and amplitude calibrators, substituted by 1418+546 if either calibration target was unavailable. Observations of the calibrators were executed every ~ 17 minutes. Absolute flux calibration was performed using IRAM models for MWC349 and LkHa101, providing about 50 independent measurements of the flux of J1259+516 and J1332+473 and quasar 2010+723 over a period of about one year. This allowed us to confirm that variations in the flux of these quasars happen mostly over longer time periods and are relatively smooth. We show the flux of J1259+516, J1332+473, and 2010+723 over time in Fig. 18, inferred by the `GILDAS` pipeline solution, and after manual adjustments. While the pipeline is deriving the flux gain for each observation separately by ensuring that the flux of a primary flux calibrator is equal to the modeled value, the manual solution uses the temporal stability of the most stable quasar from one day to the next. That means we take advantage of the fact that observations were executed over consecutive days. For sets of observations taken on consecutive days, we identify as new flux reference the quasar whose flux is most stable over this time range. We used its derived flux value from the day with best observing conditions as a reference to solve again for the flux gains of the other observations in each set. Significant changes in the derived flux gains only occurred when the observations of the primary flux calibrator were not taken under good conditions; for example, when the elevation of the primary flux calibrator was low. Since the full mosaic is observed between two phase calibrator observations, the flux calibration has the same effect for all its 17 pointings. The same is true for all lines, as they are observed simultaneously and a global spectral factor is applied per sideband. In short, while the flux calibration impacts the absolute fluxes of the SWAN data, it does not impact the relative strengths between the different lines observed. Based on Fig. 18, we estimate that the absolute flux uncertainty for the NOEMA observations is $\sim 10\%$.

4.2.2 IRAM-30m single-dish observations

Spatially extended emission accounts for a significant fraction of the total flux in galaxies (e.g., Appendix D of Leroy et al., 2021a). Since interferometers are not sen-

1 https://www.iram.fr/IRAMFR/GILDAS/doc/html/clic-html/clic.html

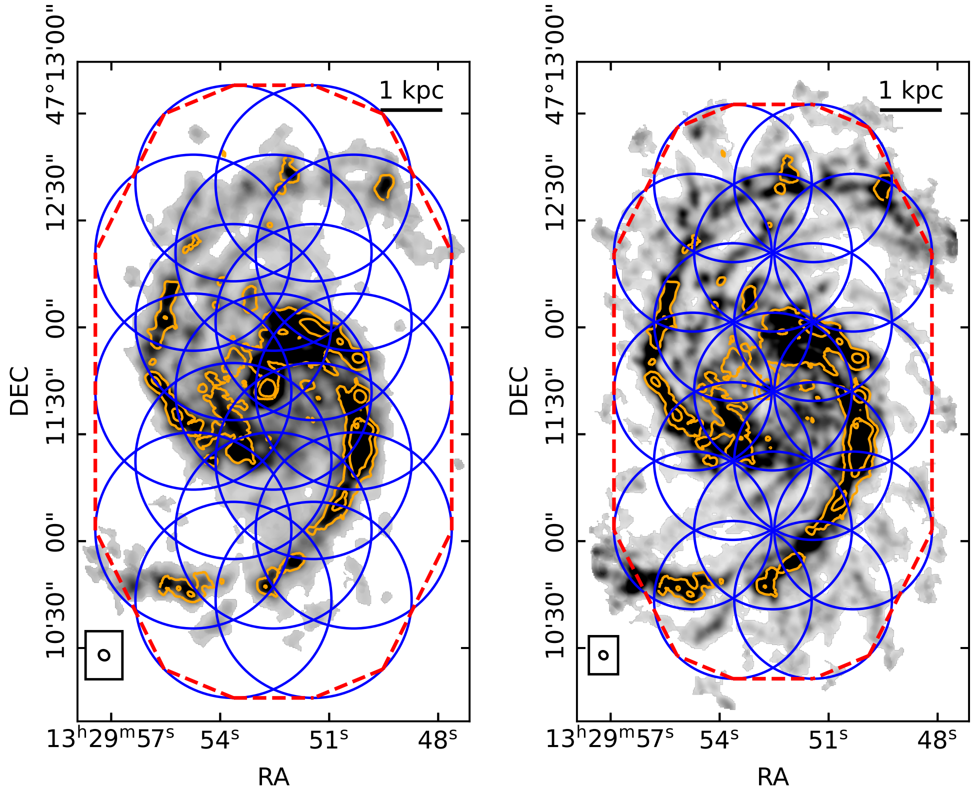

Figure 17: Primary beam of individual mosaic pointings (blue circles) of the NOEMA observations for SWAN overlaid on a map of the integrated intensity of HCN(1-0) emission (left) and ^{13}CO(1-0) emission (right). Contours represent integrated N_2H^+ emission at 0.5 and 2 K km s^{-1}. The pointings shown have a radius of ~ 28″ (HCN) and ~ 22.5″ (^{13}CO, our highest frequency detected line). We interpolate the outer edges of the individual mosaic pointings to define the area inside which we measure the integrated flux of each observed emission line (red line). Because the primary beam changes with frequency, so does the area used to calculate the line flux.

Table 2: NOEMA and 30m observations.

Survey	Telescope	Lines	Δt_{obs} (in SWAN FoV)	native res.
SWAN	NOEMA	C_2H(1-0), HNCO(4-3), HCN(1-0), HCO^+(1-0), HNC(1-0), N_2H^+(1-0),$C^{18}O$(1-0), HNCO(5-4), ^{13}CO(1-0)	214h	2.4″ – 3.0″
SWAN-new	IRAM-30m	same as SWAN-NOEMA	55h	23.6″ – 29.8″
CLAWS	IRAM-30m	$C^{18}O$(1-0), ^{13}CO(1-0), N_2H^+(1-0)	~ 14h	27 – 32″
EMPIRE	IRAM-30m	HCN(1-0), HNC(1-0), HCO^+(1-0)	~ 14h	26 – 34″

Observational data used in the SWAN survey, including archival data from EMPIRE (Jiménez-Donaire et al., 2019) and CLAWS (den Brok et al., 2022). The observing time t_{obs} refers to the estimated observing time inside the FoV of SWAN (see Fig. 17). All 30m datasets (SWAN-new, EMPIRE, CLAWS) are combined to the "SWAN-30m" dataset before merging with the NOEMA data via joint deconvolution. Native resolution refers to the resolution after imaging.

Table 3: NOEMA and 30m data used for SWAN.

Line				10 $\mathrm{km\,s^{-1}}$		5 $\mathrm{km\,s^{-1}}$		2.5 $\mathrm{km\,s^{-1}}$		1 $\mathrm{km\,s^{-1}}$	
Line	ν_{rest}	native res.	b_{pa}	T_{peak}	rms	T_{peak}	rms	T_{peak}	rms	T_{peak}	rms
Line	[GHz]	[″×″]	[°]	[mK]	[mK]	[mK]	[mK]	[mK]	[mK]	[mK]	[mK]
(1)	(2)	(3)	(4)	(5)	(6)	(7)	(8)	(9)	(10)	(11)	(12)
NOEMA+30m data											
C_2H(1–0)	87.3169	3.1×2.7	49	141.0	12.4	121.4	15.7	204.7	22.9	308.1	33.4
HNCO(4–3)	87.9252	3.1×2.7	49	197.0	8.4	-	-	-	-	-	-
HCN(1–0)	88.6319	3.0×2.7	49	555.5	9.8	564.4	16.9	570.4	22.1	586.4	30.5
HCO^+(1–0)	89.1885	3.0×2.7	50	451.1	9.8	459.9	17.7	473.3	18.0	499.7	30.0
HNC(1–0)	90.6635	3.0×2.6	49	308.8	9.6	343.6	13.5	361.5	18.8	379.1	27.8
N_2H^+(1–0)	93.1738	2.9×2.5	48	271.7	8.6	290.8	14.1	317.4	17.5	339.0	26.1
$C^{18}O$(1–0)	109.7822	2.4×2.2	45	436.3	14.4	549.2	20.2	578.7	27.9	606.3	42.2
HNCO(5–4)	109.9058	2.4×2.1	49	210.9	12.8	-	-	-	-	-	-
^{13}CO(1–0)	110.2014	2.4×2.1	47	1461.1	16.3	1725.8	23.9	1763.6	31.0	1808.9	44.8
NOEMA data											
C_2H(1–0)	87.3169	3.0×2.6	48	161.4	12.9	127.9	16.1	210.9	23.2	326.6	34.2
HNCO(4–3)	87.9252	3.0×2.6	49	207.1	8.8	-	-	-	-	-	-
HCN(1–0)	88.6319	2.9×2.6	47	570.8	10.3	577.5	18.0	584.2	22.8	596.9	31.8
HCO^+(1–0)	89.1885	2.9×2.6	47	448.2	10.2	469.3	18.9	481.1	17.7	511.6	31.1
HNC(1–0)	90.6635	2.9×2.5	47	318.4	10.0	362.9	14.3	378.7	19.1	392.0	28.1
N_2H^+(1–0)	93.1738	2.6×2.6	88	283.2	9.6	290.2	14.9	323.2	18.1	341.6	26.1
$C^{18}O$(1–0)	109.7822	2.3×2.1	47	448.5	15.0	550.7	21.1	577.3	28.5	599.5	43.5
HNCO(5–4)	109.9058	2.3×2.1	47	219.2	12.6	-	-	-	-	-	-
^{13}CO(1–0)	110.2014	2.3×2.1	47	1492.7	16.9	1755.2	24.6	1771.3	31.0	1802.6	44.0
30m data											
C_2H(1–0)	87.3169	29.7×29.7	0	16.5	3.0	22.3	4.1	26.0	5.6	39.8	7.9
HNCO(4–3)	87.9252	29.5×29.5	0	12.2	2.3	-	-	-	-	-	-
HCN(1–0)	88.6319	29.3×29.3	0	56.4	2.3	58.8	3.3	62.6	4.6	67.8	6.2
HCO^+(1–0)	89.1885	29.1×29.1	0	36.6	2.5	39.2	3.4	44.8	4.6	51.8	6.4
HNC(1–0)	90.6635	28.6×28.6	0	22.2	2.4	26.1	3.3	33.8	4.6	40.8	6.7
N_2H^+(1–0)	93.1738	27.9×27.9	0	17.2	2.0	22.8	2.9	27.5	4.1	31.4	6.1
$C^{18}O$(1–0)	109.7822	23.7×23.7	0	44.2	3.8	50.9	5.0	60.2	7.0	72.0	9.9
HNCO(5–4)	109.9058	23.6×23.6	0	15.8	3.7	-	-	-	-	-	-
^{13}CO(1–0)	110.2014	23.6×23.6	0	154.9	3.9	170.4	5.6	178.4	7.6	190.1	11.5

Properties of SWAN datasets: For the combined NOEMA+30m data, the NOEMA data, and the 30m data we list the molecular emission line (1), its rest frequency (2), the native beam size (3), and the beam position angle (4), as well as the peak temperature, T_{peak}, and typical rms for different spectral resolutions (10 $\mathrm{km\,s^{-1}}$: (5),(6); 5 $\mathrm{km\,s^{-1}}$: (7),(8); 2.5 $\mathrm{km\,s^{-1}}$: (9),(10), 1 $\mathrm{km\,s^{-1}}$: (11),(12)). T_{peak} refers to the peak intensity of the brightest pixel in the data cube. The rms is the average rms of the first and last five channels, which are free of emission. For all datasets, both peak intensity and rms were calculated inside the area covered by the mosaic (see Fig. 17). In this area, the sensitivity is comparably constant and to avoid the increased noise towards the edges of the mosaic. The 30m data refers to combined datasets of archival EMPIRE and CLAWS data and the newly obtained IRAM 30m observations.

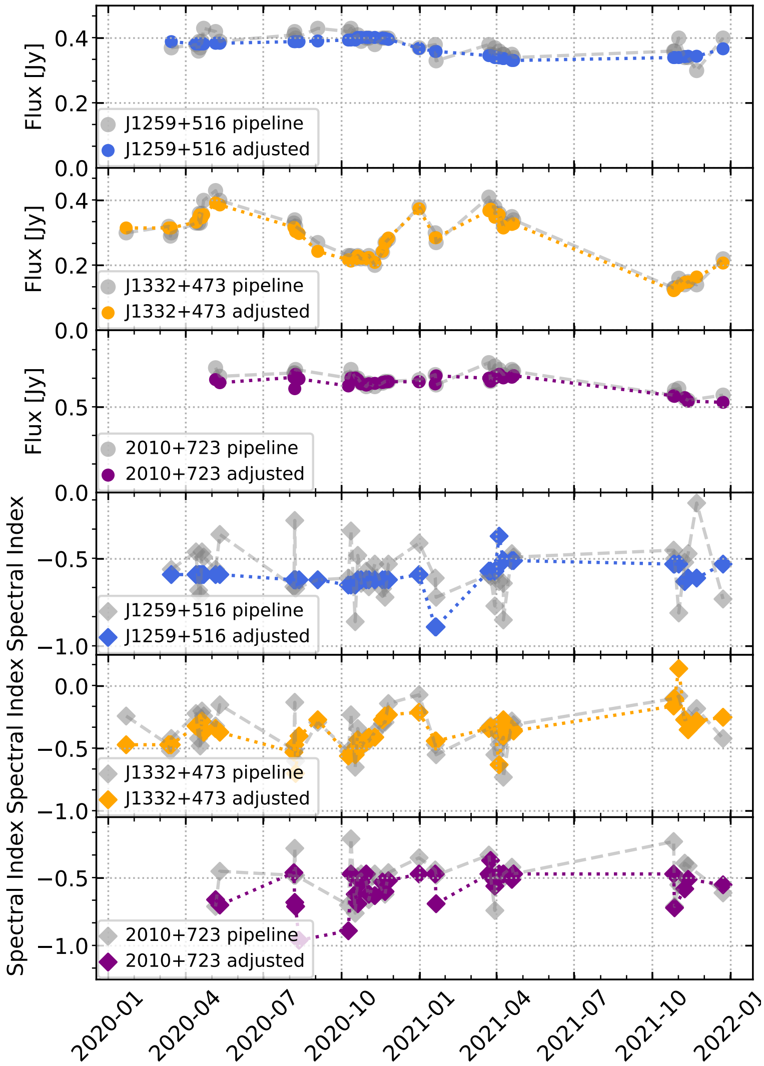

Figure 18: Observed flux (top three rows) and spectral index (bottom three rows) over time for the three used phase and amplitude calibrators of the SWAN NOEMA observations. In addition to the adopted solution (colored points), we show the flux solution determined by the pipeline (gray circles). The temporal variation in the flux of these quasars is relatively smooth. Manual adjustments result in smaller time variations in the spectral index.

sitive to emission from coarser scales, we complement the NOEMA interferometric data with single-dish data from the IRAM-30m telescope to provide the low spatial frequency (or "short-spacing") information.

The SWAN 30m data partially consists of archival IRAM 30m observations. We used archival HCN(1–0), HNC(1–0) and HCO^+(1–0) data from the IRAM-30m EMPIRE survey (Jiménez-Donaire et al., 2019), and N_2H^+(1–0), $C^{18}O$(1–0) and ^{13}CO(1–0) data from the IRAM-30m CLAWS survey (055-17, PI: K. Sliwa; den Brok et al., 2022). More detailed information about the EMPIRE and CLAWS observations can be found in the corresponding survey papers (Jiménez-Donaire et al., 2019; den Brok et al., 2022). Both surveys cover a field of view (FoV) that is significantly larger than that of the NOEMA observations. Within the NOEMA FoV, the EMPIRE and CLAWS observations represent about 14 hours of 30m observations (see also Table 2), insufficient for our sensitivity requirements and to avoid any degradation when combining 30m and NOEMA data (according to eq. 19 of memo IRAM-2008-2 (Rodrıguez-Fernandez et al., 2008)).

We therefore obtained ~ 55 hours of new observations with the IRAM-30m between 2020 February and April (project 238-19). M51 was observed with EMIR combined with the Fast Fourier Transform Spectrometers (FTS). We used a frequency bandwidth of 2×7.9 GHz, regularly sampled at 195 kHz. We used on-the-fly (OTF) mapping mode with scan legs of lengths 200 and 300″ along the RA and Dec axes, respectively. The distance between two scan legs (i.e., perpendicular to the scanning direction) was 8″. Additionally, we shifted the center of the mapped box in each iteration by multiples of 2″ to get a final grid with a finer step of order 2″.

We typically observed under good weather conditions (median PWV=2^{+4}_{-2} mm, where, hereafter, the subscript and superscript indicate the offsets of the 16th and 84th percentiles from the median, respectively) and at high elevation ($69^{\circ}{}^{+10^{\circ}}_{-16^{\circ}}$). The typical system temperatures on the T_A^* scale were 89^{+10}_{-12} K for lines below 91 GHz, 79^{+12}_{-6} K for N_2H^+(1-0), and 109^{+17}_{-16} K for the CO isotopolog lines and HNCO(5-4).

The absolute flux calibration of the 30m observations was monitored with the bright carbon-rich AGB star IRC+10216, which was observed for a few minutes at the start of most of the observing runs. For each observation, we extracted and integrated ten well-detected lines (signal-to-noise ratio (S/N) $\gtrsim 50$) with frequencies spaced across the observed bandwidth ($88.6 - 110.2$ GHz). This allowed us to check the relative calibration of the telescope as a function of time and frequency disregarding thermal noise effects. We confirmed that the spectral shape of every line is constant with time up to a varying scaling factor. This suggests that the observed amplitude variations are not caused by pointing errors. In short, since the lines are distributed in different ways across the envelope of IRC+10216, pointing errors would tend to change the shape of the lines with widespread emission. We also found that the correlation between the integrated intensities of pairs of lines was better when considering lines within the same EMIR subband, suggesting that the observed amplitude variations are driven by calibration errors that depend sensitively on frequency. Overall, the root mean square (rms) uncertainty in the integrated intensities is of order ~ 5% for most molecular lines studied, and $\sim 10 - 15\%$ for the four lines in the 93-102 GHz regime. We also detected systematic differences between polarizations of order $\sim 5 - 10\%$ for all lines. In the end, we can assume a relative flux calibration uncertainty on the order of $5 - 10\%$ for all lines, consistent with typical expectations.

4.3 DATA REDUCTION AND IMAGING

4.3.1 NOEMA data reduction and imaging

We calibrated the NOEMA observations using the standard `GILDAS/CLIC`[2] pipeline. We extracted calibrated uv tables for each velocity resolution (i.e., 10, 5, 2.5, and 1 km s^{-1}) and line before imaging with `GILDAS/MAPPING`. The exact spectral extent of the resulting cubes depends on the line, as is described in Sect. 4.2.1. We did not subtract a continuum in the visibilities in order to avoid biasing the very broad line (typically several hundred km s^{-1}) that appears near the galaxy center. The produced cubes thus contain a contribution from continuum emission. However, for the purposes of line analysis, this continuum contribution is only significant in very small regions along the southern nuclear radio jet axis (XNC; Ford et al., 1985). Hereafter,

2 https://www.iram.fr/IRAMFR/GILDAS

we subtract this contribution in the image plane when needed (see Sect. 4.3.3). We imaged all the uv tables on the same spatial grid, which we centered at RA=13:29:52.532, Dec=47:11:41.982 (J2000). The grid has a pixel size of 0.31″ and a total map size of 768×1024 pixels. Cleaning was performed with the Högbom cleaning algorithm with a constant number of clean components. The number of clean components was chosen to obtain residuals that look like noise (i.e., no coherent spatial structures are present any longer). Since the emission of the brighter lines (e.g., ^{13}CO) extends across the full FoV we did not use any support (i.e., cleaning mask) during the cleaning. We used 64 000 clean components for the 10 and 5 km s^{-1} cubes and 32 000 for the 2.5 and 1 km s^{-1} ones. We used fewer clean components for the higher spectral resolution cubes since the S/N is lower at higher spectral resolution. Finally, we converted the intensity scale from Jansky per beam to Kelvin with the standard `GILDAS-MAPPING` GO JY2K command.

The final NOEMA dataset yields detections of nine molecular lines between ~87.1 and 110.3 GHz: C_2H(1–0), HNCO(4–3), HCN(1–0), HCO^+(1–0), HNC(1–0),N_2H^+(1–0), $C^{18}O$(1–0), HNCO(5–4) and ^{13}CO(1–0). We detect the two brightest C_2H(1-0) hyperfine transitions at rest-frequencies of 87.317 and 87.402 GHz, as well as a fainter transition at 87.284 GHz overlapping along the velocity axis of the first transition mentioned. We do not attempt to separate them, but instead generate one data cube that contains all the detected C_2H emission. The spectral axis of the delivered C_2H data cube is centered on 87.3169 GHz (N= 1-0, J=3/2-1/2, F= 2-1). We list the rest frequencies of our detected lines in Table 3, as well as the typical rms, peak temperature and native resolution of the data cubes with 10, 5, 2.5, and 1 km s^{-1} spectral resolution.

4.3.2 30m data reduction and imaging

The new IRAM 30m data were reduced to a set of common spectral and spatial grids to ensure a homogeneous treatment for all lines. First, the data for each target line was isolated by extracting frequency windows of 350 MHz ($\sim 950-1200$ km s^{-1}) centered on the rest frequency of each line. For C_2H(1-0), we increased the window width to 400 MHz to ensure that all the hyperfine structure components were included. Using the Ruze formula with the `CLASS` command `MODIFY BEAM_EFF /RUZE`, the temperature scale was converted from $T_A^\star$ to T_{mb}. Next, the data were spatially reprojected to match the NOEMA projection center of RA=13:29:52.532, Dec=47:11:41.982 (J2000). The Doppler correction was then recomputed for each spectrum to take into account 1) the change of velocity convention from optical during the observations to radio during the analysis, and 2) its variation as a function of position (because the Doppler tracking is computed only at the projection center and kept fixed during each scan to avoid creating standing waves). The velocity scale was updated to ensure that the redshifted frequency of the line in the local standard of rest (LSR) frame corresponds to a systemic velocity of 0 km s^{-1}. The mean rms noise across each data cube was measured using the baseline residuals. We removed spectra for which the rms noise was greater than three times the mean value in the cube ($\sim 3\%$ of all acquired spectra were rejected in this step).

The IRAM-30m observations were imaged using standard `GILDAS/CLASS` procedures. The data was regridded spectrally to match the NOEMA data, with four different spectral resolutions: 10 km s^{-1}, 5 km s^{-1}, 2.5 km s^{-1} and 1 km s^{-1}. All were imaged using a Gaussian kernel of FWHM $\sim 1/3$ the 30m HPBW. We produced two sets of

30m data products with different spatial grids. The first grid has a pixel size of 4″ for distribution as a stand-alone product. The second grid is identical to the one used to grid the NOEMA data to ensure a good spatial sampling when merging the single-dish and interferometric datasets. We list the typical peak intensities and noise levels of the SWAN 30m data in Table 3.

We conducted several checks on the 30m data reduction and imaging, which we describe in more detail in the appendices. Specifically, we tested for consistency between the new and archival 30m datasets (Appendix A.2). Overall, we find that the datasets agree to within 10%. Finally, we analyzed the impact of the 30m error beams onto the flux filtered out by the interferometer in Appendix A.1. For ^{13}CO, the contribution of the error beam is <10% for the vast majority (i.e., 98%) of sightlines, and the median error beam contribution is 1.5% per pixel inside the NOEMA SWAN FoV. As the main beam efficiency decreases with increasing frequency, we expect the error beam contribution to be less significant for other emission lines in the SWAN survey.

4.3.3 Combined NOEMA+30m imaging

The 30m data were combined with the NOEMA data in the uv plane using the `GILDAS/MAPPING UV_SHORT` command (see Pety and Rodríguez-Fernández, 2010, for details). For the combination, we used the calibrated but non-continuum-subtracted NOEMA uv tables and the baseline-subtracted single-dish uv tables. This is slightly inconsistent, but there is currently no reliable method to measure the continuum emission at 3 mm with the IRAM 30m. For several lines, this can result in the noise level in the center being on average offset towards slightly positive values (compare this with Fig. 20). For N_2H^+(1-0) and HNCO(4-3), we apply an order 1 baseline subtraction in the final data cube during post-processing. We confirm that the baseline subtraction does not affect any of the quantitative results for these lines. To verify this, we performed all analyses shown below using both the baseline-corrected and uncorrected data cubes for N_2H^+. The overall scientific conclusions and observed trends remain unchanged.

We image the combined data in a similar way as for the NOEMA-only data (Sect. 4.3.1). The resulting data cubes have the same spatial grid as for the stand-alone NOEMA data (i.e., a pixel size of 0.31″, which is $\sim 7-10$ times smaller than the native resolution beam size, on a grid of 768×1024 pixels) and cleaned via Högbom-cleaning without cleaning masks until the cleaned flux reaches a stable number. We used twice as many clean components as for the NOEMA-only data (128 000 clean components for the 10 and 5 km s^{-1} cubes and 64 000 for the 2.5 and 1 km s^{-1} ones), since the short-spacing data introduces additional complexity. Lastly, we convert the intensity scale from Jansky per beam to Kelvin. We confirmed that the noise is "well behaved" in each NOEMA+30m line cubes. The rms noise level shows little dependence on frequency across the whole bandwidth, if at all, and there is negligible correlation between adjacent channels.

4.3.4 Flux recovery

In Table 4, we list the fraction of flux recovered by the native-resolution NOEMA observations for different spectral versions of the SWAN data cube for each emission line. The flux recovery was calculated by smoothing and spatially regridding the NOEMA

Table 4: Interferometric flux recovery fraction

Line	Flux recovery			
	$10\,\mathrm{km\,s^{-1}}$	$5\,\mathrm{km\,s^{-1}}$	$2.5\,\mathrm{km\,s^{-1}}$	$1\,\mathrm{km\,s^{-1}}$
^{13}CO(1-0)	0.48 ± 0.01	0.45 ± 0.01	0.42 ± 0.01	0.33 ± 0.01
C^{18}O(1-0)	0.29 ± 0.04	0.18 ± 0.04	0.23 ± 0.04	0.15 ± 0.02
HCN(1-0)	0.43 ± 0.02	0.40 ± 0.04	0.33 ± 0.02	0.25 ± 0.01
HCO$^+$(1-0)	0.42 ± 0.06	0.39 ± 0.04	0.32 ± 0.02	0.23 ± 0.03
HNC(1-0)	0.49 ± 0.07	0.40 ± 0.06	0.35 ± 0.05	0.23 ± 0.04

The data were extracted from the central $100 \times 100''$ of the SWAN FoV. The native angular resolution NOEMA data were smoothed and regridded to match the 30m data spatially and spectrally. The tabulated values are the summed flux measured from the NOEMA data, divided by the summed flux measured from the 30m data. The quoted errors are statistical uncertainties only. We tabulate measurements for data imaged at spectral resolutions of 10, 5, 2.5, and 1 $\mathrm{km\,s^{-1}}$. Each line's native angular resolution is the same across all spectral resolutions (see Table 3).

data to match the 30m data (the spectral grid of the NOEMA data is already matched to the 30m data during the imaging), then summing the emission from the central $100 \times 100''$ across all channels. The ratio of integrated NOEMA flux to 30m flux yields the flux recovery estimate. We limit the FoV during this computation to avoid contribution from the increased noise toward the edges of the mosaic (Fig. 17). For most lines, the NOEMA observations recover $\lesssim 50\%$ of the 30m flux at $10\,\mathrm{km\,s^{-1}}$ spectral resolution. This fraction is consistently lower for all lines when the data products are imaged with narrower channels, falling to a typical value of $20-30\%$ flux recovery at a spectral resolution of $1\,\mathrm{km\,s^{-1}}$. This is probably due to the lower sensitivity of the data at higher spectral resolution, which affects the deconvolution. Our method for calculating flux recovery is not effective for the fainter lines like N_2H^+, C_2H, and HNCO. Regridding and smoothing the NOEMA-only data of those lines to match the 30m data strongly reduces the line S/N. As a result, we cannot make precise conclusions about these specific lines (uncertainties as large as $\gtrsim$80% of the flux recovery value). Table 4 only lists the flux recovery for lines with peak temperature to rms ratio of $\gtrsim$10 at a spectral resolution of $10\,\mathrm{km\,s^{-1}}$ in the 30m-only data (compare Table 3).

We also studied the relation between synthesized angular resolution and flux recovery. We tapered the data during the data reduction to coarser angular resolutions of 3, 4, and 6$''$ and recalculated the flux recovery per channel. Figure 19 shows the flux recovery of the native resolution NOEMA ^{13}CO(1–0) data compared to the 30m data for each channel as a function of the angular resolution associated with different tapering distance in the *uv* plane. At fixed spectral resolution, the flux recovery of the NOEMA data improves as the angular resolution increases from 2 to 4$''$. Above $\gtrsim 4''$, the flux recovery converges and no longer increases with increasing beam size. Our SWAN flux recovery results are consistent with findings for the PAWS survey (Schinnerer et al., 2013), where only a marginal improvement in the flux recovery was reported when the resolution was degraded from 3$''$to 6$''$(Pety et al., 2013). Our tests indicate that all the flux present in the SWAN NOEMA data is deconvolved at scales $\gtrsim 4''$.

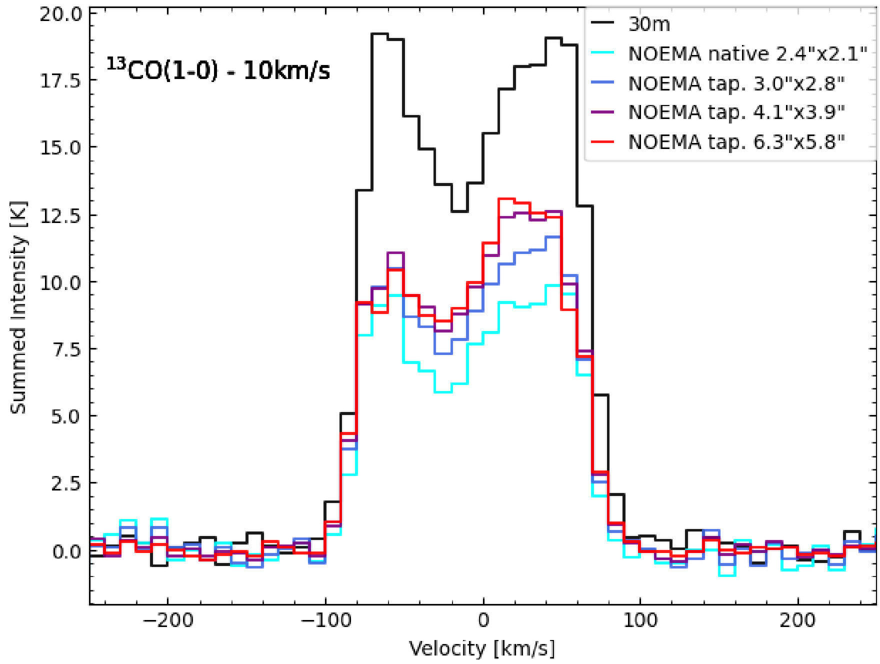

Figure 19: Flux recovery for ^{13}CO(1-0) at 10 km s^{-1} spectral resolution. The native resolution NOEMA data (cyan line) was convolved and regridded to match the 30m data (black line) in resolution. The flux shown is the summed flux per channel inside the central $100 \times 100''$. NOEMA data tapered to coarser spatial resolutions of about 3, 4, and 6$''$ (blue, purple, red lines) have higher recovery rates.

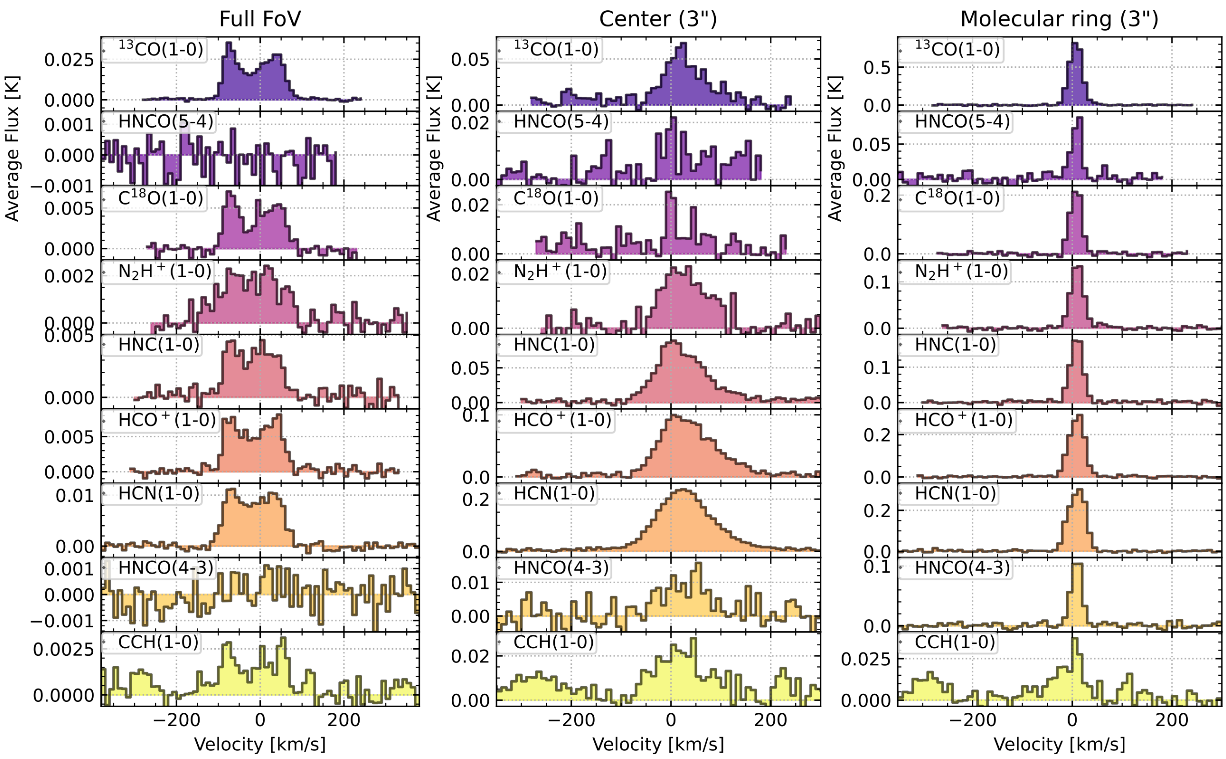

Figure 20: Spectra of all molecular lines for the full disk (left panel), a 3$''$sized region in radius in the center (middle panel) and the western edge of the molecular ring (right panel) where N_2H^+ is particularly bright. The full disk spectra are extracted using the area covered by the perimeter ("hull") of the mosaic of all pointings (see Fig. 17) for ^{13}CO. Since this hull is frequency dependent, this corresponds to the smallest area out of all lines.

4.3.5 Signal in the NOEMA+30m data cubes

The NOEMA+30m data were imaged at spectral resolutions of 10, 5, 2, and 1 $\mathrm{km\,s^{-1}}$. We list the typical rms and peak temperature per channel for each spectral resolution at the native angular resolution for all lines in Table 3.

Figure 20 shows spectra at 10 $\mathrm{km\,s^{-1}}$ spectral resolution for the combined NOEMA+30m data for all detected molecular lines: ^{13}CO(1-0), C^{18}O(1-0), HNCO(5-4), N_2H^+(1-0), HCO^+(1-0), HNC(1-0), HCN(1-0), HNCO(4-3), and C_2H(1-0). We show spectra of the full FoV inside the perimeter (hereafter "hull") covered by the mosaics (compare this with Fig. 17), as well as inside a 3″ sized region located at the galaxy center and the bright spot at the southwestern edge of the molecular ring (RA 13:29:50.0633, DEC: 47:11:25.2040 (J2000)). As expected, most central spectra, especially from HCN, HNC and HCO^+, are broader than those in the molecular ring, likely due to the complex kinematics due to the active galactic nucleus (AGN)-driven outflow in the galaxy center. The multiple peaks in the C_2H(1-0) spectra are hyperfine transitions.

4.3.6 Moment map creation

The final SWAN data cubes of combined NOEMA and IRAM-30m data are publicly available[3]. Integrating all emission within a fixed velocity range at all lines of sight will add noise to the already faint emission. Therefore, a number of masking techniques that select regions and channels within the data cube to integrate emission have been used in the literature and depending on the method used the total recovered flux this will differ (see, e.g., Appendix B in Pety et al., 2013). The advantages and disadvantages of different masking strategies depend on the science objective, and the relative importance of completeness versus avoiding false positives (see, e.g., Leroy et al., 2021a) Utilizing these data cubes at a spectral resolution of 10 $\mathrm{km\,s^{-1}}$, we test two commonly used methods of moment-map creation.

First, we created moment-maps with the `GILDAS/CUBE` "Island method" (Einig et al., 2023). The resulting maps are shown in Fig. 21 (and for a better comparison with an alternative method in Fig. 51) at each line's native angular resolution. For each line, this method identifies connected structures as follows. We calculated the noise in channels with velocities $|v| > 200\,\mathrm{km\,s^{-1}}$. We then smoothed the data cube with a Gaussian kernel of size $B_{maj} \times B_{min} * \mathrm{PA}$ and calculated the S/N at each pixel based on the smoothed cube and the calculated noise. Next, we identified connected structures above a selected threshold of S/N = 2 in the position-position-velocity (ppv) cube. These structures were applied to the original data cube and emission was integrated over the pixels within those structures. By doing this for each line at its native resolution, we minimized noise that would otherwise be added in the integration process, while still conserving fainter emission from connected structures. Figure 21 (and Fig. 51) show the moment-0 maps created when selecting structures based on each line individually at their native angular resolution. In addition to moment-0 maps, we created velocity field maps (moment-1), line-width maps (moment-2), peak temperature maps, and associated uncertainty maps, which are available in the public data release.

In contrast to selecting connected significant emission structures identified in the same data cube that is being used to generate moment maps, another common strategy is to construct a significant emission mask based on a single bright line (e.g., ^{12}CO, aka

3 https://oms.iram.fr/dms and https://www.canfar.net/storage/list/

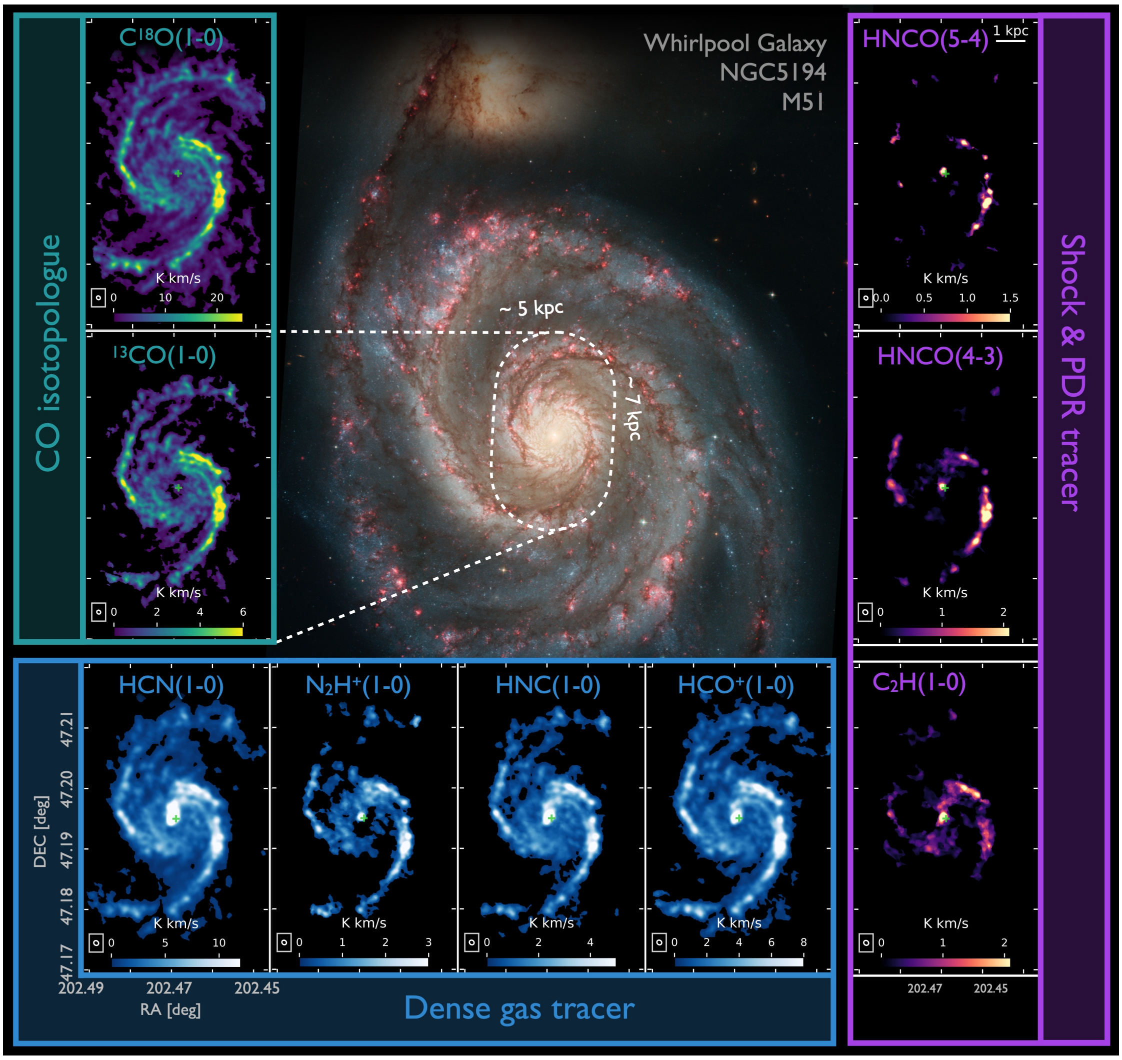

Figure 21: Integrated intensity (moment-0) maps of the SWAN dataset (combined NOEMA and IRAM 30m observations) for the J=1–0 transitions of ^{13}CO, C^{18}O, N$_2$H$^+$, HCO$^+$, HNC, HCN, and C$_2$H plus HNCO(J=4–3) and HNCO(J=5–4) at their native angular resolution ($\sim 2.3 - 3.1''$). The lines are grouped in different subsets based on their commonly used applications. The maps were created with the `GILDAS` Island-method (see Appendix A.3). We show the beam size in the bottom left of all panels as well as a 1 kpc scale bar in the top right panel. The outline of the SWAN FoV is indicated by a dashed ellipse on top of a multicolor HST image (credit: S. Beckwith (STScI) Hubble Heritage Team, (STScI/AURA), ESA, NASA).

the "prior") and applying the resulting mask to the data cubes of fainter lines. Since M51 has an unusual center that is mostly devoid of ^{12}CO emission (including the ^{13}CO and C^{18}O isotopologs; see Figs. 20 and 21), a ^{12}CO-based prior does not accurately capture the emission from all the lines in the SWAN survey field. Bright HCN HNC, and HCO^{+} emission in the center of M51, for example, are evident in Fig. 20. The spectra inside a 3″ sized central aperture (Fig. 20) are comparably broad for all three of these lines, with FWHM $\sim 100\,\mathrm{km\,s^{-1}}$. We generate another set of moment maps using both ^{12}CO and HCN emission to construct a mask. This mask contains regions in which either HCN or ^{12}CO is detected. This mask captures the bulk molecular gas distribution best traced by ^{12}CO emission outside of the central kiloparsec, as well as the central region, which is best traced by the bright HCN emission (Fig. 21). This is done by using the so-called "PyStructure"[4] code (den Brok et al., 2022; Neumann et al., 2023b) and after convolving the data to a common resolution of 3.05″. High-resolution ^{12}CO (1-0) data were taken from the PdBI Arcsecond Whirlpool Survey (PAWS; Schinnerer et al., 2013) and matched to our resolution. Pixels in ppv space were thus selected for integration if either HCN or ^{12}CO was detected. The PyStructure code further allows the user to resample the data with hexagonal pixels, which capture the circular beam of the observations well. We hexagonally resampled all data to a matched grid with two hexagons across each beam length. Integrated moment maps were then created by selecting the spectral windows where both ^{12}CO and HCN are significantly detected. This data were saved in a `numpy` table that we refer to as a "PyStructure table" from hereon.

While the former method is best suited when investigating individual lines, the latter is often preferable for the comparison of several lines, since it ensures that the same pixels of the ppv cube are used for integration. However, it tends to increase the noise in the integrated emission maps of fainter lines (e.g., HNCO(5-4), HNCO(4-3) and C_2H(1-0)). This is apparent when we compare Figs. 51 and 52, where differences between them are driven by either the difference in methodology, or the difference in resolution (and therefore S/N). As an example, HNCO(5-4) is shown at its native 2.3″ in Fig. 51, but smoothed to a 3″ resolution in 52. As the native resolution of C_2H is $\sim 3''$, differences in the moment maps arise due to the differences in methodology.

Given that both the `GILDAS` and PyStructure methods are useful for different analysis, we conduct a pixel-by-pixel comparison for ^{13}CO in Appendix A.3. Overall, we find good agreement between both methods, with the `GILDAS` method recovering more flux than the Pystructure at lower intensities.

The SWAN public data release includes data cubes and the moment maps created with `GILDAS` and are available on the IRAM Data Management System and the Canadian Advanced Network for Astronomical Research (CANFAR). The PyStructure table is utilized in upcoming SWAN publications analyzing the CO isotopologs (den Brok et al., 2025; Galic et al, submitted) as well as dense gas tracers HCN, HNC, HCO^{+} and N_2H^{+} (Stuber et al. in prep). The PyStructure table are distributed as a complementary product on the CANFAR.

4 Pystructure documentation: https://pystructure.readthedocs.io/en/latest/

4.4 RESULTS: 3MM LINE EMISSION ACROSS M51

We present an overview of the integrated intensity maps (moment-0) of all lines from the SWAN survey in Fig. 21. The resulting maps from the two different methods of moment map generations (see Sect. 4.3.6) can be compared via Figs. 51 and 52). To compare the emission of all detected molecular lines, we utilized the moment maps created based on common priors (^{12}CO and HCN, Fig. 52), created with the PyStructure-code.

In this section, we compare the spatial distribution of the integrated molecular line emission across the full FoV below. Further, we compare emission of molecular lines against each other (Sect. 4.4.1), and compare line ratios with ^{12}CO between the central 1 kpc and the disk (Sect. 4.4.2). In Sect. 4.4.4, we compare the SWAN dataset to high- and low-resolution observations from the literature for individual lines.

To first order, the SWAN maps show that 3mm molecular line emission is similarly distributed across M51's inner disk. For all tracers, the emission is bright along the spiral arms and in the molecular ring. Roughly half of the SWAN emission lines are also bright in M51's center, where an AGN with low-inclined radio jet is located. The notable exceptions are ^{13}CO and C^{18}O, which – similar to ^{12}CO (PAWS; Schinnerer et al., 2013) – show relatively faint emission in the central region compared to elsewhere in the inner disk.

Within the disk, the emission of all lines is particularly bright along the western side of the molecular ring, at the base of the southern spiral arm. Some lines, including N_2H^+(1-0), C^{18}O(1-0), ^{13}CO(1-0) and HNCO(4-3) are brightest in this particular region (RA: 13:29:50.06332, DEC: 47:11:25.20404 (J2000)). Spectra of all lines inside a 3″-aperture centered on this region and centered on the galaxy center (Fig. 20) reveal that most lines reach higher intensities in this region compared to the center. The N_2H^+ emission in this region was previously studied by S23, who reported unusually high N_2H^+-to-HCN and N_2H^+-to-^{12}CO ratios compared to elsewhere in M51's inner disk. Other lines in the SWAN dataset, such as the shock-tracer HNCO, are also bright in this region. This region will be investigated in more detail, using the full suite of SWAN emission lines, in a forthcoming paper (Stuber et al., in prep.).

4.4.1 Comparison of line intensities

In Fig. 22, we present a pixel-by-pixel comparison of the integrated intensity for all emission line pairs in the SWAN dataset. We highlight data points inside the central, inclination-corrected 1 kpc (in diameter) region, and overlay a linear relation through the average line ratio to aid visual inspection. As is shown in S23, an aperture of 1 kpc captures most of emission that is likely affected by the AGN, and is in agreement with the spatial extent of optical AGN-typical line ratios, X-ray and radio emission (Blanc et al., 2009). We note that within this area, a nuclear bar coexists. This central region contains ~ 200 hexagonal pixels. For each panel, we calculate the mean logarithmic line ratio ($b = \text{mean}\left(\log_{10}(y/x)\right)$, with x and y referring to the values on the x and y axes) for pixels where both of the lines involved in the line ratio are significantly detected ($> 3\sigma$). All values are listed in Table 13. Additionally, we list b_{cen} and b_{disk}, which refer to the same calculations performed inside and outside the central 1 kpc, respectively. We add the significance (see Appendix A.4) of the difference of b_{cen} and b_{disk} in Table 13. Only a few pixels in the SWAN FoV show significant HNCO(5-4)

detections, so the regression results including this line are highly uncertain. The few detections of this line are located in the center of the galaxy, as well as the southwestern edge of the molecular ring, where all lines are remarkably bright.
We find the following:

(a) Most emission line pairs exhibit a roughly linear (slope of 1) correlation, when pixels in the central 1 kpc are excluded. This is particularly the case for emission lines that are associated with denser molecular gas, such as HCN, HNC, and HCO^+, which visually follow a linear correlation over 1-2 orders of magnitude.The isotopologs $C^{18}O$ and ^{13}CO are both also visually well correlated with HCN, HNC, and HCO^+.

(b) In most panels, pixels in the central region show a clear offset relative to pixels elsewhere in the disk, indicating that the line emission is driven by different mechanisms in the disk compared to the center. HCN, HNC, HCO^+, N_2H^+, HNCO, and C_2H emission in the center are significantly enhanced compared to both $C^{18}O$ and ^{13}CO emission (compare Table 13). HCN emission in the center is clearly enhanced compared to all other lines. The enhancement is strongest when compared to ^{13}CO, and weakest relative to its isomer, HNC. Line combinations that do not vary significantly between the center and disk regions are $C^{18}O$ and ^{13}CO, N_2H^+ and HCO^+, and combinations including the fainter HNCO and C_2H lines. N_2H^+(1-0) is enhanced in the center compared to $C^{18}O$ and ^{13}CO, but it is fainter compared to HCN, HNC, and HCO^+.

(c) Correlations in the disk that visually appear to deviate from a linear trend include the trends between N_2H^+ and most lines except HNCO(4-3), and between C_2H and most lines except ^{13}CO and potentially $C^{18}O$. We note that these visual trends are mostly driven by the brightest pixels of each line and could be biased by the differences in S/N. As an example, in S23 we measured a super-linear trend between N_2H^+ and HCN emission ($m = 1.2$), which was mainly driven by the brightest pixels in N_2H^+ emission.

Our data show that while all molecular lines are bright in similar regions in the disk (Fig. 21), there are significant variations in the line ratios, both on 125 pc scales and across larger ~kiloparsec-scale environments such as the center. Moreover, the not exactly linear correlation between several molecular emission lines suggests that these cloud-scale observations are sufficient to detect some variations in the excitation, chemical abundance, and opacity in the molecular gas across M51's disk. Overall, the variations in line emission ratios between the central 1 kpc, which potentially arise due to the AGN, and the disk are larger than the variations observed elsewhere in the disk.

4.4.2 Global line ratios with ^{12}CO

^{12}CO is often used to study the bulk molecular gas distribution in galaxies (i.e., Helfer et al., 2003; Bolatto et al., 2013; Leroy et al., 2021b), because it is relatively abundant and its rotational transitions easily excited, producing bright millimeter-wavelength emission under typical ISM conditions. When studying other usually fainter molecular lines, it is thus often of interest to measure their intensity relative to ^{12}CO. In Fig. 23, we show the logarithmic distribution of the emission in the SWAN moment-0 maps divided by the integrated intensity ^{12}CO emission (from Schinnerer

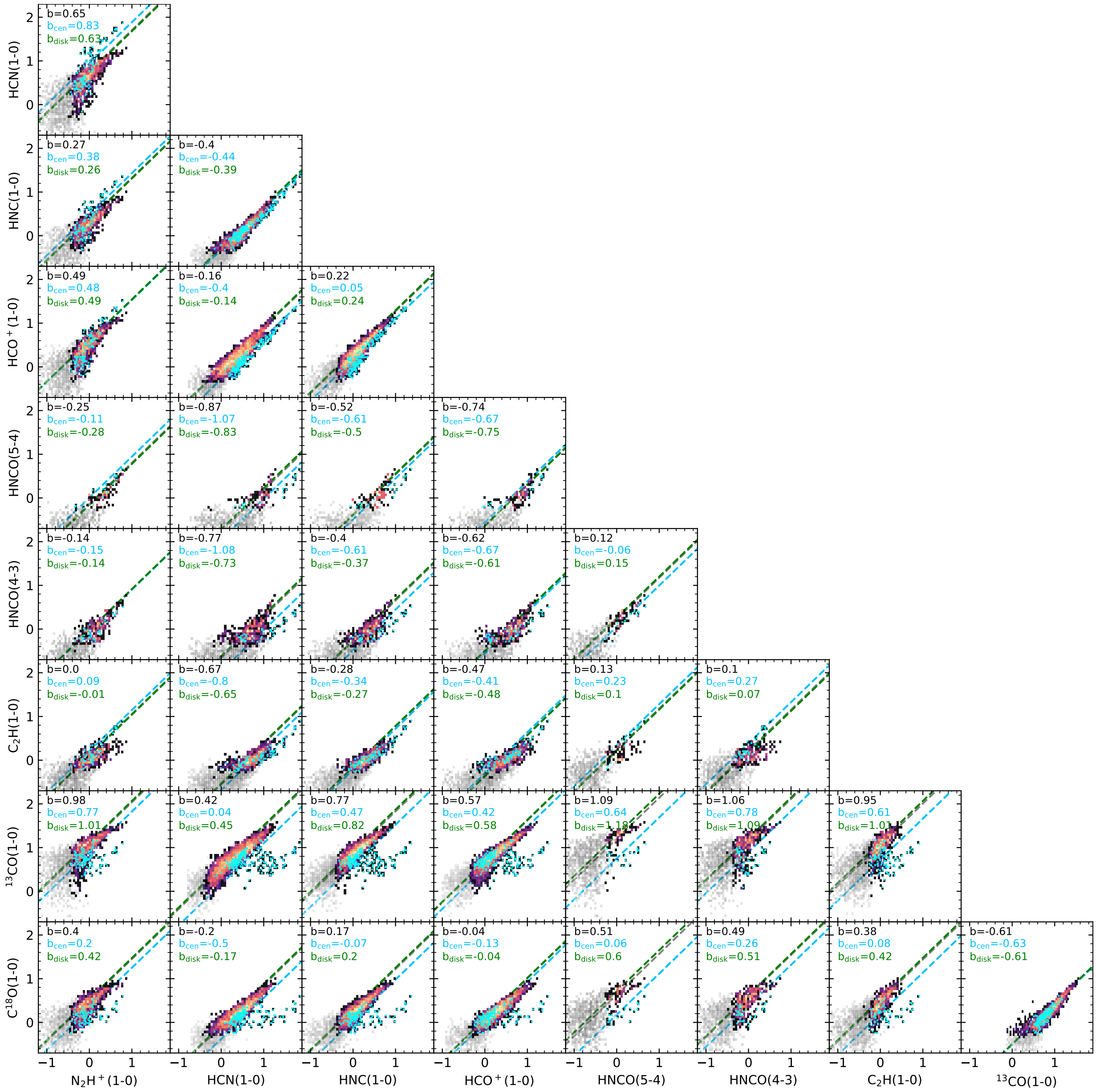

Figure 22: Logarithmic integrated line emission in K km s^{-1} of all lines compared on a pixel-by-pixel scale. We show the 2D distribution of emission from both significant detections (colored points, $>3\sigma$) and non-detections (gray points, $< 3\sigma$). The color scale of both detected and undetected points indicates the point density and is for visual purposes only. We mark pixels inside the central 1 kpc (in diameter, $\sim 8''$) in cyan. The dashed gray line corresponds to a power-law with a slope of unity and offset b being the average line ratio calculated from pixels with significant detections, including the central pixels. We define $b = \text{mean}\left(\log_{10}(y/x)\right)$, with x and y referring to the values on the x and y axes. We further show b_{cen} (dashed blue line) and b_{disk} (dashed green line) which were calculated using only pixels inside and outside the central 1 kpc, respectively. b_{disk} and b often overlap. Uncertainties were calculated following Gaussian error propagation and are listed together with all values of b in Table 13.

et al., 2013, see Section 4.3.6). The distribution of the integrated intensity ratios are shown separately for the full disk and the central 1 kpc and central 0.4 kpc. Here, full disk refers to the area inside the SWAN FoV, where we avoid the increased noise towards the edges of the mosaic (compare this with Fig. 17). We only consider pixels where the respective line and CO are significantly detected ($> 3\sigma$). Table 5 provides the average integrated intensity line ratios in the full disk, central 1 kpc and disk excluding the center, as well as their scatter. To assess the effect of the 3-sigma masking on the total flux, we also quote the fraction of masked-to-unmasked flux. Even within the environments, we note large variations in the ^{12}CO line ratios (Fig. 23). We estimate how much noise is contributing to this scatter in Sect. 4.4.3.

As before, the central 1 kpc distribution is clearly offset from the full disk distribution for most lines except for the ^{12}CO line ratios with the CO isotopologs. This offset is even stronger for the HCN-to-CO, HCO$^+$-to-CO, HNC-to-CO and C$_2$H-to-CO ratio in the central 0.4 kpc (diameter). This is caused by ^{12}CO emission being nearly absent in the very center of the galaxy, presumably due to photodissociation, mechanical evacuation, or radiative transfer effects (Querejeta et al., 2016b). The similar behavior of the ^{13}CO- and C^{18}O-to-^{12}CO (1-0) ratios is consistent with results from SMA observations (SMA-PAWS; den Brok et al., 2025), which cover the (2-1) transitions of these CO isotopologs. The similar radial trends observed in the ^{13}CO-to-^{12}CO (1-0) and (2-1) ratios suggest that these transitions are influenced by similar excitation mechanisms. Still, by integrating the SWAN and SMA-PAWS CO isotopolog line observations, the non-LTE modeling analysis in den Brok et al. (2025) indicates opacity variations at cloud scales within the disk. To assess possible effects of increased ^{12}CO opacity, we provide histograms of line ratios with ^{13}CO in Appendix A.5. Qualitatively, the same increases for the dense gas tracer to CO line ratios in the central enhancements can be seen.

We discuss this in more detail in Sect. 4.5. Since both C^{18}O and ^{13}CO show a similar lack of emission in the center as ^{12}CO, their distributions of center and disk agree well.

On average, HCN emission is ~ 17 times fainter than ^{12}CO, but this factor varies strongly between ~ 6 in the galaxy center, and ~ 20 in the disk. This emphasizes the importance of mapping emission not only in individual environments but across a larger set of environments such as in our SWAN FoV. The faintest lines detected in our data, N$_2$H$^+$(1-0) and HNCO(4-3), are roughly a factor of ~ 70 times fainter than ^{12}CO in the disk.

4.4.3 Effect of noise on measured line ratios with ^{12}CO

In addition to the variations in ^{12}CO line ratios between center and disk, we observe a large scatter in the histograms presented in Fig. 23, reflected by the large percentiles in Table 6). Our goal is to determine whether the scatter in our dataset can be attributed solely to noise, or if it might be linked to physical properties. The 3-sigma clipping threshold applied during the analysis can introduce a bias in the measurement of line ratios and their scatter.

To explore this, we built a simple toy model for which we assume that the line-to-CO ratio remains constant, and is represented by the median line ratio, which we provide in Table 6. This median line ratio was calculated for pixels where both the line and ^{12}CO are significantly detected ($>3\sigma$), similar to the mean values in Table 5. In addition, we provide the median absolute deviation, s_{measured}, which we use as an indication of the scatter. For each pixel, we predicted the expected line intensity based on the ^{12}CO

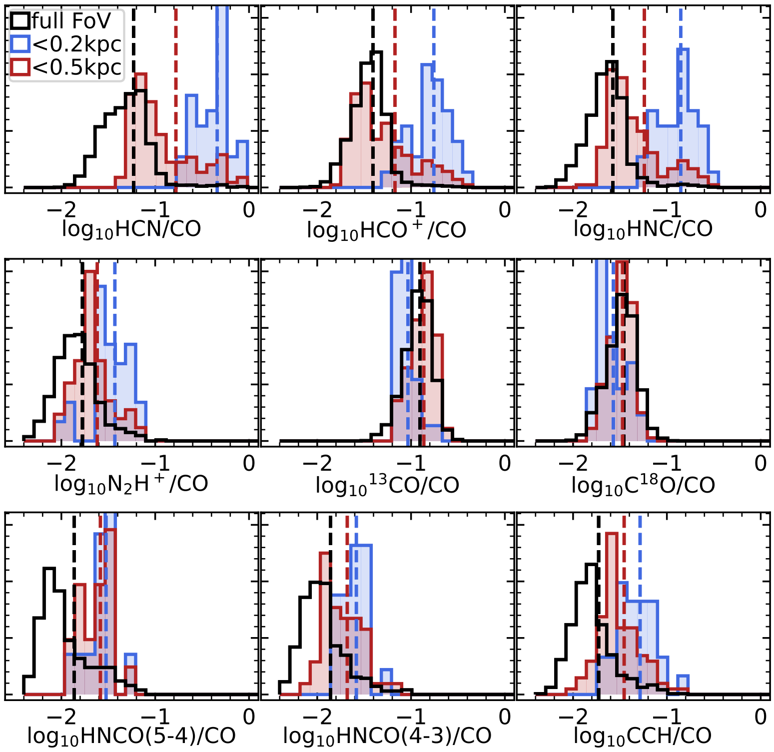

Figure 23: Histograms of line ratios with ^{12}CO for pixels where both the line emission and ^{12}CO emission are significantly detected ($> 3\sigma$) inside the full FoV (black) and the central 1 kpc (blue) and central 0.4 kpc (in diameter, red). We mark averages ($\log_{10}$(mean(line/CO))) for the full FoV and central apertures (dashed gray, blue, and red line, respectively). The histograms are normalized to have an integrated area of unity.

Table 5: Typical line ratios with ^{12}CO

Line ratio	full disk	center	disk	F_{line}	F_{CO}
HCN(1-0)/CO	$0.059\pm^{0.027}_{0.009}$	$0.166\pm^{0.101}_{0.015}$	$0.049\pm^{0.018}_{0.015}$	0.95	0.83
HNC(1-0)/CO	$0.027\pm^{0.010}_{0.003}$	$0.058\pm^{0.029}_{0.001}$	$0.022\pm^{0.006}_{0.005}$	0.87	0.66
HCO$^+$(1-0)/CO	$0.039\pm^{0.012}_{0.006}$	$0.067\pm^{0.039}_{0.006}$	$0.037\pm^{0.01}_{0.008}$	0.93	0.78
N_2H^+(1-0)/CO	$0.017\pm^{0.007}_{0.002}$	$0.024\pm^{0.008}_{0.002}$	$0.016\pm^{0.006}_{0.002}$	0.75	0.45
HNCO(5-4)/CO	$0.014\pm^{0.007}_{0.001}$	$0.026\pm^{0.010}_{0.007}$	$0.011\pm^{0.004}_{-0.0}$	0.74	0.09
HNCO(4-3)/CO	$0.014\pm^{0.006}_{0.001}$	$0.021\pm^{0.008}_{0.006}$	$0.013\pm^{0.005}_{0.010}$	0.68	0.25
C^{18}O(1-0)/CO	$0.035\pm^{0.009}_{0.007}$	$0.034\pm^{0.007}_{0.006}$	$0.035\pm^{0.009}_{0.007}$	0.89	0.77
^{13}CO(1-0)/CO	$0.125\pm^{0.028}_{0.024}$	$0.137\pm^{0.028}_{0.028}$	$0.124\pm^{0.028}_{0.024}$	0.98	0.96
C_2H(1-0)/CO	$0.019\pm^{0.007}_{0.001}$	$0.035\pm^{0.012}_{0.006}$	$0.016\pm^{0.005}_{0.001}$	0.55	0.32

Average line ratios with ^{12}CO (1-0) inside the full FoV (limited to the area covered by the mosaics (see Fig. 17), the central 1 kpc (in diameter), and the disk excluding the central 1 kpc. Average line ratios were determined from pixels in the moment-0 maps where both lines are detected significantly ($> 3\sigma$). We provide the difference between the average and the 25th and 75th percentiles as an uncertainty. To estimate the fraction of emission that originates from regions of significant detection, we provide the masked-to-unmasked flux ratio for both the specific emisison line (F_{Line}) and CO (F_{CO}). This ratio was calculated by comparing the total flux in the full FoV within regions were the flux exceeds the $> 3\sigma$ threshold (masked flux) to the total flux without applying any threshold (unmasked flux).

Table 6: Typical scatter of median ^{12}CO line ratios

Line ratio	full disk median	$s_{measured}$	$s_{calculated}$	$s_{physical}$
HCN(1-0)/CO	0.049	0.026	0.005	0.025
HNC(1-0)/CO	0.023	0.009	0.003	0.009
HCO^+(1-0)/CO	0.036	0.013	0.004	0.013
N_2H^+(1-0)/CO	0.014	0.006	0.003	0.006
HNCO(5-4)/CO	0.009	0.004	0.002	0.003
HNCO(4-3)/CO	0.011	0.004	0.002	0.004
$C^{18}O$(1-0)/CO	0.033	0.012	0.005	0.011
^{13}CO(1-0)/CO	0.121	0.039	0.011	0.038
C_2H(1-0)/CO	0.015	0.006	0.003	0.005

Median line ratios with ^{12}CO (1-0) inside the full FoV calculated from pixels where both lines are detected significantly ($> 3\sigma$; see Table 5). We list their median absolute deviation to estimate the scatter ($s_{measured}$) and calculate the expected scatter based on the uncertainty maps and the median line ratio ($s_{calculated}$). The calculation of $s_{calculated}$ is described in the text. Under the assumption that the measured line ratio consists of a constant line ratio with statistical noise and a physical contribution, we can estimate the scatter due to physical effects as $s_{physical} = \sqrt{s^2_{measured} - s^2_{calculated}}$.

intensity and the constant line ratio. We added a Gaussian noise distribution that is based on each pixel's noise estimate on both the predicted line intensity and the ^{12}CO intensity. Next, we calculated the scatter of the line ratio of these two modified intensities. This procedure was repeated 100 times and the median scatter, $s_{calculated}$, is quoted in Table 6. For all line ratios, the calculated scatter is several times smaller than the measured one. This implies that the measured scatter cannot be fully explained by noise and physical mechanisms might be contributing to the scatter.

We estimated the physical contribution by assuming a linear dependency of the line ratio and a statistical and physical noise contribution. This leads to $s_{physical} = \sqrt{s^2_{measured} - s^2_{calculated}}$. We list $s_{physical}$ for all lines in Table 6. We find that noise uncertainties make a minor contribution to the scatter measured for all line ratios, meaning that the variations in line ratios that we measure at 125 pc resolution are mostly driven by physical mechanisms.

The simple assumption of a constant line ratio is not correct for all lines. As is shown by S23, N_2H^+ depends superlinearly on ^{12}CO (power of ~ 1.1) and HCN depends sublinearly on ^{12}CO (power of ~ 0.5). Since most of these trends are driven by a small number of brighter pixels (i.e., surrounding the AGN), their contribution to the scatter is small. To first order, we consider this a reasonable assumption. We conclude that the variations observed are the effect of physical properties changing and not due to variations associated with the noise of the images.

4.4.4 Comparison of SWAN data with other surveys

Here, we compare the SWAN results with previous observations to (a) test for consistency with high-resolution ($\sim 3''$) observations of HCN(1-0) in three individual pointings in M51 (Querejeta et al., 2019), and (b) put the data into context with lower-resolution ($\sim 30''$), but larger-FoV observations of HCN, HCO^+, and HNC from the EMPIRE survey (Jiménez-Donaire et al., 2019) and ^{13}CO, $C^{18}O$, and N_2H^+ from the

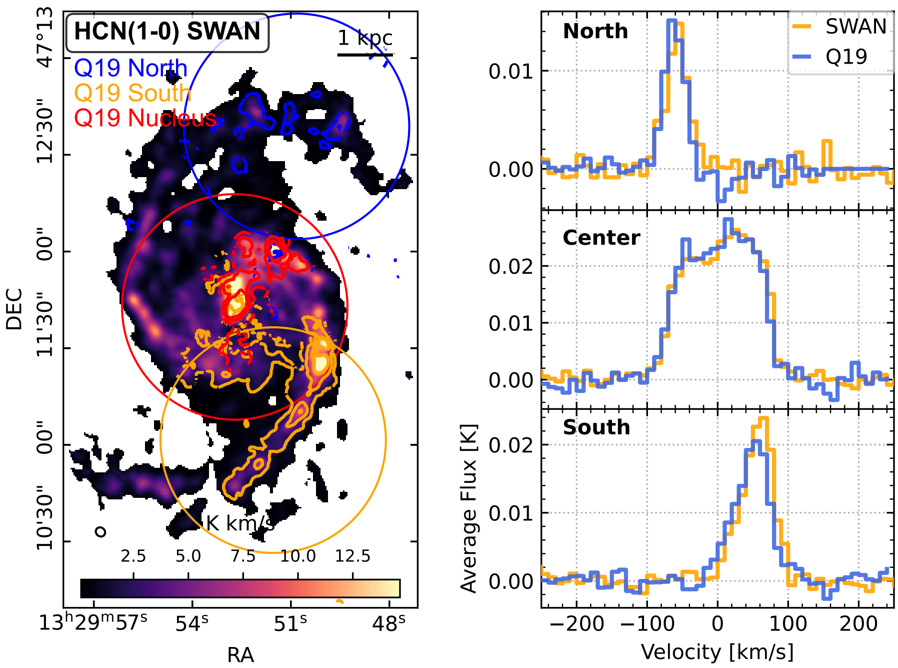

Figure 24: Comparison with HCN observations from Querejeta et al. (2019) (Q19). Left panel: SWAN HCN moment-0 map with contours ($\sim 5, 50, 200\sigma$ with σ the average noise) of Q19 HCN maps. Both maps are at 3″ resolution, spatially and spectrally regridded to the same grid, and the maps were created via the same GILDAS island method (using just the HCN line). Circles depict radii of 35″ centered according to Q19. Right panels: Average spectra of SWAN 3″ data at 10 km s^{-1} resolution as well as the matched Q19 data. Spectra are the average flux inside of the circular area shown in the left panel.

CLAWS survey (den Brok et al., 2022). While the PyStructure table is well suited for the line-by-line comparison done before, the GILDAS moment-maps and cubes are best suited for such a comparison with literature works (compare Sect. 4.3.6).

Comparison with high-resolution HCN observations

HCN has previously been observed in M51 at a similar resolution (3″) with the IRAM 30m and PdBI interferometer by Querejeta et al. (2019) (Q19) in three pointings in the disk. This survey mapped the HCN(1-0) flux inside 35″-sized pointings centered on M51's center (RA = 13:29:52.708, Dec = +47:11:42.81 (J2000)), the northern spiral arm (RA = 13:29:50.824, Dec = +47:12:38.83(J2000)) and the southern spiral arm (RA = 13:29:51.537, Dec = +47:11:01.48 (J2000)). We convolved the data to a spatial (3.04″) and spectral (10 km s^{-1}) resolution matched to our SWAN data. The dataset from Q19 was integrated via the same GILDAS island method that we used for SWAN (Sect. 4.3.6). Figure 24 indicates the HCN observations by Q19 as contours overlaid on our SWAN HCN(1-0) map, as well as average spectra from both datasets corresponding to the 35″ apertures.

We find good agreement between both the spatial and the spectral distribution of the HCN emission in the Q19 and SWAN datasets. The total emission integrated over the matched spectra in the northern region of Q19 represents $\sim$ 119% of the total SWAN emission integrated over the spectra inside the same region. This is likely due to the northern region of Q19 slightly exceeding the SWAN FoV, and thus capturing a slightly larger area. For the center, this fraction is $\sim$ 96% and for the southern pointing $\sim$ 91%.

Comparison of HCN, HCO^+, and HNC emission from EMPIRE and CLAWS

Observations of HCN, HCO^+, and HNC at both lower and higher resolution have proven to be crucial for studying the conditions of molecular gas (Helfer and Blitz, 1993; Aalto et al., 1997; Meier and Turner, 2005; Kohno, 2005; Bigiel et al., 2016; Jiménez-Donaire et al., 2019; den Brok et al., 2022; Imanishi et al., 2023; Neumann et al., 2023b; Nakajima et al., 2023). To showcase the difference in resolution, Fig. 25 depicts ~kiloparsec observations from EMPIRE for HCN, HCO^+, and HNC(1-0) emission, as well as from CLAWS for $C^{18}O$, ^{13}CO, and N_2H^+(1-0), and SWAN contours on top. While the EMPIRE/CLAWS maps cover the outer parts of M51 better due to their larger FoV, their coarse resolution misses several structures that we can resolve in SWAN. SWAN shows a clear difference in molecular line emission between the spiral arms and interarm regions. Additionally, in contrast to EMPIRE/CLAWS, in SWAN we can differentiate between the molecular ring and the AGN-impacted center, which are regions with very different physical conditions.

4.5 DISCUSSION

The SWAN survey provides a view of CO isotopologs, dense gas tracing molecular emission lines, and PDR and shock-tracing lines at the sensitivity and spatial resolution (125 pc) required to bridge extragalactic and Galactic studies. The $5 \times 7\,\mathrm{kpc}^2$ FoV of SWAN covers the central region, which hosts an AGN, a nuclear bar, and a molecular ring, as well as spiral arms and the interarm region. Although all lines are prone to different excitation conditions, our high-resolution maps show general similarities between their distributions across the FoV (Figs. 21, 52, and 51). All lines are detected along the northern to southwestern side of the molecular ring, with the brighter lines extending well along the spiral arms. This work provides a first analysis of this dataset and we report stark differences between the emission of these lines and their line ratios with ^{12}CO between the central 1 kpc and disk.

CO emission is commonly used to trace the bulk molecular gas distribution. Hence, line ratios with ^{12}CO are used to gauge the abundance of molecules or estimate the average gas density (Leroy et al., 2017b; Jiménez-Donaire et al., 2019). We compare our average CO line ratios from the center, disk, and full FoV to literature values from the Milky Way and to high-redshift studies in Figs. 26 and 27. The error bars indicate the change in the average line ratio when applying different masking. When we only require ^{12}CO to be detected, instead of selecting pixels where both the line and ^{12}CO are significantly detected (Table 5), the average line ratio with ^{12}CO decreases for most lines. The distribution of significantly detected pixels is shown for the full FoV as violins for visual comparison. We discuss the variations in line intensities and CO line ratios within M51 and in comparison to other galaxies below.

CO ISOTOPOLOGS ^{13}CO AND C^{18}O: The general deficit of the otherwise abundant ^{12}CO, $C^{18}O$, and ^{13}CO emission in the center (Figs. 21 and 23) might suggest the chemical or mechanical destruction or excitation of these molecules via the jet and associated mechanisms. The former is in agreement with findings by Saito et al. (2022) in the outflow of NGC 1068, where ^{12}CO isotopologs are faint and potentially destroyed by dissociating photons and electrons (see also Cecil et al., 2002).

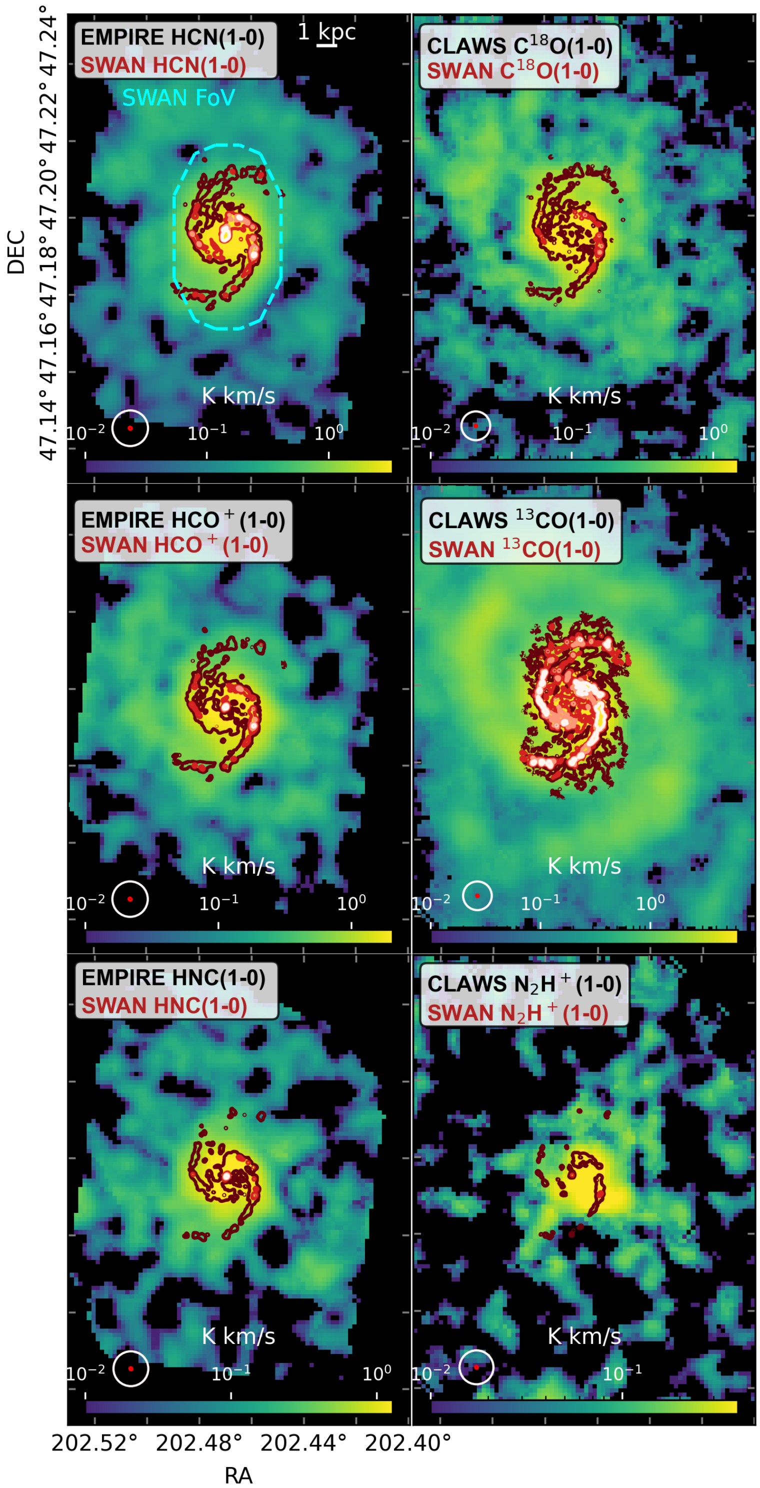

Figure 25: Integrated emission maps (moment-0) from EMPIRE at 33″ for HCN, HCO^+, HNC (1-0) (left columns) as well as from CLAWS at 15-30″resolution for $C^{18}O$, ^{13}CO and N_2H^+ (1-0) (right columns) with SWAN 1,5,10 and 15 $K\ km\ s^{-1}$ contours at native resolution ($\sim 3''$) on top. Beam sizes of EMPIRE/CLAWS and SWAN are shown in the bottom left corner of each panel (white and red circles, respectively)

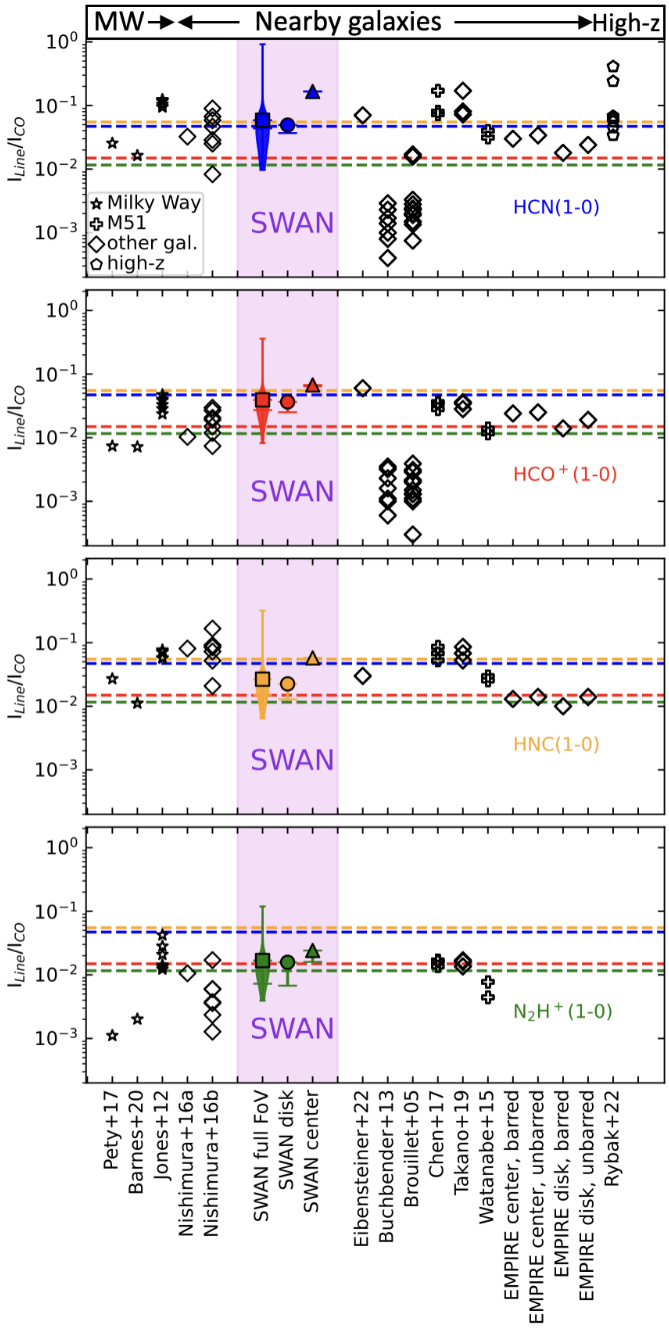

Figure 26: Literature comparison of integrated intensities for the J=1-0 transition of (from top to bottom:) HCN, HNC, HCO^+, and N_2H^+ emission compared to ^{12}CO. We show the SWAN integrated emission (light-shaded area) for the full FoV (squares), the central 1 kpc (triangle), and the remaining disk (circle). These values are obtained by integrating emission from pixels where both the line emission and ^{12}CO emission is significantly detected ($> 3\sigma$). The distribution of pixels in the full FoV is added as violins. The error bars correspond to the difference between this calculation (both ^{12}CO and the line are significantly detected) and when instead using pixels where ^{12}CO is significantly detected. Average literature values (horizontal dashed lines, calculated on a linear scale) are based on values from Milky Way (Pety et al., 2017; Barnes et al., 2020; Jones et al., 2012) and extragalactic sources: M51 studies at lower resolution (Watanabe et al., 2014) and in the outer spiral arm (Chen et al., 2017); different galaxy averages from EMPIRE (Jiménez-Donaire et al., 2019); $\sim$ 100pc studies in M33 (Buchbender et al., 2013), M31 (Brouillet et al., 2005) and NGC6946 (Eibensteiner et al., 2022); ~ 10 pc observation in the LMC (Nishimura et al., 2016a) and 80 pc in the dwarf galaxy IC10 (Nishimura et al., 2016b); $\sim 15 - 19''$ in three nearby galaxies (Takano et al., 2019) and upper limits from $z \sim 3$ galaxies (Rybak et al., 2022). The values are basically sorted by their physical resolution from a few parsecs in the Milky Way (left) to several kiloparsecs in external galaxies (right).

In general, all SWAN average line ratios between ^{12}CO and ^{13}CO or C^{18}O agree well with estimates for the Milky Way and nearby galaxies from the literature (Fig. 27). Since ^{13}CO is significantly brighter than the other molecules (i.e., N_2H^+) studied here, masking methods affect the obtained ratio less (compare this with F_{line}, Table 5). Still, a slight decrease in the line ratio with increased physical resolution might be inferred from Fig. 27, but only a few data points are available. Further, we do not see a large difference in line ratios between the center and disk of M51 that is evident for the dense gas tracers. This is in contrast to findings at 100 pc scales in the active galaxy NGC 3627 (Bešlić et al., 2021) where the ^{13}CO-to-^{12}CO (2-1) ratio is decreased in the center with respect to outer regions such as bar ends. Since NGC 3627 hosts a larger bar than M51 does, the central dynamics might play a critical role.

The C^{18}O-to-^{12}CO ratio increases with increasing physical resolution (Fig. 27, studies roughly sorted by physical resolution), which indicates that masking might affect the measurements. Interestingly, the SWAN measurements are generally higher than measurements from individual regions in both the Milky Way and other galaxies and are comparable to the kiloparsec measurements from CLAWS (den Brok et al., 2022), which cover a larger FoV including the entire molecular-gas-dominated disk of M51.

SHOCK TRACER HNCO: The higher rotational transitions of HNCO in the 3 mm range have been suggested as tracers of low-velocity shocks (e.g., Martín et al., 2008; Kelly et al., 2017). HNCO emission thus might suggest the presence of shocks in M51's center consistent with the location of a low-inclination radio jet and a dense-gas outflow containing both ^{12}CO and HCN emission (Querejeta et al., 2019). This is in agreement with findings by Martín et al. (2015), who report enhanced HNCO emission in the cicumnuclear disk surrounding the AGN in NGC 1097 at $\sim$ 100 pc resolution, and observations of HNCO arising from two lobes at both sides of the AGN of the Seyfert galaxy NGC 1068 (Takano et al., 2014).

The average HNCO(4–3)-to-^{12}CO line ratios of M51's center and disk are comparable to the high-resolution study in the outer arm of M51 (Chen et al., 2017), as well as the lower-resolution study in M51 (Watanabe et al., 2014) and other galaxy measurements (NGC 253, NGC 1068, and IC 342; Takano et al., 2019). As HNCO(5-4) emission is only detected from very few sight lines, the error bar on its average line ratio with ^{12}CO is very large (Fig. 27). Masking pixels without significant detections elevates the HNCO(5–4) average significantly (compare this with the error bar in Fig. 27, which showcases the average when including non-detections). With only 9% of the total ^{12}CO flux found in the area where HNCO(5–4) is significantly detected (Table 5), we caution the use of this masked full FoV HNCO(5–4)-to-^{12}CO ratio.

DENSE GAS TRACING LINES – HCN, HNC, HCO^+, N_2H^+: While some molecules such as C^{18}O and ^{13}CO (and ^{12}CO) are very faint in the center, other lines, such as HCN(1-0), are very bright (Figure 22, Table 13) and enhanced compared to ^{12}CO emission (Fig. 23, Table 5) or ^{13}CO emission (Fig. 54). This enhancement is increased when considering even smaller central apertures, suggesting that the outflow and/or AGN could be the potential cause (Fig. 23).

M51 has long been known to exhibit increased HCN emission in the very center both from kiloparsec-scale studies (Jiménez-Donaire et al., 2019) and those at 30 and 100 pc resolution (Helfer and Blitz, 1993; Matsushita et al., 2015; Querejeta et al., 2019). Infrared pumping, weak HCN masing, and an increased HCN abundance or electron excitation in the X-ray-dominated region (XDR) of the AGN are some possibilities suggested throughout the literature (e.g., Blanc et al., 2009; Matsushita et al., 2015; Querejeta et al., 2016b; Goldsmith and Kauffmann, 2017; Stuber et al., 2023a). HCN might potentially partake in the outflow driven by M51's AGN and radio jet. Similarly, bright HCN emission is colocated at the location of the AGN-driven outflow in the center of the galaxy merger NGC 3256 (Michiyama et al., 2018; Harada et al., 2018), in Mrk 231 (Aalto et al., 2012), in the starburst galaxy NGC 251 (Bešlić et al., 2021), in NGC 1068 (Saito et al., 2022), and in the center of NGC 4321 (Neumann et al., 2024). While both NGC 1068 and M51 host a small weak radio jet, there are differences: no N_2H^+ emission is detected from the outflow in NGC 1068 (Saito et al., 2022), while bright N_2H^+ emission is evident in M51's center and outflow, with increasing average N_2H^+-to-CO ratios for smaller central apertures (Fig. 23).

Shocks might also be an effective way to destroy or excite ^{12}CO molecules to higher states. A potentially young or weak jet might not yet have been able to mechanically remove large quantities of molecular gas. We might be viewing an early stage of molecular gas destruction, where lower density molecular gas such as ^{12}CO, which usually covers a larger volume than for example HCN molecules, is destroyed in large quantities, while HCN, which is brighter in denser regions (smaller volume) is not yet affected, or even shock-enhanced. (i.e., weak maser or abundance increase). However, dynamical age estimates of the jet or central objects in M51 range from $\sim 10^4 - 10^5$yr (Ford et al., 1985; Matsushita et al., 2007) up to a few Myrs (Rampadarath et al., 2018). The destruction of ^{12}CO might allow molecules such as N_2H^+ to form more abundantly as they would otherwise rapidly react with ^{12}CO (Bergin and Tafalla, 2007). Dissociation of other molecules by the radio jet might provide a large quantity of free electrons in the center of M51, which then leads to an efficient dissociative recombination of N_2H^+. The exact mechanisms driving the line emission in M51's center will be discussed in more detail in Thorp et al. (in prep.) and Usero et al. (in prep.).

Similarly to M51, Meier and Turner (2005) find bright N_2H^+ emission in the center of IC342 at 5″, which they explain by an increased cosmic ray ionization rate or an enhanced N_2 abundance. An increased N_2H^+ abundance could then promote the formation of HCO^+ which can form from N_2H^+ molecules (Harada et al., 2019). This is consistent with the fact that HCO^+ emission in the center follows a significantly different relation with HCN emission and is more tightly related to N_2H^+ than HCN (compare Appendix A.4). This is in agreement with findings by Butterworth et al. (2024) that HCO^+ and its isotopologs have larger column densities than HCN in the starbursting center of NGC 253 from the ALMA Comprehensive High-resolution Extragalactic Molecular Inventory (ALCHEMI) survey (Martín et al., 2021). Given that neither IC342, nor NGC 253 host an AGN, and M51 does not host a starburst in its center, the similarities between these galaxy centers are puzzling.

Emission from HCN and its isomer HNC are tightly correlated and show only a weak difference in their relation between the center and disk, suggesting that the chemical conditions able to convert one molecule into the other are not changing between the two environments. This is in agreement with findings by Meier and Turner (2005) in IC342. A detailed study of the cloud-scale variations in the HCN-to-HNC ratio will be presented in Stuber et al. (in prep.).

Figure 26 shows a large spread between the average ratios of the dense gas tracers to ^{12}CO from the literature and SWAN, especially for HCN, HNC, and HCO^+. Milky Way studies at high resolution report lower values compared to SWAN, except for the CMZ (Jones et al., 2012), which is consistent with our central averages being increased for all lines. The variation between multiple lines per literature study (i.e., average HCN/CO ratio compared to the HCO^+/CO line ratio for a single study) is typically smaller than the variation in one line ratio across all studies (e.g., HCN/CO varies strongly from study to study). This might indicate that different masking techniques drastically change the resulting ratios. While some studies apply cloud-finding algorithms to isolate individual clouds, other studies quote full FoV averages. Studies at kiloparsec-resolution such as Watanabe et al. (2014) in the center and southwestern molecular ring in M51 and the EMPIRE survey (Jiménez-Donaire et al., 2019) in general report lower line ratios, and so do high-resolution Milky Way studies. Generally, we find no clear trend with resolution (Fig. 26, studies are basically sorted by resolution).

As can be seen from Fig. 23, the pixel-by-pixel distribution of the line ratios with ^{12}CO generally spans over at least one or even two orders of magnitude for most lines. In Sect. 4.4.3, we estimated how much of the scatter can be attributed to noise and found that there is significant scatter in all line ratios with ^{12}CO that cannot be explained by noise only. Several studies report dependencies of ratios between dense gas tracers and ^{12}CO on dynamical equilibrium pressure or stellar surface density (Usero et al., 2015; Querejeta et al., 2019; Neumann et al., 2023b). A strong radial dependency is found in EMPIRE (Jiménez-Donaire et al., 2019), and their line ratios with ^{12}CO are generally enhanced in galaxy centers compared to disks (Fig. 26). Still, the difference between their centers and disks is smaller than our SWAN variations between center and disk, despite EMPIRE covering a larger FoV. HCN, HCO^+, and HNC emission in the center of NGC 6946 (Eibensteiner et al., 2022) sit between our disk and center measurements, despite NGC 6946 not hosting an AGN. Elevated central line emission is a feature common to galaxies with and without an AGN (Usero et al., 2015; Bigiel et al., 2016; Gallagher et al., 2018a; Jiménez-Donaire et al., 2019; Heyer et al., 2022; Neumann et al., 2024) and attributed to the gas-rich high surface density common to galaxy centers. Studies at a similar resolution to ours in M 33 and M 31 both find significantly lower HCN and HCO^+, which they consider a result of the sub-solar metallicity in both M 33 and M 31 (Buchbender et al., 2013). The variation in dense gas tracers N_2H^+, HCO^+, HCN, and HNC with various physical quantities on cloud scales is investigated in detail by Stuber et al. (in prep).

Overall, we find significant differences that can arise between the center (where an AGN, outflow, and a nuclear bar are present) and the disk of M51, whereas the variations in the disk are more subtle, but significant (Sect. 4.4.3). The exact mechanisms affecting the molecular gas in the center and in particular the outflow will be studied in more detail in forthcoming papers (A. Usero et al. in prep., M. Thorp et al. in prep.), we emphasize that all lines except ^{12}CO and its isotopologs show enhanced emission in the center. Further, we find large variations in literature ^{12}CO line ratios across various resolutions and targets. The least variations are seen for ^{13}CO-to-^{12}CO, which is consistent across the literature. Both the selected environment (center compared to disk) as well as the masking methods likely influence the line ratios.

4.6 SUMMARY

We present the first-of-its-kind high-resolution ($\lesssim$ 125 pc), high-sensitivity map of 3mm lines covering an area of $\sim 5 \times 7\,\mathrm{kpc}^2$ in the inner disk of the Whirlpool galaxy. We detect emission from the CO isotopologs ^{13}CO and $C^{18}O$(1-0) and the dense gas tracing lines HCN, HNC, HCO^+, and across the largest FoV to date N_2H^+(1-0). In addition, we detect HNCO(5-4), (4-3) and hyperfine transitions of C_2H(1-0) in the

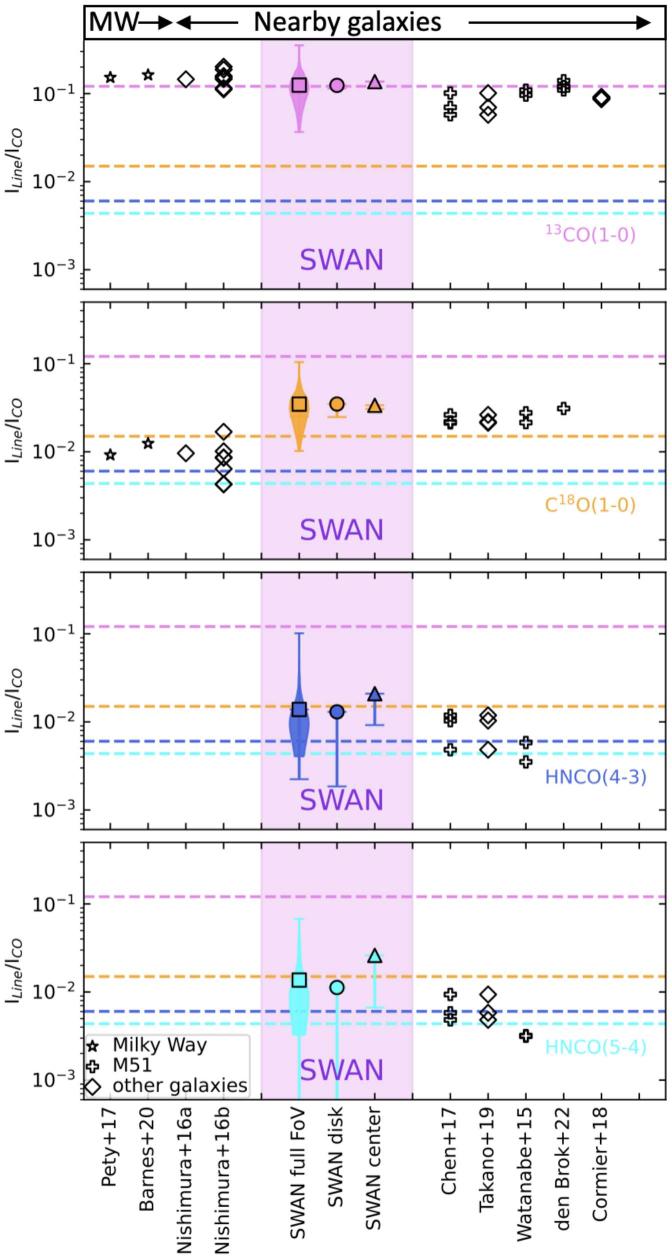

Figure 27: Same as Fig. 26, but for the J=1-0 transition of the CO isotopologs C^{18}O, and ^{13}CO, as well as the HNCO(5-4) and HNCO(4-3) lines. The EMPIRE isotopologs are measured by Cormier et al. (2018) instead of the survey paper. Further, we add CLAWS measurements of M51 (den Brok et al., 2022). The measurements are sorted by physical resolution (increasing to ~ kiloparsec scales at the right side of the plot).

center and molecular ring of M51. Comparing the emission of those lines to each other and to ^{12}CO(1-0) emission from PAWS (Schinnerer et al., 2013) at matched resolution, we find the following:

1. The high-resolution maps show general structural similarities across all molecular lines: bright emission of all molecular lines is detected along the western side of the molecular ring. Emission of the brighter lines is well detected in the southern and northern spiral arm, and all lines except the CO isotopologs are bright in M51's center.

2. We calculated typical ratios of line brightness with ^{12}CO brightness inside the full FoV for pixels where each line is significantly detected. We find the highest value for the ^{13}CO-to-^{12}CO ratio (0.125), followed by HCN-to-^{12}CO (0.059), HCO$^+$-to-^{12}CO (0.039), C^{18}O-to-^{12}CO (0.03), HNC-to-^{12}CO (0.027), C_2H-to-^{12}CO (0.019), N_2H^+-to-^{12}CO (0.017), and HNCO-to-^{12}CO (5-4: 0.014, 4-3: 0.014).

3. Emission of HCN is significantly enhanced in the central 1 kpc compared to all other detected lines, and emission of ^{12}CO isotopologs is significantly reduced in the center compared to non-isotopologs. The only line combinations that do not exhibit a significant offset relation to each other between the center and the disk are the isotopologs ^{13}CO and C^{18}O, the molecular ions N_2H^+ and HCO$^+$, and combinations including the faint HNCO and C_2H lines. ^{12}CO line ratios are increased in the central 1 kpc compared to the remaining disk for all lines except C^{18}O. The largest difference can be seen for the HCN-to-^{12}CO line ratio, which is more than a factor of three times larger in the central 1 kpc compared to the disk. HNCO emission might suggest the presence of shocks in the galaxy center, linked to a low-inclined radio jet and a dense-gas outflow. This points to complex conditions, possibly involving increased HCN abundance, infrared pumping, weak HCN masing, or electron excitation in the AGN's XDR.

4. Line ratios with CO qualitatively compare well to lower-resolution literature studies in other galaxies; that is, we find a similar increase in CO line ratios for HCN, HNC, HCO$^+$, and N_2H^+ in the centers of other galaxies. Still, the overall spread in CO line ratios across Galactic and extragalactic sources is significantly larger than both the differences between center and disk in M51, and the differences between different lines (such as HCN, HNC, HCO$^+$, and N_2H^+). We find that the scatter of SWAN ^{12}CO line ratios cannot be explained solely by noise and is likely attributed to local physical mechanisms.

SWAN allows us to study the molecular gas properties at cloud-scale resolution across multiple environments in the iconic Whirlpool galaxy. Dedicated studies focusing on the relationship of ^{12}CO isotopologs (den Brok et al., 2025; Galic et al, submitted), the dense-gas tracing lines (Stuber et al. in prep.), and the outflow in the center of M51 (Usero et al. in prep., Thorp et al. in prep.) will showcase the utility of this rich dataset for investigating physical conditions in the ISM.

DATA AVAILABILITY

The data is publicly available at the IRAM data management system, which can be accessed via the following link: `https://oms.iram.fr/oms/?dms=showprograms`.

ACKNOWLEDGEMENTS

This work has been carried out as part of the PHANGS collaboration and made use of data from the IRAM large program 'Surveying the Whirlpool galaxy at Arcseconds with NOEMA' (SWAN). We thank the referee for their valuable and constructive feedback. SKS acknowledges financial support from the German Research Foundation (DFG) via Sino-German research grant SCHI 536/11-1. JdB acknowledges support from the Smithsonian Institution as a Submillimeter Array (SMA) Fellow. CE acknoledges the support of the Jansky Fellow of the National Radio Astronomy Observatory. DL acknowledges the support from the Strategic Priority Research Program of the Chinese Academy of Sciences, grant No. XDB0800401. HAP acknowledges support from the National Science and Technology Council of Taiwan under grant 110-2112-M-032-020-MY3. AU acknowledges support from the Spanish grant PID2022-138560NB-I00, funded by MCIN/AEI/10.13039/501100011033/FEDER, EU.

5 MAPPING THE HCN AND N_2H^+ 3MM LINES

This chapter including appendix B comprises the article published in the Astronomy & Astrophysics journal volume 680 in 2023 with the title "Surveying the Whirlpool at Arcseconds with NOEMA (SWAN) - I. Mapping the HCN and N_2H^+ 3mm lines". The paper has been reformatted to match the style of this thesis. This work was published prior to the previous chapter.

Stuber, S.K., Pety, J., Schinnerer, E., Bigiel, F., Usero, A., Bešlić, I., Querejeta, M., Jiménez-Donaire, M., Leroy, A., den Brok, J., Neumann, L., Eibensteiner, C., Teng, Y., Barnes, A., and the PHANGS team

Abstract

We present the first results from "Surveying the Whirlpool at Arcseconds with NOEMA" (SWAN), an IRAM Northern Extended Millimetre Array (NOEMA)+30m large program that maps emission from several molecular lines at 90 and 110 GHz in the iconic nearby grand-design spiral galaxy M 51 at a cloud-scale resolution (~3″=125 pc). As part of this work, we have obtained the first sensitive cloud-scale map of N_2H^+ (1–0) of the inner $\sim 5 \times 7$ kpc of a normal star-forming galaxy, which we compared to HCN (1–0) and ^{12}CO (1–0) emission to test their ability in tracing dense, star-forming gas. The average N_2H^+-to-HCN line ratio of our total FoV is 0.20 ± 0.09, with strong regional variations of a factor of $\gtrsim 2$ throughout the disk, including the south-western spiral arm and the center. The central ~ 1 kpc exhibits elevated HCN emission compared to N_2H^+, probably caused by AGN-driven excitation effects. We find that HCN and N_2H^+ are strongly super-linearly correlated in intensity ($\rho_{Sp} \sim 0.8$), with an average scatter of ~ 0.14 dex over a span of $\gtrsim 1.5$ dex in intensity. When excluding the central region, the data are best described by a power law of an exponent of 1.2, indicating that there is more N_2H^+ per unit HCN in brighter regions. Our observations demonstrate that the HCN-to-CO line ratio is a sensitive tracer of gas density in agreement with findings of recent galactic studies utilising N_2H^+. The peculiar line ratios present near the AGN and the scatter of the power-law fit in the disk suggest that in addition to a first-order correlation with gas density, second-order physics (such as optical depth, gas temperature) or chemistry (abundance variations) are encoded in the $N_2H^+/^{12}$CO, HCN/^{12}CO, and N_2H^+/HCN ratios.

5.1 INTRODUCTION

The emission lines of molecules such as ^{12}CO are considered to be good tracers of the bulk molecular mass distribution (e.g. BIMA-SONG, Helfer et al., 2003; PAWS, Schinnerer et al., 2013; PHANGS, Leroy et al., 2021b) and found to correlate with (e.g. infrared) emission tracing recent star formation (e.g. Kennicutt and Evans, 2012; Bigiel et al., 2008). However, molecular clouds contain a wide range of densities, with star formation typically associated with the densest gas (e.g. Lada et al., 2010, 2012). Extragalactic studies show that CO emission does not distinguish between lower density, bulk molecular gas and the star-forming, dense material with H_2 densities of $\gtrsim 10^4$ cm^{-3} (e.g. Gao and Solomon, 2004; Jiménez-Donaire et al., 2019; Querejeta et al., 2019).

Tracers of dense gas are by definition challenging to observe due to the lower abundances of these molecules relative to CO and the smaller volume occupied by the dense phase, which both lead to a significantly reduced line brightness when compared to CO. With typical HCN-to-CO line ratios in disk galaxies of ~1/30 or lower (Usero et al., 2015; Bigiel et al., 2016), extragalactic studies were focusing on HCN (J=1–0) finding a tighter correlation between HCN line emission with star formation rate (SFR) than for CO emission (Gao and Solomon, 2004; Jiménez-Donaire et al., 2019). The higher critical density (n_{crit}) of HCN (1–0) has led to the common interpretation that this line preferentially traces the denser sub-regions of molecular clouds (Shirley, 2015), making HCN a commonly used tracer of dense molecular gas in extragalactic studies (Bigiel et al., 2016; Gallagher et al., 2018b; Jiménez-Donaire et al., 2019; Querejeta et al., 2019; Bešlić et al., 2021; Eibensteiner et al., 2022; Neumann et al., 2023b; Kaneko et al., 2023).

Galactic studies have questioned the use of HCN as a dense gas tracer at cloud scales (<10 pc) and favour the use of another molecule, N_2H^+, which has successfully been detected towards several molecular clouds in the Milky Way (e.g. Pety et al., 2017; Kauffmann et al., 2017; Barnes et al., 2020; Tafalla et al., 2021; Beuther et al., 2022; Santa-Maria et al., 2023; Tafalla et al., 2023). Since N_2H^+ is destroyed in the presence of CO, it is linked to the dense clumps of clouds, where CO freezes to dust grains (e.g. Bergin and Tafalla, 2007). This makes N_2H^+ not only a chemical tracer of cold and dense cores within clouds, but also leads to its emission being beam-diluted and, thus, even fainter than HCN (e.g. $N_2H^+/^{12}$CO ~ 1/100 at ~ 150 pc scales in a starburst galaxy; Eibensteiner et al., 2022, $N_2H^+/^{12}$CO ~ 1/140 at kpc scales in M 51 den Brok et al., 2022). Extragalactic observations of N_2H^+ are thus challenging and limited to low-resolution studies (e.g. ~kpc scales; den Brok et al., 2022; Jiménez-Donaire et al., 2023) or individual regions of galaxies (e.g. the center of starburst galaxy NGC 253; Martín et al., 2021). Jiménez-Donaire et al. (2023) summarize Galactic and extragalactic observations of HCN and N_2H^+. Although it may stand as a challenging task, the IRAM Northern Extended Millimetre Array (NOEMA) is capable of obtaining high sensitivity and high angular resolution observations needed to map the distribution of the faint emission of N_2H^+ and HCN in star-forming galaxy disks.

We present the first results from Surveying the Whirpool at Arcsecond with NOEMA (SWAN) IRAM Large Program (PIs: E. Schinnerer & F. Bigiel), including the first cloud-scale (125 pc) extragalactic map of N_2H^+ in the central 5–7 kpc of the Whirlpool galaxy (a.k.a M 51). SWAN targets nine molecular lines (C_2H (1–0), HNCO (4–3), HCN (1–0), HCO$^+$ (1–0), HNC (1–0), N_2H^+ (1–0), C^{18}O (1–0), HNCO (5–4), ^{13}CO (1–0)) at ~ 3″ (~ 125 pc) to study the role of dense gas in the star formation process across galactic environments.

M 51 (NGC 5194) is a nearby (D = 8.58 Mpc; McQuinn et al., 2016) close to face-on ($i = 22\,°$, P.A.= $173\,°$; Colombo et al., 2014a), massive ($\log_{10} M_*/M_\odot = 10.5$; den Brok et al., 2022), spiral galaxy that hosts a low-luminosity AGN (Ho et al., 1997; Dumas et al., 2011; Querejeta et al., 2016b). The HCN emission has been mapped at 3″ resolution (125 pc) for three circular regions of ~ 3 kpc diameter (Querejeta et al., 2019) in M 51, at 4″in the outer spiral arm at ~ 5 kpc galactocentric distance (Chen et al., 2017) and out to ~ 8 kpc in the disk at 1–2 kpc resolution by EMPIRE (Bigiel et al., 2016; Jiménez-Donaire et al., 2019). Watanabe et al. (2014) detected both HCN and N_2H^+ (1–0) at ~kpc resolution in two 30m pointings in the south-western spiral arm, and den Brok et al. (2022) presented N_2H^+ observations of its center at ~kpc resolution. In Sect. 5.2, we describe our observations and data reduction, followed by a comparison of the N_2H^+, HCN, and CO line emission in Sect. 5.3, a discussion in Sect. 5.4, and a summary in Sect. 5.5.

5.2 DATA

We used observations from the IRAM large program LP003 (PIs: E. Schinnerer, F. Bigiel) that combine NOEMA (integration time of ~ 214h) and the 30m single dish observations (about ~ 69h integration time from EMPIRE, CLAWS, and this program) to map 3-4 mm emission lines from the central 5×7 kpc of the nearby galaxy M 51. A detailed description of the observations and data reduction is presented in Appendix B.1.

The combined data as well as ^{12}CO data from PAWS (Schinnerer et al., 2013) were smoothed to a common angular and spectral resolution of 3″ and 10 km/s per channel. We integrated each line by applying the so-called GILDAS-based "island method" (see Einig et al., 2023, and references therein), where structures with ^{12}CO emission above a selected S/N of 2 in the position-position-velocity cube are selected. For all lines, the emission is then integrated over the same pixels from the ^{12}CO-based 3D mask.

5.3 RESULTS ON DENSE GAS IN M 51

Our SWAN observations have imaged the line emission of both HCN (1–0) (hereafter, HCN) and N_2H^+ (1–0) (hereafter N_2H^+) in M 51 at 125 pc resolution. In order to analyze which physical conditions might impact the brightness of these potential dense molecular gas tracers, we study the N_2H^+-to-HCN ratio across the disk of M 51 (Sect. 5.3.1), identify regions where the ratio deviates from the global trend (Sect. 5.3.2), and quantify the correlation between N_2H^+ and HCN emission (Sect. 5.3.3).

5.3.1 Distribution of N_2H^+ and HCN in the disk of M 51

Figure 28 shows the integrated intensity maps of HCN (1–0) and N_2H^+ (1–0), their ratio (upper panels), and the PAWS ^{12}CO (1–0) map (bottom-left). For five beam-sized N_2H^+-bright regions in the disk (see ^{12}CO map) we extract average spectra of HCN, N_2H^+, and ^{12}CO (bottom middle panel). N_2H^+ emission is detected from various extended regions in the disk, including both spiral arms, the molecular ring and interarm regions. Both tracers (N_2H^+, HCN) roughly follow the CO brightness distribution with

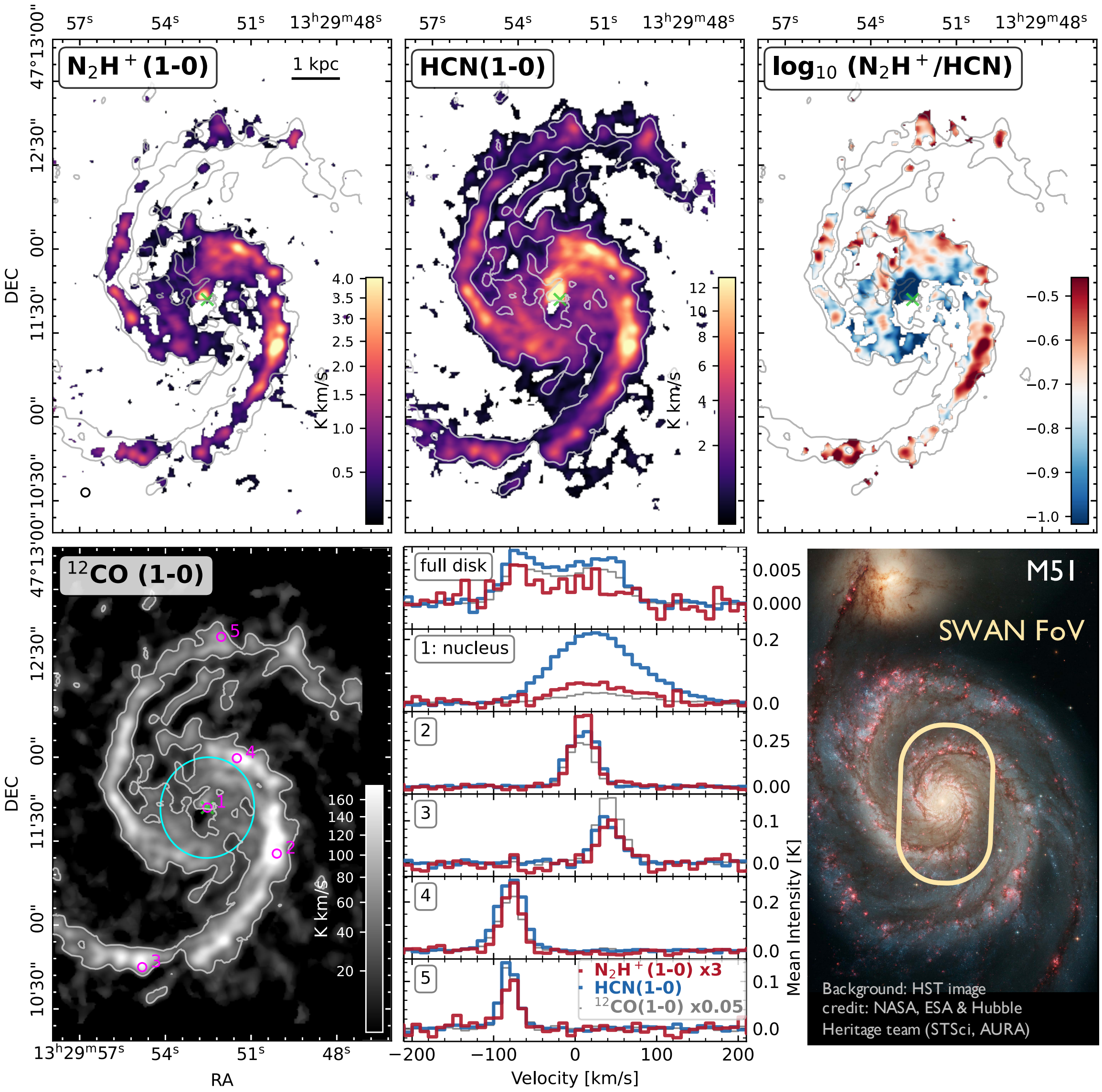

Figure 28: Integrated intensity maps of N_2H^+ (top left) and HCN (top center), as well as their ratio (top right) at $3''$($\sim$ 125 pc) resolution of the central 5 kpc $\times$ 7 kpc in M 51a. The ratio map shows emission above 3σ for both lines. The beam of $\sim 3''$ is shown in the bottom left corner of the N_2H^+ map for reference; the location of the galactic center is marked (green $\times$). We further display ^{12}CO emission at $3''$ resolution from the PAWS survey (bottom left; Schinnerer et al., 2013) for comparison and show the 30 K km/s contour of ^{12}CO for reference in all maps. The central 1.5 kpc (in diameter) is indicated by a cyan circle in the ^{12}CO map. Average spectra of five beam-sized regions in the disk (see the ^{12}CO map) are shown for N_2H^+, HCN and ^{12}CO (bottom center). We scale the spectra by a factor of 3 (N_2H^+) and 0.05 (^{12}CO) for easier comparison. The full-disk spectra contain all pixels in the FoV, shown on top of a HST image (bottom right).

Table 7: Typical line ratios of N_2H^+, HCN and ^{12}CO in M 51

Line ratio	Average ± sdev
N_2H^+/HCN (1–0)	0.20 ± 0.09
N_2H^+/HCN center	0.15 ± 0.05
N_2H^+/HCN disk	0.24 ± 0.26
N_2H^+/HCN *in beam-size regions:*	
region 1 (nucleus)	0.08 ± 0.04
region 2	0.33 ± 0.06
region 3	0.28 ± 0.07
region 4	0.23 ± 0.03
region 5	0.24 ± 0.04
HCN/CO (1–0)	0.05 ± 0.04
HCN/^{12}CO center	0.10 ± 0.07
HCN/^{12}CO disk	0.04 ± 0.02
N_2H^+/CO (1–0)	0.012 ± 0.006
N_2H^+/^{12}CO center	0.015 ± 0.007
N_2H^+/^{12}CO disk	0.011 ± 0.005

Average line ratios of N_2H^+-to-HCN as well as HCN-to-^{12}CO and N_2H^+-to-^{12}CO for regions with both HCN and N_2H^+ emission $> 3\sigma$ (see Figure 28). We list values for the full FoV, as well as for the central 1.5 kpc in diameter (center) and the remaining disk. For the N_2H^+-to-HCN ratio we further provide ratios of five N_2H^+-bright beam-sized regions in the disk selected visually (compare Fig. 28). The uncertainty is the standard deviation.

the brightest regions being the galaxy center (denoted as region 1), the southwestern spiral arm (2) as well as the northwestern part of the inner molecular ring (4).

On average, N_2H^+ is ~ 5 times fainter than HCN and ~ 80 times fainter than CO, while the line profiles are very similar (FWHM for N_2H^+: ~ 20 km/s, HCN ~ 30 km/s)[1], in agreement with ~kpc observations in NGC 6946 (Jiménez-Donaire et al., 2023). This remains true, even when imaging our data at 1 km/s spectral resolution. As observations of ~ 0.1 pc N_2H^+ clumps in the Milky Way suggest a factor of ~10 smaller N_2H^+ linewidths relative to HCN (e.g. 1–2 km/s; Tatematsu et al., 2008), our linewidths probably trace cloud-to-cloud velocity dispersion or turbulence scaling with physical lengths. Further, the typical ^{12}CO luminosity measured per beam (for details see Appendix B.2) indicates multiple clouds per beam. We conclude that the similar HCN and N_2H^+ linewidths suggest that HCN and N_2H^+ spatially coexist inside GMCs at these > 100 pc scales and only differ at scales below our resolution.

5.3.2 N_2H^+-to-HCN line ratios

Our average N_2H^+-to-HCN ratio is ~ 0.20 ± 0.09 (see Table 7) in regions with detected N_2H^+ emission (> 3σ) in the integrated intensity map. Table 7 lists average N_2H^+/HCN, N_2H^+/^{12}CO and HCN/^{12}CO ratios derived for the full FoV, the central 1.5 kpc in diameter, as well as the remaining disk[2]. The size of the central region is visually set to conservatively encapsulate the area surrounding the center, where low N_2H^+-to-HCN ratios are observed (see Fig. 28), but also to avoid other morphologi-

1 When considering Gaussian line profiles and that HCN is on average ~ 5 times brighter than N_2H^+, the inferred linewidths at matched brightness agree for HCN and N_2H^+.

2 The maps are regridded to 1.5″pixel size to minimize oversampling effects.

Table 8: Fit parameters and Spearman correlation coefficients of N_2H^+ as function of HCN

Region	Power a	Offset b	ρ_{Sp}	p-value
All data	1.10 ± 0.02	-0.72 ± 0.02	0.832 ± 0.009	< 0.001
All w/o AGN	1.20 ± 0.02	-0.79 ± 0.02	0.834 ± 0.009	< 0.001
AGN, yellow	1.13 ± 0.04	-1.20 ± 0.06	0.90 ± 0.05	< 0.001
SW.Arm, pink	1.49 ± 0.09	-1.06 ± 0.10	0.75 ± 0.05	< 0.001

Fit parameters for a linear fit in log-log space ($\log_{10} I_{N_2H^+} = a \cdot \log_{10} I_{HCN} + b$) that corresponds to a power-law relation in linear space ($I_{N_2H^+} = 10^b \cdot I_{HCN}^a$). We added Spearman correlation coefficients ρ_{Sp} and corresponding p-values. We only considered pixels with significant emission (i.e. $> 3\sigma$).

cal structures such as the molecular ring at larger radii. For these $\gtrsim$kpc regions, the N_2H^+-to-HCN line ratio in the center (disk) is lower (higher) by a factor of ~ 1.3 (~ 1.2) compared to the full FoV value, but still agrees within the uncertainties.

On approximately cloud-size scales (125pc), the N_2H^+-to-HCN ratio is significantly ($> 3\sigma$) lower in the center (1) than in region 2 in the south-western spiral arm (see Fig. 28 & Table 7) and deviates by a factor of 2.5 from the full FoV average. These findings suggest the presence of systematic trends that drive the high scatter of the full FoV line ratios (see next section).

5.3.3 Correlation of HCN and N_2H^+ line emission

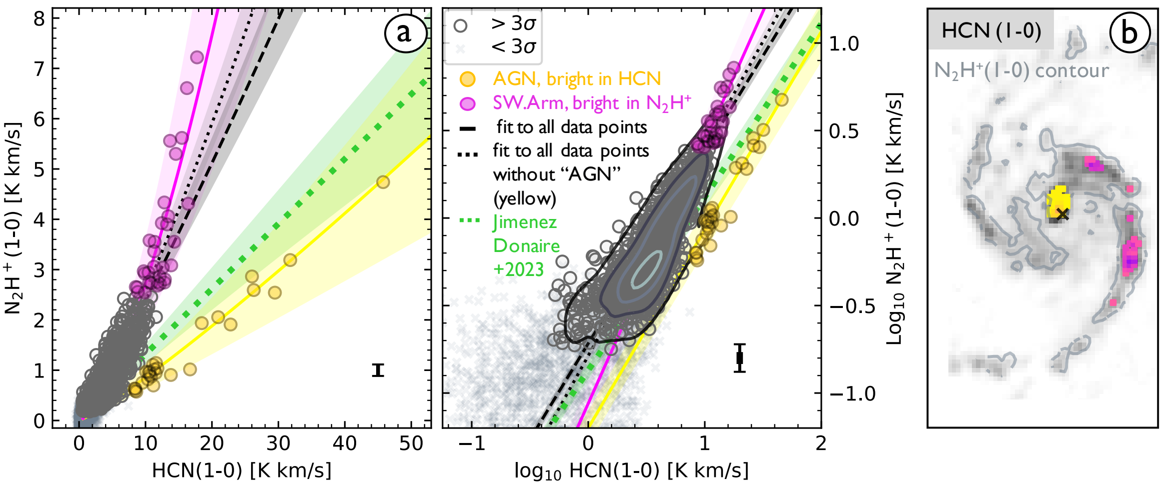

Figure 29: Comparison of N_2H^+ and HCN emission. a) Pixel-by-pixel distribution of integrated N_2H^+ and HCN emission in linear (left panel) and logarithmic (right panel) scaling. Subsets of pixels are visually isolated based on their high N_2H^+ (pink, SW.Arm) or HCN (yellow, AGN) values. Their location relative to the distribution of HCN emission in M 51 is shown in b) (contour marks 5σ N_2H^+ integrated intensity). Power-law fits are applied to all data points (black dashed line), the subsets identified (solid lines), as well as all data points excluding the yellow (AGN-affected) subset (black dotted line). Fit parameters and Spearman correlation coefficients for all data points and the subsets are given in Table 8. Data points below the 3σ noise level are presented as grey crosses. The N_2H^+-to-HCN relation from Jiménez-Donaire et al. (2023) is shown as a green dotted line.

To study how well the N_2H^+ and HCN emission are correlated, we analyzed the pixel-by-pixel distribution of N_2H^+ intensity as a function of HCN intensity[2] (Fig. 29, for N_2H^+ and HCN as a function of ^{12}CO emission see Appendix B.3).

To first order, the N_2H^+ emission is strongly correlated with the HCN emission (Spearman correlation coefficient $\rho_{Sp} = 0.832 \pm 0.009$, see Table 8). Although some data deviate from the correlation. The linear presentation (left panel) reveals two clusters with different mean slopes. We visually devise subsets of pixels that: (a) belong to the main cluster containing the bulk of the data points (grey), (b) have comparably low N_2H^+ flux while very high HCN fluxes (yellow), and (c) show the highest N_2H^+ intensities where the apparently linear trend becomes exponential (pink). Locating these pixels in the HCN moment-0 map (Fig. 29 b) reveals that subset (b) originates from the galaxy center (yellow, hereafter "AGN") and subset (c) from the south-western arm (pink, hereafter "SW.Arm"). Pixels in the central part of the galaxy thus follow a distribution that is significantly fainter in N_2H^+ emission than in HCN emission compared to the rest of the sample. We discuss the impact of the AGN in Section 5.4.1.

The logarithmic presentation (right panel of Fig. 29 a) confirms that subset (c, pink) from the south-western arm follows the bulk data (grey) for a power-law distribution. The comparably large scatter in this subset (c, SW.arm) emerges from two different spatial locations that have slightly different slopes than the subset's average one (see also Appendix B.5.1).

We fit all data points plus the subsets (emission $> 3\sigma$) with linear functions in logarithmic scaling. The fit parameters as well as Spearman correlation coefficients (ρ_{Sp}) and p-values are provided in Table 8). Details on the fitting process and the uncertainties derived via jackknifing are given in Appendix B.4. For all subsets, N_2H^+ emission is (similarly) aptly ($\rho_{Sp} > 0.75$) and super-linearly (best-fit power $a > 1$) correlated with HCN emission. However, the fit of the central (yellow) data points significantly deviates from the fit for all data points including and excluding the central ones (black dashed and dotted line, see also Appendix B.4). The central subset contributes $\sim 7\%$ of the total HCN and $\sim 4\%$ of the total N_2H^+ flux in our FoV, and contains most of the brightest HCN pixels. Although the disk data points (without AGN and SW.arm, grey points), can be best described with a linear relation (power $a = 0.97 \pm 0.013$), the power index monotonically increases when the upper limit of the range in integrated N_2H^+ emission used to select the fitted point is increased. This is likely due to the scatter around the power law decreasing at the same time as the data explores a larger part of the power law, increasing the range spanned by the data.

The N_2H^+-to-^{12}CO and HCN-to-^{12}CO distributions (Fig. B.3) behave similarly, as the central data points clearly deviate from the bulk distribution. Similarly to the N_2H^+-to-HCN distribution, the N_2H^+-to-^{12}CO distribution (Fig. 55) is best described by a super-linear power-law, with its brightest end being mainly populated by the pixels from subset (c, SW.arm) (Table 14). In contrast, the HCN-to-^{12}CO distribution is best described by a sub-linear to linear power-law. We quantified the scatter of these distributions in Appendix B.5.2 and find that for all distributions, the scatter is of order ~ 0.14 dex, while the total range covered by the lines cover $\gtrsim 1.5$ dex.

5.3.4 Density-sensitive line ratio

The ratio of emission lines from HCN and ^{12}CO ($f = I_{HCN}/I_{CO}$) has been commonly used as an indication of the (average) gas density f_{dense} (e.g. Usero et al., 2015; Bigiel

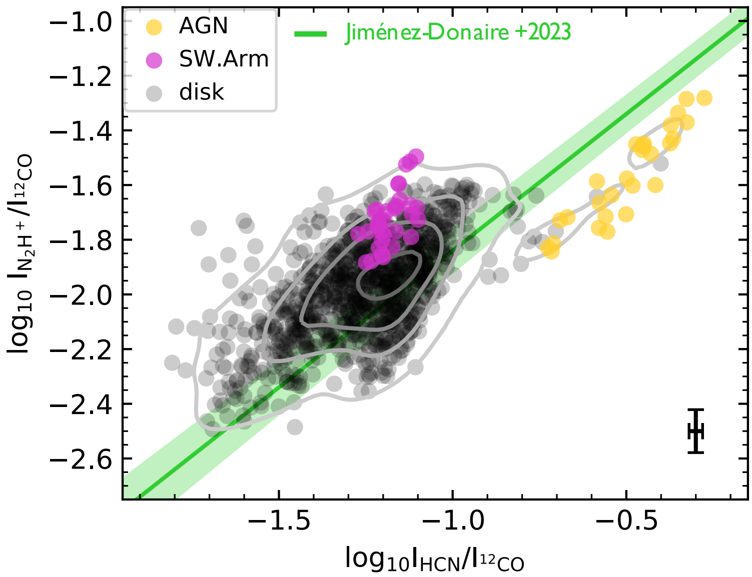

Figure 30: I_{N_2H+}/I_{CO} as function of I_{HCN}/I_{CO} for all data points and subsets above a 3σ noise level. We show the average uncertainty in the bottom right corner, as well as the best-fit from Jiménez-Donaire et al., 2023, Eq. 2 with a power law slope of 1.0 derived for extragalactic and Galactic data points (green line). Contours indicate the number density of data points.

et al., 2016; Jiménez-Donaire et al., 2019). We compare I_{N_2H+}/I_{CO} to f in Fig. 30 and find them to be correlated ($\rho_{Sp} = 0.70$, p-value < 0.001). Overall, 82% (97%) of our data points agree within 3σ (5σ) with the fit from Jiménez-Donaire et al., 2023, Eq. 2 with a power-law index of 1.0 obtained when fitting all available Galactic and extragalactic data (green line).

Our result indicates that to a first order, both line ratios are correlated. Although the difference has a low statistical significance, the AGN subset (b, yellow) is offset from the remaining data, and the N_2H^+-bright SW.arm subset (c, pink) clusters at higher $N_2H^+/^{12}CO$ values.

5.4 DISCUSSION ON MOLECULAR GAS DENSITY IN M 51

We discuss which physical conditions might impact the brightness of the potential dense molecular gas tracers based on the found distribution of N_2H^+ and HCN in the disk (Sect. 5.3.1), the high and low line ratios in isolated regions (Sect. 5.3.2), and the correlations between the emission of N_2H^+ and HCN (Sect. 5.4.2).

5.4.1 The AGN impacts the central emission in M 51

The N_2H^+-to-HCN line ratio is significantly lower in the center of M 51 compared to regions in the disk, and the central data points are offset from those in the disk (Fig. 29). In contrast, the HCN-to-^{12}CO ratio is higher in the center compared to the remaining disk (compare with Fig. 55), in agreement with Jiménez-Donaire et al. (2019) at ~kpc scales. Very-high-resolution (~ 30 pc) observations of HCN and ^{12}CO in M 51 by Matsushita et al. (2015) reveal extraordinarily high HCN/CO ratios (> 2) at the location of the AGN, which they explain by infrared pumping, possibly weak HCN masing and an increased HCN abundance. Electron excitation in the XDR of the AGN might also contribute to the enhanced HCN emission (Goldsmith and Kauffmann, 2017). Blanc et al. (2009) identified [NII]λ6584/Hα line ratios typical of AGN in M 51's central $\sim 700\,\mathrm{pc}$ and spatially coincident with X-ray and radio emission. HCN and ^{12}CO arise both from the outflow associated with nearly coplanar radio jet, with significant effects seen out to a distance of 500 pc (Querejeta et al., 2016b). While the central 1.5 kpc (diameter) region as used for the line ratios likely overestimates the area of influence of the AGN, our visually selected subset (b) likely underestimates the area impacted.

While both the HCN-to-^{12}CO and the N_2H^+-to-^{12}CO distributions (Fig. 55) show an enhancement in HCN or N_2H^+ emission in the central data points, the effect is less strong for N_2H^+-to-^{12}CO, as the fit to its central points agrees with the disk fit unlike the HCN-to-^{12}CO distribution (Appendix B.3). This implies that N_2H^+ is less affected by the AGN than HCN. Galactic studies do not find correlations between N_2H^+ and mid-infrared (MIR) photons (e.g. Beuther et al., 2022) suggesting that N_2H^+ is not affected by infrared-pumping via the AGN. While an increased temperature in the AGN vicinity can also increase HCN emission (Matsushita et al., 2015; Tafalla et al., 2023), this would lead to CO sublimating, reacting with and destroying N_2H^+ in contrast to our findings. High cosmic-ray ionization rates in the AGN surroundings might counter this effect by increasing the N_2H^+ abundance (Santa-Maria et al., 2021), which is not seen for HCN (Meijerink et al., 2011). The complex mechanisms happening in the AGN vicinity will be explored in a future paper.

5.4.2 The emerging N_2H^+-to-HCN relation

Our global average N_2H^+-to-HCN ratio of 0.20 ± 0.09 agrees well with ratios obtained at ~kpc resolution in M 51 of ~ 0.14 for the galaxy center and ~ 0.19 in the southern spiral arm (Watanabe et al., 2014; Aladro et al., 2015). A recent literature compilation (Jiménez-Donaire et al., 2023) reported that a N_2H^+-to-HCN ratio of $0.07 - 0.22$ for extragalactic regions and $\sim 0.05 - 0.23$ when including Galactic sources. Line ratios of five ~kpc size regions in NGC 6946 range between $0.12 - 0.20$, leading to a global ratio of 0.15 ± 0.03, or a linear fit in log-space of power 0.99 ± 0.04 and offset 0.87 ± 0.04 (Jiménez-Donaire et al., 2023) shown for reference in Fig. 29. This fit agrees with our fit to the central subset (b), but shows a significant ($> 3\sigma$) deviation from our fits focusing on the disk.

Given the AGN impact (Section 5.4.1), we considered the power-law fit without the central subset being most representative of typical conditions: The N_2H^+ emission as a function of HCN emission in the disk at 125 pc can be described as:

$$\log_{10} I_{N_2H^+} = (1.20 \pm 0.02) \cdot \log_{10} I_{HCN} - (0.825 \pm 0.009)\,. \quad (3)$$

The super-linearity in our relation, driving the discrepancy between our results and the literature, comes from the bright south-western spiral arm, where our N_2H^+-to-HCN ratio is the highest (Table 7, region 2). Strong streaming motions present in the southern spiral arm are likely stabilizing the gas resulting in low star formation efficiencies (Meidt et al., 2013). This region (at $\sim 28 - 38''$) is at the transition between the normal star formation efficiency and the extremely low star formation efficiency seen further south (Querejeta et al., 2019) and has a high dynamical complexity (i.e. coinciding with the co-rotation radius of a m=3 mode; Colombo et al., 2014a). Although its N_2H^+-to-HCN ratio is larger than the global average, it extends the general distribution in a smooth manner (Fig. 29), unlike the clearly offset emission from M 51's center. We speculate the following:

Firstly, HCN-bright regions have more dense gas (as traced by N_2H^+) than what we would expect from the HCN intensities. This effect should potentially be correlated with the resolution, as higher-resolution observations able to resolve clouds would be able to better to isolate the spatially smaller dense clumps.

Secondly, galactic studies find that HCN luminosity is sensitive to far-UV light from young massive stars (e.g. Pety et al., 2017; Kauffmann et al., 2017; Santa-Maria et al., 2023). The HCN emission is linked to dense molecular clouds, but it is also well correlated with regions of recent star formation. This effect is not seen for N_2H^+, which is abundant in cold and dense regions where the depletion of CO onto dust grains inhibits the main route of N_2H^+ destruction. In the southern-spiral arm, where star-formation is found to be comparably lower, this could explain our power law of 1.2.

As the focus of this study is the comparison of HCN to N_2H^+ emission, we selected pixels in the disk where N_2H^+ is detected. Since N_2H^+ is a chemical tracer of dense gas, we thus selected regions where dense gas can be expected. This can introduce a bias towards higher values, as we potentially mask out regions of low N_2H^+ emission.

5.5 SUMMARY AND CONCLUSION

We present the first map of N_2H^+ (J=1–0) and HCN (1–0) from the NOEMA+30m large program SWAN in the central 5×7 kpc of the nearby star-forming disk galaxy M 51 at cloud-scale resolution of 125 pc (3″). We study where the chemical dense gas tracer N_2H^+ emits with respect to larger-scale dynamical features and how it relates to emission from other molecules, such as HCN and CO. Comparing these lines, we have drawn the following conclusions:

1. Extended N_2H^+ emission is detected from various regions across the disk, with the brightest emission found in the south-western spiral arm, followed by the center and the north-western end of the molecular ring. Overall, HCN emission is bright in the same regions, but it shows the highest intensity in the center.

2. We find an average N_2H^+-to-HCN ratio of 0.20 ± 0.09 for regions detected in N_2H^+ emission ($> 3\sigma$) with strong variations throughout the disk of up to a factor of $\sim 2-3$ in the south-western spiral arm and the center that hosts an AGN. The N_2H^+ and HCN emission are strongly correlated ($\rho_{Sp} \sim 0.83$), but the central 1.5 kpc clearly deviates. The disk emission can be described with a super-linear power-law function of index 1.20 ± 0.02, indicating that HCN-bright regions have higher gas densities as traced by N_2H^+ than we would infer from their HCN emission alone.

3. The N_2H^+-to-HCN ratio is significantly lower in the M 51's center where an AGN is present and its distribution is offset from the bulk of the disk data. The affected region accounts for $\sim 9\%$ of the total HCN emission and $\sim 4\%$ of total N_2H^+ emission in pixels in our FoV where N_2H^+ is detected. MIR pumping might be one explanation for the bright and enhanced HCN flux surrounding the AGN.

Our ~ 120 pc observations in M 51 demonstrate that to first order, N_2H^+ and HCN are strongly super-linearly correlated. In addition to first-order correlations with gas-density, the peculiar line ratio present near the AGN and the scatter of the power-law fit suggest additional second-order physics (such as optical depth, gas temperature) or chemistry (abundance variations).

ACKNOWLEDGEMENTS

This work was carried out as part of the PHANGS collaboration. We thank the anonymous referee for their constructive feedback. This work is based on data obtained by PIs E.Schinnerer and F.Bigiel with the IRAM-30m telescope and NOEMA observatory under project ID M19AA. SKS acknowledges financial support from the German Research Foundation (DFG) via Sino-German research grant SCHI 536/11-1. JP acknowledges support from the French Agence Nationale de la Recherche through the DAOISM grant ANR-21-CE31-0010 and from the Programme National "Physique et Chimie du Milieu Interstellaire" (PCMI) of CNRS/INSU with INC/INP co-funded by CEA and CNES. ES acknowledges funding from the European Research Council (ERC) under the European Union's Horizon 2020 research and innovation programme (grant agreement No. 694343). AU acknowledges support from the Spanish grant PID2019-108765GB-I00, funded by MCIN/AEI/10.13039/501100011033. MQ and MJJD acknowledge support from the Spanish grant PID2019-106027GA-C44, funded by MCIN/AEI/10.13039/501100011033. JdB acknowledges support from the Smithsonian Institution as a Submillimeter Array (SMA) Fellow. LN acknowledges funding from the Deutsche Forschungsgemeinschaft (DFG, German Research Foundation) - 516405419. The work of AKL is partially supported by the National Science Foundation under Grants No. 1615105, 1615109, and 1653300. CE acknowledges funding from the Deutsche Forschungsgemeinschaft (DFG) Sachbeihilfe, grant number BI1546/3-1. Y-HT acknowledges funding support from NRAO Student Observing Support Grant SOSPADA-012 and from the National Science Foundation (NSF) under grant No. 2108081. MC gratefully acknowledges funding from the Deutsche Forschungsgemeinschaft (DFG) through an Emmy Noether Research Group, grant number CH2137/1-1. COOL Research DAO is a Decentralized Autonomous Organization supporting research in astrophysics aimed at uncovering our cosmic origins. SCOG acknowledges support from the DFG via SFB 881 "The Milky Way System" (sub-projects B1, B2 and B8) and from the Heidelberg cluster of excellence EXC 2181-390900948 "STRUCTURES: A unifying approach to emergent phenomena in the physical world, mathematics, and complex data", funded by the German Excellence Strategy. HAP acknowledges support by the National Science and Technology Council of Taiwan under grant 110-2112-M-032-020-MY3.

6 THE SWAN VIEW OF DENSE GAS IN THE WHIRLPOOL

This chapter including appendix C comprises the article submitted to the Astronomy & Astrophysics journal in March 2025 under the title "The SWAN view of dense gas in the Whirlpool - A cloud-scale comparison of N_2H^+, HCO^+, HNC and HCN emission in M51". The paper has been reformatted to match the style of this thesis.

Stuber, S.K., Schinnerer, A. Usero, E., Bigiel, den Brok, J., Pety, J., Neumann, L., Jiménez-Donaire, M., Sun, Jiayi, Querejeta M., Barnes, A., and the PHANGS team

Abstract

Tracing dense molecular gas, the fuel for star formation, is essential for the understanding of the evolution of molecular clouds and star formation processes. We compare the emission of HCN (1-0), HNC (1-0) and HCO^+ (1-0) with the emission of N_2H^+ (1-0) at cloud-scales (125 pc) across the central 5×7 kpc of the Whirlpool galaxy, M51a, from "Surveying the Whirlpool galaxy at Arcseconds with NOEMA" (SWAN). We find that the integrated intensities of HCN, HNC and HCO^+ are more steeply correlated with N_2H^+ emission compared to the bulk molecular gas tracer CO, and we find variations in this relation across the center, molecular ring, northern and southern disk of M51. Compared to HCN and HNC emission, the HCO^+ emission follows the N_2H^+ emission more similarly across the environments and physical conditions such as surface densities of molecular gas, stellar mass, star-formation rate, dynamical equilibrium pressure and radius. Under the assumption that N_2H^+ is a fair tracer of dense gas at these scales, this makes HCO^+ a more favorable dense gas tracer than HCN within the inner disk of M51. In all environments within our field of view, even when removing the central 2 kpc, HCN/CO, commonly used to trace average cloud density, is only weakly depending on molecular gas mass surface density. While ratios of other dense gas lines to CO show a steeper dependency on the surface density of molecular gas, it is still shallow in comparison to other nearby star-forming disk galaxies. The reasons might be both physical conditions in M51 different from other normal star-forming galaxies and the limited FoV which might be impacted by effects due to the AGN. Increased ionization rates, increased dynamical equilibrium pressure

in the central few kpc and the impact of the dwarf companion galaxy NGC 5195 are proposed mechanisms that might enhance HCN and HNC emission over HCO^+ and N_2H^+ emission at larger-scale environments and cloud scales.

6.1 INTRODUCTION

Star formation is one of the most fundamental processes in the Universe (see reviews by Krumholz, 2014; Klessen and Glover, 2015; Schinnerer and Leroy, 2024). As the birth of a star is ultimately linked to collapsing clouds of dense gas, the molecular gas phase is the key objective to study. Modern extragalactic observations (e.g., surveys like PHANGS-ALMA; Leroy et al., 2021b,a), show that molecular clouds are linked sensitively to their galactic environment. As an example, a cloud's velocity dispersion, surface density and virial state all vary depending on whether the cloud is located in the main disk or near the center, in a spiral arm or interarm region, or in a stellar bar (Querejeta et al., 2019; Bešlić et al., 2021; Neumann et al., 2024). This implies that the host galaxy impacts the initial conditions for star formation. However, how exactly those changes in cloud properties translate into the global pattern of star formation is still unsettled (see recent review by Schinnerer and Leroy, 2024). As stars must form out of the densest gas in molecular clouds (Gao and Solomon, 2004; Wu et al., 2005; Lada et al., 2012; Evans et al., 2014), two of the key open questions in astronomy are a) how to reliably access those densest molecular regions observationally and b) how the properties of dense gas and therefore the star formation is influenced by larger-scale environmental processes.

Line emission of molecules such as CO (1-0) is well suited for tracing the bulk molecular gas distribution in regions of high metallicity, such as local galaxy disks (e.g., Leroy et al., 2021b). In contrast to CO, the higher-dipole moment molecular species such as HCN, HNC and HCO^+ preferentially emit at higher physical densities. HCN has long been used to trace dense gas by the extragalactic community due to its relatively bright transition lines making it accessible in extragalactic targets (e.g., Helfer and Blitz, 1993; Aalto et al., 1997, 2002; Gao and Solomon, 2004; Meier and Turner, 2005; Aalto et al., 2012; Bigiel et al., 2016; Jiménez-Donaire et al., 2019; Querejeta et al., 2019; Bemis and Wilson, 2019; Krieger et al., 2020; Bešlić et al., 2021; Eibensteiner et al., 2022; Imanishi et al., 2023; Neumann et al., 2023b).

Still, at sub-cloud scales, studies from the Milky Way remain inconclusive about whether HCN reliably traces only the actual star-forming gas phase (e.g., Pety et al., 2017; Kauffmann et al., 2017; Mills and Battersby, 2017; Barnes et al., 2020; Tafalla et al., 2021, 2023), as sub-thermal emission from low density regions can in some of these cases dominate the emission output. Further, HCN emission can be excited by electrons in addition to collisional excitation by H_2 molecules (Goldsmith and Kauffmann, 2017) and, e.g., Santa-Maria et al. (2023) showed that low visual extinction gas can amount to about 30% of the total HCN luminosity in Orion B. Recent numerical simulations of star-forming clouds in conditions similar to the local ISM (e.g., Jones et al., 2023; Priestley et al., 2023, 2024) also suggest that a significant fraction of the HCN emission emanates from regions with densities of a few thousand cm^{-3} that are unlikely to form stars.

An improved approach to gauging the gas density is therefore to contrast the emission of HCN with emission of a bulk molecular gas tracer that emits preferentially at lower densities than HCN. This is a promising probe of the average physical cloud density as shown by simulations (Leroy et al., 2017a; Neumann et al., 2023b) and observations at $\gtrsim 300$ pc resolution in nearby galaxies (e.g., Neumann et al., 2023b, 2024; Schinnerer and Leroy, 2024; Neumann et al., 2025).

An alternative to these lines is the molecular ion diazenylium (N_2H^+), a tracer of dense gas due to chemical reasons. Within the Milky Way N_2H^+ (1-0) seems to be exclusively detected in dense and cold regions (H_2 column densities above 10^{22} cm^{-2}; Pety et al., 2017; Kauffmann et al., 2017; Tafalla et al., 2021). At these column densities, CO molecules start to freeze to dust grains in the coldest and densest parts of clouds, allowing N_2H^+ molecules thrive as reactions of N_2H^+ and CO and H_3^+ and CO are inhibited, which is the main destruction mechanism of N_2H^+ and the main mechanism limiting the formation of N_2H^+ out of H_3^+. After the onset of star formation, stellar feedback heats the dust and evaporates the CO molecules, which increases the destruction of N_2H^+. This makes N_2H^+ molecules selective only for certain cold and high density regimes (i.e., Tafalla et al., 2023; Barnes et al., 2020). Hydrodynamical simulations show, in contrast to HCN, HNC and HCO^+, N_2H^+ exist mostly in regions dense enough that they irreversibly undergo gravitational collapse (Priestley et al., 2023).

To understand the interplay between larger-scale dynamical features in galaxies and star formation, it is crucial to observe and study the properties of dense gas not just in individual clouds but across entire ensembles of clouds within different environments, making local galaxies the ideal testbeds to study dense gas. Since N_2H^+ (1-0) emission is several order of magnitude fainter than ^{12}CO (1-0) (Schinnerer and Leroy, 2024), and several times fainter than HCN (1-0) emission (Jiménez-Donaire et al., 2023), extragalactic observations of N_2H^+ have so far been limited to either larger-scale lower-resolution studies (i.e., kpc-scales, Sage and Ziurys, 1995; den Brok et al., 2022; Jiménez-Donaire et al., 2023), or higher-resolution studies of individual regions such as starburst galaxy centers (e.g., the centers of NGC 253, IC342 and NGC 6946; Martín et al., 2021; Meier and Turner, 2005; Eibensteiner et al., 2022).

Surveying the Whirlpool galaxy at Arcseconds with NOEMA (SWAN), a IRAM-NOEMA+30m Large Program, therefore represents the next logical step in understanding the dense molecular gas: SWAN (Stuber et al., 2025) is a high-resolution (125 pc), high-sensitivity survey, mapping the emission of several 3 mm lines, including the J=1-0 transition of so-called dense gas tracers HCN, HNC, HCO^+ and N_2H^+ across the central $\sim 5 \times 7\,\mathrm{kpc}^2$ of the Whirlpool galaxy (NGC 5194 or M51a). As the fraction of dense gas (as traced by HCN) is found to vary drastically with galaxy environment at both kpc and cloud-scale resolutions (Usero et al., 2015; Gallagher et al., 2018a; Jiménez-Donaire et al., 2019; Querejeta et al., 2019; Bemis and Wilson, 2019; Bešlić et al., 2021; Neumann et al., 2023b), it is vital to reliably study the denser molecular gas phase across different environments. With the SWAN survey, we can for the first time access not only the common dense gas tracer HCN, but also the chemical tracer N_2H^+ at unprecedented resolution in M51 across the inner spiral arms and interarm regions, molecular ring, nuclear bar and center with known AGN and outflow (Ho et al., 1997; Dumas et al., 2011; Querejeta et al., 2016b). M51a, also known as the Whirlpool galaxy or NGC 5194, (M51 hereafter) is a massive star-forming galaxy in the northern hemisphere, known for its iconic grand-design spiral arm structure, high surface brightness, low inclination and proximity. Many molecular line studies have targeted M51 in the past (Koda et al., 2011; Schinnerer et al., 2013; Watanabe et al., 2014; Chen et al., 2017; Querejeta et al., 2019; den Brok et al., 2022) and its complex dynamics, partially triggered by interactions with the dwarf galaxy M51b, are well studied (Meidt et al., 2013;

Table 9: Overview of the main properties of M51 (NGC 5194).

Property	Value	Source
RA	13h29m52.7s	1
DEC	47°11′43″	1
PA	$173 \pm 3\,^{\circ}$	2
i	$22 \pm 5\,^{\circ}$	2
D	8.58 Mpc	3
v_{sys}	471.7 ± 0.3 km/s	4
$\log_{10} M_*/M_\odot$	10.5	5
$\langle \Sigma_{SFR} \rangle$	$20 \times 10^{-3}\ M_\odot\,yr^{-1}\,kpc^{-2}$	5
morphology	SA(s)bc	6

Main parameters of M51a. 1: galaxy coordinates from NED, 2: position angle and galaxy inclination from Colombo et al. (2014a), 3: distance from McQuinn et al. (2016), 4: systemic velocity (Shetty et al., 2007), 5: average SFR surface density and integrated stellar mass (within $0.75 \times R_{25}$) derived from 3.6 µm (den Brok et al., 2022) 6: galaxy morphology (de Vaucouleurs et al., 1991)

Colombo et al., 2014a; Querejeta et al., 2016b). We list the main properties of M51 in Table 9.

In Stuber et al. (2023a, S23 hereafter) we presented the first high-resolution map of N_2H^+ across a larger-scale field of view (FoV) ($5 \times 7\,kpc^2$) in an extragalactic target, M51. As the formation of stars is also closely connected with dense molecular clouds (Schinnerer and Leroy, 2024), we further probe the impact of surface densities of SFR (Σ_{SFR}) and stellar mass (Σ_*) on the dense gas emission. In addition, we test hypothesized links between dense gas mass, CO velocity dispersion (σ_{CO}), galactocentric radius and dynamical equilibrium pressure (P_{DE}). In a hydrostatic equilibrium, the midplane pressure P_{DE} determines the ability of the ISM to form molecular gas, and is expected to rise with a cloud's mean density (Jiménez-Donaire et al., 2019). At 125 pc scales, we find a super-linear correlation between N_2H^+ (1-0) and HCN(1-0) when excluding the AGN-affected center. Here, we expand this work to include emission of additional high-dipole molecules HNC and HCO^+ (1-0), and to study what sets the density distribution and cloud-scale chemistry across M51's environments. We will compare those emission lines to tracers of the surface density of molecular gas, as a proxy for the average gas density and other physical properties of the gas disk related to star formation.

Section 6.2 describes our observations and data reduction, followed by our methodology (Section 6.3) and a direct comparison of the molecular emission lines with each other and how the emission compares to the bulk molecular gas tracer ^{12}CO (Section 6.4). We then probe the dependency of dense gas tracing molecular emission with various surface densities (Section 6.5). We discuss the chemical composition and environmental dependency of the quiescent and star-forming dense gas in Section 6.6 and summarize our results in Section 6.7.

6.2 OBSERVATIONS AND DATA

To study the relation between galaxy environment and competing tracers of dense gas, we use the N_2H^+, HCN, HNC and HCO^+ maps from the SWAN survey (Stuber et al., 2025, Section 6.2.1) that cover the AGN and outflow, nuclear bar, molecular ring and inner spiral arms and interarm region in M51a at cloud-scales. We combine 3 mm line emission observations with observations of bulk molecular gas tracer ^{12}CO (1-0) from the PdBI Arcsecond Whirlpool Survey (PAWS, Schinnerer et al., 2013). To test the physical conditions driving changes in the emission of dense gas tracing lines, we obtain surface density maps of SFR ($\Sigma_{\rm SFR}$), molecular gas surface density ($\Sigma_{\rm mol}$), stellar mass (Σ_*), as well as estimate the dynamical equilibrium pressure ($P_{\rm DE}$) from ancillary data (Section 6.2.3). The utilized maps are presented in Figure 31.

6.2.1 Dense gas and CO observations

The SWAN survey combines observations from the IRAM large program LP003 (PIs: E. Schinnerer, F. Bigiel) that used $\sim$ 214 hours of observations with the Northern Extended Millimetre Array (NOEMA) and 69 hours of observations with the 30m single dish to map 3 mm line emission from the central 5×7 kpc of the nearby galaxy M51. A more detailed description of this survey, the observations, data calibration, imaging and moment map creation can be found in a dedicated survey paper (Stuber et al., 2025). The NOEMA observations are performed by combining 17 pointings into a hexagonally spaced mosaic. The observations cover the $\sim 85-110$ GHz range allowing for simultaneous observations of 9 molecular lines: ^{13}CO(J=1–0), HNCO(5–4), C^{18}O(1–0), N_2H^+ (1–0), HNC(1–0), HCO^+ (1–0), HCN(1–0), HNCO(4-3) as well as hyperfine transitions of C_2H(1–0). Calibration and joint deconvolution of NOEMA and 30m data were carried out using the IRAM standard calibration pipeline in GILDAS (Gildas Team, 2013). The native resolution of the data varies from $\sim 2.3''$ (for ^{13}CO) to $3.0''$ (for HCN). The resulting data set has an rms of $\sim$ 20 mK per 10 km s^{-1} channel for the brightest line (^{13}CO(1-0)).

For this study, we utilize the N_2H^+, HCN, HNC and HCO^+ data cubes at 10 km s^{-1} spectral resolution per channel and native spatial resolution, which we convolve to a common spatial resolution of $3''$($\sim$ 125 pc). For CO we directly use the PAWS data cube at $3''$spatial resolution[1].

6.2.2 Moment map creation

The creation of moment-0 maps is described in Stuber et al. (2025). We integrate the molecular data cubes along their spectral axis using the *PyStructure* tool (den Brok et al., 2022; Neumann et al., 2023a). Creating moment maps is a common procedure to increase the signal-to-noise ratio (SNR), and to ease the comparison of the lines with each other and within the disk. These moment maps are created by using two selected priors, CO and HCN, to identify connected structures with emission above a selected SNR theshold of 2. This 3D signal mask is then used for integration. As described in Stuber et al. (2025) this ensures that all emission is captured in the final maps, including emission from the center, where CO is comparably faint, in contrast to HCN. The emission of HCN, HNC, HCO^+, N_2H^+ and ^{12}CO is then integrated over these

1 https://www2.mpia-hd.mpg.de/PAWS/PAWS/Data.html

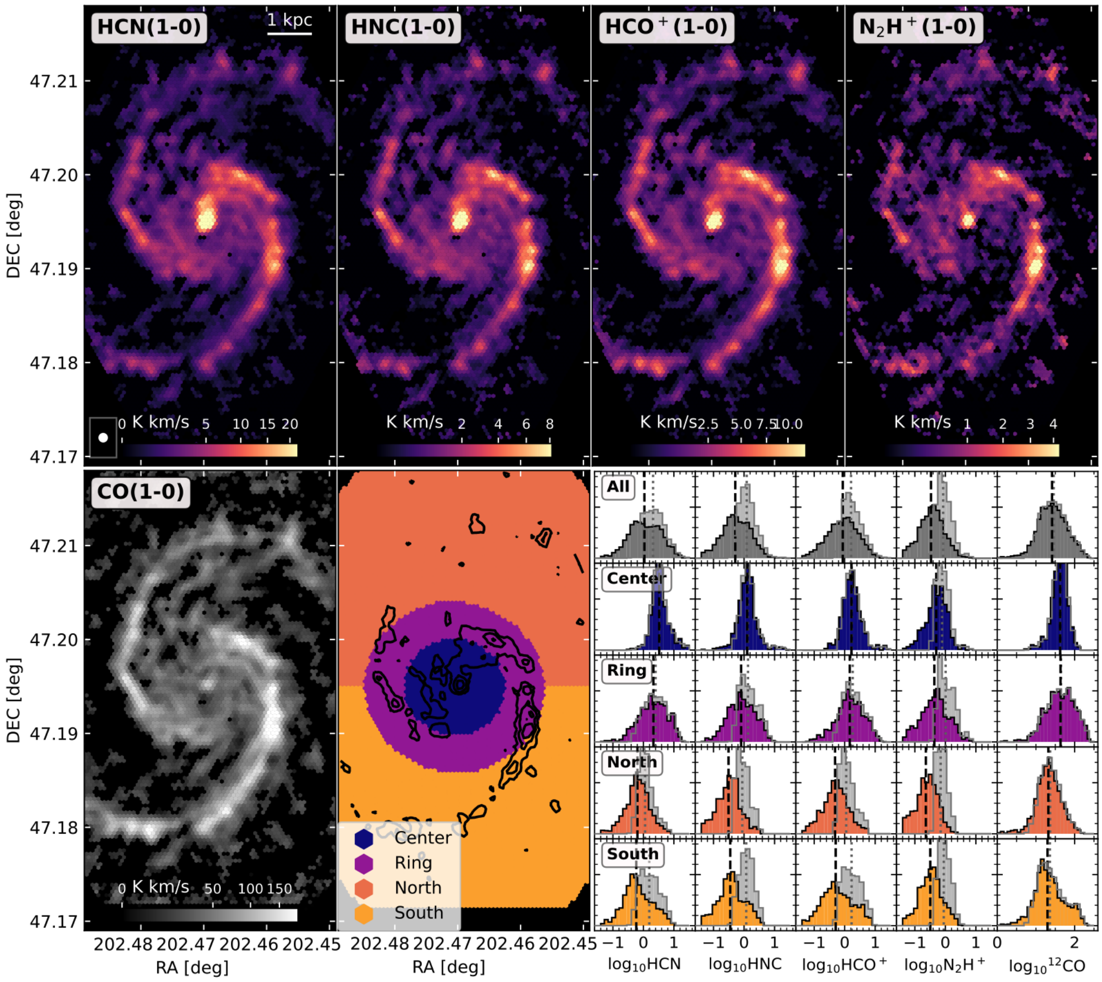

Figure 31: Integrated intensity maps of dense gas tracers HCN, HNC, HCO+ and N_2H^+ from SWAN at a common resolution of $3''$ (top row from left to right), as well as from ^{12}CO (PAWS, bottom left). We divide the disk into a center and ring environment (Colombo et al., 2014a), and the outer disk into northern and southern halves (bottom row, second panel from left). We add contours of integrated N_2H^+ emission of 0.75, 2 and 4 K km/s to the environment map. We show the pixel-based integrated intensity distribution (in K km/s) in various environments in the disk for all pixels in the FoV (colored shaded area), as well as for pixels where emission is detected (emission $> 3\sigma$, light grey shaded area) in the bottom right panels. The area of each histogram is normalized to unity. We indicate the median of all pixels (black dashed grey line) and median of masked pixels (dotted grey line) of each environment. The median represents the median value of logarithmic emission ($\mathrm{med}(\log_{10}(I))$. Pixels with negative emission are excluded in the logarithmic scaling of the histograms. Since CO is detected across most of the FoV and is used as a prior in the creation of the moment-0 map (Section 6.2.2), its masked histogram distribution agrees well with the unmasked one.

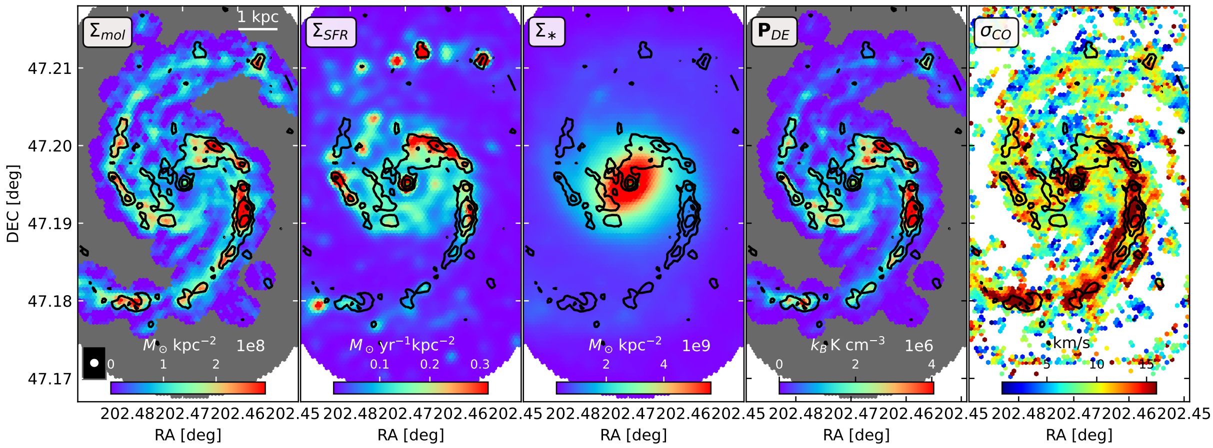

Figure 32: Molecular gas mass surface densities $\Sigma_{\rm mol}$, star formation rate surface densities $\Sigma_{\rm SFR}$, stellar mass surface density Σ_*, dynamical equilibrium pressure $P_{\rm DE}$ as well as CO velocity dispersion $\sigma_{\rm CO}$ at $3''$ resolution. We show contours of integrated N_2H^+ emission (0.75, 2,4 K km/s) on top.

structures, ensuring that the same pixels in the ppv cube are used for integration for all lines. This approach differs slightly from the one used in S23, where only ^{12}CO was a prior for the mask instead of both CO and HCN. As described in Stuber et al. (2025), we interpolate and remove the area outside of the mosaic of pointings observed, as the noise increases towards the edges. The resulting maps have a resolution of $3''$, and are regridded onto a hexagonal grid with four hexagonal spacings per beam (compare Figure 31).

6.2.3 Ancillary data

We use ancillary data to generate maps of SFR surface density ($\Sigma_{\rm SFR}$), molecular gas mass surface density ($\Sigma_{\rm mol}$), stellar mass surface density (Σ_*) and dynamical equilibrium pressure ($P_{\rm DE}$) at a resolution of $3''$. Those maps are incorporated into the PyStructure table and share the same hexagonal pixel grid as the molecular gas maps. All ancillary data are shown in Figure 32.

SFR tracers

We combine the *Spitzer* 24 µm map processed by Dumas et al. (2011), tracing recent star formation obscured by dust with $3''$ resolution Hα maps from Kessler et al. (2020) tracing recent emission from HII regions powered by massive young stars. The 24µm map is deconvolved with the so-called *HiRes* algorithm (Backus et al., 2005) to achieve a resolution of $2-3''$ (Dumas et al., 2011). We obtain a map of SFR surface density ($\Sigma_{\rm SFR}$) via linear combination of the above mentioned SFR maps as described in equation 6 from Leroy et al. (2013) and correcting for inclination:

$$\begin{aligned}\Sigma_{\rm SFR}[{\rm M_\odot\,yr^{-1}\,kpc^{-2}}] = [&634\,{\rm I_{H\alpha}}[{\rm erg\,s^{-1}\,sr^{-1}\,cm^{-2}}] \\ &+0.00325\,{\rm I_{24\mu m}}[{\rm MJy\,sr^{-1}}]] \times \cos(i)\,.\end{aligned} \quad (4)$$

Molecular gas mass surface density and CO(1-0) velocity dispersion

We utilize observations of ^{12}CO (1-0) from the PAWS survey (Schinnerer et al., 2013). The 1″ resolution data are convolved to 3″ spatial and 10 km/s spectral resolution to match our observations. Applying a CO-to-H_2 conversion factor α_{CO} map to the integrated ^{12}CO intensity (I_{CO}) and correcting for inclination i yields the molecular gas mass surface density map via:

$$\Sigma_{mol} = I_{CO} \times \alpha_{CO} \times \cos(i) \tag{5}$$

The spatially varying α_{CO} is estimated based on modeling the observed ^{12}CO (1-0), (2-1) and ^{13}CO (1-0), (2-1) lines from SWAN and SMA imaging (den Brok et al., 2025). The measured values at 4″ resolution are extrapolated with a Gaussian process regression towards neighboring pixels to cover a larger area (compare area where Σ_{mol} is shown in Figure 32). We test the impact of using different α_{CO} prescriptions on our results in Appendix C.2, including Σ_{mol} calculated with a constant α_{CO} and with a metallicity and stellar mass based α_{CO}.

We further estimate the CO velocity dispersion following the prescription of Heyer et al. (2001), applied in, e.g., Bešlić et al. (2021) and Neumann et al. (2023b). This method estimates the "effective width" of a line via the integrated intensity I_{CO} (a.k.a. moment-0) and the peak intensity (T_{peak}) at each pixel. Assuming a Gaussian line profile for these spectra with peak T_{peak}, we can estimate the rms velocity dispersion of the line $\sigma_{measured}$ via:

$$\sigma_{measured} = \frac{I_{CO}}{\sqrt{2\pi}T_{peak}} . \tag{6}$$

To account for line broadening caused by the instrument, we subtract the instrumental contribution $\sigma_{instrument}$ in quadrature (Rosolowsky and Leroy, 2006; Sun et al., 2018). For M51, we use $\sigma_{instrument}$ estimates for CO from Sun et al. (2018) at 120 pc resolution (see their equations 16, 17 and table 9).

Stellar mass map

We obtain stellar mass surface density maps (Σ_*) based on *Spitzer* 3.6 µm maps from the *Spitzer* Survey of Stellar Structure in galaxies (S^{4}G; Sheth et al., 2010) that are further corrected for dust emission (Querejeta et al., 2015). A more detailed description of this process and the obtained stellar mass map for M51 can be found in Querejeta et al. (2019). We convolve this map from 2.4″ resolution to our common resolution of 3″, and apply an inclination correction to obtain surface densities.

Dynamical Equilibrium Pressure

We estimate the ISM pressure in each individual, cloud-scale region following the prescription from Sun et al. (2020, equation 15). This "cloud-scale dynamical equilibrium pressure" formalism accounts for the weight of the gas from not only molecular cloud self-gravity but also external gravity by stars and gas across the galactic disk, as expressed below:

$$P_{DE} = \frac{3\pi G}{8}\Sigma^2_{mol,''} + \frac{\pi G}{2}\Sigma_{mol,''}\Sigma_{mol,kpc} + \frac{3\pi G}{4}\rho_{*,kpc}\Sigma_{mol,''}D_{cloud} . \tag{7}$$

Here, $\Sigma_{\mathrm{mol},''}$ is the molecular gas surface density at 3″ resolution (as derived in Section 6.2.3); $\Sigma_{\mathrm{mol,\,kpc}}$ is the corresponding kpc-scale surface density, derived by convolving CO data from 3″ to 1 kpc resolution. D_{cloud} is the adapted cloud diameter, for which we use the beam size of 125 pc assuming a single cloud fills each beam. $\rho_{*,\mathrm{kpc}}$ is the stellar mass volume density near the disk mid-plane, which we estimate from the kpc-scale stellar mass surface density $\Sigma_{*,\,\mathrm{kpc}}$ and stellar disk scale height H_*:

$$\rho_* = \frac{\Sigma_{*,\,\mathrm{kpc}}}{4 \times H_*} \,. \tag{8}$$

Based on Kregel et al. (2002) and Sun et al. (2020), we estimate H_* from the stellar disk radial scale length $R_* = 7.3 \times H_*$. For M51 we adopt $R_* = 4.0 \pm 0.2\,\mathrm{kpc}$ from Dumas et al. (2011), adapted to our distance of $D = 8.6\,\mathrm{Mpc}$, while Dumas et al. (2011) used $D = 8.2\,\mathrm{Mpc}$.

6.3 METHODOLOGY AND SIMULATED DATA TESTS

We describe our methodology to obtain average intensities, average line ratios, as well as deriving relations between line intensities and line ratios and other galaxy parameters such as surface densities. To ensure that our results are not impacted by the different SNR of our dense gas tracing lines, we test all of the methods on a simple mock-data set created based on the ^{12}CO data, which we describe in more detail in Appendix C.1. In short, we scale the ^{12}CO intensity in the CO data cube at 3″ resolution to lower values. We use four different scaling factors, chosen to be plausible estimates of our faintest observed line (N_2H^+ (1-0)) from literature results. Those scaling factors further match our average HNC-to-^{12}CO, HCO^+-to-^{12}CO and N_2H^+-to-^{12}CO ratios (Table 10) plus an even smaller scaling factor to test the effect of even lower SNR.

For each scaled CO intensity we adjust the noise to simulate the corresponding SNR. The mock-data cubes are all then treated in the exact same way that we are treating our science data (Section 6.2.2), including the integration into the PyStructure to obtain moment maps that we can use for comparison (for more details see Appendix C.1.1).

To investigate potential environmental variations, we divide the disk of M51 into four regimes: A kinematically determined center and molecular gas-rich ring based on Colombo et al. (2014b) and sub-dividing the remaining disk into northern (north of the galaxy center) and southern (south of the galaxy center, see Figure 31) halves. To highlight the importance of separating the environments, we note that the ^{12}CO distribution reveals a brightness asymmetry in gas emission between the fainter northern and brighter southern spiral arm which is speculated to be caused by M51b (e.g., Egusa et al., 2017). The center, which hosts both nuclear bar, AGN and low-inclined radio jet (Matsushita et al., 2015; Querejeta et al., 2016b) also provides physical conditions very different from the molecular ring and spiral arms further out. In addition to the full FoV, we will apply the methods mentioned in this Section to the individual environments throughout this work.

6.3.1 Determination of average line ratios

Average global and regional line ratios between the emission of two lines are an effective way to measure the underlying physical conditions of the observed region, while reducing the impact of noise or peculiar outliers. We calculate average line ratios between different lines (I_{line1}, I_{line2}) by using the ratio of the integrated intensities in the full FoV. We integrate the intensity of all pixels in the moment-0 map within the FoV for the first line (line1) and divide by the integrated intensity of all pixels in the moment-0 map within the FoV for the second line (line2). Statistical uncertainties are calculated following standard Gaussian error propagation:

$$R_{\mathrm{line2}}^{\mathrm{line1}} = \mathrm{Sum}\left(I_{\mathrm{line1}}\right)/\mathrm{Sum}\left(I_{\mathrm{line2}}\right) \ . \tag{9}$$

Our tests with the mock data (Appendix C.1.2) confirm that these methods robustly recover the expected line ratios. Masking will bias specifically data sets with lower SNR compared to those with higher SNR, and so do the other tested methods (median and mean line ratios, Appendix C.1.2).

6.3.2 Binning the data

Averaging data in increments of galactic parameters (e.g., surface density) is a useful technique (referred to as "binning" hereafter) to reduce the noise (i.e., negative and positive noise will cancel on average) and recover possible physical relations between intensity and those galactic parameters. To bin our data, we select bins of property A ranging from three times its average uncertainty (ΔA) up to the maximum value of A. For each bin, we first select the pixels that fall within the bin range and average the intensity of a line corresponding to those pixels, including non-detections ($< 3\sigma$). We calculate average line ratios R (both CO-line ratios and line ratios of dense gas lines) analogue to Equation 9. As shown in Appendix C.1, excluding pixels will introduce biases (see also Neumann et al., 2023a).

In Appendix Figure 60 we show that with the method described above and by including all pixels we can recover the expected relation for this simple mock-data model. To ensure that the binned intensity measurements are not predominantly noise, we remove measurements where the binned average is below 5 times the corresponding statistical uncertainty. The statistical uncertainty is much lower than the average noise per bin (see Appendix C.1). We do not mask any data prior to the binning.

For binned intensities we provide the statistical uncertainty from error propagation. For binned line ratios $R = M_1/M_2$, the uncertainty is calculated as follows:

$$\Delta R = |R| \cdot \sqrt{\left(\frac{\Delta M_1}{M_1}\right)^2 + \left(\frac{\Delta M_2}{M_2}\right)^2} \ . \tag{10}$$

With ΔM_i being the relative error of binned intensity of line $i = 1, 2$, respectively. It is calculated following standard Gaussian error propagation $\Delta M_i = 1/N\sqrt{\Sigma_{a=1}^{N} \Delta s_a^2}$, for pixels $a = 1...N$ and the error of the intensity at each pixel being s_a. For ratios between fainter dense gas tracing lines, we further provide the 25th and 75th percentile range as visual guidance for each relation in addition to the statistical uncertainty presented above.

Table 10: Average line ratios of dense gas tracers

line ratio	all	center	ring	north	south
HCN/HNC	2.729 ± 0.013	3.007 ± 0.014	2.583 ± 0.013	2.612 ± 0.056	2.665 ± 0.048
HCN/HCO^+	1.530 ± 0.005	2.213 ± 0.009	1.391 ± 0.005	1.363 ± 0.019	1.133 ± 0.012
HNC/HCO^+	0.560 ± 0.003	0.736 ± 0.004	0.538 ± 0.003	0.522 ± 0.012	0.425 ± 0.008
HCN/N_2H^+	5.991 ± 0.053	8.512 ± 0.097	5.955 ± 0.061	6.36 ± 0.282	3.437 ± 0.074
HNC/N_2H^+	2.195 ± 0.021	2.83 ± 0.034	2.306 ± 0.025	2.435 ± 0.116	1.290 ± 0.034
HCO^+/N_2H^+	3.917 ± 0.036	3.846 ± 0.045	4.283 ± 0.044	4.667 ± 0.21	3.033 ± 0.066
HCN/^{12}CO	0.0504 ± 0.0001	0.1153 ± 0.0003	0.0558 ± 0.0001	0.0273 ± 0.0002	0.0274 ± 0.0002
HNC/^{12}CO	0.0185 ± 0.0001	0.0384 ± 0.0002	0.0216 ± 0.0001	0.0104 ± 0.0002	0.0103 ± 0.0002
HCO^+/^{12}CO	0.0330 ± 0.0001	0.0521 ± 0.0002	0.0401 ± 0.0001	0.0200 ± 0.0002	0.0242 ± 0.0002
N_2H^+/^{12}CO	0.0084 ± 0.0001	0.0136 ± 0.0002	0.0094 ± 0.0001	0.0043 ± 0.0002	0.0080 ± 0.0002

Average line ratios for all combinations of dense gas tracers (J=1–0 transitions) and ^{12}CO (1-0) for the full FoV, and for various galactic environments (center, ring, northern and southern disk, see Figure 31). Averages are calculated as the ratio of the summed intensities with standard Gaussian error propagation as statistical uncertainty for line ratios between combinations of dense gas lines (Section 6.3.1).

In our analysis, we want to find simple correlations between our observed line emission or line ratios and physical quantities to identify possible driving mechanisms. To quantify the slope and scatter of some of the observed trends, we fit a linear function of shape $a \times x + b$ (in log space) to the binned data with `scipy-optimize`, including the bin uncertainties. The scatter is then measured as the median absolute deviation of the residual intensity (or line ratio) within the fitted range after subtracting the best-fit relation. This scatter depends on the average SNR of a line and is used to compare how the scatter in each line's intensity varies with different physical galactic parameters, rather than between different lines. As this scatter is measured with respect to a linear relation, it measures both a non-linear behavior indicative of secondary dependencies, as well as the intrinsic uncertainty.

6.4 LINE EMISSION OF DENSE GAS TRACERS IN COMPARISON

HCN, HNC and HCO^+ are the favored tracers of dense gas in the extra-galactic community, as they are much brighter in emission than, for example, N_2H^+ and have higher critical densities than, e.g., CO. Therefore, this theoretically allows them to trace regions of denser gas. They all correlate well with star formation rate surface densities on galactic scales (Gao and Solomon, 2004). To study the effect that the environment within M51 might have on these molecular lines, we compare their emission at cloud-scales (Section 6.4.2) and within larger scale galactic environments (northern and southern disk, ring, center, Figure 31, Section 6.4.1). Comparing the emission of those dense gas tracing lines with emission of the Milky Way preferred dense gas tracer N_2H^+ will help understand their ability to trace dense regions. Lastly, we compare ratios of all dense gas tracers with ^{12}CO, which are found to be density-sensitive at $\gtrsim 100$ pc scales (Leroy et al., 2017a; Jiménez-Donaire et al., 2019; Usero et al., 2015).

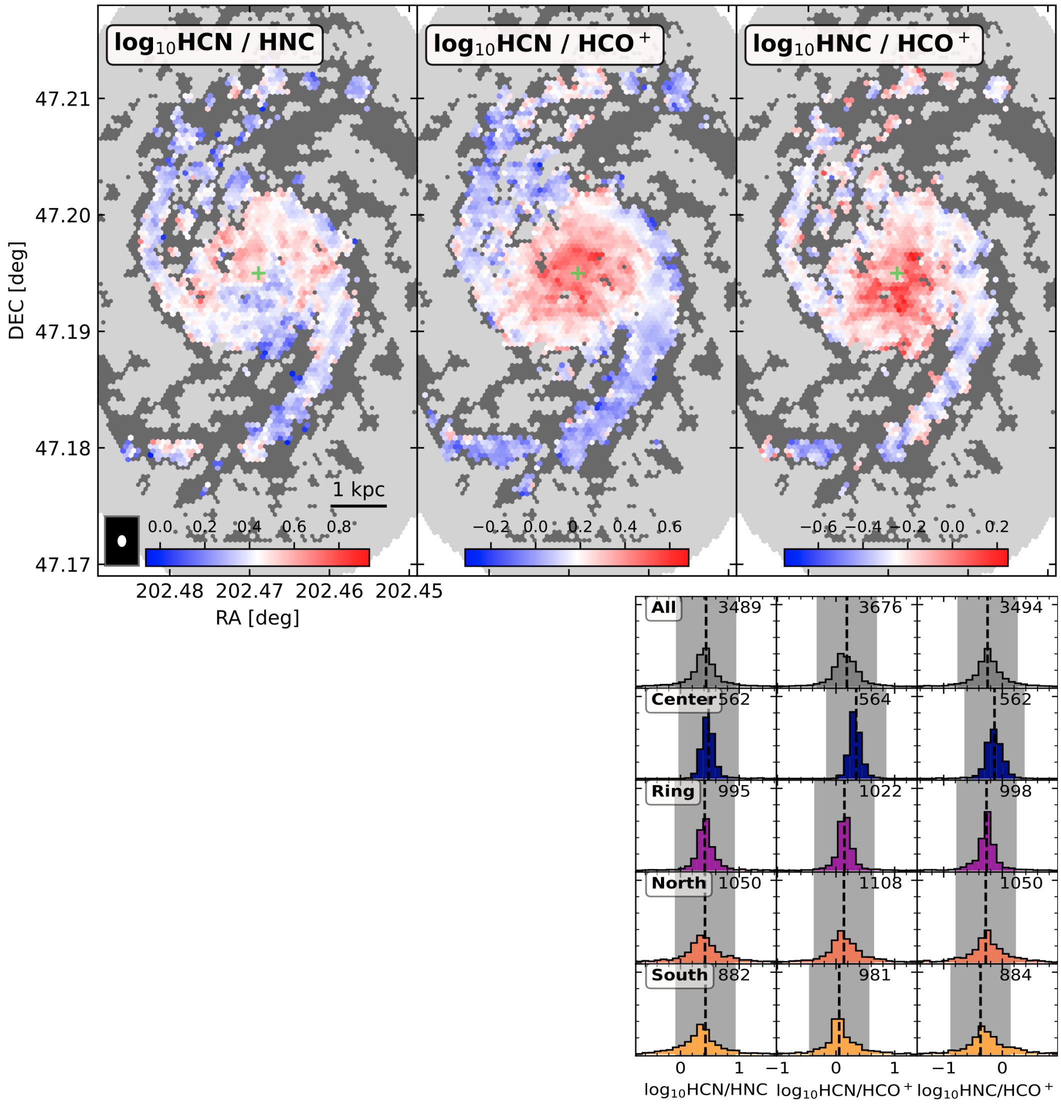

Figure 33: Top panels: Line ratios of integrated line emission from dense gas tracers HCN, HNC and HCO^+. For visual purpose, we only show line ratios for significant detected pixels ($> 3\sigma$), but include non-detections in all calculations. We mark pixels in which CO is detected (grey points) and the center of the galaxy (green plus). The intensity scale is centered logarithmically on the average line ratios ($\log_{10}R$, with R from Table 10) determined for all pixels in the FoV, including non-detections. The average line ratio ($\log_{10}R$) and the total range of 1 dex covered by the color bar are indicated by the black dashed line and greyshaded area in the right panel. Bottom panel: Histogram of line ratios per environment analogous to Figure 31 but for HCN/HNC, HCN/HCO^+ and HNC/HCO^+ (colored histograms). We indicate the amount of pixels shown in the histogram (top right corner), which varies slightly, as values with negative noise can not be shown in the logarithmic scale.

6.4.1 Distribution of HCN, HNC, HCO^+, N_2H^+ and ^{12}CO across environments

We show the emission of HCN, HNC, HCO^+, N_2H^+ and ^{12}CO in the central disk of M51 in Figure 31. In our FoV, HCN, HNC, HCO^+ and N_2H^+ are on average $\sim 29, 71, 38, 142$ times fainter than ^{12}CO emission (Table 10) and their emission is well correlated with each other (Spearman correlation coefficients all $\rho_{Sp} > 0.54$), while their intensity probes about 2 orders of magnitude.

Figure 31 illustrates that all dense gas tracing lines are bright in the central few ~ 100 pc, and along the molecular ring (Figure 31, bottom right). A peculiar bright region, where N_2H^+ is brightest, is located at the south-western brink of the molecular ring (compare also S23). ^{12}CO is distributed in the FoV in a similar fashion to the dense gas tracers, yet its emission is less enhanced in the galaxy center compared to the disk than is seen for the dense gas tracing lines. Average line ratios among dense gas tracing lines and ^{12}CO (Table 10) are enhanced in the central environment compared to other environments (factor of $\sim 1.6 - 2.3$ from N_2H^+ to HCN between center and full FoV). Further, all line ratios among the dense gas tracers (HCN/HNC, HCN/HCO^+, HNC/HCO^+, HCN/N_2H^+, HNC/N_2H^+, HCO^+/N_2H^+) vary significantly (>3σ) between the central environment and other environments. All line ratios are increased in the center compared to other regions, except the HCO^+/N_2H^+ line ratio, which is decreased.

While we see an asymmetry between a brighter southern and fainter northern arm in all lines, the overall intensity distribution of all molecules in the entire northern and southern disk match well (Figure 31, bottom right panel). Still, average dense gas line ratios only agree between ring and northern disk environment, while line ratios in the southern disk are decreased (except the HCN/HNC ratio) by up to a factor of ~ 1.9 compared to both ring and northern disk (Table 10). Line ratios with CO are increased in the southern disk compared to northern disk for N_2H^+ (factor ~ 2) and HCO^+ (factor $\sim 1/2$).

6.4.2 Cloud-scale comparison of HCN, HNC, HCO^+, N_2H^+ and ^{12}CO

Larger-scale environments within galaxies are found to impact the physical conditions (Sun et al., 2022; Schinnerer and Leroy, 2024) and thus emission pattern of molecules. Still, the exact mechanisms driving these large-scale changes, which we also see within M51 (Section 6.4.1) as well as variations within those environments are not well understood. In this Section, we analyze the cloud-scale variations within M51's environments by comparing emission from the extragalactic dense gas tracers HCN, HNC and HCO^+ with each other (Section 6.4.2) and with the much fainter dense gas tracer N_2H^+ (Section 6.4.2). Cloud-scale variations of density sensitive line ratios with ^{12}CO are analyzed in Section 6.4.2.

Correlation between HCN, HCO^+, and HNC

In Figure 33 we display the cloud-scale distribution of line ratios HCN/HNC, HCN/HCO^+ and HNC/HCO^+ where for visual purpose only line ratios for detected sightlines ($> 3\sigma$) are shown in the maps. Of all line combinations, the HCN/HNC line ratio has the smallest variations within the disk (± 0.2 dex to the global average). It is slightly increased in the northern disk and molecular ring compared to the southern half and spiral arms.

The line ratios with HCO^+ exhibit larger variations ($\pm 0.2 - 0.4$ dex to the global average). HCN/HCO^+ increases azimuthally symmetrically in the center out to a radius of ~ 1 kpc. The line ratio in the southern arm is smaller than the global average, but shows little variations, while there are $\sim$ beam-sized variations in the line ratios in the northern arm. Similarly to the HCN/HCO^+ ratio, the HNC/HCO^+ ratio is increased in the center relative to the global average and spiral arms, with a slightly stronger azimuthally asymmetric increase towards the south-western half of center and molecular ring up to a radius of ~ 1.5 kpc, in accordance with the asymmetric HCN/HNC distribution. Beam-sized variations in the HNC/HCO^+ ratio are seen across the entire disk.

In summary, both HCN and HNC are enhanced in the central $\sim 1 - 1.5$ kpc compared to HCO^+ and compared to the spiral arms and global average.

Comparing line intensities to N_2H^+

Unlike HCN, HNC and HCO^+, emission from the molecular ion N_2H^+ has been the favored tracer of dense regions in Milky Way clouds (e.g., Kauffmann et al., 2017; Pety et al., 2017). We show the spatial distribution of line ratios of HCN, HNC and HCO^+ with N_2H^+ emission in Figure 34. The intensity scale depicts the same range (in dex) around the average line ratio as in Figure 33. The variations seen in the N_2H^+-line ratios are larger ($\gtrsim 0.5$ dex around the global average) than the variations seen among the brighter dense gas lines (e.g., HCN/HNC).

All N_2H^+ line ratios increase compared to the global average in a region north-east of the center of a few ~ 100 pc in size, and decrease at even larger radii east of the center. The increase in line ratios is strongest for HCN/N_2H^+ (~ 0.5 dex) and weakest for HCO^+/N_2H^+ (~ 0.1 dex) compared to the global average. N_2H^+ is not detected in the south-western half of the center and molecular ring, where the HNC/HCO^+ line ratios are increased.

N_2H^+ line ratios are decreased in the spiral arms in pixels where N_2H^+ is significantly detected compared to the global average. Again, the strongest variations in line ratios are seen for HCN/N_2H^+ (± 0.5 dex across many pixels), the smallest for HCO^+/N_2H^+ (mostly ± 0.2 dex with only few pixels with larger line ratios).

Proposed average gas density tracer: Line ratios with CO

While dense gas tracers such as HCN, HNC and HCO^+ are efficiently emitting at densities above their critical densities, less efficient emission from sub-critical density regions can still significantly contribute to the total integrated intensity of those lines (Kauffmann et al., 2017; Leroy et al., 2017b). In spite of those effects, line ratios with the bulk molecular tracer CO are found to be sensitive to the average gas density (e.g., review by Neumann et al., 2023b; Schinnerer and Leroy, 2024; Neumann et al., 2025). We show the spatial distribution of ^{12}CO line ratios of HCN, HNC, HCO^+ and N_2H^+ in Figure 35. We refer to these line ratios as R_{CO}^{Line}.

We find that for all lines, R_{CO}^{Line} increases in the center and molecular ring compared to the global average, with a particular increase of up to $\gtrsim 0.8$ dex in an elongated feature that expands towards north-east of the center, which corresponds to the same region where N_2H^+ line ratios are increased. Visually, the HCO^+/CO ratio is less enhanced in the central ~ 2 kpc than the HCN/CO and HNC/CO ratio. All R_{CO}^{Line} are decreased in the spiral arms compared to the global average, and exhibit a gradient

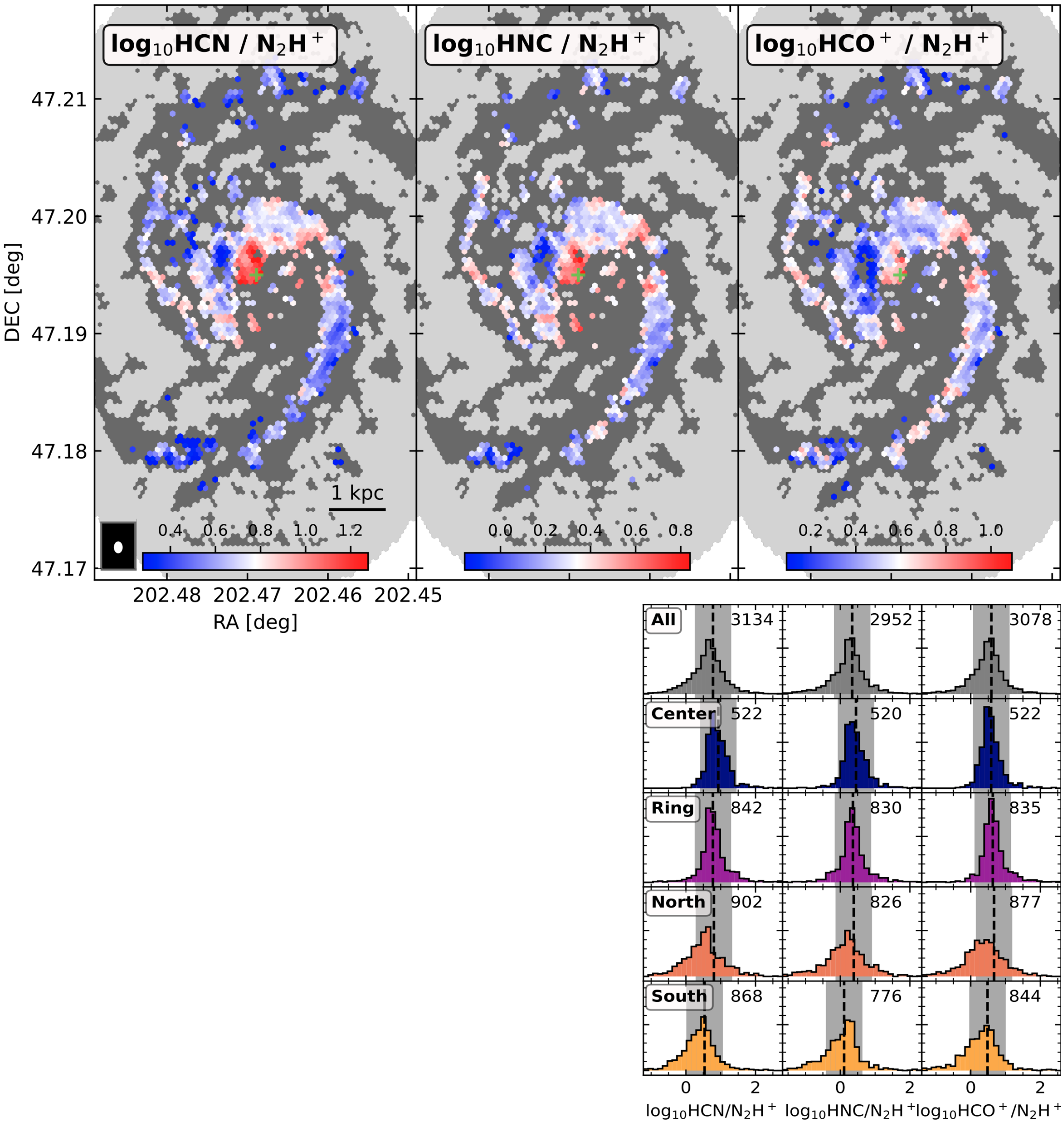

Figure 34: Same as Figure 33 but for the HCN-to-N_2H^+, HNC-to-N_2H^+ and HCO^+-to-N_2H^+ line ratios. The colorbar spans the same 1 dex range as in Figure 33, and is centered logarithmically on the average line ratios ($\log_{10} R$, with R from Table 10).

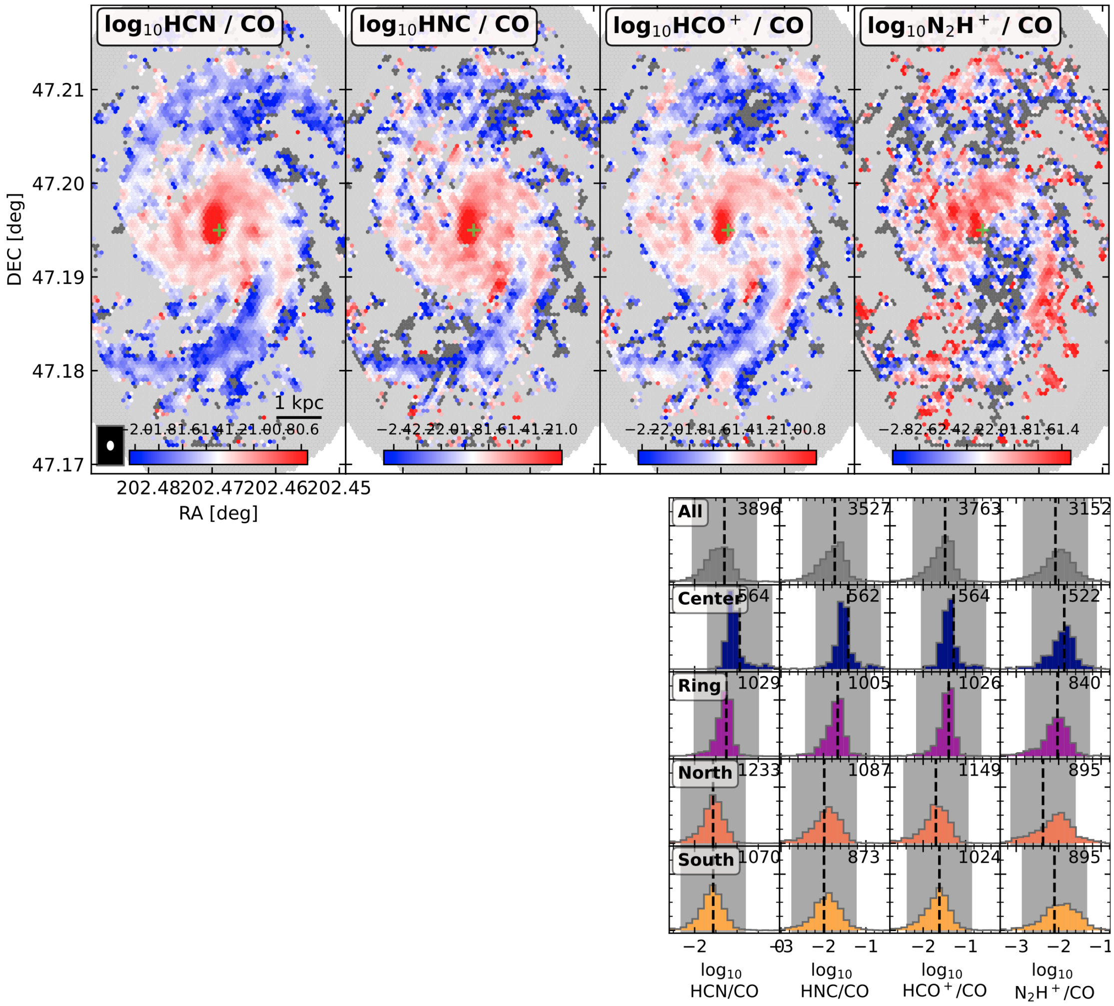

Figure 35: Same as Fig. 33 and 34 but for line ratios with CO. In contrast to the previous Figures, the colorbar spans a larger range of 1.5 dex, centered on the average line ratios (Table 10) and we add line ratios in pixels with non-detections. Since we are showing the logarithmic line ratio, negative values arising due to negative noise can not be shown in either the spatial map or the histograms. We mark pixels where CO is significantly detected, but the line ratio can not be shown in logarithmic scaling in dark grey.

Table 11: Fitting average line intensities and average CO-line ratios as function of N_2H^+ intensity or N_2H^+/CO ratio per environment

line	Full FoV slope	Full FoV offset [dex]	Full FoV scatter [dex]	Center slope	Ring slope	North slope	South slope
Binned line intensities per environments vs N_2H^+ intensity							
CO	0.71±0.02	1.9±<0.1	0.24	0.46±0.06	0.61±0.02	0.89±0.09	0.77±0.07
HCN	1.13±0.06	0.7±<0.1	0.30	0.98±0.10	0.75±0.03	1.39±0.11	1.19±0.05
HNC	1.14±0.05	0.2±<0.1	0.28	0.91±0.08	0.82±0.03	1.57±0.13	1.27±0.06
HCO^+	1.07±0.03	0.5±<0.1	0.26	0.90±0.07	0.80±0.02	1.48±0.13	1.18±0.06
Binned CO line ratios per environments vs the N_2H^+/CO line ratio							
HCN/CO	0.80±0.08	0.3±0.2	0.39	0.90±0.18	0.26±0.05	0.22±0.19	0.29±0.19
HNC/CO	0.77±0.09	-0.2±0.2	0.34	1.00±0.16	0.42±0.02	0.35±0.32	0.44±0.26
HCO^+/CO	0.54±0.07	-0.4±0.1	0.30	0.91±0.15	0.37±0.02	0.05±0.19	0.18±0.20
Binned CO-line ratios per environments vs N_2H^+ intensity							
HCN/CO	0.37±0.06	-1.2±<0.1	0.25	0.39±0.11	0.14±0.02	0.48±0.06	0.51±0.04
HNC/CO	0.47±0.06	-1.7±<0.1	0.24	0.42±0.11	0.23±0.02	0.68±0.07	0.62±0.06
HCO^+/CO	0.39±0.04	-1.4±<0.1	0.17	0.40±0.10	0.20±0.01	0.58±0.05	0.51±0.04

Fit parameters when fitting a linear relation to binned line emission as function of N_2H^+ emission in log space, binned ^{12}CO line ratios as function of N_2H^+/CO and binned ^{12}CO line ratios as function of N_2H^+ intensity. We provide slopes and offsets of linear trends applied to the logarithmic binned values for the full FoV, and provide slopes when fitting binned values obtained in individual environments. For the full FoV we provide the average scatter after subtracting the best-fit from the data (Section 6.3.2).

from low to high line ratios across the arms from trailing to leading side, which is more prominent in the southern arm.

6.4.3 Average line intensities and CO line ratios compared to N_2H^+ emission

Combining the results from Section 6.4.2 and 6.4.2, we see clear variations in line ratios both per galactic environment and from cloud-to-cloud. To quantify the impact of these variations on the average N_2H^+ emission, we probe the binned intensity of HCN, HNC, HCO^+ as well as their binned ^{12}CO line ratios as a function of N_2H^+ emission in Figure 36 for the total FoV and the individual environments. Fit parameters obtained by fitting the binned intensities and binned CO line ratios as function of N_2H^+ emission and N_2H^+/CO (Section 6.3.2) are provided in Table 11.

Across the total FoV, the average HCN, HNC and HCO^+ emission agrees well with the N_2H^+ emission (slopes are within 3σ of unity), while the average ^{12}CO emission is significantly sub-linearly related with N_2H^+ emission across the full FoV (Table 11) and our defined environments. This is in agreement with the super-linear inverse N_2H^+-to-^{12}CO and N_2H^+-to-HCN relations, found by S23 using the preliminary SWAN data. The scatter in the full FoV for the line vs N_2H^+ relation is highest for HCN, followed by HNC, HCO^+ and ^{12}CO as function of N_2H^+ intensity (Table 11). In contrast to ^{12}CO, the slopes of HCN, HNC and HCO^+ as function of N_2H^+ intensity agree well with each other across all environments. Still, their slopes are sub-linear in the center and ring, and super-linear in northern and southern disk.

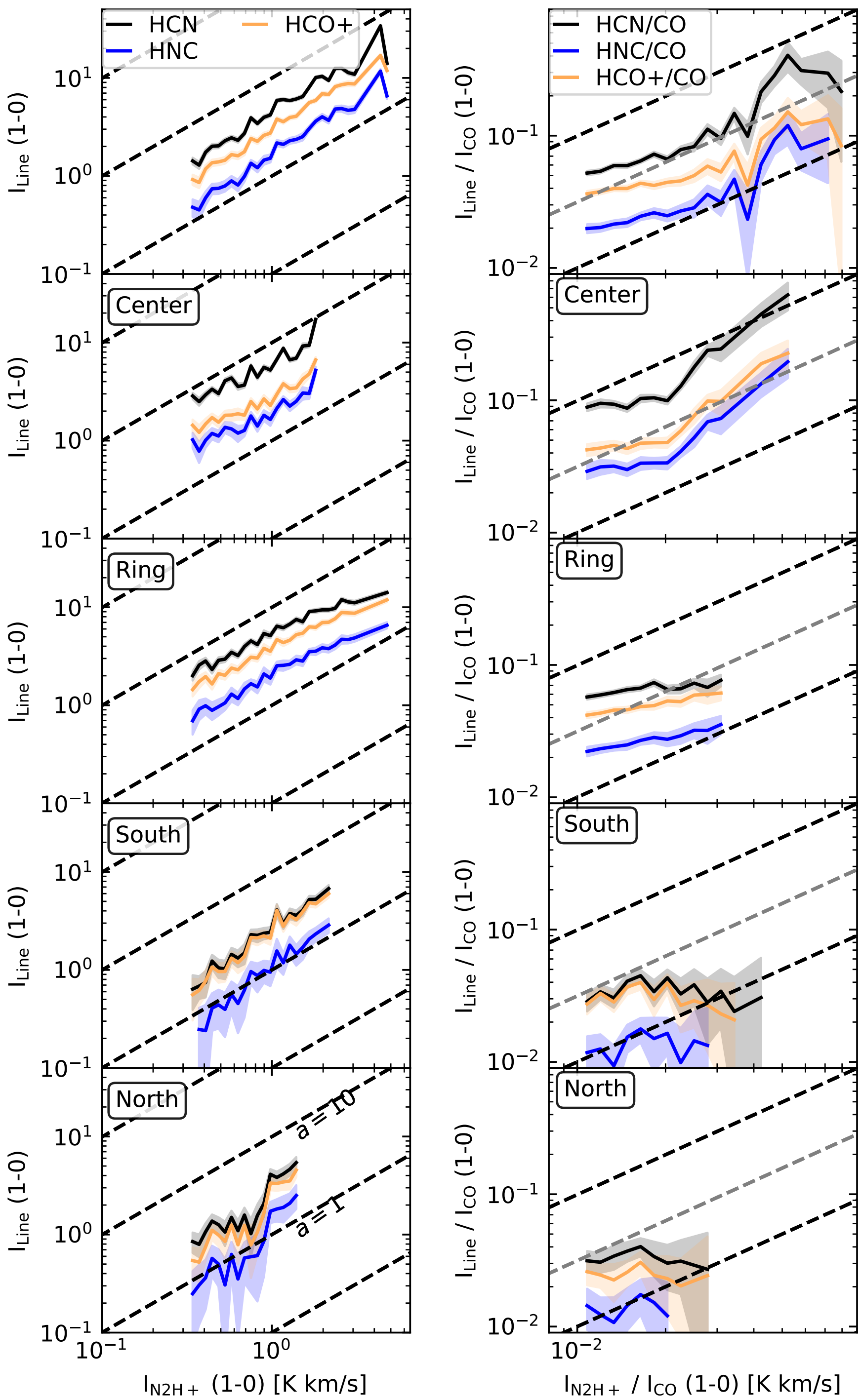

Figure 36: Average intensities of HCN, HNC and HCO^+ as function of N_2H^+ intensity (left) as well as average ^{12}CO line ratios of HCN, HNC and HCO^+ (right) as function of the N_2H^+/CO line ratio emission. We do not apply any masking, but utilize all pixels in the FoV. We show the binned intensities/line ratios for the total FoV (top) as well as for individual environments (Figure 31). We provide lines of constant slopes in log space for visual guidance (black dashed lines). The bins cover a range between 3 times the average N_2H^+ (N_2H^+/CO) uncertainty up to the maximum N_2H^+ intensity (N_2H^+/CO line ratio).

While it is unclear wether R_{CO}^{N2H+} is sensitive to the average cloud density similar to what is proposed for R_{CO}^{HCN}, we test the R_{CO}^{Line} vs R_{CO}^{N2H+} relation (Figure 36) and list scatter and slopes in Table 11. As the N_2H^+ molecule is chemically bound in existence to very dense and cold regions where CO, its main reactant, is frozen to dust grains, its emission is found to depend non-linearly on column density in clouds in the Milky Way (Tafalla et al., 2023). On our ~ 100 pc scales we find R_{CO}^{Line} to depend mostly sub-linearly on R_{CO}^{N2H+} across the environments. The slopes range between very low values $0.05 - 0.44$ in ring, northern and southern disk, up to slopes of ~ 1.0 in the center. The scatter of the R_{CO}^{Line} vs R_{CO}^{N2H+} relation is the largest among all relations tested.

The ^{12}CO line ratios of HCN, HNC and HCO^+ as function of N_2H^+ intensity reveal significantly sub-linear slopes across all environments, with slopes as low as 0.14 for R_{CO}^{HCN} vs N_2H^+ in the ring and as large as 0.68 for R_{CO}^{HNC} in the northern disk. Despite the low slopes, the average scatter of R_{CO}^{Line} vs N_2H^+ are the lowest among all relations tested, and is particularly low for the R_{CO}^{HCO+} vs N_2H^+ relation.

6.5 ENVIRONMENTAL IMPACT – PHYSICAL PARAMETERS DRIVING THE LINE EMISSION

While all dense gas tracers are similarly distributed in the disk of M51, systematic variations as function of both larger-scale and cloud-scale environment are seen (see Section 6.4). Here we aim to identify the physical conditions that best describe the intensity distribution of dense gas tracing molecules and variations between them by comparing the dense gas emission with different physical parameters, including Σ_{mol}, Σ_*, Σ_{SFR}, P_{DE}, σ_{CO} and galactocentric radius. All values are corrected for inclination and described in more detail in Section 6.2. Figure 32 shows our estimates of Σ_{mol}, Σ_{SFR}, Σ_*, P_{DE} and σ_{CO} across our FoV.

We test both the intensity of HCN, HNC, HCO^+ and N_2H^+ and their ratios with the ^{12}CO line as a function of this set of properties in Section 6.5.1 and 6.5.2, respectively. In Section 6.5.3 we investigate how line ratios between dense gas lines depend on the environmental properties.

6.5.1 Line intensity as a function of physical parameters

We show the binned average intensities of HCN, HNC, HCO^+, N_2H^+ and ^{12}CO as function of physical parameters in Figure 37. The same analysis per spatially distinct environment (center, ring, north, south), as well as a pixel-by-pixel version of these plots is provided in Appendix C.4 and C.5, respectively. We provide fit parameters from the full FoV in Figure 37 and Table 16, and for each environment in Appendix C.4. The scatter with respect to the full FoV fits is depicted in Figure 38. Further, we show spearman correlation coefficients of the full FoV in Figure 39.

The average line intensity of all lines is monotonically positively correlated with Σ_{mol} and P_{DE} (deviations from a monotonic relation $\lesssim 0.2$ dex) and non-monotonically with Σ_*, Σ_{SFR}, σ_{CO}, and galactocentric distance, which suggests secondary dependencies. Consequently, the scatter with respect to a linear relation between line intensity and physical properties is lowest (Figure 38) and spearman correlation coefficients are highest for P_{DE} and Σ_{mol} (Figure 39).

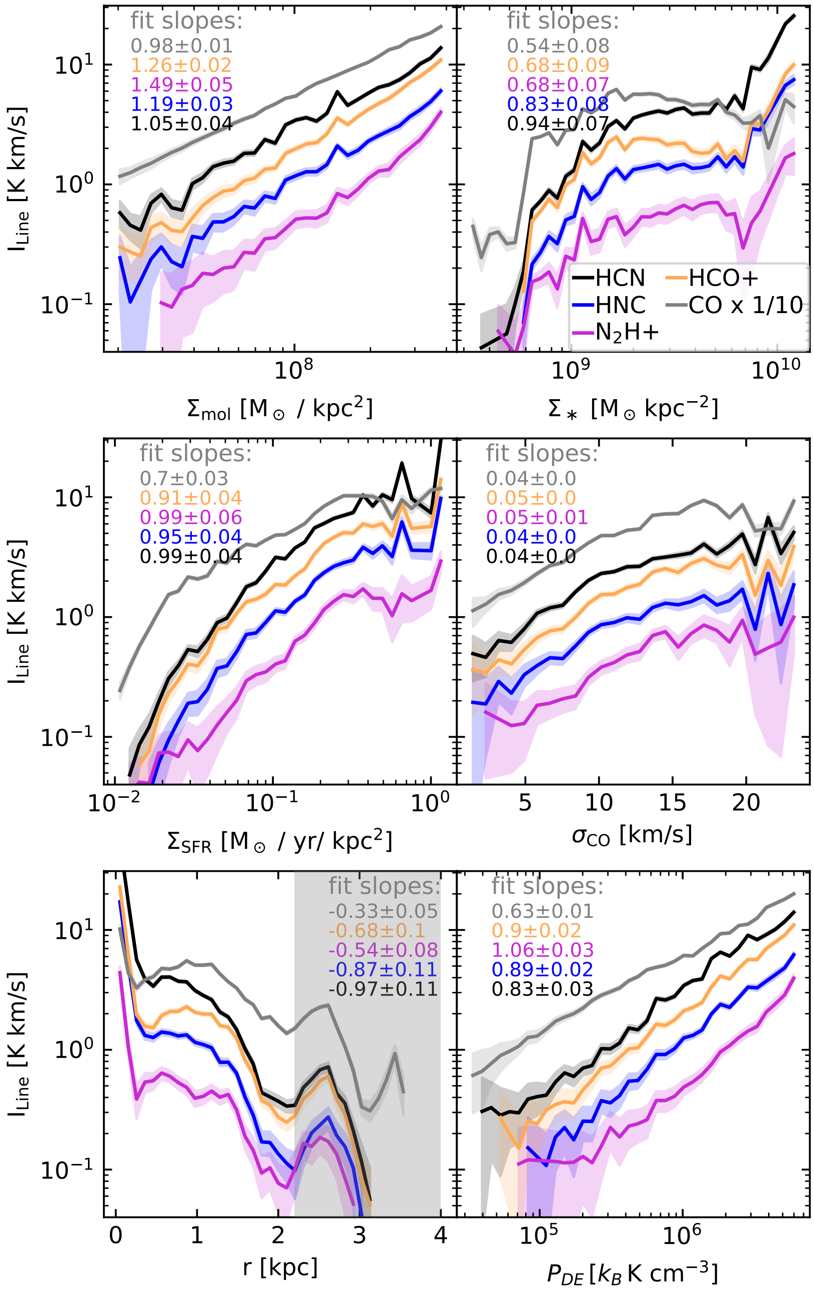

Figure 37: Average line intensity I_{Line} as a function of surface densities of molecular gas mass (Σ_{mol}), stellar mass (Σ_*) and star formation rate (Σ_{SFR}), as well as velocity dispersion (σ_{CO}), dynamical equilibrium pressure (P_{DE}) and galactocentric radius for all dense gas tracers. Shaded areas mark the standard deviation per bin. The ^{12}CO intensity scaled by a factor of 1/10 is added for comparison (grey line). For $r > 2.2$ kpc, the shape of our FoV leads to incomplete sampling of these radial bins (grey shaded area). The obtained slopes for a linear fit (in log space) to the binned averages are provided in each panel.

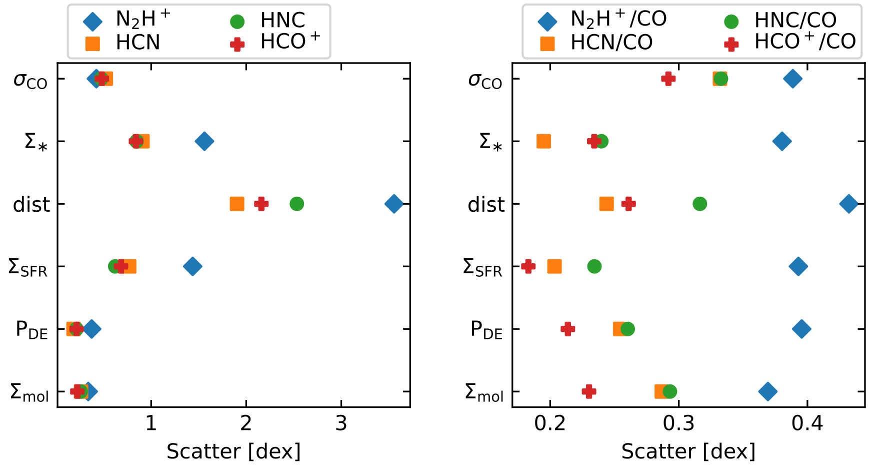

Figure 38: Average scatter of dense gas line intensity (left panel) and average dense gas to CO line ratios (right panel) as function of physical galactic properties with respect to a linear relation (Section 6.3.2). The impact of SNR on this plot is shown in Appendix C.1.4.

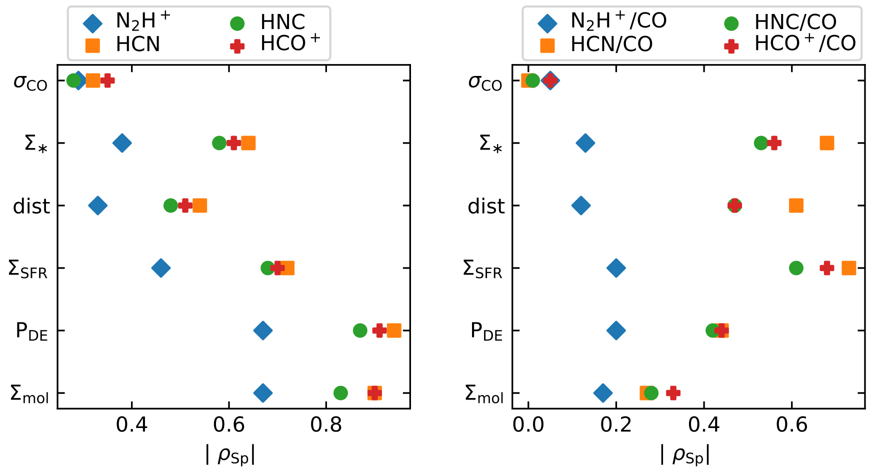

Figure 39: Spearman correlation coefficients of line intensity (left panel) and average dense gas to CO line ratios (right panel) as function of physical galactic properties (Section 6.3.2). An increased SNR will directly result in a lower correlation coefficient. We therefore expect higher correlation coefficients for HCN, followed by HCO^+, then HNC, then N_2H^+ as function of the same galactic properties. All p-values are below 5% except p-values for the Line/CO ratios as function of σ_{CO}.

Fitted slopes of average intensity as function of $\Sigma_{\rm mol}$ range from unity (CO, HCN), to significantly super-linear (HNC, HCO^+, N_2H^+). These values confirm that N_2H^+ has a significantly steeper dependency on $\Sigma_{\rm mol}$ than the other lines, while HCN has a similar shallower dependency on $\Sigma_{\rm mol}$ than CO does. While slightly reduced in the center, the slopes obtained in the environments are consistent with this result (Appendix C.4). We note a turn-up in the N_2H^+-to-$\Sigma_{\rm mol}$ relation at high values of $\Sigma_{\rm mol}$, where the trend steepens, which corresponds to the N_2H^+-brightest region located at the south-western brink of the molecular ring (Section 6.4.1).

Slopes of average intensity as function of $P_{\rm DE}$ range from significantly sub-linear (CO, HCN, HNC, HCO^+) to linear (N_2H^+) and while they vary slightly with environment (Appendix C.4), the increased order or slopes from CO to N_2H^+ is mostly consistent with the full FoV environment. The dependency of CO and HCN on $P_{\rm DE}$ is significantly different.

As the relations of line intensity with other physical galactic parameters are depicting larger variations deviating form a straight-line relation, we suspect a dependency on secondary properties. We find the following: Average line intensities all increase with increasing Σ_*, except for a plateau (N_2H^+, HNC, HCN) or decline (CO, HCO^+) at $\Sigma_* \sim 2-7\times10^9\ {\rm M_\odot\,kpc^{-2}}$, which corresponds to radii of $r \sim 0.2-1$ kpc. This is consistent with the flatter trend seen in line ratio as function of galactocentric radius.

All lines are similarly well correlated with $\Sigma_{\rm SFR}$ up to values of $4\times10^{-1}\ {\rm M_\odot\,yr^{-1}\,kpc^{-2}}$, where the distribution flattens. We identify a shallower distribution in the northern disk compared to the other environments, which, when averaged, produces the flattening (Appendix C.4). The same effect is driving the flattening seen with $\sigma_{\rm CO}$.

6.5.2 Line ratios with CO as function of physical parameters

Ratios between dense gas tracers and bulk tracer CO are found to be density sensitive (e.g., Leroy et al., 2017a; Schinnerer and Leroy, 2024). To explore the physical mechanisms driving these CO line ratios, we show $R^{\rm HCN}_{\rm CO}$, $R^{\rm HNC}_{\rm CO}$, $R^{\rm HCO+}_{\rm CO}$ and $R^{\rm N2H+}_{\rm CO}$ as function of physical properties $\Sigma_{\rm mol}$, Σ_*, $\Sigma_{\rm SFR}$, $\sigma_{\rm CO}$, $P_{\rm DE}$ and galactocentric radius in Figure 40. We provide fit slopes when fitting a linear to the binned data in Figure 40 and for the distinct environments and full FoV in Appendix C.4.

The average $R^{\rm Line}_{\rm CO}$ follows a nearly straight-line relation with $\Sigma_{\rm mol}$ and $P_{\rm DE}$, albeit the $R^{\rm N2H+}_{\rm CO}$-to-$\Sigma_{\rm mol}$ relation steepens at high values of $\Sigma_{\rm mol}$. Ratios related with other parameters depict stronger variations and deviations from a linear relation. Despite this linear dependency of CO line ratios and $\Sigma_{\rm mol}$, fitted slopes are surprisingly low, with slopes for $R^{\rm HCN}_{\rm CO}$ consistent with being zero. Spearman correlation coefficients are lowest for $R^{\rm HCN,HNC,HCO+}_{\rm CO}$-to-$\Sigma_{\rm mol}$ ($\rho_{\rm Sp} \lesssim 0.35$) compared to any other property (except $\sigma_{\rm CO}$, Figure 39).
This indicates that in the full FoV, $R^{\rm HCN}_{\rm CO}$ is nearly independent of $\Sigma_{\rm mol}$ at cloud-scales in M51. We explore possible biases that affect these measurements, such as different estimates of $\Sigma_{\rm mol}$ (Appendix C.2), the impact of the AGN (Appendix C.3), or the relation within individual environments (Appendix C.4). All tests agree that the $R^{\rm HCN}_{\rm CO}$ ratio has a very shallow and variable dependency on $\Sigma_{\rm mol}$, that even turns negative depending on the prescription used to estimate $\Sigma_{\rm mol}$ and the environment studied. $R^{\rm HNC}_{\rm CO}$ and $R^{\rm HCO+}_{\rm CO}$ behave similarly, although they generally have steeper slopes as a function of $\Sigma_{\rm mol}$. Within distinct environments, the slope of the $R^{\rm N2H+}_{\rm CO}$ to $\Sigma_{\rm mol}$ relation varies from -0.04 ± 0.1 in the center up to 0.8 ± 0.05 in the molecular ring (Appendix C.4). Re-

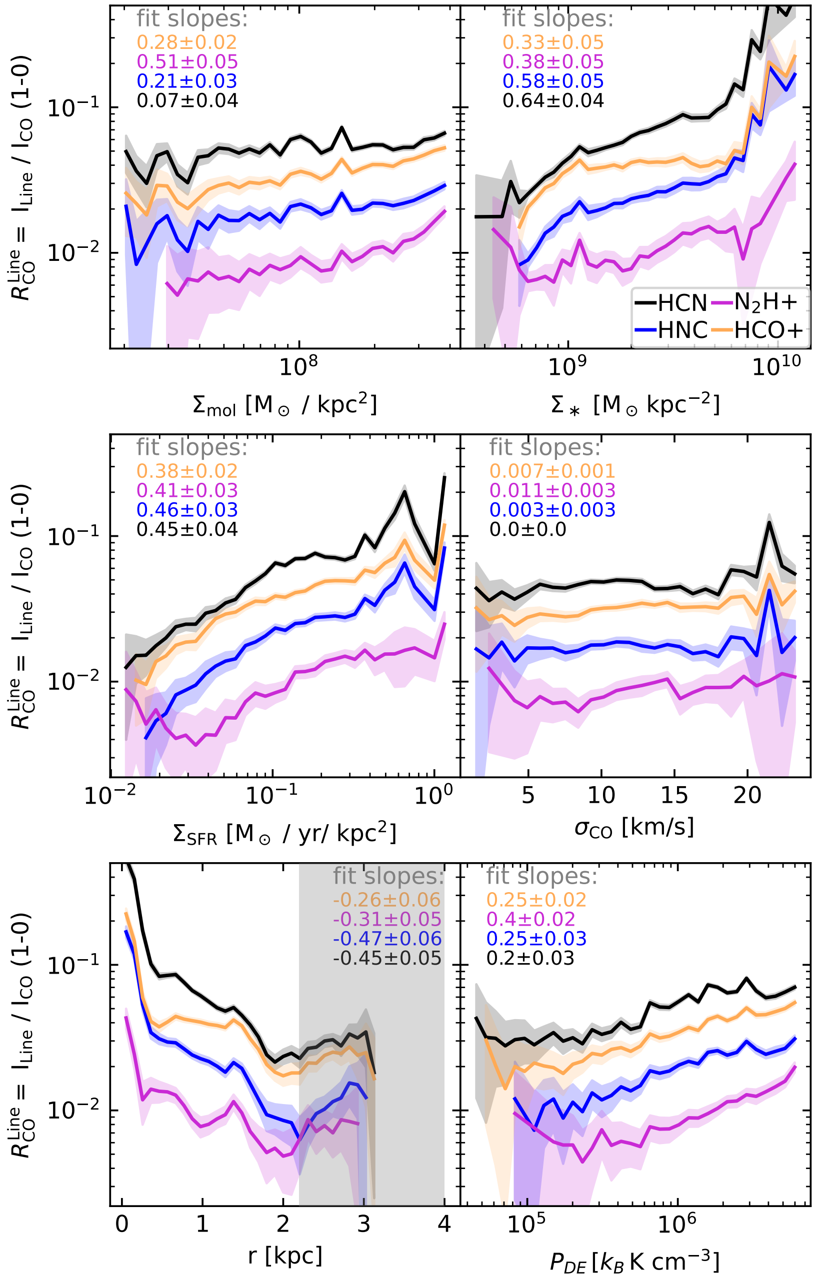

Figure 40: Same as Figure 37 but for line ratios with ^{12}CO.

moving the central 1 kpc data including the brightest pixels of HCN, HNC and HCO^+, increases the slopes of all R_{CO}^{Line} to Σ_{mol} relations, particularly for the R_{CO}^{HCN} ratio (i.e., slope of 0.36 ± 0.02 for R_{CO}^{HCN}, and 0.68 ± 0.06 for R_{CO}^{N2H+}, Appendix C.3). Even in the environments outside of the center, the R_{CO}^{HCN} to Σ_{mol} relation is shallower than common literature results (compare Section 6.6).

The dependency of R_{CO}^{Line} to P_{DE} is positive albeit shallow across all environments (Appendix C.4) with lowest slopes for R_{CO}^{HCN} followed by R_{CO}^{HNC}, R_{CO}^{HCO+} and R_{CO}^{N2H+}. Spearman correlation coefficients are higher than compared to Σ_{mol}, but lower than Σ_*, r and Σ_{SFR} (Figure 39. While the scatter relative to a linear correlation (Figure 38) is lower for R_{CO}^{HCN}, R_{CO}^{HNC} and R_{CO}^{HCO+} as function of P_{DE} compared to Σ_{mol}, the scatter is even lower for other physical parameters, i.e. Σ_{SFR} for R_{CO}^{HCO+} and Σ_* for R_{CO}^{HCN}. Similarly, spearman correlation coefficients (Figure 39) are highest for R_{CO}^{Line} for all lines except N_2H^+ as function of Σ_{mol}, r and Σ_{SFR}, followed by P_{DE} and are lowest for Σ_{mol}. Due to the low SNR of the N_2H^+ emission, the variation seen in the scatter and spearman coefficients of R_{CO}^{N2H+} as function of physical parameters is consistent with noise (compare Appendix C.1.4).

Similar to Section 6.5.1, the ^{12}CO line ratios as function of Σ_* and radius change slope at radii of $\sim 0.2 - 1.2$ kpc.

6.5.3 Dense gas line ratios as function of physical parameters

We show average line ratios between HCN, HNC and HCO^+ and line ratios between those lines and N_2H^+ as function of Σ_{mol}, Σ_*, Σ_{SFR}, σ_{CO}, galactocentric radius and P_{DE} in Figure 41, and separated into environments in Appendix C.4.

Among the brighter dense gas tracers HCN, HNC and HCO^+ we find the largest dependency on physical properties of line ratios with HCO^+, with a nearly linear dependency with Σ_{mol} and radius. Consistent with findings in Section 6.4.2, the HCN/HNC ratio is basically independent of physical properties or dependencies are very shallow (slopes range from −0.14 to 0.11, Table 12). HCN/HCO^+ is positively correlated with Σ_{mol}, Σ_{SFR} and negatively correlated with radius and Σ_{mol}.

Ratios of HCN, HNC and HCO^+ with N_2H^+ show no clear linear dependencies on any of the properties. All ratios monotonically decrease at high values of Σ_{mol} and P_{DE} and all except for the HCO^+/N_2H^+ ratio decrease with galactocentric radius. We find the steepest slopes for the HCN/N_2H^+-to-Σ_{mol} relation (−0.42) and shallowest for HCO^+/N_2H^+-to-Σ_{mol} (−0.2). A local minima in N_2H^+ line ratios as function of both Σ_* and radius can be associated with radii of $r \sim 0.2 - 1$ kpc.

We highlight the impact environment has on the slopes of average N_2H^+ line ratios as function of Σ_{mol} in Figure 42. We show the same relation for all physical properties in Appendix C.4, but provide here a version easier to compare. In contrast to the other environments, the slope measured in the ring environment is significantly negative with a steep slope of −0.63 (see Figure caption).

Our results suggest that the line most closely related to N_2H^+ is HCO^+, as the HCO^+/N_2H^+ line ratio shows the smallest slopes as function of galactic parameters compared to the HCN/N_2H^+ and HNC/N_2H^+ ratios. The most different to N_2H^+ is the molecule HCN, with the largest line-ratio to galactic property slope of HCN/N_2H^+-to-Σ_{mol} of -0.42. The molecular line emission closest to the HCN(1-0) emission is HNC(1-0), as the HCN/HNC line ratio is smaller than HCN line ratios with HCO^+ or N_2H^+. The largest differences between N_2H^+ ratios (if present) is re-

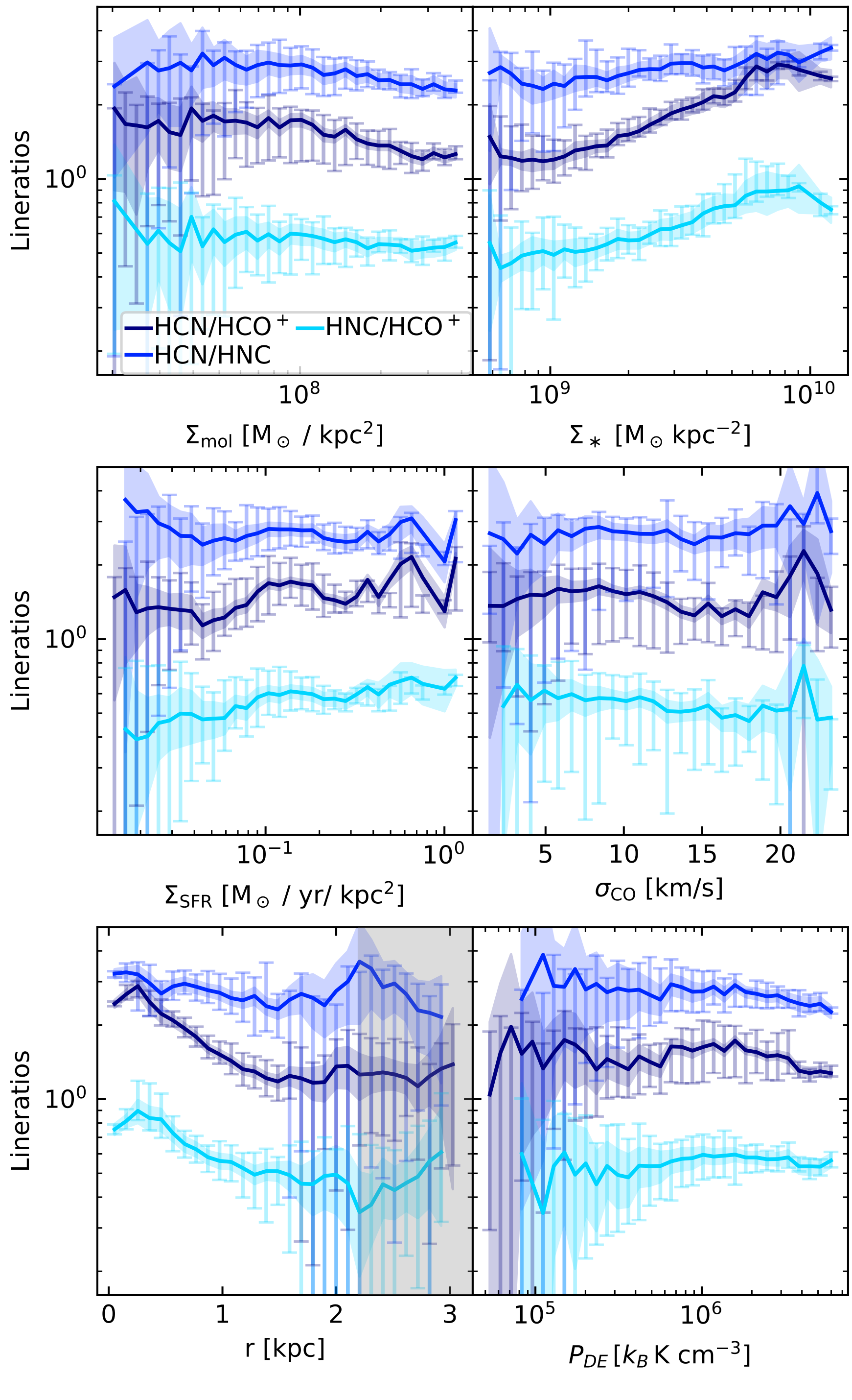

Figure 41: Average line ratios of HCN/HNC, HCN/HCO$^+$ and HNC/HCO$^+$ (these panels) as function of physical properties as well as for HCN/N$_2$H$^+$, HNC/N$_2$H$^+$, HCO$^+$/N$_2$H$^+$ (continued figure panels below). Error bars depict the 25/75th percentiles.

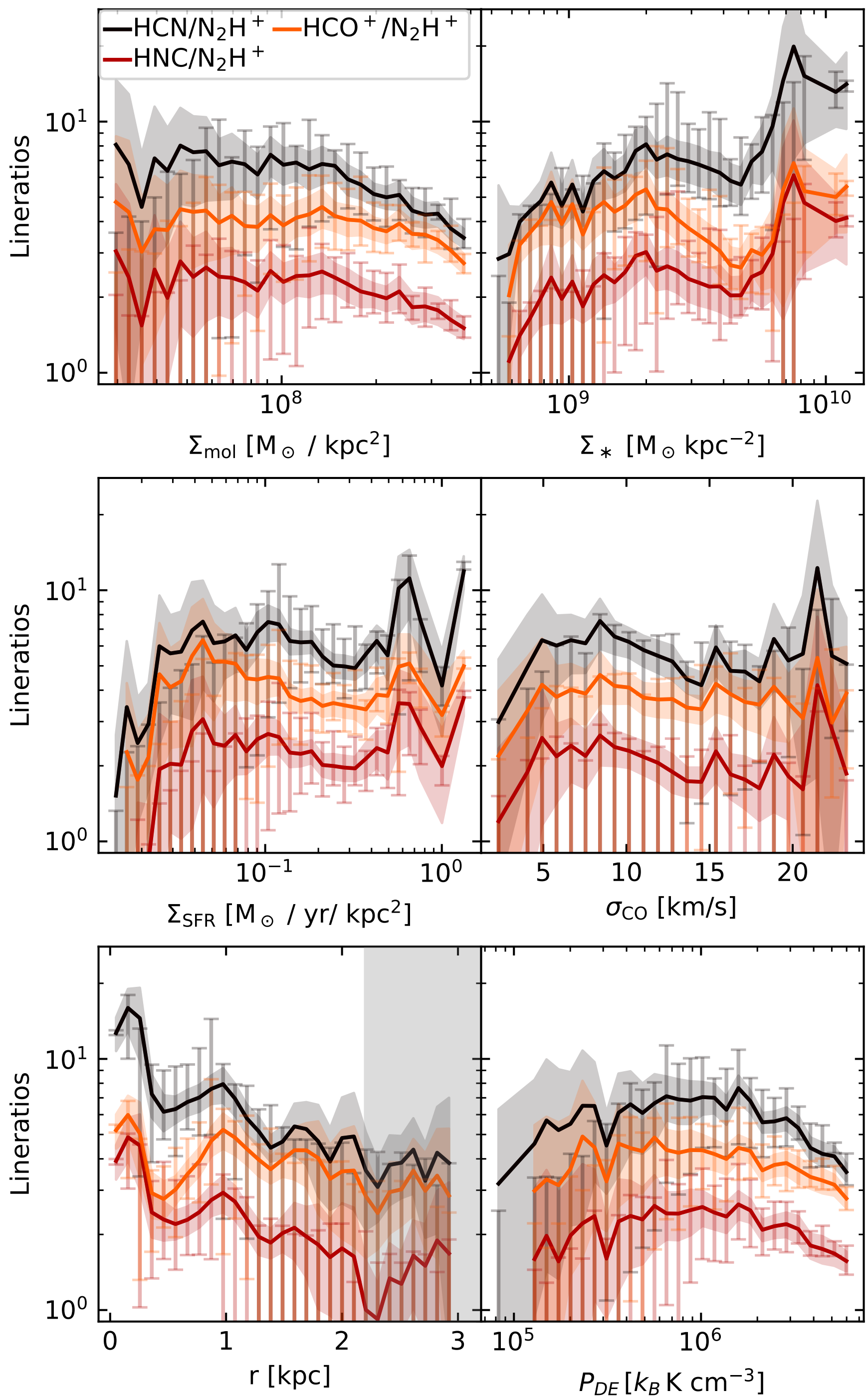

Figure 41: Continued

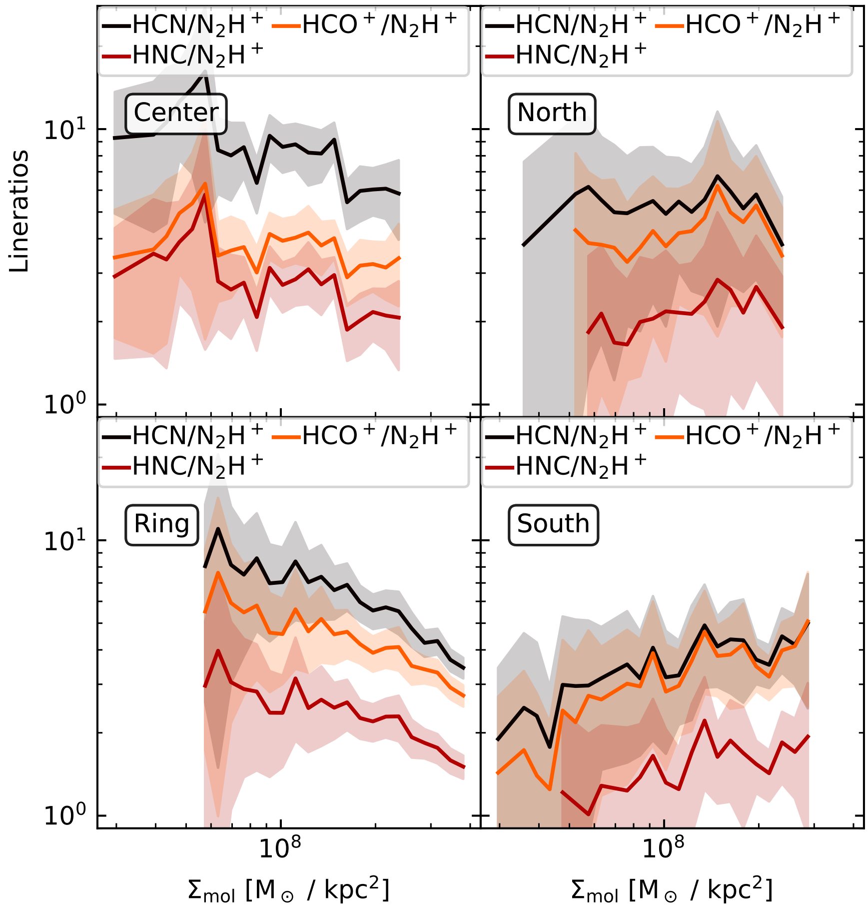

Figure 42: Same as right panels of Figure 41, but only for relations with Σ_{mol} and separated into the different environments. We note that fitting the binned averages as function of Σ_{mol} results in slopes that are within 5σ to a slope of zero for all line ratios as function of Σ_{mol}, except for the ring environment, where the slopes are significantly negative. The slopes for the HCN-, HNC- and HCO^+-to-N_2H^+ line ratio as function of Σ_{mol} in the ring environment are -0.63 ± 0.04, -0.48 ± 0.04 and -0.46 ± 0.04, respectively.

Table 12: Fitted slopes to binned line ratios as function of Σ_{mol}, Σ_{SFR}, Σ_*, P_{DE}, σ_{CO} and radius.

LR	Σ_{mol}	Σ_{SFR}	r	Σ_*	σ_{CO}	P_{DE}
HCN/N_2H^+	-0.42±0.04	0.09±0.05*	-0.32±0.04	0.29±0.04	-0.29±0.10*	-0.25±0.04
HCO^+/N_2H^+	-0.20±0.03	-0.01±0.04*	-0.08±0.04*	-0.04±0.05*	-0.10±0.06*	-0.16±0.03
HNC/N_2H^+	-0.27±0.03	0.07±0.04 *	-0.24±0.04	0.20±0.04 *	-0.27±0.08 *	-0.18±0.03
HCN/HNC	-0.14±0.01	0.04±0.02*	-0.07±0.01	0.11±0.01	-0.01±0.03*	-0.08±0.01
HCN/HCO^+	-0.21±0.02	0.13±0.03	-0.22±0.02	0.34±0.02	-0.18±0.05*	-0.08±0.02*
HNC/HCO^+	-0.07±0.01	0.10±0.01	-0.14±0.02	0.24±0.01	-0.15±0.04*	-0.01±0.01*

Fitted slopes of binned line ratios as function of Σ_{mol}, Σ_{SFR}, Σ_*, r, P_{DE} and σ_{CO}. Binned averages are calculated as described in Section 6.3.2 for all pixels in the FoV. The fitting is performed as before (i.e, Table 11). We mark values where the slope agrees within 5σ to a slope of zero with *.

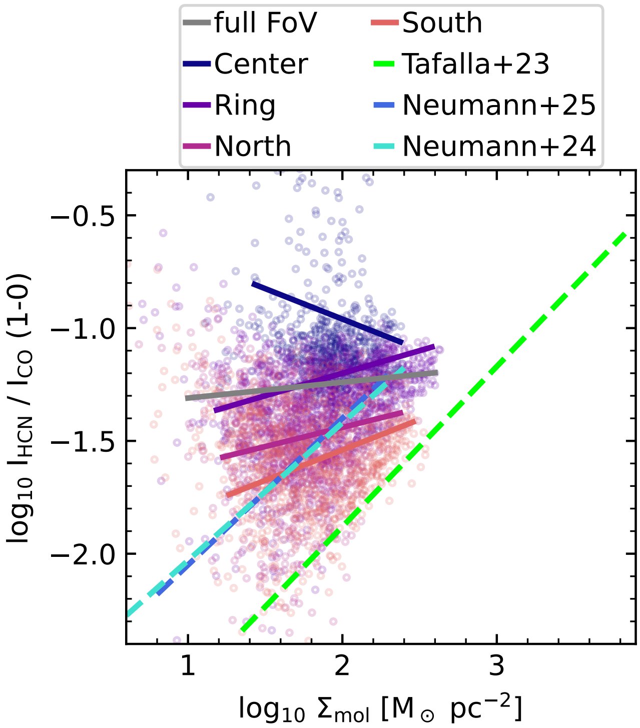

Figure 43: Literature comparison of fits best describing HCN/CO as function of Σ_{mol}. We include estimates from Milky Way clouds (Tafalla et al., 2023, green dashed line), fits of individual environments and full FoV in M51 (this work, solid lines), fits based on HCN/CO at 260 pc resolution in NGC 4321 (Neumann et al., 2024) and fits based on 31 local spiral galaxies from the ALMOND (Neumann et al., 2023b) and EMPIRE (Jiménez-Donaire et al., 2019) surveys at ~kpc resolution (Neumann et al., 2025). We add our HCN/CO observations for visual comparison for each environment within M51 (colored open circles).

vealed by Σ_{mol}, followed by galactocentric radius, Σ_* and P_{DE}. The largest difference between line ratios among HCN, HNC and HCO^+ is revealed by Σ_*, followed by galactocentric radius and Σ_{mol}. In summary, at our 125 pc scales, there are no two molecules that have the exact same emission pattern across all environmental conditions.

6.6 DISCUSSION ON DENSE GAS IN M51

Our observations of HCN, HNC, HCO^+ and N_2H^+ in the disk of M51 cover different galactic environments, including spiral arms, a molecular ring and AGN affected center, and span a range of physical conditions. We discuss the impact of environment and physical conditions on the dense gas emission, and ultimately the ability of this emission to trace dense regions.

6.6.1 Are dense gas tracers reliably tracing dense gas?

The emission of N_2H^+, which originates from regions where ^{12}CO is frozen out on dust grains, is undisputedly an ideal indicator of cold and dense regions within Milky Way clouds, and likely also a good indicator of dense regions in M51. The emission of a "dense gas tracer" is thus expected to agree reasonably well with the emission of

N_2H^+. Our data show that, in contrast to the emission of the bulk tracer ^{12}CO, the emission of HCN, HNC and HCO^+ performs well at tracing N_2H^+ emission linearly in our FoV, but this correlation clearly varies with environment. When compared on cloud-scales and across the environments and physical conditions present in M51, the emission of HCO^+ is favoured over the emission of HCN and HNC, as it is more closely related to the N_2H^+ emission and has higher values of ρ_{Sp} across the environments when compared to Σ_{mol} despite being fainter than HCN on average.

When comparing the emission of dense gas molecules with estimates of Σ_{mol}, often assumed to be indicative of the gas volume density, we find that the relation between HCN and Σ_{mol} is more similar (in slope) to the relation between CO and Σ_{mol}, while the relationship between HCO^+ and Σ_{mol} (in slope) is closer to the relationship between N_2H^+ and Σ_{mol}. At much smaller than our resolutions within three individual clouds in the Milky Way, Tafalla et al. (2023) find strong and similar correlations between HCN, HNC and HCO^+ emission and column density and clear deviations from the CO relation. Tafalla et al. (2023) further find that N_2H^+ emission rises more steeply with estimates of column density than any of the other lines, and emission only arises above column densities of $10^{22}\,\mathrm{cm}^{-2}$. This is in disagreement with our general similar trends found between N_2H^+, HCO^+, HCN and HNC, but at our resolution (and different measurements of Σ_{mol}) we are averaging many clouds and do not expect to recover the same relation. However, we note that in our observations, N_2H^+ emission as function of Σ_{mol} changes slope at highest values of Σ_{mol} ($\gtrsim 2 \times 10^8 M_\odot\,\mathrm{kpc}^{-2}$), which is not the case for the other lines. This steepening in the N_2H^+-to-Σ_{mol} relation is mainly driven by the N_2H^+-brightest region located at the south-western brink of the molecular ring. We discuss possible mechanisms responsible for the high N_2H^+ emission in Section 6.6.3.

The ^{12}CO line ratios depend super- or sub-linearly on the N_2H^+/CO ratio depending on the environment, suggesting that the molecules are not similarly sensitive to density. The scatter is minimized when comparing CO line ratios directly with N_2H^+ intensity, albeit the relations are significantly sub-linear with exception of the central environment. When comparing their emission with estimates of surface density, Σ_{mol}, a commonly used proxy of gas density, we find that the HCN/^{12}CO line ratio is not significantly correlated with Σ_{mol} across the FoV of our SWAN data, with Spearman correlation coefficients of $\rho_{Sp} \sim 0.3$, which are smaller than when comparing HCN/^{12}CO to any other physical parameter (except σ_{CO}). Typical HCN/CO line ratios from lower-resolution surveys follow a relation with Σ_{mol} of slope ~ 0.65 (Neumann et al., 2025), which is obtained by combining $\gtrsim$ kpc-scale observations of 31 local spiral galaxies in the EMPIRE survey (Jiménez-Donaire et al., 2019) and ALMOND survey (Neumann et al., 2023b). Similarly, the 300 pc resolution observations in NGC 4321 match these literature slopes well (Neumann et al., 2024, Figure 43) Even estimates from three Milky Way clouds find slopes in the HCN/CO-to-Σ_{mol} relation of ~ 0.71 (Tafalla et al., 2023). The relation found in our data, both from the total FoV as well as obtained from individual environments, is significantly shallower and weaker ($\rho_{Sp} \lesssim 0.4$) than any of these literature correlations or even negative, as we show in Figure 43.

Our results are similar to 150 pc resolution observations in the central 1 kpc of NGC 6946 (Eibensteiner et al., 2022), that only find a weak and shallow correlation between HCN(1-0)/CO(2-1) and CO(2-1) intensity as proxy for Σ_{mol} (slopes of ~ 0.23, $\rho_{Sp} \sim 0.39$), and instead find a stronger correlation for HNC/CO followed by HCO^+/CO. In their observations, HCO^+ is best correlated with Σ_{SFR}. NGC 6946 does not exhibit signs to host an AGN that could explain an enhancement in HCN emission.

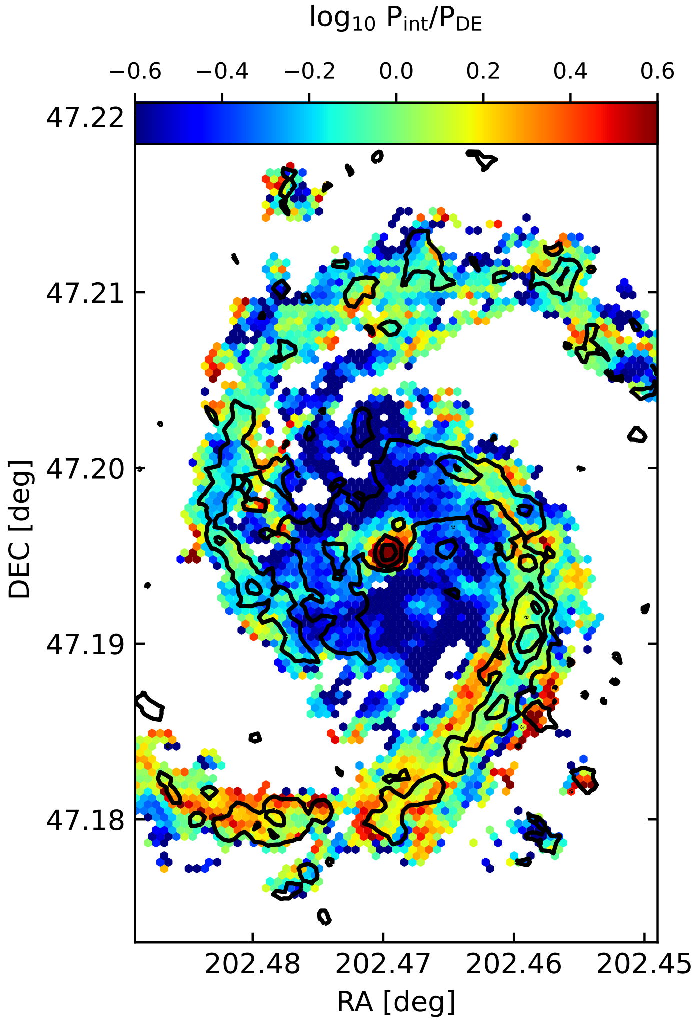

Figure 44: Logarithmic ratio of P_{int}/P_{DE}. We calculate $P_{int} = 3/2\,\Sigma_{mol} \times \sigma_{CO}^2/D$ according to equation 10 from Sun et al. (2020) and with $D = 125$ pc. We show N_2H^+ contours at 0.5, 2, 4 K.

Our results show that in the inner disk of M51 at cloud-scales, the HCN/CO ratio does not trace Σ_{mol} well at all and also the HCO^+/CO or HNC/CO ratios are shallow. Removing central apertures (Appendix C.3) or using different prescriptions to calculate Σ_{mol} (Appendix C.2) do not resolve this issue. While we find steeper slopes for some of those treatments, the high variability of the slope with aperture and Σ_{mol} prescription makes the HCN/CO ratio a very questionable tracer of Σ_{mol} in M51. Spearman correlation coefficients do not change when removing central apertures, and are all significantly lower than when comparing R_{CO}^{Line} to any other physical parameter except σ_{CO}. The dynamical range of Σ_{mol} is not reduced when removing the central 1 kpc (Section C.3). While the N_2H^+/CO-to-Σ_{mol} relation reveals higher slopes, those slopes vary greatly across the different environments.

6.6.2 Physical conditions driving gas emission

While molecular gas mass surface density is commonly used as a proxy for the volume density and thought to directly drive the emission of dense gas molecules, dynamical equilibrium pressure is suggested to directly determine the ability of gas to form stars (e.g., Usero et al., 2015; Jiménez-Donaire et al., 2019; Neumann et al., 2025). In comparison to $\Sigma_{\rm mol}$, we find less variation in the slopes of $R_{\rm CO}^{\rm Line}$ as a function of $P_{\rm DE}$ across environments (i.e., no negative slopes), but slopes are similarly shallow. In contrast to a linear correlation, Neumann et al. (2024) suggests a dynamical equilibrium pressure threshold above which the HCN/CO to $P_{\rm DE}$ and HCN/SFR to $P_{\rm DE}$ relations change slope, falling at $P_{\rm DE} \sim 4 \times 10^5 k_B\,{\rm K\,cm^{-3}}$ for HCN/CO vs. $P_{\rm DE}$ and $P_{\rm DE} \sim 1 \times 10^6 k_B\,{\rm K\,cm^{-3}}$ for HCN/SFR vs. $P_{\rm DE}$. Our data reveals no clear change in the HCN/CO vs $P_{\rm DE}$ relation, despite covering the same dynamical range, but all line ratios with N_2H^+ visually appear to turn from positive to negative slopes at $P_{\rm DE} \sim 1 \times 10^6\,k_B$ K cm^{-3}. This matches with sub-cloud-scale simulations by Priestley et al. (2023) that find N_2H^+ largely traces gas in dense regions which are irreversibly collapsing to form stars, in contrast to HCN, HNC and HCO^+ which also trace a significant amount of gas that will not eventually form stars in this set of simulations.

While $P_{\rm DE}$ and $\Sigma_{\rm mol}$ are promising drivers of the gas emission, line ratios with CO have an increased scatter when compared to those physical properties compared to others. Despite there being secondary trends and local minima in relations with other physical quantities, the scatter measured with respect to a linear relation of the HCO^+/CO ratio is minimized when compared to Σ_*, whereas the scatter of HCN/CO is smallest when compared to Σ_* and $\Sigma_{\rm SFR}$. Both Σ_* and $\Sigma_{\rm SFR}$ however depict local minima and changes of slopes that might be connected with $P_{\rm DE}$ as follows. Figure 44 shows the ratio of internal to dynamical equilibrium pressure ($P_{\rm int}/\,P_{\rm DE}$). This ratio is decreased in the central ~ 1.5 kpc in radius, except for the very central few ~ 100 pc, suggesting that the midplane pressure supporting the gas against collapse is increased. The $P_{\rm int}/P_{\rm DE}$ ratio further reveals an asymmetry between the northern and southern spiral arms, which we discuss in more detail below. The decrease of $P_{\rm int}/P_{\rm DE}$ in the center coincides spatially with the shallower relation between line intensity, CO line ratios and Σ_* or radius found at radii of $\sim 0.2 - 1.2$ kpc. In comparison, the bulge of M51 is thought to be only $\sim 450 \times 650$ pc in size (Lamers et al., 2002). In the central environment coinciding with this region, emission of HCN, HNC and HCO^+ is sublinearly correlated with $\Sigma_{\rm mol}$, and CO line ratios are negatively correlated with $\Sigma_{\rm mol}$ while being most steeply correlated with both Σ_* and $\sigma_{\rm CO}$ compared to other environments.

Further, the HCN/HCO^+ (and HNC/HCO^+) ratio is increased in the central $\sim$ 1.5 kpc, which might indicate high cosmic ray ionization rates (Harada et al., 2019). An increased ionization rate can boost the abundance of free electrons. These electrons could then enhance the destruction of HCO^+ (via dissociative recombination) but might also increase the abundance of H_3 which is the key molecule for HCO^+ formation. Free electrons, however, also enhance the HCN excitation, which, in combination, might lead to an increased HCN to HCO^+ emission ratio (Krolik and Kallman, 1983; Maloney et al., 1996; Papadopoulos, 2007; Goldsmith and Kauffmann, 2017).

While some studies find a correlation between cosmic ray ionization rates and X-ray emission produced by inverse Compton scattering of hot gas (Schober et al., 2015), the contribution of this mechanism to the total X-ray flux is expected to be fairly small for local non-starbursting galaxies. Zhang et al. (2025) that find a sharp decrease in the surface brightness profile of hot gas from X-ray observations with Chandra in M51 at $r \sim 2$ kpc as well as a steeper relation between kpc-scale HCN emission in the central ~ 2 kpc and hot gas luminosity compared to the disk. They further conclude a negligible impact of the AGN on the hot X-ray gas luminosities, and suggest that instead core-collapse supernovae (SN) dominate the energy source in M51's center.

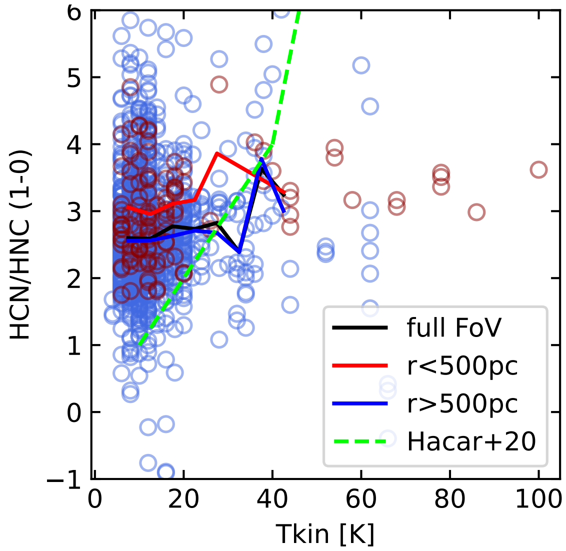

Figure 45: HCN/HNC line ratio from this work as function of kinetic gas temperature measurements at 4″ resolution from den Brok et al. (2025). We separate pixels in the center ($r < 500$ pc, red points) and disk ($r > 500$ pc, blue points), and provide binned estimates for the full FoV (black line), center and disk (red, blue, respectively) in steps of 5 K in the range $\sim 10-50$ K, suggested by Hacar et al. (2020). We add the fitted relation from Hacar et al. (2020) (green dashed line).

This is in agreement with the good correlation between HCO^+/CO and SFR surface density that is expected to be correlated with SNe.

Increased ionization rates can also be found in the CMZ of the Milky Way compared to its disk, where they also result in increased gas temperatures (Oka et al., 2019; Indriolo et al., 2015). Variations in kinetic gas temperature can increase the scatter of HCN intensity as function of gas column density (Tafalla et al., 2023). With the gas temperature in merging galaxy systems generally being increased (Schinnerer and Leroy, 2024), this can increase the scatter of the HCN/CO ratio. However, kinetic gas temperature estimates by den Brok et al. (2025) combining SWAN and SMA CO and CO isotopologue observations reveal average gas temperatures in our FoV of $\sim 13 \pm 5$K with no significant increase towards M51's center. High HCN/HCO^+ ratios similar to our results (Figure 33) are also common in centers in Ultra Luminous Infrared Galaxies (ULIRGs, e.g., Aalto, 2005; Imanishi et al., 2023), LIRGs (Papadopoulos, 2007) as well as centers hosting AGNs of normal galaxies (Usero et al., 2004; Nakajima et al., 2023), including M 51 (Kohno, 2005). However, the molecular gas in centers of ULIRGs is often warm (i.e., $T \gtrsim 100$ K Imanishi et al., 2023), which is – again – not the case for M51's center.

The HCN/HNC ratio has been suggested to track kinetic gas temperature in Milky Way clouds (Hacar et al., 2020). We show the HCN/HNC ratio as function of T_{kin} from den Brok et al. (2025) in Figure 45. Theoretically, at a temperature of $T > 30$ K, the equal formation of HCN and HNC is offset by the conversion of HCN into HNC. We find no clear correlation between our line ratios and kinetic gas temperature, in agreement with other extragalactic studies at kpc scales in the EMPIRE galaxies (Eibensteiner et al., 2022) and ~ 100 pc in NGC 6946, M51, NGC3627 (Eibensteiner et al., 2022) and M83 (Harada et al., 2024b). The latter find HCN/HNC to depend on UV illumination instead.

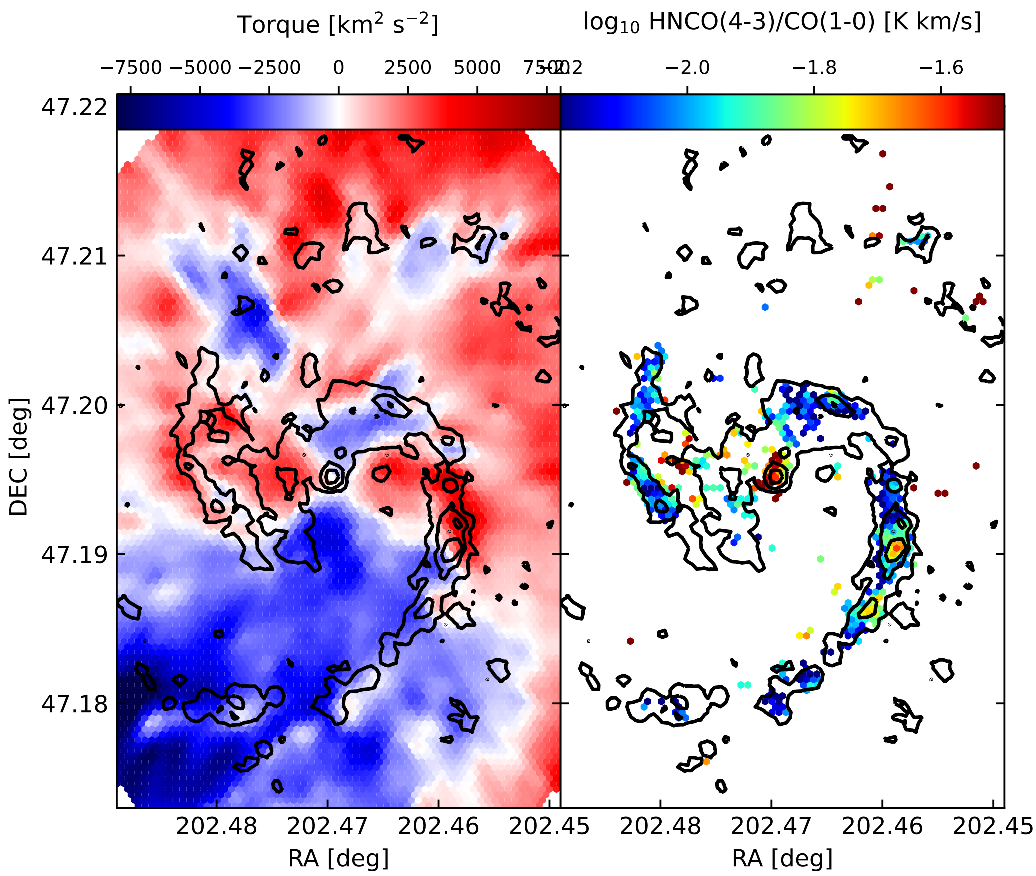

Figure 46: (left) Torques per unit mass from Querejeta et al. (2016a) estimated from dust corrected (3.6 ţm) Spitzer images. (right) HNCO(4-3)/CO(1-0) emission from SWAN (Stuber et al., 2025) for pixels where HNCO(4-3) is detected >3σ. N_2H^+ contours are plotted on top.

We note that the effects of AGN feedback on the molecular ISM and the extent of this impact is not well known in M 51. Our data reveal both a clear enhancement in line intensities and line ratios in the very center (r$\lesssim$ 500 pc, i.e., Figure 35), which might agree with radio emission from a low-inclined radio jet (Matsushita et al., 2015; Querejeta et al., 2016b). Querejeta et al. (2019) find a clear enhancement of HCN/CO due to the AGN in M51's center at 4″ resolution. In fact, observations of dense-gas tracing molecules such as HCN, HCO^+ and HNC in galactic starburst-driven (NGC 253; Meier et al., 2015) or AGN-driven outflows (Mrk231; NGC1068;NGC1377; Aalto et al., 2012, 2015; García-Burillo et al., 2014; Aalto et al., 2020) at resolutions down to a few pc suggest the survival, formation and/or emission enhancement of dense gas in outflows (Jørgensen et al., 2004; Tafalla et al., 2010; Aalto et al., 2015). The nuclear outflow will be discussed in much greater detail in upcoming papers (Thorp et al. in prep., Usero et al. in prep),

6.6.3 Anomalies in the molecular ring

The molecular ring in M51 stands out as a peculiar environment: Average line intensities of HCN, HCO^+ and HNC follow N_2H^+ emission only sub-linearly (Table 11), and consequently, line ratios with N_2H^+ as function of Σ_{mol} exhibit significantly negative trends (Figure 41). The N_2H^+/CO-to-Σ_{mol} relation in the ring has the largest slope (0.8 ± 0.05, Appendix C.4) compared to all other environments and all other CO line ratios. The ring environment has the largest absolute number of pixels in which N_2H^+ is detected ($> 3\sigma$) compared to the other environments. As it has the second highest fraction of detected pixels (28%, compared to the center with 52%), effects of SNR and beam dilution are expected to play a much lesser role than for the northern and southern spiral arm. In addition, the brightest N_2H^+ emission is located in the ring. This region was previously speculated to drive the super-linear relation between N_2H^+ and HCN emission (S23) and the steepening of N_2H^+ intensity function of Σ_{mol} and P_{DE} (Figure 37) is likely driven by this region. While P_{DE} is generally high in this region (Figure 32), the ratio of internal to dynamical equilibrium pressure (Figure 44) is not particularly enhanced in the N_2H^+ bright region compared to other regions along the southern arm.

The redistribution of gas and gas flows are crucial in shaping cloud conditions and are not explicitly contained in the P_{int}/P_{DE} ratio. Therefore, we show a map of torques in M51 from Querejeta et al. (2016a) based on 3.6 µm Spitzer images that are corrected for dust emission in Figure 46. These estimates give insights into the gravitational torques exerted by the stellar potential on the gaseous disk. The torque map multiplied with the total gas mass per pixel - which can be inferred from the line intensity - describes the change rate of angular momentum over time. This N_2H^+-brightest region is located at the transition between normal star-forming regions and the star-formation *desert* where torques are high (Querejeta et al., 2016a). We find that this N_2H^+-bright region is located at a spot of minimum torque, between two regions of opposing torques (Figure 46). We speculate that the observed high fractions of dense gas might stem from the action of torques in the immediate vicinity that preferentially bring material to that location from both smaller and larger galactocentric radii (where torques are positive and negative, respectively). This is in agreement with a peak in HNCO(4-3)/CO(1-0) emission which we also display in Figure 46). HNCO emission is known to trace shocks induced by the spiral arms, and is comparably bright in the exact location of the N_2H^+-bright spot. HNCO/CO being elevated perhaps supports this opposing flow/shock interpretation.

While this is a speculative explanation for non-linear behavior of the N_2H^+-bright spot, it does not explain the general offset of the ring environment compared to other environments. We find no global trends between average line ratios and torques, nor with average line intensity and torques.

6.6.4 Differences and similarities in northern vs southern spiral arm

M51 is known for an asymmetric behavior between northern and southern spiral arm likely induced by the dwarf companion galaxy M51b (e.g., Henry et al., 2003; Schinnerer et al., 2013). While the northern spiral arm shows prominent regions of high Σ_{SFR}, the southern arm is rich in molecular gas emission (CO, HCN) but lacks high values of Σ_{SFR} (see Figure 31). Many literature studies have found the southern arm to be inefficient in forming stars (e.g., Querejeta et al., 2019). Querejeta et al. (2019) studied HCN at the same resolution in three pointings in M51 and when comparing peaks of HCN emission to the corresponding SFRs traced by 33 GHz emission, they find lower dense gas SFEs in the southern arm in contrast to the northern arm.

Our data, however, reveals that when averaging the northern disk and southern disk instead of focusing on bright spots only, the northern disk is overproducing stars, while the southern arm shows consistent behavior with the molecular ring and center. Per unit value of Σ_{SFR}, all average line intensities of HCN, HNC, HCO^+ and N_2H^+ are reduced in the northern disk compared to not only the southern disk, but also the center and ring environment (Appendix C.4). This overproduction seems independent of dense gas properties, as the dense gas line ratios as function of all physical properties agree between northern and southern disk (Figure 65). Thus while there are differences related to Σ_{SFR} in the two spiral arms, the molecular gas chemistry might be more or less unaffected.

Potential explanations for these differences could include that the high SFR in the northern arm is destroying denser gas, thus reducing the average dense gas emission, whereas the southern arm, revealing high values of σ_{CO}, and high values of P_{int}/P_{DE} (Figure 44) is in a complex dynamical state.

6.7 SUMMARY

We present observations of the J=1-0 emission of HCN, HNC, HCO^+ and N_2H^+ tracing the dense gas in the inner 5×7 kpc of the Whirlpool galaxy (M51) at 125 pc resolution from *Surveying the Whirlpool at Arcseconds with NOEMA* (SWAN). These observations cover very diverse environments, including spiral arms, a molecular ring, and the AGN affected center. We compare the emission of these molecules with each other, as well as with surface densities of molecular gas mass (Σ_{mol}), SFR (Σ_{SFR}), stellar mass (Σ_*) and estimates of P_{DE} and σ_{CO}, and find the following:

1. The average emission of HCN, HNC, HCO^+ and N_2H^+ is generally correlated with each other. Average HCN, HNC and HCO^+ intensities follow N_2H^+ intensities, and so do HCN/CO, HNC/CO and HCO^+/CO ratios, but we find clear variations in slopes with galactic environments.

2. While average HCN, HNC, HCO^+ and N_2H^+ are well correlated with Σ_{mol}, Σ_{SFR}, Σ_*, P_{DE} and σ_{CO} over several orders of magnitude, the slopes of these correlations vary from line to line and from environment to environment. The average N_2H^+ emission depends significantly steeper on Σ_{mol} (slope of 1.48 ± 0.05) compared to HCN, HNC and HCO^+ (1.05 ± 0.04, 1.26 ± 0.02, 1.19 ± 0.03, respectively). The slope of the average HCN-to-Σ_{mol} relation is in agreement with the slope of the average CO-to-Σ_{mol} relation. Consequently, the HCN-, HNC- and HCO^+-to-N_2H^+ ratios are anti-correlated with Σ_{mol}. The different dependency of dense gas lines on Σ_{mol} could imply a different dependency on column densities as found in Milky Way studies, or it could stem from beam dilution effects.

3. The average HCN/CO, HNC/CO, HCO^+/CO and N_2H^+/CO relation shows a surprisingly shallow relation with Σ_{mol}, with slopes of the average HCN/CO-to-Σ_{mol} relation as low as 0.07 ± 0.03 and consistently shallower (or negative) in all environments compared to typical literature trends. While the N_2H^+/CO-to-Σ_{mol} relation is steeper (slope of 0.50 ± 0.05), large variations in the slopes across the environments can be found.

4. Dynamical equilibrium pressure P_{DE} is a promising parameter well related to both dense gas emission and line ratios with CO, with smaller variations in slope across the environments compared to Σ_{mol}. We find indications of a P_{DE} threshold, above which N_2H^+ emission is increased compared to HCN, HNC and

HCO^+. Still, these CO line ratios have increased scatter when correlated with P_{DE} compared to Σ_* and Σ_{SFR}.

5. Variations in line ratios can be seen from one environment to the other, and on cloud-scales within individual environments. First, the nuclear outflow towards north-east of the center increases emission of HCN, HNC and HCO^+ compared to N_2H^+, and of all those lines compared to ^{12}CO. Secondly, further out in the center the increased dynamical equilibrium pressure might prevent the gas from collapsing, resulting in increased N_2H^+ and HCO^+ emission compared to the other lines and other regions in the disk. Thirdly, the molecular ring hosts the region with the brightest N_2H^+ emission, where gas flows might converge resulting in large-scale shocks. Lastly, we find asymmetries between the spiral arms. While the intensity pattern of all molecular lines as function of Σ_{SFR} in the northern arm deviates from those of all other environments, its the southern spiral arm in which we see enhanced velocity dispersion, enhanced P_{int}/P_{DE} and generally high quantities of bulk and dense molecular gas.

These cloud-scale relations of HCN, HNC, HCO^+ and N_2H^+ across these environments in the inner disk of M51 reveal, that while to first-order, the molecules agree in their emission, when considering different environments and different physical properties, no two molecules have exactly the same emission pattern at those scales. Only with SWAN can we reveal these variations that occur on both larger-scale environments and on cloud-scales within environments. In other galaxies, where the faint N_2H^+ emission is difficult to obtain, and the conditions are similar to the conditions in the inner disk of M51, the emission of HCO^+, which is nearly as bright as HCN, might be the favorable option to trace dense molecular gas.

ACKNOWLEDGEMENTS

This work was carried out as part of the PHANGS collaboration and is based on data obtained by PIs E. Schinnerer and F. Bigiel with the IRAM-30 m telescope and NOEMA observatory under project ID M19AA. IRAM is supported by INSU/CNRS (France), MPG (Germany) and IGN (Spain) SKS thanks several PHANGS team members, specifically Adam Leroy for helpful discussions. SKS acknowledges financial support from the German Research Foundation (DFG) via Sino-German research grant SCHI 536/11-1. AU, MJD, and MQ acknowledge support from the Spanish grant PID2022-138560NB-I00, funded by MCIN/AEI/10.13039/501100011033/FEDER, EU. JS acknowledges support by the National Aeronautics and Space Administration (NASA) through the NASA Hubble Fellowship grant HST-HF2-51544 awarded by the Space Telescope Science Institute (STScI), which is operated by the Association of Universities for Research in Astronomy, Inc., under contract NAS 5-26555. HAP acknowledges support from the National Science and Technology Council of Taiwan under grant 113-2112-M-032 -014 -MY3. J.d.B. acknowledges support from the Smithsonian Institution as Submillimeter Array (SMA) Fellow. SCOG and RSK acknowledge financial support from the European Research Council via the ERC Synergy Grant "ECOGAL" (project ID 855130), from the German Excellence Strategy via the Heidelberg Cluster of Excellence (EXC 2181 - 390900948) "STRUCTURES", and from the German Ministry for Economic Affairs and Climate Action in project "MAINN" (funding ID 50OO2206). RSK also thanks the 2024/25 Class of Radcliffe Fellows for highly interesting and stimulating discussions.

SUMMARY, CONCLUSION AND FUTURE DIRECTIONS

7

SUMMARY AND CONCLUSION

From the local to higher redshift universe, understanding star formation and the conditions within galaxies that promote it, are some of the major unsolved problems in modern astronomy. Star formation sets the foundation of our view on galaxy evolution – the stellar mass growth over cosmic time, but also the future secular evolution of galaxies. To study a galaxy's ability in regulating star formation, a cloud-scale view of the molecular gas phase is key. While molecular clouds are the small-scale objects within which star formation occurs, their properties and distribution is found to be regulated by large-scale dynamical features such as spiral arms, bars and rings. Of particular interest is the dense molecular gas phase (i.e. n$\gtrsim 10^4$cm^{-3}), which resides at cores of (star-forming) molecular clouds and fuels star formation. Observing this denser molecular gas, however, is challenging, as its faint emission arises from small regions. Observations require long integration times to detect this emission at high sensitivity and cloud-scale resolution, particularly in extragalactic targets. Yet, only in extragalactic (face-on) galaxies can we gain an unbiased view of the large-scale dynamical features to study their impact on the molecular gas phase. Many surveys have so far observed dense gas emission at either low resolution, unable to resolve giant molecular clouds (GMCs), or at high-resolution but in single environments, that do not allow a cross-environmental comparison.

This thesis presents one of the latest endeavours of the astronomical community, *Surveying the Whirlpool at Arcseconds with NOEMA (SWAN)*, the large IRAM-NOEMA+30m survey that required 200 hours of NOEMA observations. This survey is presented and analyzed in Stuber et al. (2023a, 2025, and subm., see Chapters 4, 5 and Chapter 6) and combines all the above-mentioned aspects: A cloud-scale imaging of a large field of view capturing dynamically distinct environments in nine molecular lines.

The data reduction, calibration, data quality assurance and delivery of science ready data products has been a vital achievement of this thesis and a substantial contribution for the astronomical community to exploit. With this first-of-its kind data set we can answer the following questions at unprecedented resolution and sensitivity:

1. Where is dense gas located in galactic environments within galaxies?

2. How do dense gas tracers compare to each other under different physical and chemical conditions?

3. Can we isolate conditions that set the dense molecular fraction within the bulk molecular gas distribution?

This thesis shows that our understanding of these so-called "dense-gas tracers" needs to be revised. Long thought universal tracers of gas density loose their universality when faced with the multiplicity of well resolved environments in M51, and even the average cloud population in M51 does not behave as expected from other (lower-resolution) galaxy studies. Centers of galaxies, in particular, are extreme environments that can not be treated equally to a galaxy's remaining disk and especially dense gas tracers need to be evaluated with care. To fully grasp whether we have understood the laws of star formation, additional high-resolution studies of other galaxies and their galactic environments (apart from galaxy centers) are urgently needed. I will elaborate on these findings below in more detail:

7.1 MAPPING MOLECULAR GAS ACROSS GALAXY ENVIRONMENTS

The SWAN data set is one of the highest-sensitivity, cloud-scale large-field of view set of maps of 3-4 mm lines to date. Among the nine detected molecules are the emission of the commonly used extragalactic dense gas tracers HCN, HNC and HCO^+. HCN emission is $\sim 20-40$ times fainter than ^{12}CO and has been linked to star formation for decades (e.g., the Gao-Solomon relation, Gao and Solomon, 2004). It is suggested to trace dense gas due to its high theoretical critical density (Section 2.3.1). Studies of individual clouds in the Milky Way have questioned the use of HCN as a reliable dense gas tracer, due to its brightness in low-density regions (i.e., densities below critical, Section 2.3.1). Regardless, it has remained the favorite dense gas tracer for extragalactic targets to date and shows a consistent behavior at low kpc-scale resolution across extragalactic targets (e.g., review by Schinnerer and Leroy, 2024). Those extragalactic studies find HCN emission bright on spiral arms, and particularly bright in galaxy centers, in agreement with the common idea of increased star formation efficiency in (density wave-) spiral arms.

At cloud-scale resolution, this thesis (Chapter 4) shows: In M51, HCN emission is bright on spiral arms and the molecular ring – but also unexpectedly well detected between the spiral arms, within the molecular ring where a nuclear bar is present and also at the location where the molecular outflow is found. This is not only the case for the common extragalactic dense gas tracers HCN, HNC and HCO^+, which are sometimes questioned in their ability in tracing dense gas, but also the case for the undisputed Galactic dense gas tracer N_2H^+. This molecule is of particular interest, as it is chemically linked to dense regions: N_2H^+ is efficiently reacting with CO molecules, and therefore thrives in dense (and cold) regions where ^{12}CO is frozen onto dust grains (Section 2.3.3).

Within the typical lifetime of a GMC in M51 ($\sim 20-30$ Myrs Meidt et al., 2015), the typical timescale for dense gas formation is $\sim 4-20$ Myr (Schinnerer and Leroy, 2024). During 20 Myrs, a molecular cloud in our FoV could well travel a distance of up to ~ 1 kpc from spiral arm into the interarm region, sufficient to explain my observations. Consequently, a significant fraction of star formation might occur outside of the spiral arms (Schinnerer et al., 2017) in agreement with recent observations of star formation rates in NGC 628 (Williams et al., 2022).

The bright emission of dense gas tracers in the center of M51, where little star formation is observed, suggests that the galactic environment and its physical conditions might inhibit the onset of star formation despite the presence of large quantities of dense gas. My work suggests that gas density alone is not the only significant contributor in determining the evolution of a molecular cloud.

7.2 FIRST-OF-ITS KIND COMPARISON OF DENSE GAS TRACERS

Many Galactic studies have questioned the use of HCN as dense gas tracer, as much of its emission is found to originate from lower density regions in some clouds observed. In contrast, the undisputed tracer of dense gas, N_2H^+, chemically linked to dense and cold regions, is often preferred. Despite the faintness of the latter (~ 7 times fainter than HCN), I have imaged the largest cloud-scale map of N_2H^+(1-0) in an external target today (Chapter 4). Comparing the emission of N_2H^+, HCN, HNC and HCO^+ in Chapter 5 and 6, I find significant variations among those molecules at both cloud-scale and across environments and with various physical conditions. As an example, emission of HCN and N_2H^+ is well but superlinearly correlated, and is completely offset in the center of M51 (Chapter 5, see Figure 29). As both molecules are expected to trace gas density in a similar fashion based on their theoretical qualities (i.e., critical density Section 2.3.1), these variations reveal that the emission of those molecules is not only sensitive to density, but to other excitation mechanisms as well. Particularly HCN emission could be boosted by infrared pumping, temperature and other mechanisms while at low gas density. While kiloparsec-scale studies suggest a constant HCN/N_2H^+ ratio, which matches Milky Way cloud observations (e.g., Jiménez-Donaire et al., 2023), my data shows – for the first time – clear variations across galactic environments (compare Figure 29 & 30 & 34). My work shows that both the lower-resolution studies but also measurements from individual clouds in the Milky Way at much better resolution fail to capture the various conditions present in a galaxy disk.

In the simple evolutionary picture of a molecular cloud, we expect dense gas clumps to reside within the bulk molecular gas. However, when analyzing the dense-gas-to-bulk ratio (i.e. HCN/CO, HCO^+/CO), this thesis reveals an unusually high scatter and variations across the disk (Chapter 4 & 6). Within just this one galaxy, these variations are larger than the variations found between most *different* galaxies at kiloparsec-scales (e.g., Figure 26). At cloud-scale resolution, we might be at a unique spot, where we are resolving individual evolutionary stages of GMCs, some after, some before the onset of dense gas formation. In some clouds with high gas density, the formation of dense gas might be inhibited compared to other clouds, or several lower-density clouds might overlap along our line-of-sight, mimicking a high gas surface density. When analyzing how the emission of molecules is correlated with gas density, this leads to an increased scatter at high resolution.

My work also shows that in contrast to HCN (and its isomer HNC), HCO^+ showcases itself as valuable alternative in tracing dense gas, as its emission is much more closely related to the emission of N_2H^+, both across environments and as a function of various physical parameters (e.g., Figure 37). Further, its emission is nearly as bright as HCN (much brighter than N_2H^+), making it more easily accessible at high resolution with common interferometers. Particularly in the centers of galaxies, which are commonly targeted due to their high brightness, HCO^+ presents itself as the more robust density tracer (Chapter 4 & 6, e.g., Figure 22 & 33). This is in agreement with recent results by Patra et al. (2025), that find HCO^+ to be more robust in tracing gas density than HCN in the center of the Milky Way due to a metallicity dependency of HCN.

Consequently we might ask: How reliable are dense gas estimates based on HCN that include galaxy centers? Is the Milky Way CMZ actually underproducing stars based on its dense gas content? Even further: Should we revise the famous Gao-Solomon relation (see Figure 10) by using HCO^+ instead of HCN, as many of the unresolved galaxy observations are dominated by the bright HCN emission stemming from galaxy centers? While not all, part of these questions could be resolved by a better understanding of the dense gas tracers used.

7.3 IDENTIFYING PHYSICAL CONDITIONS THAT SET THE DENSE MOLECULAR GAS PHASE

Within galaxies, there are various physical conditions, which are closely connected with the large-scale galactic environments. As an example, galaxy centers are locations of high pressure and density and spiral arms have an increased density compared to regions between the arms. This thesis shows variations in the observed dense gas properties with environment. Consequently, we want to understand *how* the large-scale environment is able to impact the dense gas by probing various physical conditions present within those environments. In Chapter 6, I explore the connection between both extragalactic and Galactic dense gas tracers and surface densities of molecular gas mass ($\Sigma_{\rm mol}$), SFR ($\Sigma_{\rm SFR}$), stellar mass (Σ_*) and estimates of dynamical equilibrium pressure ($P_{\rm DE}$) and velocity dispersion ($\sigma_{\rm CO}$). Those parameters are vital measurements of the physical conditions of the disk: $\Sigma_{\rm mol}$ is often used as direct probe of the volume density of the molecular gas and long thought to be the main driving mechanism which sets the amount of dense gas within galaxy disks. Therefore, we assume that line ratios between dense and bulk molecular gas (i.e. HCN/CO) are able to trace the average cloud (volume) density $\rho_{\rm cloud}$:

$$\frac{I_{\rm HCN}}{I_{\rm CO}} \propto \rho_{\rm cloud} \tag{11}$$

As star formation is fueled by the dense molecular gas (Section 2.1.2), a tight link between dense gas emission and $\Sigma_{\rm SFR}$ is expected, and is seen across galaxies by the Gao-Solomon relation. In the modern picture of molecular cloud evolution, the onset of star formation occurs only a few Myrs after the formation of dense gas, linking those evolutionary stages tightly with each other. Σ_* describes to first order the stellar gravitational potential and influences the accumulation of molecular gas in this potential well to some degree (when ignoring secondary effects such as stellar feedback and dynamical effects). A combination of $\Sigma_{\rm mol}$ and Σ_* is provided by $P_{\rm DE}$, a measure of the midplane pressure that acts on the gas and maintains hydrostatic balance in the midplane of the galaxy. The combination of $\Sigma_{\rm mol}$ and $\sigma_{\rm CO}$ reveals the internal pressure indicative of the cloud internal support against collapse.

Recent studies have shown a close connection between HCN/CO and both $\Sigma_{\rm mol}$ and $P_{\rm DE}$ (e.g., Jiménez-Donaire et al., 2019; Neumann et al., 2024; Schinnerer and Leroy, 2024). As there are many caveats in the calculation of $\Sigma_{\rm mol}$, $P_{\rm DE}$ is sometimes suggested as a more reliable estimate of the gas density (Jiménez-Donaire et al., 2019).

My results in Chapter 6 reveal: No two dense gas tracers show the same emission pattern for all environments and physical conditions. There are variations in the emission of those dense gas tracers with Σ_*, $\Sigma_{\rm mol}$, $P_{\rm DE}$ and galactocentric radius (e.g.,

Figure 41). While N_2H^+ expectedly depends more steeply on Σ_{mol}, we find variations even among HCN, HNC and HCO^+, which – based on their theoretical critical densities – should perform similarly (e.g., Figure 37 & 36). Line ratios between HCN and CO, commonly used to gauge the fraction of dense gas are nearly independent of Σ_{mol} and P_{DE} in M51. In some environments such as the center of M51, those quantities are even anti-correlated (Figure 40 & 43). This means HCN emission performs similarly in tracing the gas surface density as does the bulk (and not dense gas) tracer CO. This is in **clear contrast** to the expectations based on lower-resolution studies from other galaxies. Further, this is in contrast to recent 260 pc scale observations by Neumann et al. (2024) that find HCN/CO to be well correlated with Σ_{mol} particularly in the center of the strongly barred galaxy NGC 4321, which also hosts an AGN similar to M51.

While there are some mechanisms that might elevate the emission of HCN without changes in gas density, I, surprisingly, find that the other dense gas tracers perform only moderately better. Ratios of HNC, HCO^+ and N_2H^+ with CO as function of Σ_{mol} are comparably flat and the scatter is much larger than when comparing those lines with physical parameters such as Σ_{SFR} or Σ_*.

What could be causing those discrepancies to the decade of literature results?

a) Resolution: Kiloparsec-scale studies of HCN in M51 have not revealed the peculiar behavior that my cloud-scale data shows, but instead find HCN/CO to be well correlated with Σ_{mol}. With improved resolution, not only does the scatter increase (beyond an increased scatter due to lower SNR), but the distribution of emission from the bright center in M51 is better resolved. At ~ 100 pc, we might be resolving the individual evolutionary stages of giant molecular clouds, with the separation being boosted by the density wave spiral arms. In M51, I find that dense-to-bulk ratios are only weakly correlated with gas mass surface density, and are more strongly correlated with Σ_{SFR}, albeit they cannot be described by a single slope. As the timescales between the dense gas formation and the onset of star formation is thought to be short ($\sim 1-3$ Myr Schinnerer and Leroy, 2024) in comparison to a cloud's total lifetime, this is in agreement with my results. However, neither Σ_{SFR} nor Σ_{mol} alone is sufficient in describing the observed dense-to-bulk ratio. If the dense gas is not (only) tracing gas density, what else is it sensitive to?

b) Tracers of gas density and other conditions: Another, even more simple explanation might be that the fraction of dense gas is not solely set by gas density but depends on other physical parameters as well. Equation 11 assumes that the gas density directly relates to an increased emission of certain molecules. Studies in clouds in the Milky Way have found that additional excitation mechanisms can increase the emission from molecules without changing the gas density. Yet, it was unclear how pronounced these excitation effects are in the context of entire cloud populations within galaxies. The fact that my results show clear differences to other galaxies at slightly worse resolution (Neumann et al., 2024) indicates that the host galaxy indeed is able to set the conditions for star formation by impacting entire populations of clouds. Asymmetries in the star formation efficiency between M51's two spiral arms (e.g., Appendix C.4, Figure 65), that can not be explained by the gas chemistry, peculiar regions within the disk (Figure 56) and the puzzling center of M51 (e.g., Figure 44) are only few of the emerging questions that showcase, that we have not yet fully understood our "dense-gas tracers".

7.4 CONCLUDING REMARKS

While many observations within the Milky Way resolve the structures and star formation within clouds at unprecedented resolutions, the universality of those results might be in question if they are not correctly placed in their environmental context. The Milky Way Central Molecular Zone might be just one example of many.

This thesis shows that the presence of dense gas alone is not sufficient in explaining star formation. Several factors, from chemical to dynamical, impact different tracers of dense gas differently and need to be considered to obtain a more universal picture on star formation that holds at cloud-scales.

7.4.1 M51 in the context of galaxy evolution

M51a and M51b appear as a complex merging system compared to many other nearby (non-merging) galaxies. Yet, in the universal pool of galaxies, this system and its conditions are typical for the earlier universe with frequent mergers of gas-rich galaxies and triggered star-formation conditions. Due to its proximity and brightness, the dynamics in M51 is superbly studied, making it an ideal bridge to the higher redshift star formation processes. With a constantly increasing but yet sparse amount of dense gas observations from higher redshift galaxies (e.g., Rybak et al., 2022), M51 might be a first glimpse into higher redshift star formation conditions.

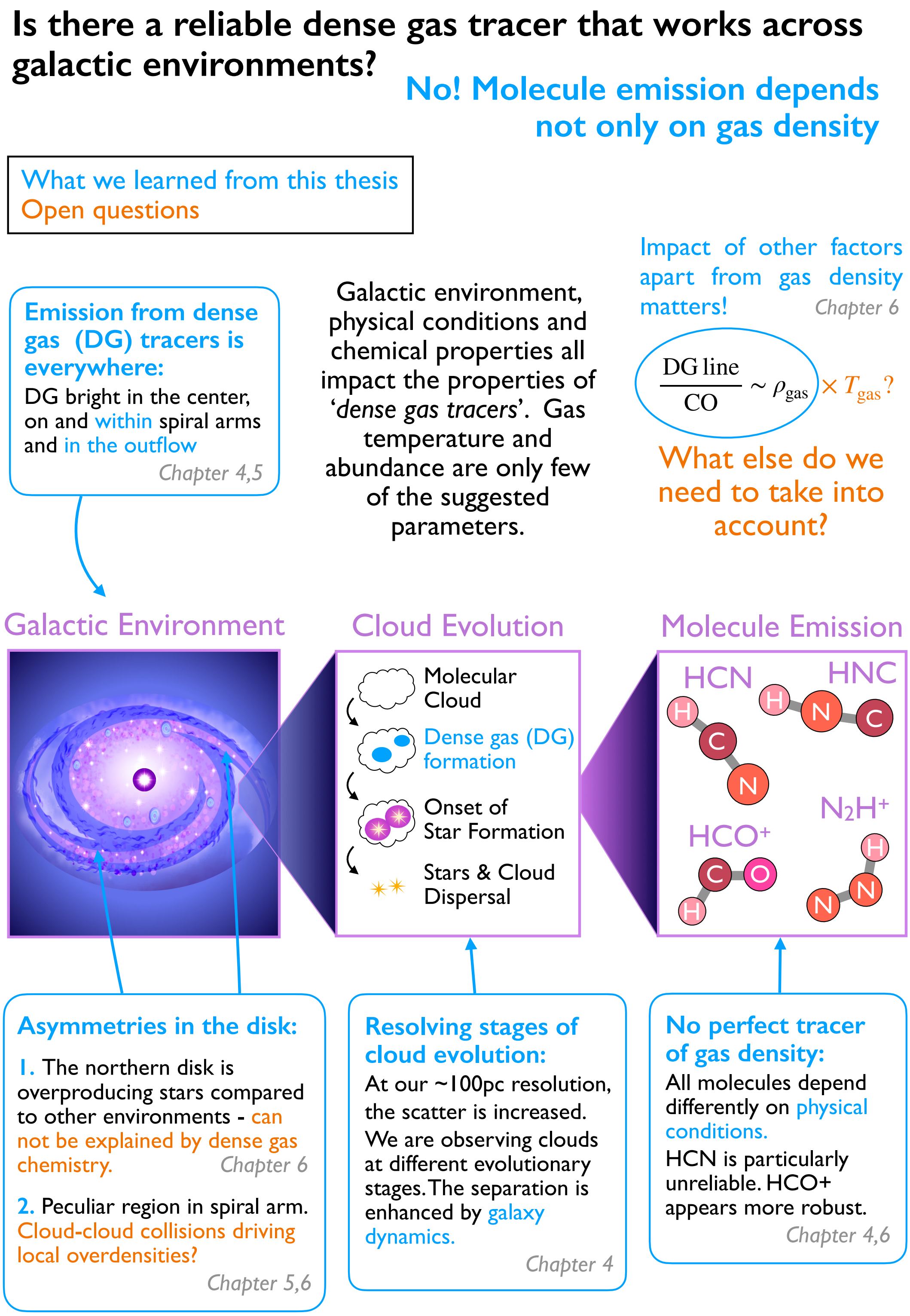

Figure 47: Summary of this thesis. This Figure is based on Figure 1, which motivated and outlined the thesis, I highlight the results (black and blue) and open questions (orange) emerging from this thesis.

8 FUTURE DIRECTIONS

Reliably accessing dense gas is crucial for our understanding of star formation processes from the presence to the early universe. As this thesis shows, there are conditions within galaxies in which common dense gas tracers loose their universality. Among the many open questions emerging from this work, we highlight a few possible future directions.

8.1 COMPLETING THE VIEW ON THE DENSE PHASE OF MOLECULAR GAS IN M51

We are at the brink of completing the view of the astrochemical and physical conditions within M51. Two paths forward are provided by a) improving our understanding of the bulk molecular gas distribution the dense gas is usually contrasted with (i.e., via a more detailed analysis of the CO isotopologues, see Galic et al, submitted; den Brok et al., 2025) and b) studying alternative tracers of the dense molecular gas phase, such as CN and CS:

An alternative approach to access the dense gas distributions is provided by the molecule CN, which is nearly as bright as HCN (Wilson et al., 2023) and observable with NOEMA. I recently proposed to observe both molecules with the IRAM NOEMA and 30m telescopes at $\sim 100\,\mathrm{pc}$ resolution to complement the SWAN data set. Recent studies reported a tight correlation of CN(1-0) emission with column density (Ledger et al., 2024), and between HCN and CN (Wilson et al., 2023), making CN a promising candidate dense gas tracer in nearby galaxies. As the CN(1-0) transition has two bright groups of hyperfine transitions, these can be directly used to estimate the optical depth of the gas (i.e., Skatrud et al., 1983; Tang et al., 2019; Ledger et al., 2024). CN is suggested as tracer of UV-illuminated gas (Gratier et al., 2017; Bron et al., 2018; Wilson et al., 2023) but also cosmic ray ionization rates (Boger and Sternberg, 2005), making CN a vital measure of physical conditions not yet probed by the other molecules targeted by the SWAN survey. As the frequencies of both CN(1-0) groups are very close to the CO(1-0) line, CN is a particularly interesting dense gas tracer for other galaxies, as emission from both molecules can be observed simultaneously. In M51, I can test and calibrate the utility of CN as dense gas tracer, which then will pave a better understanding of the astrochemical processes in other galaxies.

8.2 AN INDEPENDENT TEST USING THE DUST-TO-GAS RATIO, VIA PAH EMISSION AT 7.7µM

Dust is a major component in the ISM, which efficiently regulates its thermal and ionization balance (Sutter et al., 2024). As dust is ubiquitously filled with Polycyclic Aromatic Hydrocarbons (PAHs), those large planar molecules are key in accessing and understanding the dust distribution. PAH produce emission features that can dominate a galaxy's near- and mid-infrared spectra (Sutter et al., 2024). Most prominent are emission features at wavelengths of $\sim 6 - 12\mu$m, which occur after the dust grain absorbs ultraviolet photons energetic enough to excite their vibrational transitions. As JWST is able to capture these PAH emission features, recent observations with this telescope have imaged the dust distribution at unprecedented resolution in nearby galaxies (e.g., Lee et al., 2023). Particularly, the PAH emission has been suggested as a measure of column densities independent of the bulk molecular gas tracer CO (Leroy et al., 2023). Recent observations of M51 with JWST as part of the M51 Treasury program (PIs: D. Dale, K. Sandstrom) will allow me to investigate dust-based column densities. Since M51's center is nearly devoid of CO emission, but shows abundant emission in both JWST and SWAN images (compare Fig. 48), I expect JWST-based column densities to differ from those based on CO. Additionally, I can compare molecular gas emission to the fraction of PAH-to-total-dust mass (by using JWST (F770W+F1130W)/F2100W Sutter et al., 2024) and estimate star formation rates at unprecedented resolution (Calzetti et al in prep.). With those, I can explore the Gao-Solomon relation and shed light on how the star formation per unit gas compares to other galaxies and clouds. The sensitivity of the PAH grains to the interstellar radiation field (Dale et al., 2025) will provide further constraints on the underlying physical conditions of the ISM.

8.3 IN DEPTH VIEW OF INDIVIDUAL REGIONS AND MOLECULAR CLOUD PROPERTIES

This thesis presents only a small part of the scientific questions that can be explored with the SWAN data set. The following highlights some directions to gain a deeper understanding of M51, and how its individual environments and molecular clouds are linked.

Outflow and AGN: This includes an in-depth study of the nuclear outflow and AGN (Usero et al in prep., Thorp et al in prep.). As an example, the existing vast ancillary optical data allows for a clear characterization of the excitation sources of the ionized gas (i.e., radiation by the AGN supermassive black hole, by star-forming regions and shocks) which can be directly linked to variations in molecular line ratios seen in SWAN (Chapter 6). Further spectral decomposition of the molecular line emission tracer by SWAN can improve the separation of material associated with the AGN outflow from that in the disk allowing for characterization of the conditions in the outflowing gas. Additional ongoing SWAN follow-up observations of SWAN molecular lines in the very center of M51 at 25 pc resolution will provide an in-depth view of the AGN feedback.

Offsets in the spiral arms: As seen in Chapter 6, line ratios between dense gas lines and CO seem to increase azimuthally across the spiral arms. In the classical picture of a density wave spiral arm, (Section 2.1.3,3.1.1), this offset between bulk and

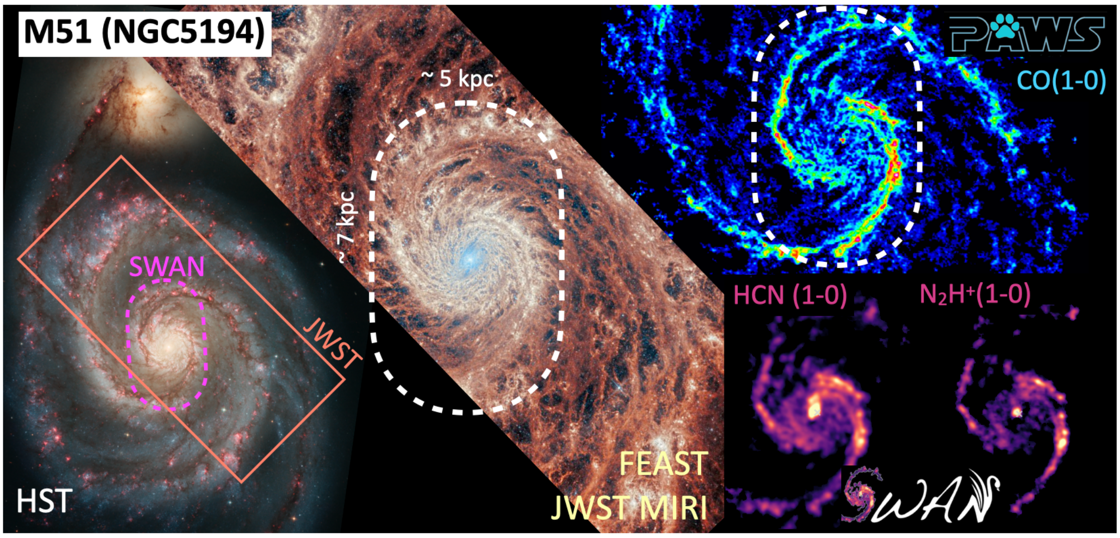

Figure 48: Multiwavelength view of the Whirlpool galaxy (M51, NGC5194). ***Left:*** HST color composite image *Image credit:* NASA, ESA, and the Hubble Heritage Team (STScI/AURA). ***Middle***: Dust emission captured by JWST-MIRI filter (FEAST survey, Feedback in Emerging extrAgalactic Star clusTers, PI:Adamo) *Image credit:* ESA/Webb, NASA & CSA, A. Adamo (Stockholm University) and the FEAST JWST team. The same area is observed with JWST MIRI+NIRCam+NIRSpec (Treasury project: PIs: Sandstrom & Dale). The elliptical region indicates the SWAN FoV (5x7kpc^2). ***Right***: Molecular gas observations of PAWS CO(1-0) observations (top right panel) at 1″ (40 pc) resolution (Schinnerer et al., 2013) and 3″ (125 pc) resolution observations of selected dense gas tracing molecular lines from this thesis from the molecular multi-line survey SWAN).

dense molecular gas might be expected: The co-rotation radius of the two grand-design spiral arms in M51 is located at $r_{CR} \sim 4$ kpc (Querejeta et al., 2016a), and includes most of the SWAN FoV. Within this radius, we expect the spiral to move at lower speed compared to the gas and stars, therefore, the gas and stars will overtake the spiral arm pattern. With the compression of gas being initiated once the molecular gas accumulates in the potential well, this can – in a simplistic picture – lead to an offset between dense and bulk molecular gas. Whether this ideal picture actually holds or whether additional effects dominate (e.g., streaming motions along the spiral arms, stellar feedback, shocks), needs to be tested and can be tested for the first time with N_2H^+ (Greve et al. in prep). By isolating the spiral arms one by one with masks (e.g., Querejeta et al., 2021), we can study the offsets of the dense gas compared to bulk gas across the width of each spiral arm and further compare this to tracers of star formation.

Molecular cloud properties: While the pixel-based approach used in this thesis does not require any assumptions on the (generally disputed) geometry of the molecular clouds in the disk, it is a common approach to dissect the molecular gas distribution into individual molecular clouds by using algorithms such as `PyCPROPS` (Rosolowsky and Leroy, 2006). This algorithm – which has been applied to the bulk gas in M51 (Colombo et al., 2014a) – can be applied to the denser gas as well to measure key parameters such as radii, masses and virial parameter of the cloud population (Bigiel et al. in prep). Those give insights into the boundedness of the gas, and common scaling relations such as the Larson (Larson, 1981) or Heyer-Keto-relation (Keto and Myers, 1986; Heyer et al., 2009).

8.4 BRIDGING GALAXY CONDITIONS

As an actively star-forming main-sequence galaxy with an AGN, M51 presents a unique opportunity for studying molecular chemistry in the presence of an interacting companion galaxy. My study has revealed systematic variations between galactic environments, and hints to physical conditions responsible for these. In order to further quantify the importance of these conditions, large samples of different environments are needed. While there is a sparse set of approximately cloud-scale observations of dense gas tracers in selected environments in other galaxies, such as the barred galaxy NGC 3627 (Bešlić et al., 2021), multi-line observations in the central ~ 1 kpc of NGC 253 (ALCHEMI survey, Martín et al., 2021; Harada et al., 2024a), or in the center of NGC 1068 (Saito et al., 2022), larger samples are needed. With ALMA and NOEMA, we can continue to map dense gas in individual environments in selected galaxies, such as galaxies with and without bars and with and without AGN to disentangle the effects these features exert on their gas reservoir. However, the very large time investment required to perform these cloud-scale dense gas observations will limit the build up of large (several tens of galaxies) samples. Future facilities such as the *ngVLA*[1]) will then open up a new direction for the time consuming cloud-scale dense gas observations. By reducing the observing time by a factor up to 200 in comparison to current observatories such as ALMA, the *ngVLA* will boost our understanding of the interplay between gas chemistry and galactic environments.

1 Construction planned in 2025, earliest first scientific observations estimated in 2028 `https://ngvla.nrao.edu/news`

APPENDIX

APPENDIX TO CHAPTER 4

A.1 ERROR BEAM CONTRIBUTION

Our test show that the 30m error beams only make a small contribution to the flux filtered out by the interferometer. We can describe the response of the 30m telescope to a point source by a set of 2D Gaussians representing the main beam and a set of error beams. As a result, depending on the morphology of the science target, the measured signal might be boosted by emission from beyond the region the telescope is pointing at as the wider side lobes pick up signals from other parts of the sky. For instance, in the case of M51, den Brok et al. (2022) demonstrated that up to 20% of the ^{12}CO(2–1) emission in the interarm regions (which sit between two brighter spiral arms) can be accounted for by contributions from the error beams. Kramer et al. (2013) provide an approximation of the 30m telescope beam pattern at different frequencies, which we use as a good first-order approximation.

Given a model for the telescope's beam pattern, several deconvolution schemes exist that provide an estimate for the error beam free signal (for example Westerhout et al., 1973; Bensch et al., 1997; Lundgren et al., 2004; Pety et al., 2013; Leroy et al., 2015). To quantify the relevance in the case of the set of lines observed by SWAN, we perform the procedure described in den Brok et al. (2022) for ^{13}CO(1–0), where we expect the effect to be the largest (as the main beam efficiency decreases with increasing frequency).

A.1.1 Mathematical framework

We provide a brief overview of the mathematical framework and the method we use to deconvolve the 30m data to estimate the error beam contribution. For details on the calculations, we refer the reader to den Brok et al. (2022). The key parameters are the observed main beam temperature, $T_{\rm mb}$ (which includes also contributions from the error beam), and the error beam free main beam temperature, $\hat{T}_{\rm mb}$. They are related via a convolution kernel K as follows:

$$T_{\rm mb} = \left(\delta^{2D} + K\right) \otimes \hat{T}_{\rm mb}, \tag{12}$$

where "$\otimes$" represents the 2D convolution operation and δ^{2D} the Dirac 2D distribution. The kernel K contains the sum of all error beam contributions after deconvolution with the main beam.

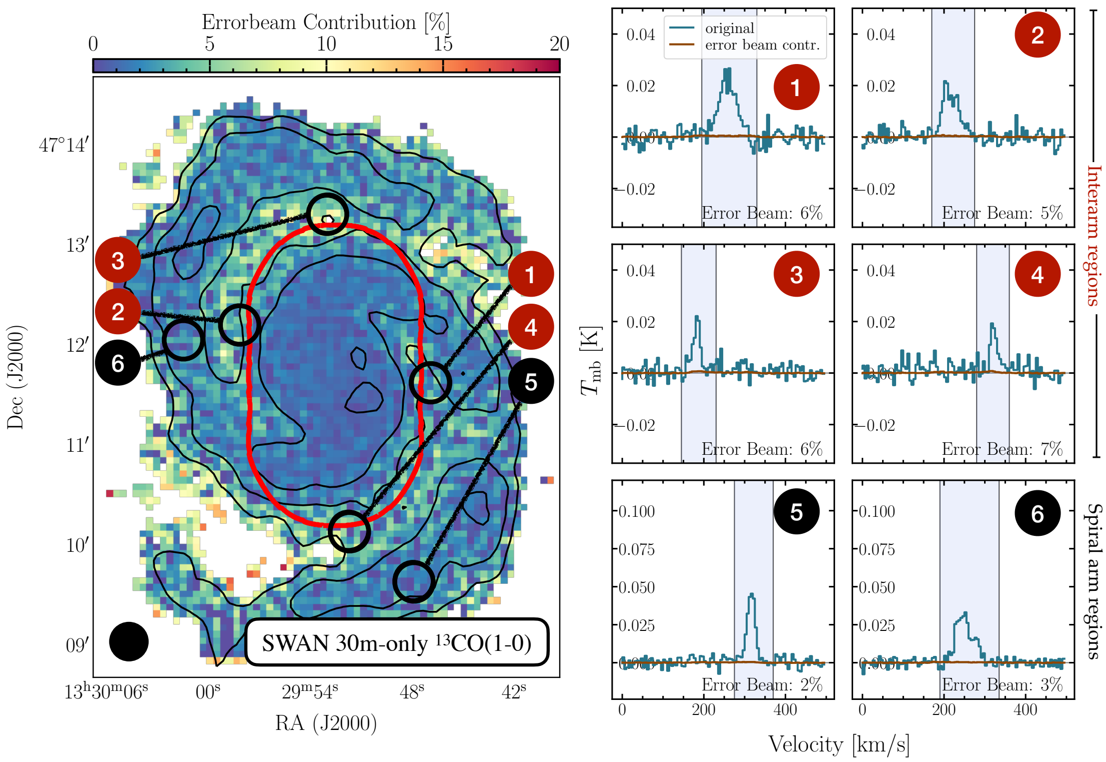

Figure 49: Quantifying errorbeam contributions to the observed ^{13}CO(1–0) emission. (Left) The map presents the percentage errorbeam contribution to individual sightlines for the 30m only data. We only consider sightlines where the integrated ^{13}CO(1–0) brightness temperature is detected at $\gtrsim 3\sigma$. Contours indicate the S/N at 5,10,20, and 50. The red contour illustrates the SWAN FoV. Overall, the error beam contribution is marginal, with elevated values up to 10% within the interarm region (and <5% within the SWAN FoV). (Right) We extract ^{13}CO(1–0) spectra in six individual apertures. Apertures 1–4 are in the interarm region and apertures 5–6 in the spiral arms of M51. Each panel shows the full spectrum which includes the contribution from the error beam in blue. The brown spectrum represents the error beam contribution and was calculated by subtracting the error beam free spectrum from the observed spectrum. The percentage contribution is computed over the spectral range where we detect emission (indicated by the blue-shaded region) and is listed in each panel.

The particular deconvolution, to obtain the error beam free signal, can be expressed using the Fourier Transform operation, $\mathcal{F}$:

$$\hat{T}_{\mathrm{mb}} = \mathcal{F}^{-1}\left(\frac{\mathcal{F}(T_{\mathrm{mb}})}{1+\mathcal{F}(K)}\right) . \tag{13}$$

We perform this calculation in `Python` with the unsupervised Wiener-Hunt deconvolution. This function estimates the hyperparameters automatically (see den Brok et al., 2022).

A.1.2 Error beam contributions for ^{13}CO(1–0)

We present an overview of the resulting deconvolution of the entire ^{13}CO(1–0) SWAN 30m data-only cube in Fig. 49. We compute the contribution, which is the difference between the measured and the error beam free spectrum, for each line of sight where S/N>3 for ^{13}CO(1–0). The error beam contribution is negligible in the center and along the spiral arms, being 2–3%. The value is elevated to around 5–10% in the interarm region. This is expected because when the telescope points to the interarm regions, part of the spiral arm will be covered by the side lobes, boosting the signal via the error beams. In Fig. 49, we also illustrate the effect for spectra extracted within six different apertures, from which four are in the interarm and two in the spiral arm region. The error beam contribution is presented by the brown spectrum in each panel. The percentage contribution is computed within the mask that contains the signal (illustrated in blue). With 6% and 7%, pointings 3 and 4 show the largest contributions in this selection of pointings.

The error beam analysis is subject to uncertainties due to the difficulty of characterizing the variations in the beam pattern with time. However, these calculations provide a reasonable upper limit for the order of magnitude of the error beam contribution. The contribution remains <10% for the vast majority (i.e., 98%) of sightlines. Within the NOEMA SWAN FoV, the median error beam contribution is 1.5% per pixel. As power within the side lobes decreases with decreasing frequency, the effect will be even less significant for the other lines, such as HCN and N_2H^+.

A.2 CONSISTENCY TESTS OF THE ARCHIVAL AND NEW SWAN 30M DATASETS

For this comparison, both the SWAN and EMPIRE 30m data were processed in the same way using the EMPIRE pipeline (see Jiménez-Donaire et al., 2019). The raw spectra were first calibrated to antenna temperatures scale using the nearest chopper-wheel calibration scan. After this, each observed line was extracted using the CLASS package. For each individual line of sight for which a spectrum is extracted, we subtracted a zeroth-order baseline, regridded the spectrum to a $4\,\mathrm{km\,s^{-1}}$ channel width, and wrote them out as FITS tables. The spectra were then processed with an IDL procedure that allows us to flag and discard pathological data. We then fit a baseline excluding a velocity window determined from the much brighter mean CO (1-0) emission, to avoid including channels that potentially contain signal. In addition, two more windows adjacent to the central one were included to fit a second-order polynomial baseline, which was then subtracted from the entire spectrum. The final spectra were

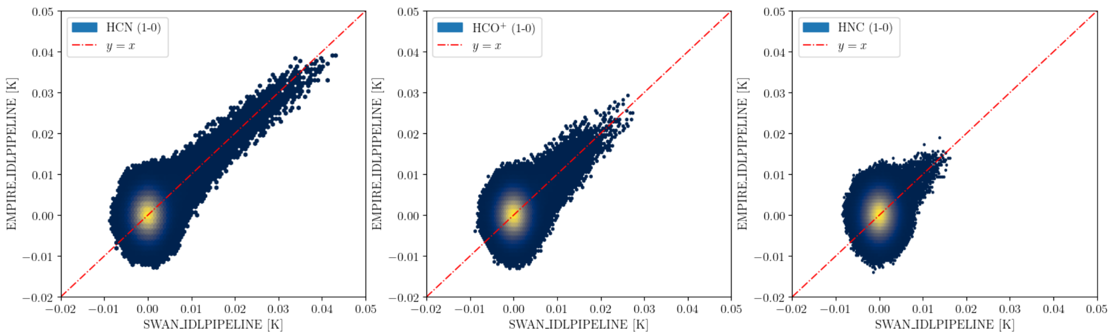

Figure 50: Pixel-by-pixel comparison of the HCN (1-0), HCO^+ (1-0), and HNC (1-0) data cubes obtained with SWAN and EMPIRE IRAM-30m observations. The red line indicates a 1-1 correlation between the EMPIRE and the SWAN datasets. Both single-dish datasets are processed with the EMPIRE pipeline for comparison and overall agree with each other.

then sorted according to their measured rms on the line-free windows, relative to the expected value from the radiometer equation, and the highest 10% were rejected (see Jiménez-Donaire et al., 2019, for a detailed description of each step in the pipeline). Finally, all data corresponding to each spectral line were gridded into a cube. We then convolved each data cube to a common working resolution of 33″, using a Gaussian kernel.

Figure 50 shows a comparison between the main dense gas products obtained with SWAN and EMPIRE 30m observations, processed using the EMPIRE pipeline described above. These include the main lines HCN (1–0) (left panel), HCO^+(1–0) (middle panel), and HNC (1–0) (right panel). The red line indicates a 1-1 correlation between the EMPIRE and the SWAN datasets. As can be seen from the figure, both datasets agree well for the three different lines. We quantify this by calculating the relative sum of all differences between both datasets. We find that the HCN (1–0), HCO^+(1–0), and HNC (1–0) measurements agree between EMPIRE and SWAN within 1%, 7%, and 12%, respectively.

A.3 COMPARISON OF MOMENT MAP INTEGRATION TECHNIQUES

Given both the `GILDAS` and PyStructure methods are useful for different analysis, we aim to confirm a general agreement between both methods. To do so, we re-grid the ^{13}CO moment-0 map produced with `GILDAS` and has rectangular pixels, to match the hexagonal pixels of the moment-0 map produced with the PyStructure code. This is done using parts of the PyStructure code. Figure 53 shows the emission in each hexagonal pixel from the re-gridded `GILDAS`-moment-0 map compared to that from the moment-0 map that was inherently produced with the PyStructure code. The moment maps generated by the `GILDAS` method recovers about 25% more flux than the Pystructure method (Fig. 53). The median flux difference between both maps is 0.9 $\mathrm{K\,km\,s^{-1}}$ with 16$^{\mathrm{th}}$ and 84$^{\mathrm{th}}$ percentiles of 0.3 and 2.1 $\mathrm{K\,km\,s^{-1}}$. For pixels at high intensities, both methods agree well. The PyStructure method is more conservative and misses broader linewings. As the PyStructure table used for the scientific analysis in this paper is based on ^{12}CO and HCN as priors (see above), we do not expect to miss any significant emission.

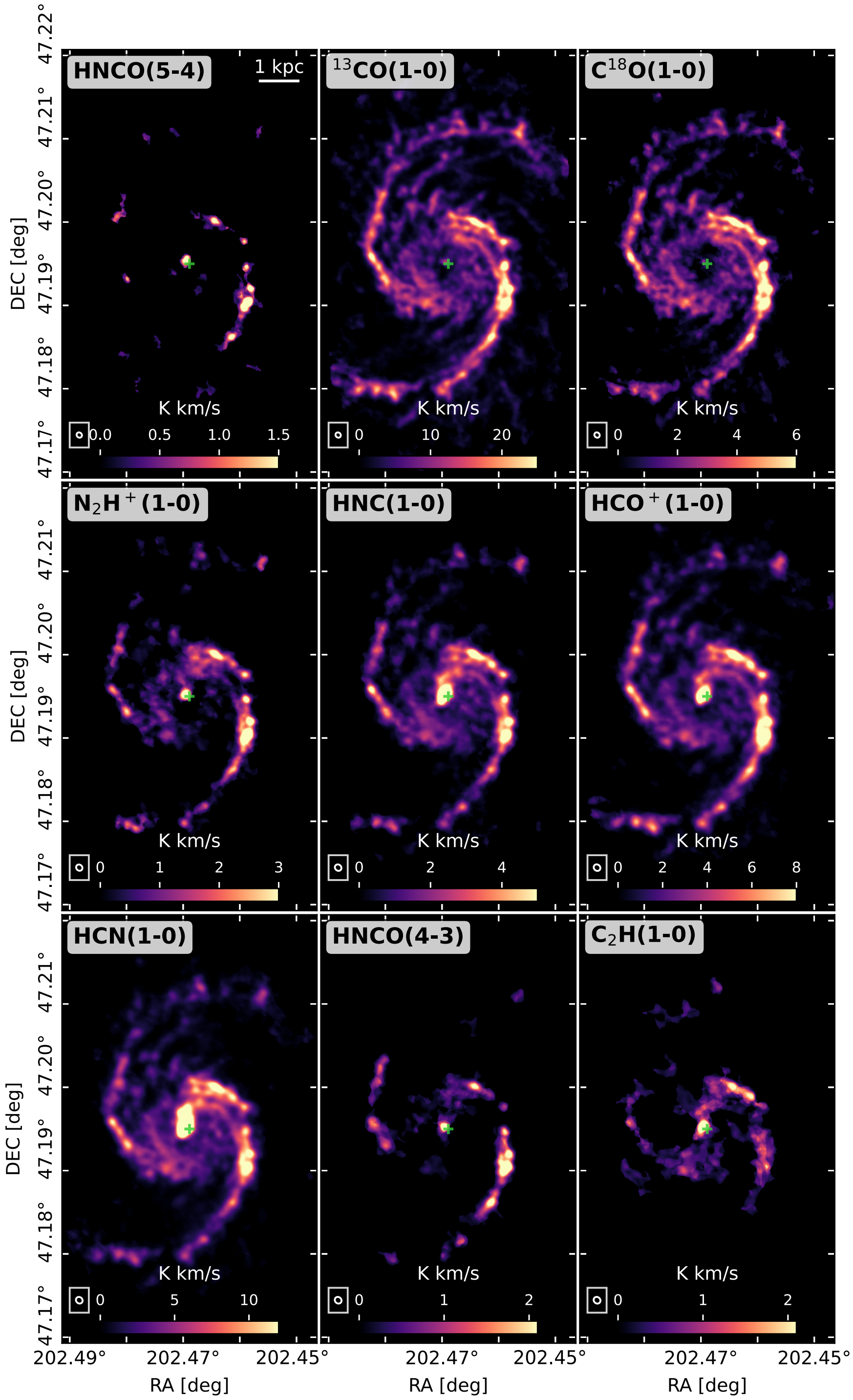

Figure 51: Integrated intensity maps (moment-0) of the SWAN dataset (combined NOEMA and IRAM 30m observations) for the J=1–0 transitions of ^{13}CO, C^{18}O, N$_2$H$^+$, HCO$^+$, HNC, HCN, C$_2$H(1–0 and HNCO(J=4–3) plus HNCO(J=5–4) at their native angular resolution ($\sim 2.3 - 3.1''$). The maps were created with the `GILDAS` Island-method. We show the beam size in the bottom of all panels as well as a 1 kpc scale bar in the top left panel.

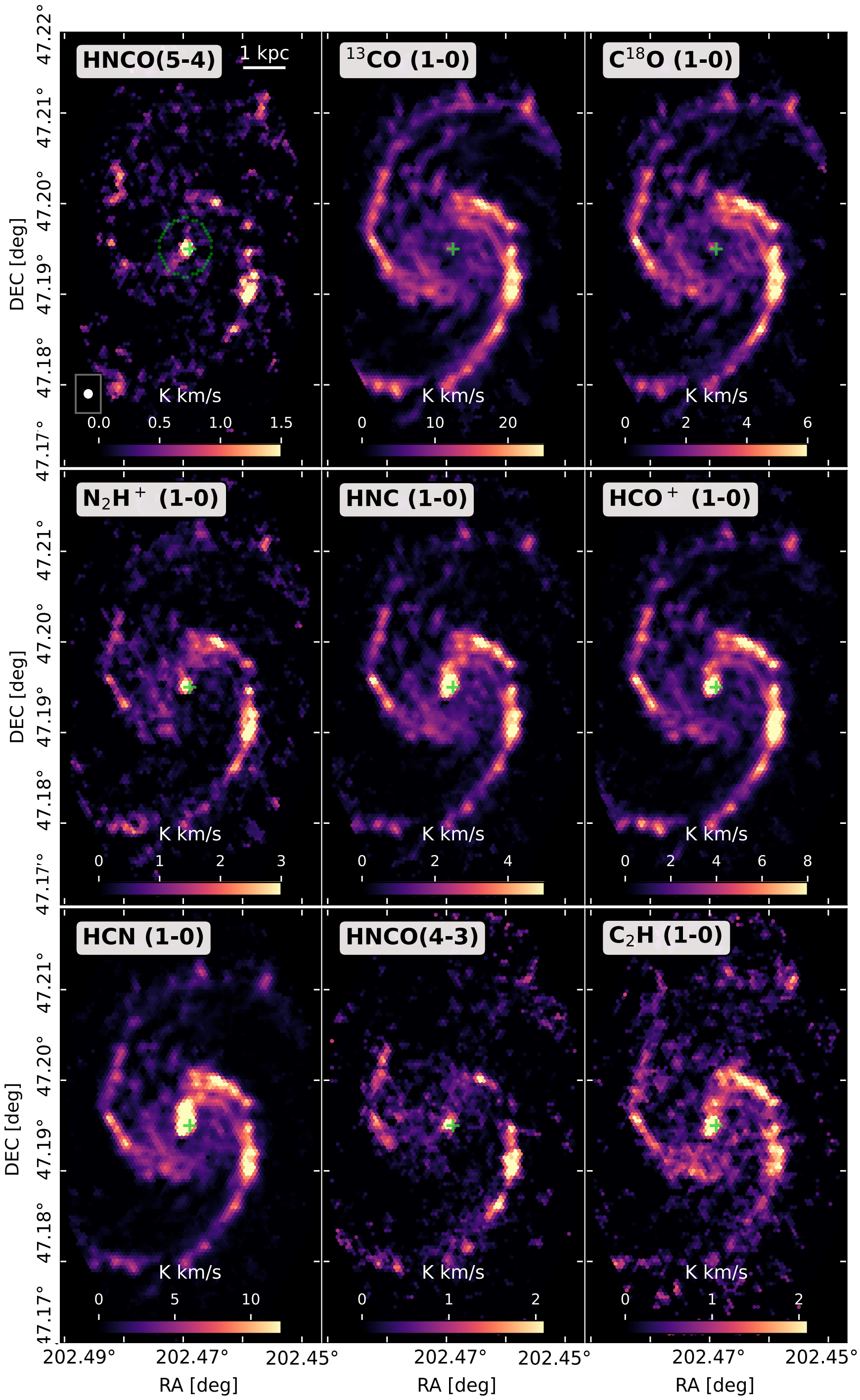

Figure 52: Integrated intensity maps (moment-0) of the SWAN dataset (combined NOEMA and IRAM 30m observations) for all detected lines at a common resolution of 3″ (125 pc). The data is binned with hexagonal spacing with the `PyStructure` code (den Brok et al., 2022; Neumann et al., 2023b). Spectral windows for the creation of the moment maps are selected based on significant detections of ^{12}CO emission from PAWS (Schinnerer et al., 2013) and HCN(1-0) emission. We show the beam size, a 1 kpc scale bar and mark the central 1 kpc circular area (green points) in the top left panel. The intensity scale is the same as in Fig. 51.

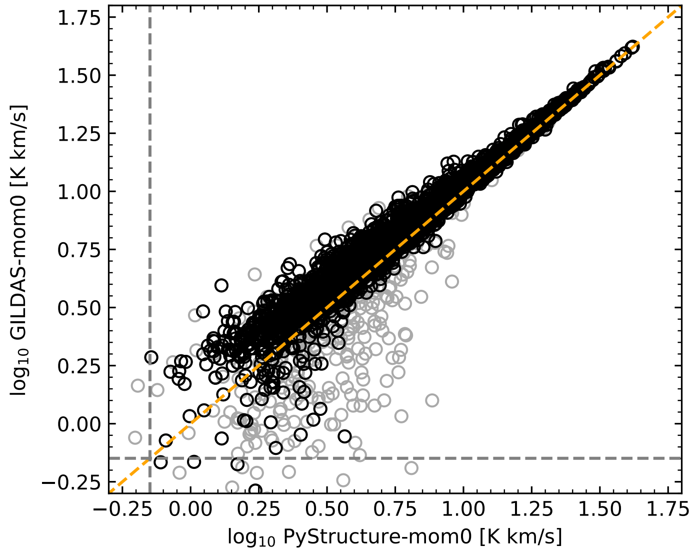

Figure 53: Pixel-by-pixel comparison of the obtained integrated line emission using two different methods for the 10 km s^{-1} resolution ^{13}CO data cube at native angular resolution. We show pixels located inside (black circles) and outside (gray circles) the hull of the mosaics (compare this with Fig. 17). We show the 1:1 relation (dashed orange line). We mark the average 5σ noise level for both lines (dashed gray line). We note that due to logarithmic spacing, data points containing noise with negative fluxes are not visible. Although this applies to most data points in the interarm region near the edges of our FoV, we emphasize that this comparison is intended to assess how both methods handle regions with significant detected emission, as these areas are typically the focus of scientific analysis. Regions with significantly detected emission is found mostly in the center, the molecular ring, and on the spiral arms.

A.4 AVERAGE LOGARITHMIC LINE RATIOS IN COMPARISON

We list mean logarithmic line ratios (b) from Fig. 22 (Sect. 4.4.1) for all detected lines in Table 13. b was calculated between two lines (line x and line y) in pixels where both lines are significantly detected ($> 3\sigma$). b is defined as $b = \text{mean}\left(\log_{10}(y/x)\right)$, with x and y referring to the values on the x and y axes from line x and line y, respectively. Additionally, we provide b_{cen} and b_{disk}, which is the same calculation performed on pixels inside and outside the central 1 kpc, respectively. To estimate how strong the central effects on the line ratios are, we calculate $\sigma_{\text{cen-disk}}$, which is the significance of the difference of b_{cen} and b_{disk}, defined as $\sigma_{\text{cen-disk}} = \frac{b_{\text{cen}} - b_{\text{disk}}}{\sqrt{\Delta b_{\text{cen}}^2 + \Delta b_{\text{disk}}^2}}$. There are only very few pixels with significant HNCO(5-4) detections, which might bias the calculation of $\sigma_{\text{cen-disk}}$.

With this, we find the following: The most extreme difference ($\sigma_{\text{cen-disk}} > 50$) in mean logarithmic line ratios between center and disk can be found for HCN and ^{13}CO, as well as for HNC and ^{13}CO. This is followed by line ratios between HCN and HCO$^+$, HCN and C^{18}O, HNC and C^{18}O, HCO$^+$ and C^{18}O, C$_2$H and C^{18}O ($30 < \sigma_{\text{cen-disk}} < 50$). The most extreme differences are therefore seen between the ^{12}CO isotopologs and most other lines. This is consistent with the visual lack of ^{13}CO and C^{18}O emission compared to all other detected lines in the galaxy center seen in Fig. 52.

Most other line combinations have significantly different line ratios in the center compared to the disk, but with a lower value of $\sigma_{\text{cen-disk}} < 30$. For HCN, the strongest offset relation between center and disk is with C^{18}O emission, the weakest with isomer HNC and the faint HNCO(5-4) line.

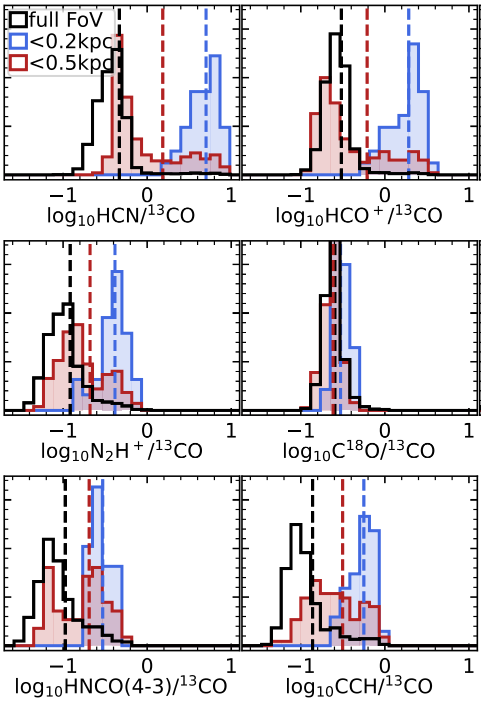

Figure 54: Same as Fig. 23 but for line ratios with ^{13}CO (1-0).

Line combinations that do not exhibit a clear offset relation between center and disk are N_2H^+ and HCO^+, $C^{18}O$ and ^{13}CO, and combinations including the HNCO and C_2H lines. All line combinations with ^{13}CO show a significant offset relation between center and disk, with the only exception being the other ^{12}CO isotopolog, $C^{18}O$.

A.5 ^{13}CO LINE RATIOS

We show histograms of line ratios with ^{13}CO emission in the full FoV, central 1 and 0.4 kpc (diameter) in Fig. 54. In agreement with the ^{12}CO line ratios (Fig. 23), we see the same qualitative behavior: Line ratios in the center are increased for all lines except the isotopolog $C^{18}O$. This increase is even stronger for the smaller (0.4 kpc) aperture for HCN, HNC, HCO^+, N_2H^+, and C_2H. We note that the average distribution of the HNCO(5-4)/^{13}CO line does not vary much between 1 and 0.4 kpc. As the HNCO(5-4) emission is only detected in few pixels in the very galaxy center, both histograms might depict the same information.

Table 13: Average logarithmic line ratios in comparison

line x (1)	line y (2)	b_{all} (3)	b_{cen} (4)	b_{disk} (5)	$\sigma_{cen-disk}$ (6)
N_2H^+(1-0)	HCN(1-0)	0.651±0.003	0.831±0.009	0.625±0.004	21
N_2H^+(1-0)	HNC(1-0)	0.273±0.004	0.377±0.010	0.257±0.004	11
N_2H^+(1-0)	HCO^+(1-0)	0.488±0.003	0.476±0.010	0.489±0.004	1.3
N_2H^+(1-0)	HNCO(5-4)	-0.249±0.011	-0.108±0.028	-0.275±0.012	6
N_2H^+(1-0)	HNCO(4-3)	-0.141±0.007	-0.151±0.020	-0.140±0.007	0.5
N_2H^+(1-0)	C_2H(1-0)	0.003±0.006	0.093±0.015	-0.012±0.007	6
N_2H^+(1-0)	^{13}CO(1-0)	0.983±0.003	0.771±0.009	1.013±0.003	25
N_2H^+(1-0)	$C^{18}O$(1-0)	0.395±0.004	0.196±0.012	0.420±0.004	18
HCN(1-0)	HNC(1-0)	-0.397±0.002	-0.440±0.005	-0.391±0.002	9
HCN(1-0)	HCO^+(1-0)	-0.160±0.002	-0.395±0.005	-0.136±0.002	48
HCN(1-0)	HNCO(5-4)	-0.872±0.010	-1.074±0.022	-0.831±0.011	8
HCN(1-0)	HNCO(4-3)	-0.769±0.005	-1.080±0.016	-0.730±0.006	21
HCN(1-0)	C_2H(1-0)	-0.674±0.004	-0.801±0.010	-0.652±0.005	13
HCN(1-0)	^{13}CO(1-0)	0.419±0.001	0.045±0.003	0.454±0.002	117
HCN(1-0)	$C^{18}O$(1-0)	-0.201±0.002	-0.496±0.007	-0.173±0.002	46
HNC(1-0)	HCO^+(1-0)	0.219±0.002	0.047±0.006	0.242±0.002	29
HNC(1-0)	HNCO(5-4)	-0.517±0.010	-0.609±0.024	-0.497±0.012	4
HNC(1-0)	HNCO(4-3)	-0.400±0.006	-0.608±0.016	-0.372±0.006	14
HNC(1-0)	C_2H(1-0)	-0.280±0.005	-0.335±0.011	-0.270±0.005	5
HNC(1-0)	^{13}CO(1-0)	0.774±0.002	0.469±0.005	0.816±0.002	68
HNC(1-0)	$C^{18}O$(1-0)	0.168±0.003	-0.074±0.008	0.196±0.003	32
HCO^+(1-0)	HNCO(5-4)	-0.740±0.010	-0.675±0.024	-0.754±0.011	3.0
HCO^+(1-0)	HNCO(4-3)	-0.620±0.005	-0.672±0.016	-0.614±0.006	3.4
HCO^+(1-0)	C_2H(1-0)	-0.473±0.005	-0.414±0.011	-0.483±0.005	6
HCO^+(1-0)	^{13}CO(1-0)	0.567±0.002	0.422±0.005	0.582±0.002	30
HCO^+(1-0)	$C^{18}O$(1-0)	-0.043±0.002	-0.126±0.008	-0.036±0.002	11
HNCO(5-4)	HNCO(4-3)	0.119±0.013	-0.058±0.033	0.147±0.014	6
HNCO(5-4)	C_2H(1-0)	0.126±0.014	0.228±0.029	0.104±0.015	3.8
HNCO(5-4)	^{13}CO(1-0)	1.086±0.010	0.636±0.023	1.175±0.011	21
HNCO(5-4)	$C^{18}O$(1-0)	0.515±0.011	0.062±0.029	0.597±0.012	17
HNCO(4-3)	C_2H(1-0)	0.102±0.009	0.272±0.023	0.072±0.010	8
HNCO(4-3)	$C^{18}O$(1-0)	0.490±0.006	0.262±0.022	0.512±0.006	11
HNCO(4-3)	^{13}CO(1-0)	1.058±0.005	0.780±0.016	1.092±0.005	18
C_2H(1-0)	^{13}CO(1-0)	0.953±0.004	0.608±0.011	1.012±0.005	35
C_2H(1-0)	$C^{18}O$(1-0)	0.384±0.005	0.083±0.015	0.422±0.005	21
^{13}CO(1-0)	$C^{18}O$(1-0)	-0.611±0.002	-0.626±0.007	-0.610±0.002	2.3

Offset b from Fig. 22 for pixels where both lines (line x and line y) are significantly detected. We define $b = \text{mean}\left(\log_{10}(y/x)\right)$ with x and y referring to the values on the x and y axes from line x and line y, respectively. We calculate b for pixels where both line x and line y are significantly detected in the full FoV (3), the central 1 kpc (4), and the remaining disk excluding the central 1 kpc (5). We add the significance of the difference of b calculated in the center compared to the disk. We define it as $\sigma_{cen-disk} = \frac{b_{cen}-b_{disk}}{\sqrt{\Delta b_{cen}^2+\Delta b_{disk}^2}}$. Values including HNCO(5-4) should be taken with caution, as this line is only significantly detected in very few pixels in the FoV.

APPENDIX TO CHAPTER 5

B.1 DATA

We utilized observations from the IRAM large program LP003 (PIs: E. Schinnerer, F. Bigiel) that used the Northern Extended Millimetre Array (NOEMA) and 30m single dish to map the 4-3 mm line emission from the central 5×7 kpc of the nearby galaxy M 51. The observations, data calibration and imaging resulting in our final datasets are briefly described below.

B.1.1 NOEMA data

NOEMA observations were taken with 9-11 antennas between January 2020 and December 2021, resulting in a total of 214 hours under average to excellent observing conditions with an average water vapor of $\sim$ 4 mm split across C (59%; 126h) and D (41%; 88h) configuration. Observations of the phase and amplitude calibrators (J1259+516 and J1332+473, replaced by 1418+546 if one of the two was not available) were executed every $\sim$ 20 minutes. The mosaic consists of 17 pointings in a hexagonal grid. Data reduction was carried out using the IRAM standard calibration pipeline in GILDAS (Gildas Team, 2013). Average to excellent temporal subsets of the observed data were selected based on the relative seeing of the different tracks. Absolute flux calibration was done using IRAM models for MWC349 and LkHa101 providing about 50 independent measurements of the flux of J1259+516 and J1332+473 over a period of about 1 year. This allowed us to confirm that the time variations of the flux of these quasars were relatively smooth.

We detect emission from 9 molecular lines between ~80 and 110 GHz, including HCN(1–0; 88.6 GHz) and N_2H^+ (1–0; 93 GHz) presented in this paper, but also C_2H(1–0), HNCO(4–3), HCO^+(1–0), HNC(1–0), $C^{18}O$(1–0), HNCO(5–4) and ^{13}CO(1–0). Continuum was subtracted from the uv visibilities by fitting a baseline of the order of 0 for each visibility, excluding channels in a velocity range of 300 km/s around the redshifted-frequency of each line. For each line, the NOEMA data were resampled to a spectral axis with 10 km/s resolution, relative to the systemic velocity of $v_{sys} = 471.7$ km/s (Shetty et al., 2007).

B.1.2 IRAM-30m single-dish data

In order to sample all the spatial scales, we needed to combine the NOEMA interferometric imaging with single dish data of the HCN (1–0) and N_2H^+ (1–0) emission lines from both archival and new observations.

The HCN (1–0) emission line was observed as part of the IRAM-30m survey EMPIRE (Jiménez-Donaire et al., 2019), using the 3 mm band (E090) of the dual-polarization EMIR receiver (Carter et al. 2012). N_2H^+ (1–0) was observed by the IRAM-30m CLAWS survey (055-17, PI: K. Sliwa; den Brok et al., 2022), where EMIR was also used to map the 1 mm (220 GHz) and 3 mm (100 GHz) emission lines in M 51. In both surveys, the integration time was spread over the full extent of M 51, while the required field of view (FoV) for the 30m imaging is the interferometric FoV plus a guard-band to avoid edge effects amounting to 5 square arcmin. We estimate that the EMPIRE and CLAWS projects obtained each about 14 hours of 30m integration time over the relevant field of view. As a rule of thumb to achieve an optimum combination one needs to observe with the 30m telescope the same amount of time as is spent in the compact D configuration[1]. Hence, we obtained 55 hours of additional IRAM 30m observations (project 19-238 observed in February and April 2020) with a similar tuning as the NOEMA one. In all three cases, we used the on-the-fly-position switching (OTF-PSW) mode, with emission-free reference positions close to the galaxy. The fast Fourier transform spectrometers (FTS) were used to record the data. We refer to Jiménez-Donaire et al. (2019) and den Brok et al. (2022) for details of the observations.

The data were (re)-reduced (1) to ensure a homogeneous treatment and (2) to avoid unnecessary spatial or spectral regridding. In short, for each observed spectrum, we first extracted a frequency range of 300 MHz centered on each target line. We then converted the temperature scale from $T_A^\star$ to T_{mb} by applying the relevant Ruze formula with the `CLASS` command `MODIFY BEAM_EFF /RUZE`. We computed the velocity scale corresponding to each line's redshifted velocity, and we reprojected the spatial offsets of each observed spectrum to the NOEMA projection center of RA=13:29:52.532, Dec=47:11:41.982. We also subtracted a polynomial baseline of the order of one fitted by excluding a velocity range of $[-170, +170\,\mathrm{km/s}]$. Finally, we gridded all the data on the same spatial and spectral grid as the NOEMA data. The achieved noise levels are 2.5 K at 29.3″ and 2.4 K at 27.9″ for the HCN and N_2H^+ (1–0) lines, respectively.

B.1.3 NOEMA+30m imaging

The 30m data are then merged with the NOEMA data in the *uv* plane using the `GILDAS UV_SHORT` command (see Pety and Rodríguez-Fernández, 2010, for details). The combined data were imaged with `UV_MAP` on a grid of 768×1024 pixels of 0.31″size. Högbom-cleaning without cleaning mask was run in order to achieve residuals consistent with a Gaussian distribution of the noise. In practice, we ran it until a stable number of clean components, which depends on the line, was reached. The intensity scale was finally converted from Jy/beam to K. The resulting dataset has a rms of ~ 20 mK per 10 km/s channel at a nominal resolution of $2.1 \times 2.4''$ for the brightest line, ^{13}CO(1–0).

We created the following sets of integrated moment-0 maps for the NOEMA+30m HCN and N_2H^+ datacubes as well as for the $^{12}CO(J = 1\text{–}0)$ data from PAWS (Schin-

1 See the IRAM technical memo IRAM-2008-2, https://cloud.iram.fr/index.php/s/Ney5P2BeN7DAEWX

nerer et al., 2013). All data are convolved to a common angular and spectral resolution of 3″ (125 pc) and 10 km/s per channel. We integrated each line by applying the so-called 'island-method' based on ^{12}CO emission (see Einig et al., 2023, and reference therein). This method isolates connected structures with ^{12}CO emission above our selected S/N threshold of 2 in the position-position-velocity (ppv) cube and integrates the emission of selected lines over the identified structures along the velocity axis. To avoid misleading oversampling effects, we regridded our maps to pixels with sizes of half the beam major axis for all calculations (i.e. 1.5″). Using ^{12}CO emission to detect the 'islands' ensures that for all lines the same pixels in the ppv cube are used for integration. Since ^{12}CO is brighter than the other lines, there are more pixels above a given S/N threshold than in N_2H^+ and HCN. Therefore, this can result in otherwise too faint emission being stacked in pixels that would not be selected for integration based on N_2H^+ emission, for instance.

For comparison, we also integrated each line individually, by selecting 'islands' based on each line's intensity. This reduces the noise for each line individually while conserving faint emission from connected structures. However, this also introduces some bias, as the emission is integrated over a varying amount of pixels in different structures for each line. While some values slightly change due to these effects, we confirm that all trends and conclusions remain unchanged.

Pixels where the N_2H^+ integrated emission is significantly ($>3\sigma$) detected, contain $\sim 50\%$ of significant ^{12}CO flux in our FoV and $\sim 70\%$ of significant HCN emission in the FoV. Pixels where HCN is significantly detected contain $\sim 90\%$ of the significant ^{12}CO emission in our FoV. Since the our analysis in section 3 is based on regions where N_2H^+ is detected, we limited our analysis to a smaller area in the FoV.

B.2 TYPICAL CLOUD MASS PER BEAM

As N_2H^+ is abundant in small dense cores, we generally expect the N2H+ emission to arise from regions with sizes much smaller than our resolution of 125 pc, which is slightly worse than the size of massive GMCs. Thus, the pixel-by-pixel variations in our observations reflect average physical trends affecting ensembles of multiple clumps. Our finding (see Sect. 5.3.1 that linewidths of N_2H^+ are comparable to HCN in selected beam-size regions, suggests that at our 125 pc scales, we are indeed averaging emission from several dense clouds. This is further supported by the typical emission found in these regions. In the selected beam-size regions (see Fig. 28), we find typical integrated ^{12}CO intensities of $I_{CO} \sim 1 \times 10^2$ K km/s. A typical large molecular cloud with cloud masses of $M_{cloud} \sim 1 \times 10^5\,M_\odot$ would (at our resolution) correspond to integrated intensities of 1.3 K km/s using a standard CO-to-H_2 conversion factor of $\alpha_{CO} = 4.35\,M_\odot\,pc^{-2}\,(K\,km/s)^{-1}$. Therefore, we can confirm that at our resolution we are likely to be averaging the emission from several clouds.

B.3 N_2H^+-TO-CO AND HCN-TO-CO RELATION

In addition to the N_2H^+-to-HCN distribution (Fig. 29), we show the N_2H^+-to-^{12}CO and HCN-to-^{12}CO distributions in Fig. 55. We mark the same subset of pixels (AGN, SW.arm) identified in the N_2H^+-to-HCN distribution accordingly. We fit power-laws

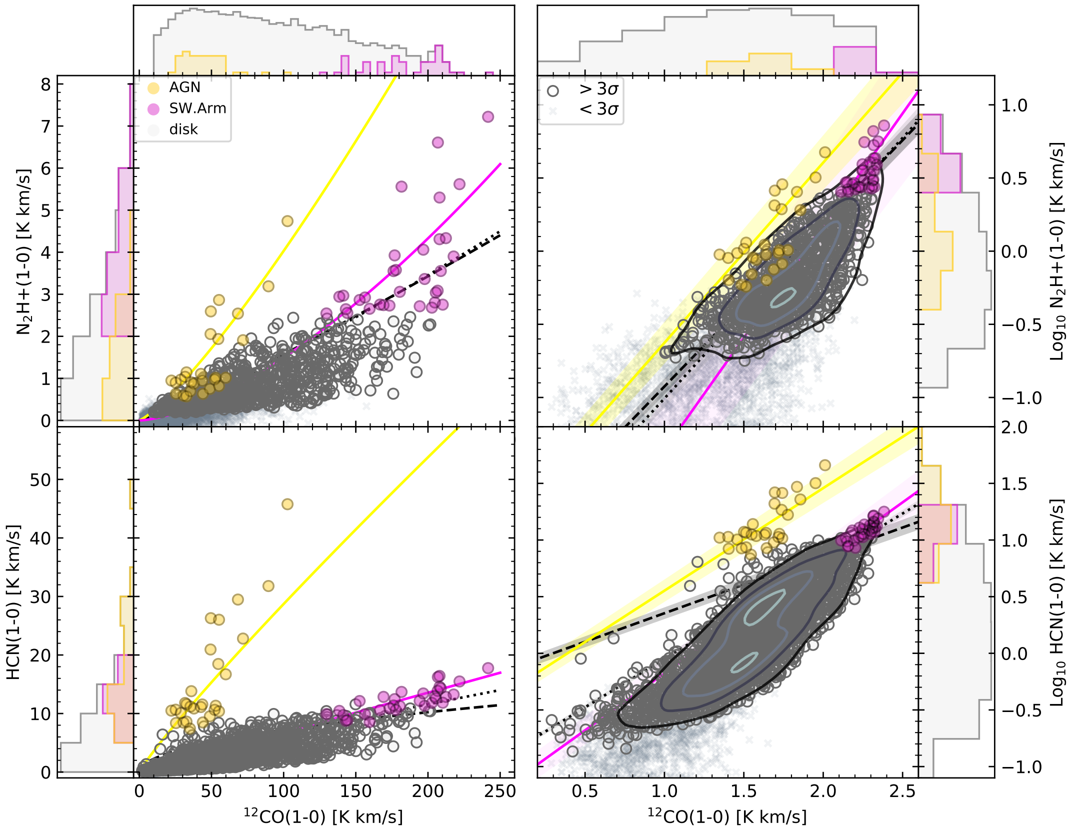

Figure 55: Pixel-by-pixel distribution of integrated N_2H^+ (top panels) and HCN (bottom panels) as a function of ^{12}CO emission, similar to Fig. 29 (a) in linear (left panels) and logarithmic (right panels) scaling. Subsets of pixels isolated in Fig. 29 are marked accordingly (pink: subset (c) SW.Arm, yellow: Subset (b) AGN). Power-law fits to the full data (black dashed), the data without the central points (black dotted) and the subsets are added (colors respectively). Fit uncertainties are only shown in log space to ease visibility.

to all the data (dashed line), the data without the central points (dotted line), as well as the subsets of data (subset (b) AGN, subset (c) SW.arm). Fit parameters can be found in Table 14 and more details on the fitting process are provided in Appendix B.4. Similarly to our previous findings, we see that the central data points follow a steeper trend than the rest of the data points. While the central points in the HCN-to-^{12}CO distribution do not overlap with the rest of the data, the central N_2H^+-to-^{12}CO distribution mostly overlaps with the rest of the data points and the central N_2H^+-to-^{12}CO trend is only slightly steeper than the global trend.

The N_2H^+-bright data points from the southern spiral arm (subset (c): pink) are also the brightest pixels in ^{12}CO. These points constitute a super-linear relation in the N_2H^+-to-^{12}CO plane. This is less clear for the HCN-to-^{12}CO distribution. While all fits to the N_2H^+-to-^{12}CO data and subsets are super-linear ($a > 1$), all fits to the HCN-to-^{12}CO data and subsets are sub-linear ($a < 1$) except for the fit to subset (c). We note, however, that there are additional data points in the HCN-to-^{12}CO distribution, which are elevated above the bulk distribution that might instead belong to the central subset (b), but are not selected since our selection of these subsets is visually determined based on the N_2H^+-to-HCN distribution. While the fit to all data points shows a large increase in offset due to the central data points, the fit without the central subset might

Table 14: Power-law fit parameters of N_2H^+ as a function of CO and HCN as a function of CO

Region	Power a	Offset b	ρ_{Sp}	p-value
N_2H^+**-to-**^{12}CO				
All data	1.12 ± 0.02	-2.05 ± 0.04	0.692 ± 0.007	<0.001
All w/o AGN	1.19 ± 0.03	-2.19 ± 0.05	0.751 ± 0.005	<0.001
AGN, yellow	1.23 ± 0.07	-1.86 ± 0.12	0.69 ± 0.03	<0.001
SW.Arm, pink	1.53 ± 0.14	-2.89 ± 0.32	0.82 ± 0.02	<0.001
HCN**-to-CO**				
All data	0.50 ± 0.02	-0.15 ± 0.04	0.836 ± 0.003	< 0.001
All w/o AGN	0.86 ± 0.01	-0.90 ± 0.01	0.844 ± 0.003	<0.001
AGN, yellow	0.91 ± 0.05	-0.35 ± 0.08	0.68 ± 0.03	<0.001
SW.Arm, pink	1.01 ± 0.05	-1.18 ± 0.11	0.82 ± 0.02	<0.001

Fit parameters and spearman correlation coefficients according to a linear fit in log-log space similar to Table 8 but for the N_2H^+-to-^{12}CO and HCN-to-^{12}CO distribution.

still be elevated due to the likely imperfect selection of data points impacted by the AGN.

The fit to the central subset (b) of the HCN-to-^{12}CO distribution significantly deviates from the fit to the disk data without this subset, similar to our findings for the N_2H^+-to-HCN distribution. Unsuprisingly, this is not the case for the central fit of the N_2H^+-to-^{12}CO distribution, which agrees well with the fit to the disk data, as most of the central subset (b) overlaps with the disk data. This indicates that the mechanism driving the offset in line emission affects N_2H^+ less than HCN (see discussion in Section 5.4).

B.4 FITTING THE N_2H^+-TO-HCN, N_2H^+-TO-CO AND HCN-TO-CO DISTRIBUTION

We fit all data points, the data subsets (b,c) as well as all disk data, namely, all data without subset (b) AGN, of the N_2H^+-to-HCN, N_2H^+-to-^{12}CO and HCN-to-^{12}CO distributions with linear functions in logarithmic scaling. We only considered pixels with significant emission ($> 3\sigma$). Parameters are fitted with `curve-fit` (python scipy-optimize tool; Virtanen et al., 2020). We fit a linear function of shape $f(x) = ax + b$ to the logarithmic data with slope a and offset b. Following error propagation, the corresponding uncertainty at each x value is $\Delta f(x) = \sqrt{(\Delta a x)^2 + (\Delta b)^2}$, with uncertainties Δa, Δb accordingly. The discrepancy to the literature fit is measured as $\sigma = |f - f_{lit}| / \sqrt{\Delta f^2 + \Delta f_{lit}^2}$, which is dependent on x. We provide the average discrepancy in the range over which our data are measured.

Uncertainties are estimated by perturbing each pixel by a random Gaussian value with standard deviation at the corresponding noise value, and randomly jackknifing 10% of the data before either calculating fit-parameters or Spearman correlation coefficients. Repeating this 100 times yields the standard deviation as uncertainty.

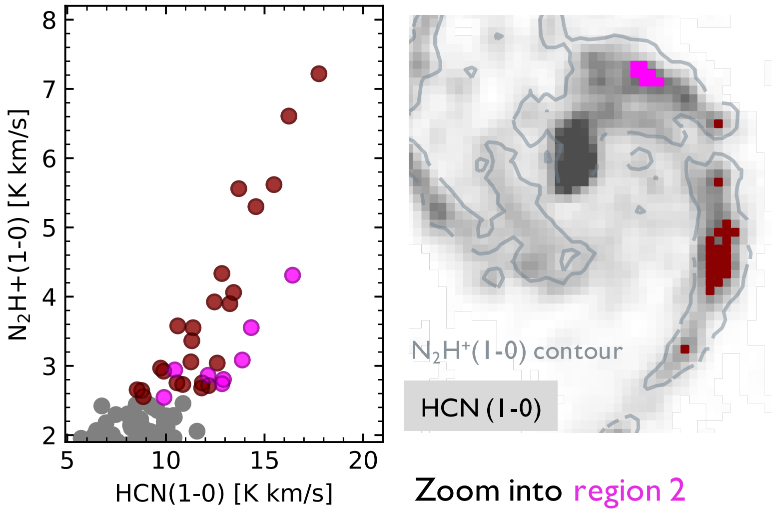

Figure 56: Close-up of HCN and N_2H^+ emission (left panel) of N_2H^+-bright pixels from subset (c), as in Fig. 29, as well as their location in the disk (right panel, compare to panel b of Fig. 29). We separate the pixels into two sub-regions (red, pink)

B.5 QUANTIFYING THE SCATTER OF LINE RATIOS

We investigated regions with increased scatter, as well as quantify the scatter between N_2H^+ and HCN, HCN, and ^{12}CO as well as N_2H^+ and ^{12}CO.

B.5.1 Disentangling emission from the southern spiral arm

In Sect. 5.4.2 we isolated pixels that are bright in HCN and N_2H^+. The region with pixels brightest in N_2H^+ (subset c: pink points in Fig. 29) shows a comparably large scatter in N_2H^+ emission, with the emission varying by nearly a factor of 2 at similar levels of HCN flux (at $I_{HCN} \sim 18$ K km/s we find $I_{N_2H^+} \sim 4 - 7.5$ K km/s). A closer look (Fig. 56) reveals that this emission originates from different spatial locations in the disk, one with a shallower N_2H^+-to-HCN distribution located in the north-western part of the molecular ring (pink circles), the other with a steeper N_2H^+-to-HCN distribution from the south-western part of the same spiral arm (dark red circles).

As noted in Sect. 5.4.2, the data points from the southern spiral arm (red points in Fig. 56) drive the non-linear but logarithmic relation between N_2H^+ and HCN emission. Interestingly, the northern region is located close to the AGN jet major axis (Querejeta et al., 2016b) and might be potentially impacted by the AGN as well, though the number of data points is lower.

B.5.2 Measuring the scatter of line ratios

We quantified the scatter of the N_2H^+-to-HCN, HCN-to-^{12}CO and the N_2H^+-to-HCN distribution as follows. For this analysis, we excluded the central subset (b) as it exhibits a quite different distribution from the rest of the data, as well as data points below the 3σ noise level. We subtracted the corresponding best-fit value (using the fit parameters when excluding the center) from each data point in the according distribution. The obtained data has an average scatter of ~ 0.14 dex for N_2H^+ as a function of HCN emission, 0.19 dex for N_2H^+ as a function of ^{12}CO emission and 0.29 dex for HCN as a function of ^{12}CO emission.

We drew the following conclusion: a) While all lines span a range of $\gtrsim 1.5$ dex in intensity, we find $\sim 10\%$ scatter, indicating that all lines are well correlated. b) The scatter of N_2H^+ as a function of HCN is least, indicating a tighter correlation between N_2H^+ and HCN than any of those lines with ^{12}CO. Since these results are strongly dependent on the fit and thus the fitting tool used, we suggest these results be taken with caution.

APPENDIX TO CHAPTER 6

C.1 MOCK DATA TO TEST THE EFFECT OF LOW SNR

Comparing the emission of molecular lines with different intrinsic intensities in data sets with similar noise levels is challenging, as fainter emission lines (such as N_2H^+ (1-0)) are much more strongly affected by noise, resulting in a lower fraction of significant detections than brighter lines. Including/excluding regions based on their SNR alone can thus bias any measurement of lines of different brightness differently. To address this issue, we simulate the effect of different brightness levels using the CO(1-0) data cube, which contains a lot of signal compared to its noise level with significant detections across most of our FoV. We present the methodology to generate data cubes representing fainter lines (Section C.1.1), and create moment-maps. We explore different commonly used approaches to determine average intensities and line ratios based on the mock-data in Section C.1.2. Since the noise in observations averages to zero, binning is commonly used to recover relations. We test the effect on binning on our mock-data sets in Section C.1.3.

C.1.1 Creation of Mock-data sets

We take the CO(1-0) data cube from PAWS matched to the SWAN data at $3''$ resolution with a spectral resolution of 10 km/s (see Section 6.2.3). First, we scale the intensity of the CO data cube by a constant line ratio S. This factor represents the true line ratio we want to recover in our analysis. We call this scaled data cube A. Next, we create a data cube filled with only simulated noise. At each pixel and for each channel we randomly draw values from a Gaussian distribution with arbitrary amplitude. We then spatially convolve the Gaussian noise for each channel of the noise cube by our beam size of $3''$. This will correlate the noise of neighboring pixels as it is the case for our interferometric observations from SWAN. While technically the noise is not just correlated across a beam, but across larger scales as well, this is not included in this simple test. The amplitude of the correlated noise in the noise data cube is scaled to match an RMS of 8.6 mK which corresponds to the RMS of N_2H^+ from our SWAN observations (Stuber et al., 2025). Lastly, we add the cube containing the correlated scaled noise to the scaled CO data cube A. We do not add the cube in quadrature, as the relative noise in the scaled CO cube is negligible compared to the noise added. This final data cube is our ”mock-data cube”.

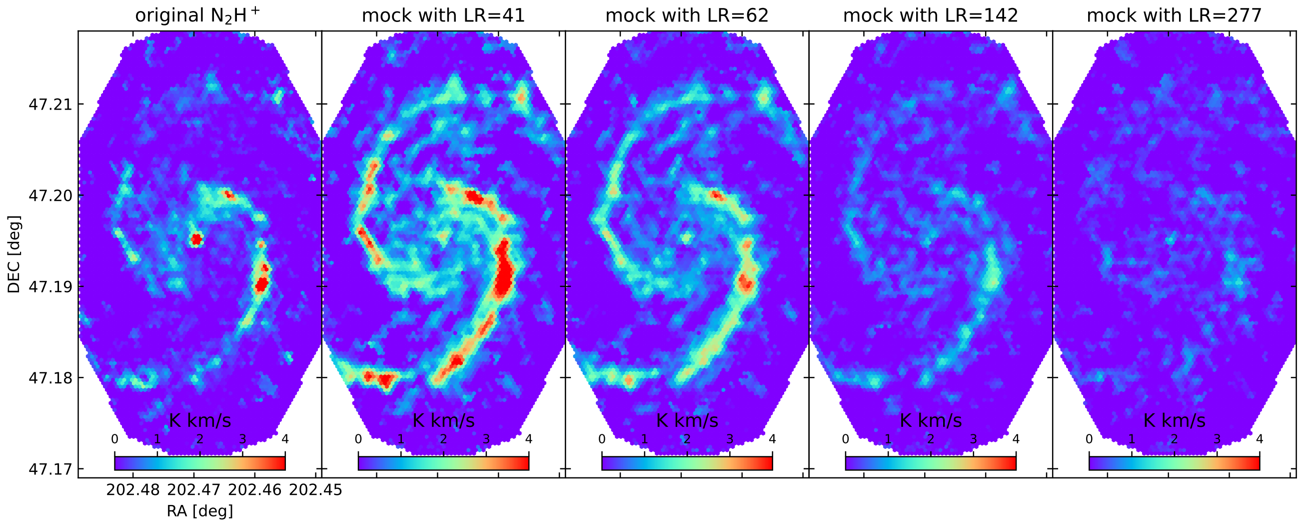

Figure 57: Integrated emission of N_2H^+ (1-0) and Mock data cubes based on the original CO(1-0) data cube, scaled down by a line ratio of (from left to right) LR=41,62,142,277 and adding noise to simulate lower SNR observations.

We perform these steps with line ratios of $S = 0.024, 0.016, 0.007, 0.0036$. The noise cube is drawn anew for each S. Those are line ratios obtained from different methods to calculate the N_2H^+-to-CO line ratio within the literature (i.e., see Jiménez-Donaire et al., 2023; Schinnerer and Leroy, 2024). Those values further roughly match our typical HCO^+-to-^{12}CO, HNC-to-^{12}CO and N_2H^+-to-^{12}CO line ratios ($0.033, 0.018, 0.008$, Table 10) with an additional even smaller line ratio to account for individual regions (i.e. norhtern disk) with increased noise.

Our measurements of the observed SWAN line emission (Section 6.4 and following) is not performed on the data cubes directly, but on the moment maps (Section 6.2.2). Therefore, we create a PyStructure based on the exact same criteria as before (using HCN and CO as priors, Section 6.2.2), integrating the Mock data cubes. The resulting moment-0 maps are shown in Figure 57. We add the moment-0 map of N_2H^+ (1-0), the faintest of the dense gas tracing lines, for comparison.

C.1.2 Recovering average intensity ratios

We compare different methods to recover average line ratios between our mock-data and the original ^{12}CO data in Figure 58. These methods are the mean and median line ratio of all pixels, as well as the integrated intensity of the mock data divided by the integrated CO data (sum(M)/sum(CO) = Σi_{mock} / Σi_{CO}). We apply these methods to a) the full FoV, excluding the edges where the noise is increased (see Stuber et al., 2025), b) a I_{CO}-based mask and c) a I_{mock}-based mask. The I_{CO} (I_{mock}) mask exclude pixels in which the CO (mock) intensity is below 3σ. In Figure 58 we show the relative difference between the measured line ratio and the true line ratio (LR_{true}) used in the generation of the mock cubes.

The deviations between measured and true line ratio between different methods are small compared to the deviations between different masking techniques. The largest deviations occur when applying the I_{mock}-based mask. The smaller the true CO-line ratio (the smaller the SNR), the larger the deviation due to masking. The I_{mock}-based

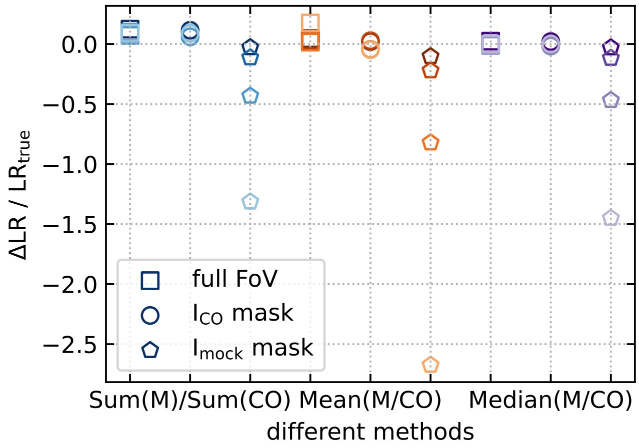

Figure 58: Testing different methods to calculate CO line ratios and the effect of masking. We show the relative difference between the true and measured line ratio $\Delta LR/LR_{true}$ with $\Delta LR = LR_{true}$ - $LR_{measured}$. We estimate the measured line ratio $LR_{measured}$ per three different methods (sum: sum(M)/sum(CO) in blue, mean: mean(M/CO) in orange, median: median(mock/CO) in purple) with M and CO indicating the intensity of the mock and CO data, respectively. We further test the impact of different masking on the moment maps: Utilizing all pixels in the FoV (squares), only pixels where CO is significantly detected ($> 3\sigma$, circle), and only pixels where N_2H^+ is significantly detected ($> 3\sigma$, pentagons). The color gradient indicates the SNR of the data cube (measured via LR_{true}), with darker color being $LR_{true} = 0.024$ and the faintest color $LR_{true} = 0.0036$. Points of the same color (albeit different gradient) belong to the same method.

mask is biased towards fewer and brighter pixels compared to the other masks. This will result in a bias towards more positive measurements.

The difference between values derived using the full FoV and within the I_{CO}-based mask is small as expected. As the moment-0 maps are created using CO and HCN emission as a prior, there are only few pixels within the resulting moment-0 map where the integrated ^{12}CO emission is less than 3 times its corresponding value.

We test the calculation of line ratios between the mock data, that are all much fainter than the CO line, in Figure 59. Similar to before we test both different calculation methods, and different masking techniques. We find the sum-method (integrated intensity of mock1 divided by integrated intensity of mock2) results in the most reliable results, even for large true line ratios. This method is also least effected by masking.

C.1.3 Binning Mock data intensities and ratios

When measuring relations between molecular line emission and other parameters such as, e.g., galactocentric radius or molecular gas surface density, binning the emission (a.k.a. averaging the emission in increments of, e.g., galactocentric radius) is a commonly used technique to recover the physical relation that is obscured by noise. Ideally, the noise (including positive and negative noise values) in each bin will average to zero and the actual signal can be recovered. We test how well binning recovers the known relation between our mock data and the ^{12}CO data in Figure 60. The binning method used is described in Section 6.3.2. The true relation is very well recovered when all data points are used. Masking pixels ($> 3\sigma$) results in a flattening of the average relation for low CO intensities.

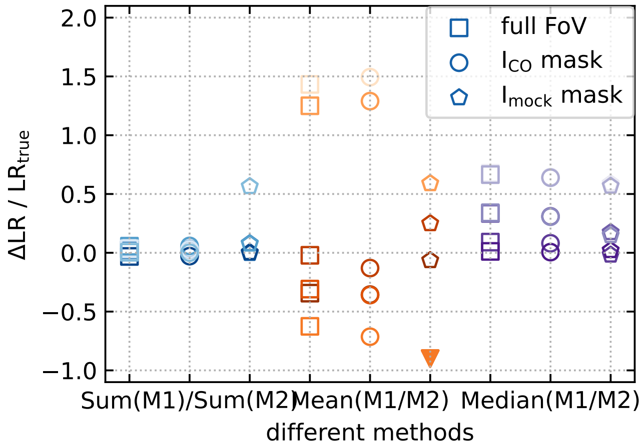

Figure 59: Testing the effect of masking on different methods to calculate average line ratios of mock-data. Same as Figure 58 but for line ratios between different mock data sets. The color gradient indicates the expected line ratio (measured via LR_{true}). The ratio of Mock41 and Mock227 results in the largest line ratio (and thus faintest data point). Two outliers with large $\Delta LR/LR_{true}$ are only shown as lower limits (colored triangle).

Fitting those masked and unmasked binned line ratios (Section 6.3.2) confirms this bias: When using all data, we can recover the true relation (slope of 1) in all of the mock data sets, even in the data with lowest SNR (LR=277). When restricting the data to $> 3\sigma$, slopes are artificially decreased with decreasing average SNR of the mock data and significantly deviate from the true slope of unity.

In addition to binning line intensities, we test if we are able to recover the relation between line ratios and other more independent parameters, such as molecular gas, star-formation rate and stellar mass surface densities, galactocentric radius, velocity dispersion and dynamical equilibrium pressure used in our analysis (Section 6.5). Figure 61 shows the binned mock-to-CO line ratios as function of those parameters. We expect a flat relation (slope 0) with different offsets along the y-axis depending on the mock data used.

Most mock-to-CO line ratios are flat as expected (Figure 61). Again, masking pixels $< 3\sigma$ introduces significant biases and results in artificial slopes that are largest for the mock-data with the lowest SNR. This bias is strongest for relations of line ratios with Σ_{mol}, σ_{CO} and PDE, with a $> 5\sigma$ deviation of slopes obtained from the lowest SNR mock data (LR=277) to the true slope of zero. When including all data, we can recover the expected slope of zero for all mock data sets as function of all galactic parameters.

This simple mock-data set is not a perfect representation of the actual noise, as it does not consider noise correlated over scales larger than a beam-size. Still, it shows the impact of excluding parts of the data on the ability to retrieve the correct result. The actual correlations shown might suffer from additional noise sources not considered in this mock-data set.

C.1.4 Estimating the scatter of mock data relations

The scatter of a relation between line emission and physical parameters is equally important in assessing the strength of the relation as the slope. As an example, if the relation between line intensity and two galactic properties show similar slopes, increased

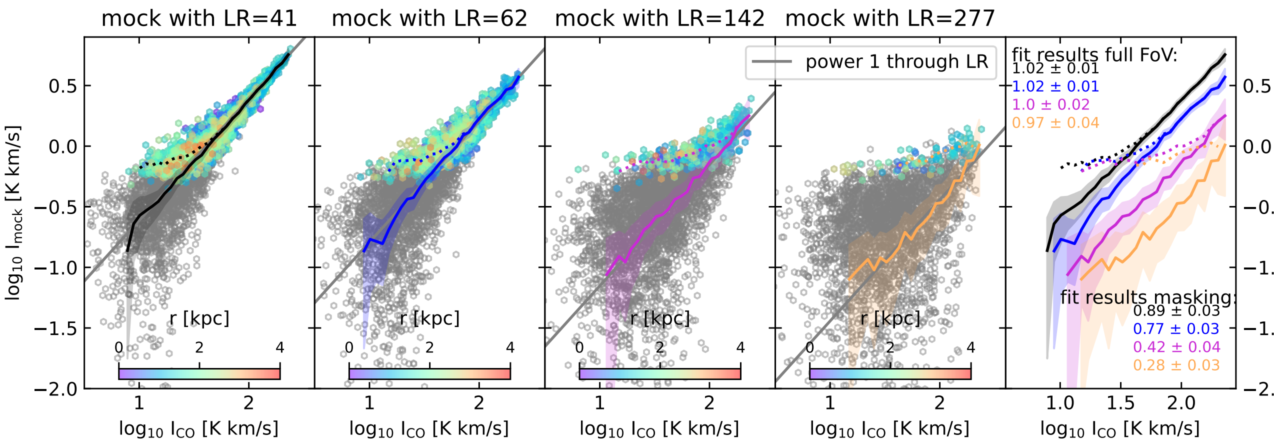

Figure 60: Testing the effect of binning to recover average line relations. We show the intensity of each pixel in the mock-moment-0 map (I_{mock}) as function of the correponding intensity in the ^{12}CO moment-0 map (I_{CO}. The different mock-data are simulated based on ^{12}CO data scaled by a line ratio of 0.024, 0.016, 0.007, 0.0036 (aka LR: 41, 62, 142, 277). The expected relation (black dashed line) corresponds to line ratio used to create the mock data (power of 1, offset corresponds to the line ratio). We highlight pixels where I_{mock} is significantly detected (>3σ, colored data points) and indicate their galactocentric distance by color. We bin I_{mock} in logarithmic steps of I_{CO} for all pixels in the FoV (solid line), as well as when only including pixels with significant detections (dotted line). We add the slopes of linear fits fitted to the binned data for the full FoV and the masked data.

scatter in one may suggest a secondary dependency on other factors. Unfortunately, a lower SNR coincides with an increased scatter, which challenges the interpretation of the scatter calculated using the line emission of lines of different average SNR. We test this impact of SNR on the calculation of the scatter with our mock data and galactic parameters. Figure 62 shows the average scatter of mock line intensities as function of physical galactic properties. The scatter is the medium absolute deviation of the line intensity as function of galactic properties after subtracting a linear relation fitted to the binned intensities (Section 6.3.2). Per galactic quantity, the maximum deviation in scatter from different mock data sets ranges from 0.2 dex (relations with P_{DE}, Σ_{mol}) to 0.5 dex (σ_{CO}, Σ_*, dist). The variations in scatter between the different galactic quantities is expected, as some quantities (Σ_{mol}, P_{DE}) depend on the ^{12}CO intensity, which is the basis for the mock data set.

In addition to line intensity, we test the scatter of relations between mock-to-^{12}CO line ratios and galactic physical properties in Figure 62. For each galactic property, the average scatter increases significantly with decreasing average SNR (lowest SNR for mock277), as expected. For each mock data set, variations in the mock-to-CO relation with different galactic properties are small: We find the least variations in scatter across galactic properties for the highest SNR data set (mock41, scatter varies by ~ 0.04, followed by ~ 0.06, ~ 0.06, ~ 0.08 for mock62, mock142 and mock277 respectively.) These variations in the average scatter are driven by the varying SNR and different sorting due to the galactic parameters.

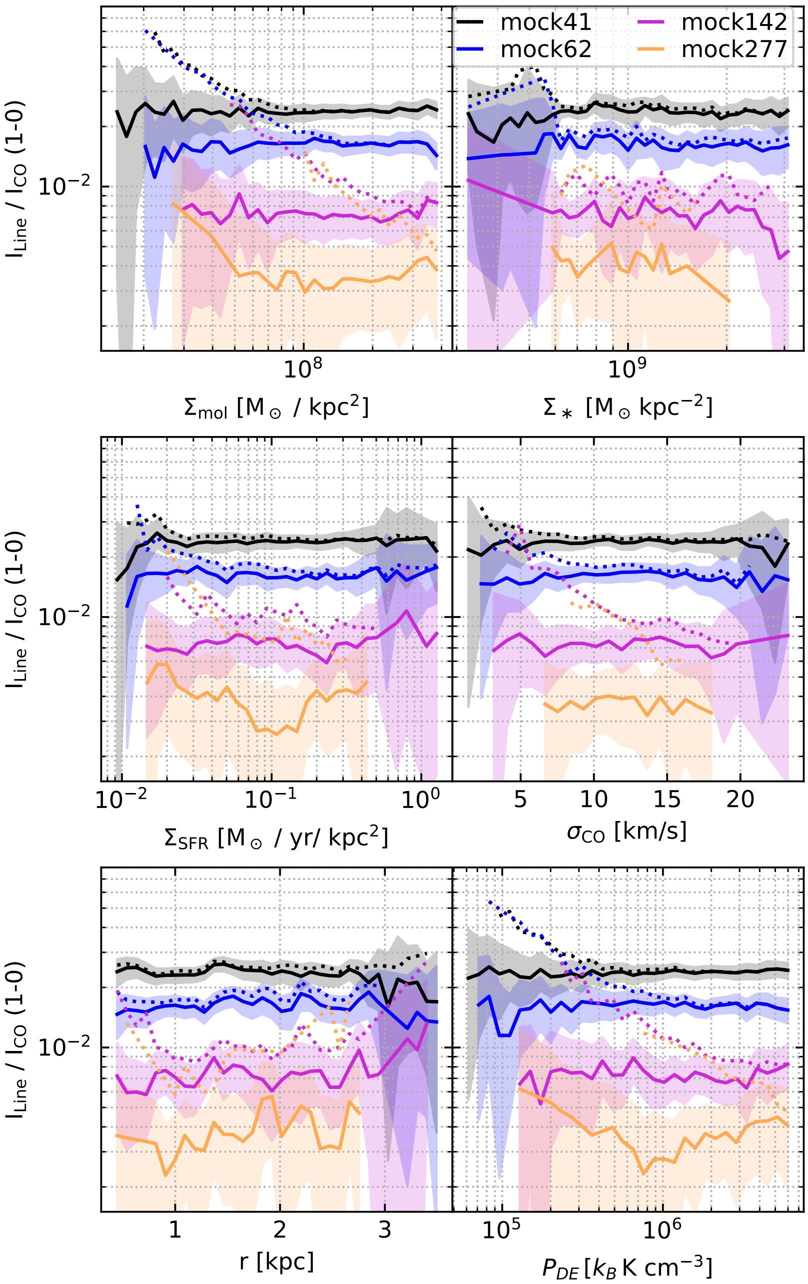

Figure 61: Binned mock-to-CO line ratios as function of physical parameters such as molecular gas mass, stellar mass and SFR surface densities, velocity dispersion, galactocentric radius and dynamical equilibrium pressure. We show the binned line ratios using all pixels (solid line), as well as restricting to detections (intensity >3σ, dotted lines).

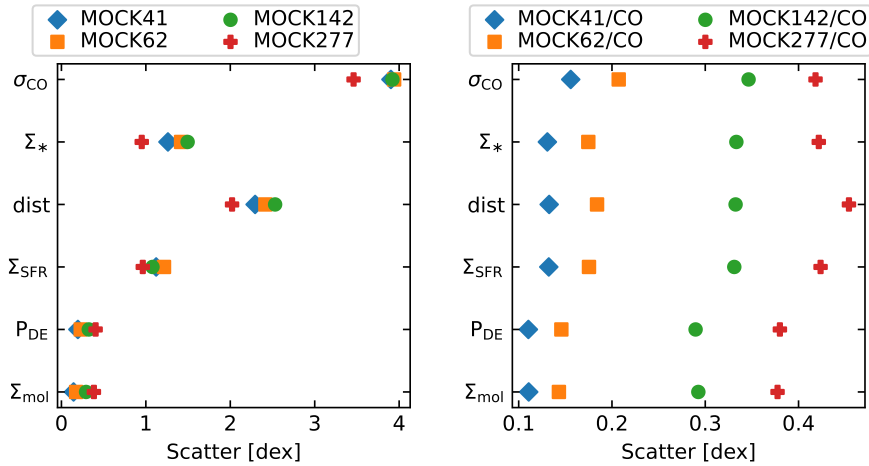

Figure 62: Average scatter of mock intensity (left panel) and mock-to-CO line ratios (left panel) as function of galactic physical properties tested for different mock data sets (Mock41-Mock277).

C.2 TESTING DIFFERENT PRESCRIPTIONS OF $\Sigma_{\rm mol}$

We test the performance of the average HCN-to-^{12}CO line ratio when comparing to different prescriptions of calculating $\Sigma_{\rm mol}$ in Figure 63 The methods to calculate $\Sigma_{\rm mol}$ are described below.

A common method to estimate the CO-to-H_2 conversion factors is via the metallicity and stellar mass surface density in the disk, which we refer to as $\Sigma_{\rm mol}^{\rm metal,*}$. We first obtain the $\alpha_{\rm CO}$ distribution based on radial metallicity profiles from CHAOS (Croxall et al., 2015). These are converted into $\alpha_{\rm CO}$ values according to the prescription in Bolatto et al. (2013), which relies not only on the metallicity but also on kpc-surface density of stellar mass, atomic gas and molecular gas. The values were calculated iteratively as described in Sun et al. (2022). Inside the SWAN FoV, $\alpha_{\rm CO}$ has a median of 1.99 $M_\odot$ (K km s^{-1} pc^{-2})$^{-1}$, with 16$^{\rm th}$ and 84$^{\rm th}$ percentiles of 1.35, 2.75 $M_\odot$ (K km s^{-1} pc^{-2})$^{-1}$, respectively. It also has a strong radial gradient: the central 1 kpc (diameter) median $\alpha_{\rm CO}$ is 0.72 $M_\odot$ (K km s^{-1} pc^{-2})$^{-1}$, the median $\alpha_{\rm CO}$ at galactocentric distance larger than 3 kpc is 2.81 $M_\odot$ (K km s^{-1} pc^{-2})$^{-1}$.

We add our first prescription, using a measured $\alpha_{\rm CO}$ that is applied to the integrated ^{12}CO intensities (see Section 6.2.3). We refer to this surface density as $\Sigma_{\rm mol}^{\rm measured}$.

If the $\alpha_{\rm CO}$ value is not known precisely, a common method is to assume a constant based on Galactic measurements (Bolatto et al., 2013). Commonly used in extragalactic targets is a value of $\alpha_{\rm CO} = 4.35 M_\odot$ (K km s^{-1} pc^{-2})$^{-1}$. We calculate the gas surface density by applying this constant conversion factor to the ^{12}CO moment-0 map. We refer to this surface density as $\Sigma_{\rm mol}^{\rm const}$.

Lastly, we add measurements of gas surface density from Faustino Vieira et al. (2024) based on HST observations for comparison. We refer to this surface density as $\Sigma_{\rm mol}^{\rm dust}$.

While there are difference in the average HCN/CO ratio as function of those different values of $\Sigma_{\rm mol}$, we note that most of them are similar, comparably flat, or even result in negative trends ($\Sigma_{\rm mol}^{\rm metal,*}$). The relation obtained using a constant CO-to-H_2 conversion factor reveals the steepest relation, but we note, that a constant value of $\alpha_{\rm CO}$ is not able to reflect the changes expected in environment, such as a generally increased $\alpha_{\rm CO}$ in galaxy centers (Schinnerer and Leroy, 2024).

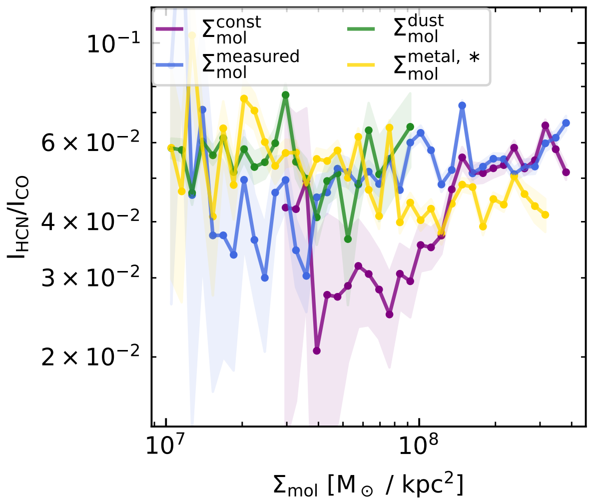

Figure 63: Average HCN/CO line ratio as function of Σ_{mol}, with Σ_{mol} being calculated with four different methods: a) a constant α_{CO} conversion factor multiplied to ^{12}CO emission (Σ_{mol}^{const}) b) the measured α_{CO} as described in Section6.2.3, $\Sigma_{mol}^{measured}$ c) a metallicity and stellar mass based α_{CO}, $\Sigma_{mol}^{metal,*}$, and an independent dust-based estimate of molecular gas surface density from Faustino Vieira et al. (2024), Σ_{mol}^{dust}.

C.3 THE IMPACT OF THE CENTRAL ENVIRONMENT ON THE AVERAGE HCN/CO TO Σ_{mol} RELATION

We test the effect of the central pixels on the performance of the HCN/CO-to-Σ_{mol} relation by removing central apertures of increasing sizes in Figure 64. Further, we fit the binned HCN/CO-to-Σ_{mol} relations and provide fit slopes in Table 15. We add spearman correlation coefficients (ρ_{Sp}) for the respective apertures in Table 15. We note that ρ_{Sp} is sensitive to the SNR of the line, therefore we expect brighter lines to have higher values of ρ_{Sp}.

While we can see an increase in the slopes of the HCN/CO-to-Σ_{mol} relation with increasing aperture that is removed from the analysis, the values stay overall small. At a radius of $\sim$ 1 kpc the molecular ring is reached. Figure 64 shows that particularly pixels at intermediate values of Σ_{mol} are removed when excluding central apertures of increasing sizes. The molecular outflow driven by the AGN is most prominent in a small region with the size of $\sim$ 200 pc in the center (Querejeta et al., 2016b). The actual impact of the AGN on the molecular gas, however, is under discussion (Querejeta et al., 2016b, 2019; Zhang et al., 2025, see also Section 6.6) and some effects might reach out to radii of $\sim$ 600 pc north of the AGN. The slopes of the HCN/CO-to-Σ_{mol} relation however, show a continuous increase with increased size of the excluded aperture. The HCN/CO ratio as function of Σ_{mol} reaches a slope of up to 0.36 ± 0.02. Spearman correlation coefficients do not change even when excluding the central 1 kpc in radius. In all cases values of ρ_{Sp} are highest for the HCO^+/CO ratio as function of Σ_{mol}, despite HCN being on average brighter than HCO^+.

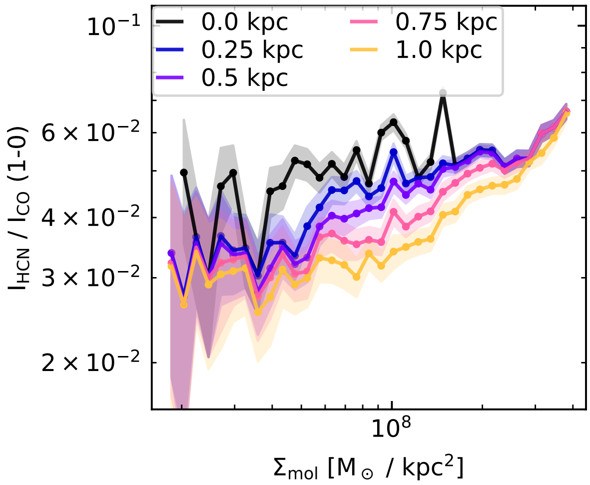

Figure 64: Average HCN/CO line ratio as function of Σ_{mol} when excluding pixels inside the central $r = 0, 0.25, 0.5, 0.75$, and 1 kpc in radius. The ratio is binned as described in Section 6.3.2 and we use the same values of Σ_{mol}, that we use in the main text.

Table 15: Fitting CO line ratios (LR) as function of Σ_{mol} when excluding central apertures of varying sizes

Cen. aperture [kpc]	LR	slope	slopeerr	ρ_{Sp}
0.0	N_2H^+/CO	0.51	0.05	0.18
0.0	HCN/CO	0.07	0.03	0.29
0.0	HNC/CO	0.21	0.03	0.29
0.0	HCO^+/CO	0.28	0.02	0.35
0.25	N_2H^+/CO	0.56	0.05	0.18
0.25	HCN/CO	0.2	0.02	0.30
0.25	HNC/CO	0.33	0.02	0.301
0.25	HCO^+/CO	0.35	0.01	0.36
0.5	N_2H^+/CO	0.62	0.05	0.18
0.5	HCN/CO	0.26	0.02	0.31
0.5	HNC/CO	0.38	0.02	0.32
0.5	HCO^+/CO	0.38	0.01	0.37
0.75	N_2H^+/CO	0.69	0.05	0.16
0.75	HCN/CO	0.33	0.02	0.27
0.75	HNC/CO	0.46	0.02	0.29
0.75	HCO^+/CO	0.41	0.02	0.35
1.0	N_2H^+/CO	0.68	0.06	0.15
1.0	HCN/CO	0.36	0.02	0.20
1.0	HNC/CO	0.51	0.02	0.25
1.0	HCO^+/CO	0.43	0.02	0.33

C.4 ENVIRONMENTAL DEPENDENCY OF LINE EMISSION AND LINE RATIOS

Figure 65 shows the average line intensities and average line ratios for all dense gas tracers as function of all environmental parameters tested for (Σ_{mol}, Σ_{SFR}, Σ_*, r, P_{DE}, σ_{CO}) for different environments in the disk. The binning is the same as for Figure 37 and Figure 41), but for pixels inside the corresponding environment. No masking is applied for average line intensities and line ratios (compare Section 6.3.2). The center and ring environments are based on a kinematic analysis of Colombo et al. (2014b), and we additionally separate the disk into northern and southern parts based on the galaxy center, to test for asymmetries between the spiral arms. All environments are shown in Figure 31.

For all molecules, the trend between line intensity and Σ_{mol} is offset to slightly higher line intensities in the center compared to the molecular ring and both northern and southern disk, which agree well. This is in agreement with the inverse radial dependency of the line emission found in Section 6.5.1. Similarly, there is an offset relation between average line intensity and σ_{CO} from one environment to the other, with the average line intensity being higher in center and ring compared to both spiral arms at the same values of σ_{CO}. Despite the offset, the shapes of the relations are very similar across all environments.

For Σ_{SFR}, however, the opposite can be seen: Center, ring and southern disk agree on a single distribution of line intensity as function of Σ_{SFR}, but the northern disk depends more shallow on Σ_{SFR}. While the line ratios differ for the center environment as function of Σ_{SFR}, the line ratios of the northern and southern arm mostly agree. The line ratios with N_2H^+ in the denominator are generally slightly lower in the southern arm compared to the northern one, but the data points agree well within their uncertainties.

Average line ratios among the dense gas tracing lines HCN, HNC, HCO^+ and N_2H^+ generally show very similar behavior with galactic properties across the individual environment. The most remarkable difference seen is the relation betweeen line ratios with N_2H^+ and their dependency on Σ_{mol}. We explore those in more detail in the main text.

C.5 PIXEL-BY-PIXEL DISTRIBUTION OF LINE INTENSITIES AND LINE RATIOS AS FUNCTION OF PHYSICAL PROPERTIES

We show the pixel-by-pixel distribution of line intensities of HCN, HNC, N_2H^+ and HCO^+ as function of galactic properties (Σ_{mol}, Σ_{SFR}, Σ_*, r, P_{DE}, σ_{CO}) in Figure 66. The data is colored by galactocentric radius, so that the impact of the central pixels can be clearly seen in the intensity-to-Σ_{mol} relation: All of the tested lines have bright emission in the center, that follows a distribution offset from the rest of the data points.

Figure 66 also shows the binned intensity trends utilizing all data points and only data points where emission is significantly detected. As discussed in Section 6.3.2 and Appendix C.1.3, excluding data points from the analysis can significantly bias the results.

We add spearman correlation coefficients ρ_{Sp} using all data (no masking) in Figure 66. These coefficients are strongly dependent on the SNR of the data and therefore we expect to find a decrease in coefficient value from brighter to fainter lines, or in

Table 16: Fitting average line intensities as function of physical properties per environment

	Full FoV		Center	Ring	North	South
line	slope	offset [dex]	slope	slope	slope	slope
Binned line intensities per Σ_{mol}						
CO	0.98±0.01	-6.1±0.0	0.78±0.02	0.98±0.01	0.99±0.01	0.99±0.02
HCN	1.04±0.04	-7.8±0.3	0.51±0.15	1.17±0.02	1.15±0.04	1.23±0.04
HNC	1.17±0.04	-9.3±0.3	0.51±0.13	1.29±0.02	1.43±0.05	1.25±0.06
HCO^+	1.26±0.02	-9.8±0.2	0.63±0.12	1.26±0.02	1.44±0.04	1.29±0.05
N_2H^+	1.49±0.05	-12.3±0.4	0.73±0.11	1.78±0.04	1.27±0.08	1.01±0.08
Binned line intensities per P_{DE}						
CO	0.63±0.01	-2.0±0.1	0.72±0.02	0.7±0.01	0.7±0.01	0.69±0.02
HCN	0.83±0.03	-4.4±0.2	0.64±0.13	0.85±0.02	0.82±0.02	0.88±0.02
HNC	0.89±0.02	-5.3±0.1	0.59±0.12	0.92±0.02	1.01±0.03	0.91±0.04
HCO^+	0.9±0.02	-5.1±0.1	0.74±0.12	0.9±0.01	1.0±0.03	0.92±0.03
N_2H^+	1.06±0.03	-6.6±0.2	0.92±0.09	1.22±0.04	0.91±0.08	0.71±0.04
Binned line intensities per Σ_{SFR}						
CO	0.7±0.03	2.3±0.0	0.6±0.1	0.82±0.04	0.6±0.05	1.05±0.09
HCN	0.99±0.04	1.4±0.0	1.28±0.12	1.08±0.04	0.71±0.06	1.28±0.1
HNC	0.95±0.04	0.9±0.0	1.21±0.1	1.12±0.05	0.67±0.06	1.29±0.11
HCO^+	0.91±0.04	1.1±0.0	1.19±0.07	1.06±0.05	0.66±0.07	1.28±0.1
N_2H^+	0.99±0.06	0.6±0.0	1.17±0.12	1.32±0.12	0.89±0.05	1.29±0.08
Binned line intensities per dist						
CO	-0.68±0.1	1.6±0.0	-0.12±0.1	-0.69±0.14	-0.35±0.36	-0.89±0.29
HCN	-1.04±0.04	0.4±0.0	-1.11±0.07	-1.53±0.2	-0.24±0.4	-1.95±0.48
HNC	-0.96±0.05	-0.0±0.0	-1.06±0.07	-1.18±0.22	-0.6±0.43	-2.07±0.51
HCO^+	-0.84±0.06	0.2±0.0	-0.99±0.09	-0.84±0.21	-0.61±0.41	-1.64±0.48
N_2H^+	-0.77±0.07	-0.4±0.0	-0.78±0.1	-0.62±0.41	1.05±0.7	-1.41±0.4
Binned line intensities per Σ_*						
CO	0.54±0.08	-3.4±0.7	0.12±0.1	0.88±0.11	1.11±0.71	2.0±0.52
HCN	0.94±0.07	-8.3±0.7	1.36±0.13	1.45±0.12	0.78±0.85	3.13±0.52
HNC	0.83±0.08	-7.7±0.7	1.23±0.12	1.25±0.13	0.54±1.05	3.66±0.55
HCO^+	0.68±0.09	-6.1±0.8	1.07±0.14	1.08±0.13	0.68±0.98	3.1±0.55
N_2H^+	0.68±0.07	-6.6±0.7	0.79±0.15	0.99±0.2	2.43±1.05	3.12±0.59
Binned line intensities per σ_{CO}						
CO	1.14±0.06	0.5±0.1	0.44±0.13	1.19±0.11	0.82±0.11	1.58±0.14
HCN	1.16±0.06	-0.8±0.1	0.95±0.09	1.19±0.11	0.79±0.1	1.52±0.16
HNC	1.17±0.06	-1.3±0.1	0.71±0.1	1.25±0.13	1.09±0.14	1.58±0.18
HCO^+	1.32±0.07	-1.2±0.1	0.62±0.1	1.32±0.12	0.96±0.13	1.72±0.19
N_2H^+	1.4±0.11	-1.8±0.1	0.67±0.12	1.75±0.24	1.34±0.27	0.95±0.19

Fit parameters fitting a linear (in log space) to molecular line emission as function of (from top to bottom) Σ_{mol}, P_{DE}, Σ_{SFR}, dist, Σ_*, σ_{CO} and (from left to right) per environment.

Table 17: Fitting average CO line ratios as function of galactic physical properties per environment

line	Full FoV slope	Full FoV offset [dex]	Center slope	Ring slope	North slope	South slope
Binned CO line ratios per Σ_{mol}						
HCN/CO	0.07±0.03	-1.8±0.3	-0.27±0.13	0.2±0.02	0.17±0.04	0.27±0.03
HNC/CO	0.2±0.03	-3.3±0.3	-0.25±0.12	0.31±0.02	0.45±0.05	0.32±0.05
HCO^+/CO	0.28±0.02	-3.7±0.2	-0.12±0.11	0.28±0.02	0.45±0.04	0.36±0.04
N_2H^+/CO	0.51±0.05	-6.2±0.4	-0.04±0.1	0.8±0.05	0.31±0.09	0.02±0.08
Binned CO line ratios per P_{DE}						
HCN/CO	0.2±0.03	-2.4±0.2	0.05±0.12	0.16±0.01	0.13±0.02	0.21±0.02
HNC/CO	0.25±0.03	-3.2±0.2	0.02±0.11	0.24±0.02	0.33±0.03	0.29±0.03
HCO^+/CO	0.25±0.02	-3.0±0.1	0.11±0.11	0.21±0.01	0.32±0.03	0.27±0.03
N_2H^+/CO	0.4±0.02	-4.5±0.1	0.2±0.08	0.55±0.04	0.24±0.09	0.02±0.05
Binned CO line ratios per Σ_{SFR}						
HCN/CO	0.45±0.04	-0.8±0.0	0.6±0.17	0.31±0.02	0.26±0.03	0.42±0.03
HNC/CO	0.46±0.03	-1.2±0.0	0.68±0.15	0.36±0.02	0.25±0.04	0.51±0.05
HCO^+/CO	0.38±0.02	-1.1±0.0	0.7±0.11	0.29±0.02	0.23±0.04	0.45±0.03
N_2H^+/CO	0.41±0.03	-1.6±0.0	0.75±0.09	0.57±0.08	0.45±0.04	0.3±0.07
Binned CO line ratios per per dist						
HCN/CO	-0.78±0.04	-1.2±0.0	-0.8±0.09	-0.79±0.12	0.05±0.15	-0.78±0.25
HNC/CO	-0.7±0.04	-1.7±0.0	-0.77±0.07	-0.49±0.13	-0.38±0.26	-0.73±0.32
HCO^+/CO	-0.49±0.05	-1.4±0.0	-0.67±0.09	-0.16±0.12	-0.39±0.19	-0.51±0.23
N_2H^+/CO	-0.45±0.04	-2.0±0.0	-0.5±0.05	0.09±0.34	1.56±0.38	-0.27±0.16
Binned CO line ratios per Σ_*						
HCN/CO	0.64±0.04	-7.1±0.3	0.89±0.12	0.58±0.05	0.82±0.2	1.59±0.17
HNC/CO	0.58±0.05	-7.0±0.5	0.99±0.12	0.38±0.06	1.47±0.31	1.92±0.31
HCO^+/CO	0.33±0.05	-4.5±0.5	0.63±0.14	0.2±0.06	1.08±0.35	1.52±0.19
N_2H^+/CO	0.38±0.05	-5.5±0.4	0.73±0.11	0.14±0.16	0.09±1.05	0.71±0.59
Binned CO line ratios per σ_{CO}						
HCN/CO	0.05±0.07	-1.4±0.1	0.46±0.16	-0.03±0.04	-0.05±0.07	-0.02±0.07
HNC/CO	0.06±0.06	-1.8±0.1	0.29±0.15	0.04±0.06	0.22±0.12	-0.09±0.1
HCO^+/CO	0.2±0.03	-1.7±0.0	0.21±0.11	0.11±0.05	0.14±0.08	0.13±0.1
N_2H^+/CO	0.28±0.07	-2.4±0.1	0.27±0.14	0.51±0.14	0.51±0.38	-0.51±0.12

Same as Table 16, but for CO line ratios

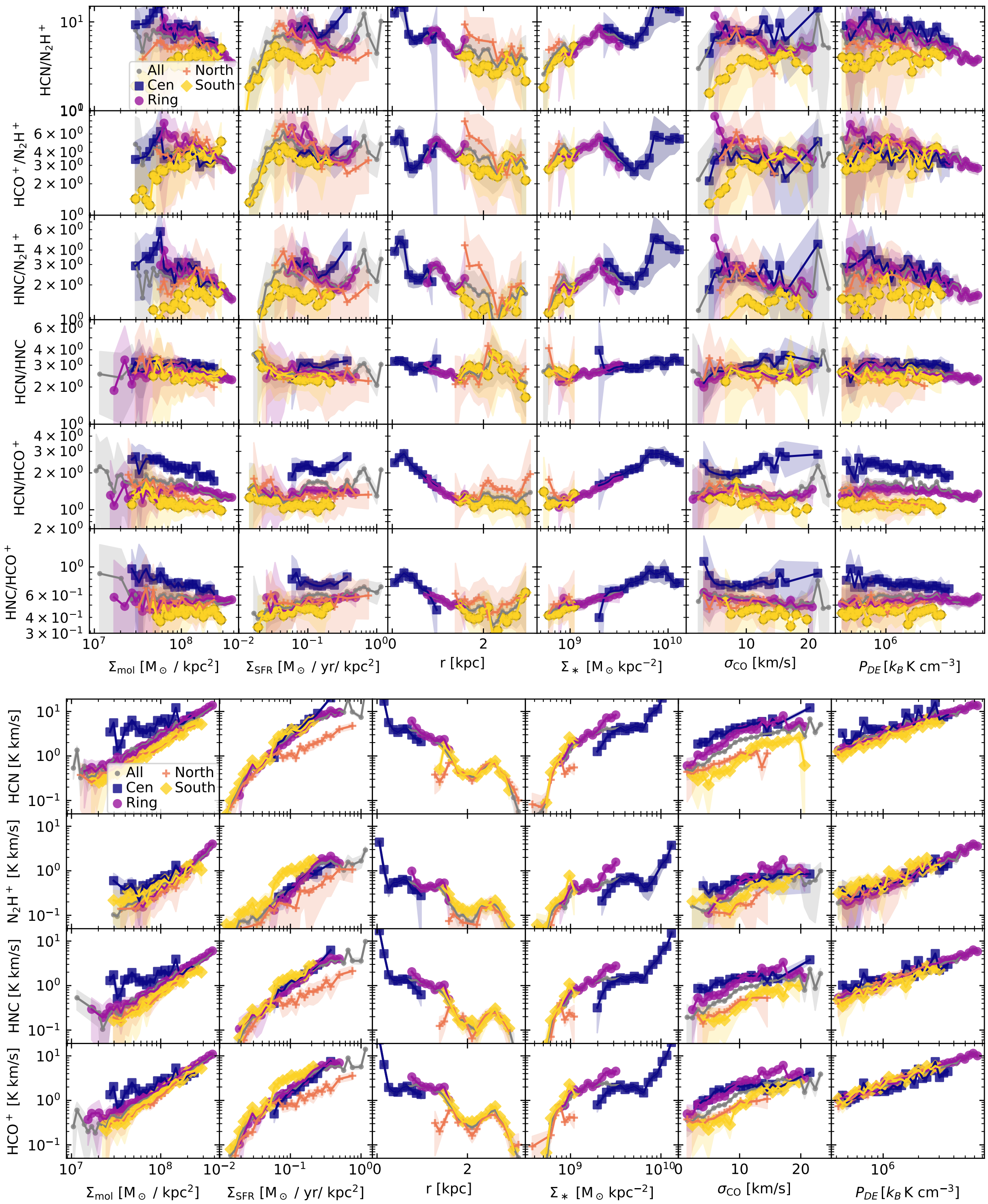

Figure 65: Average line ratios (top panels) and average line intensities (bottom panels) and as function of Σ_{mol}, Σ_{SFR}, r, Σ_*, σ_{CO} and P_{DE} for different environments in the disk (see Figure 31.

our case, from HCN to N_2H^+. For each line we find ρ_{Sp} highest for line intensity as function of P_{DE}, followed by Σ_{mol}, Σ_{SFR}, Σ_*, r and σ_{CO}.

Similarly, we show the pixel-by-pixel distribution of line intensities of HCN, HNC, N_2H^+ and HCO^+ divided by ^{12}CO emission as function of galactic properties (Σ_{mol}, Σ_{SFR}, Σ_*, r, P_{DE}, σ_{CO}) in Figure 67. Lastly, we also show the pixel-by-pixel distribution of line ratios among the dense gas tracing lines in Figure 68.

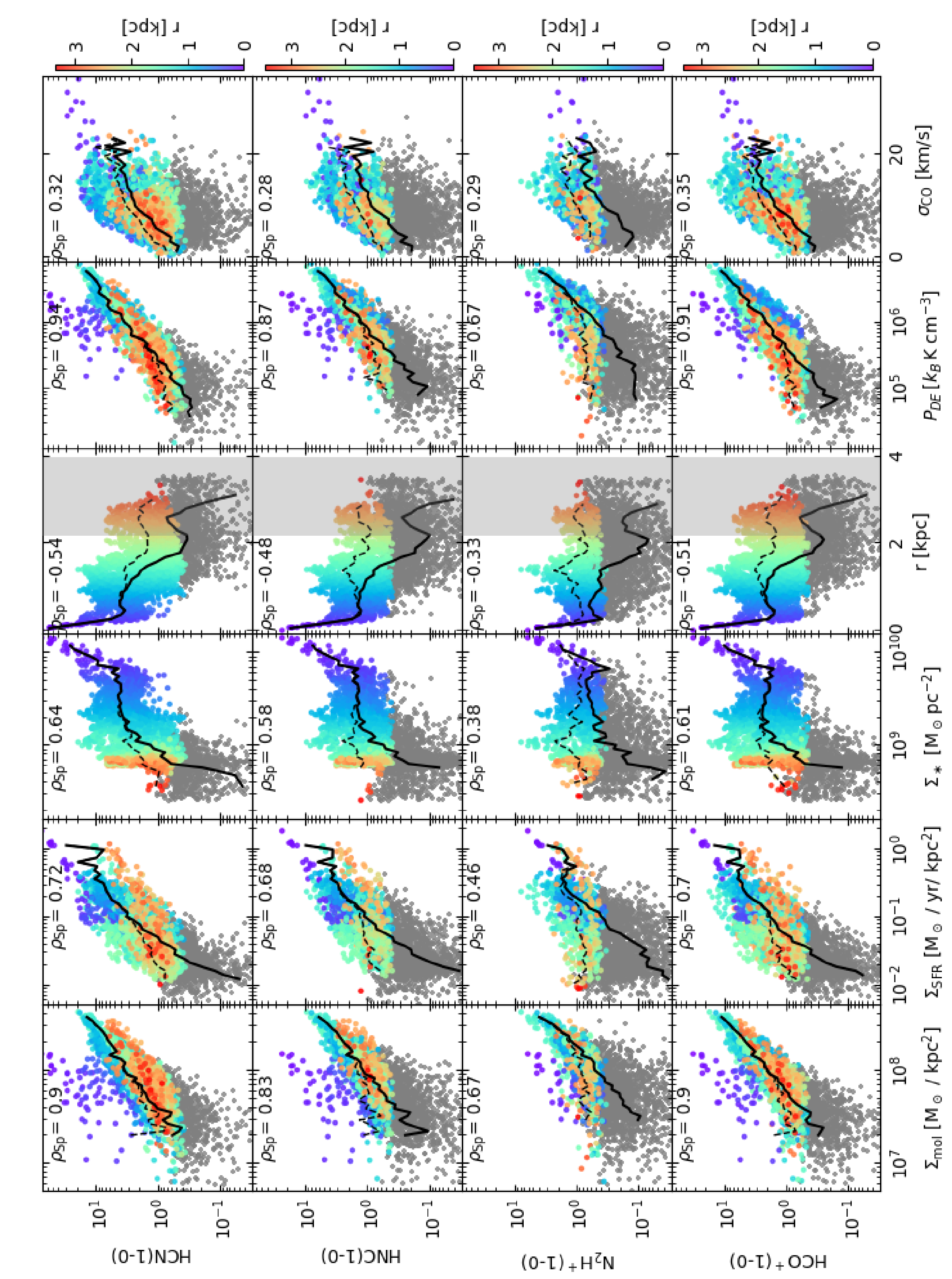

Figure 66: Pixel-by-pixel integrated line intensities for HCN, HNC, N_2H^+, HCO^+ (1-0) as function of Σ_{mol}, Σ_{SFR}, Σ_*, galactocentric radius, P_{DE} and σ_{CO} for both detected emission ($> 3\sigma$, colored by galactocentric distance) as well as all data (grey). Pixels with detected emission are colored by galactocentric radius. We show the binned average for all data (black solid line) and significant data (black dashed line). We add Spearman correlation coefficients using all data in the top left corner of each panel, but note that those coefficients strongly depend on the SNR of the line and a decrease in coefficients from brighter to fainter lines is expected (i.e. from HCN to N_2H^+). All p-values are below 5%.

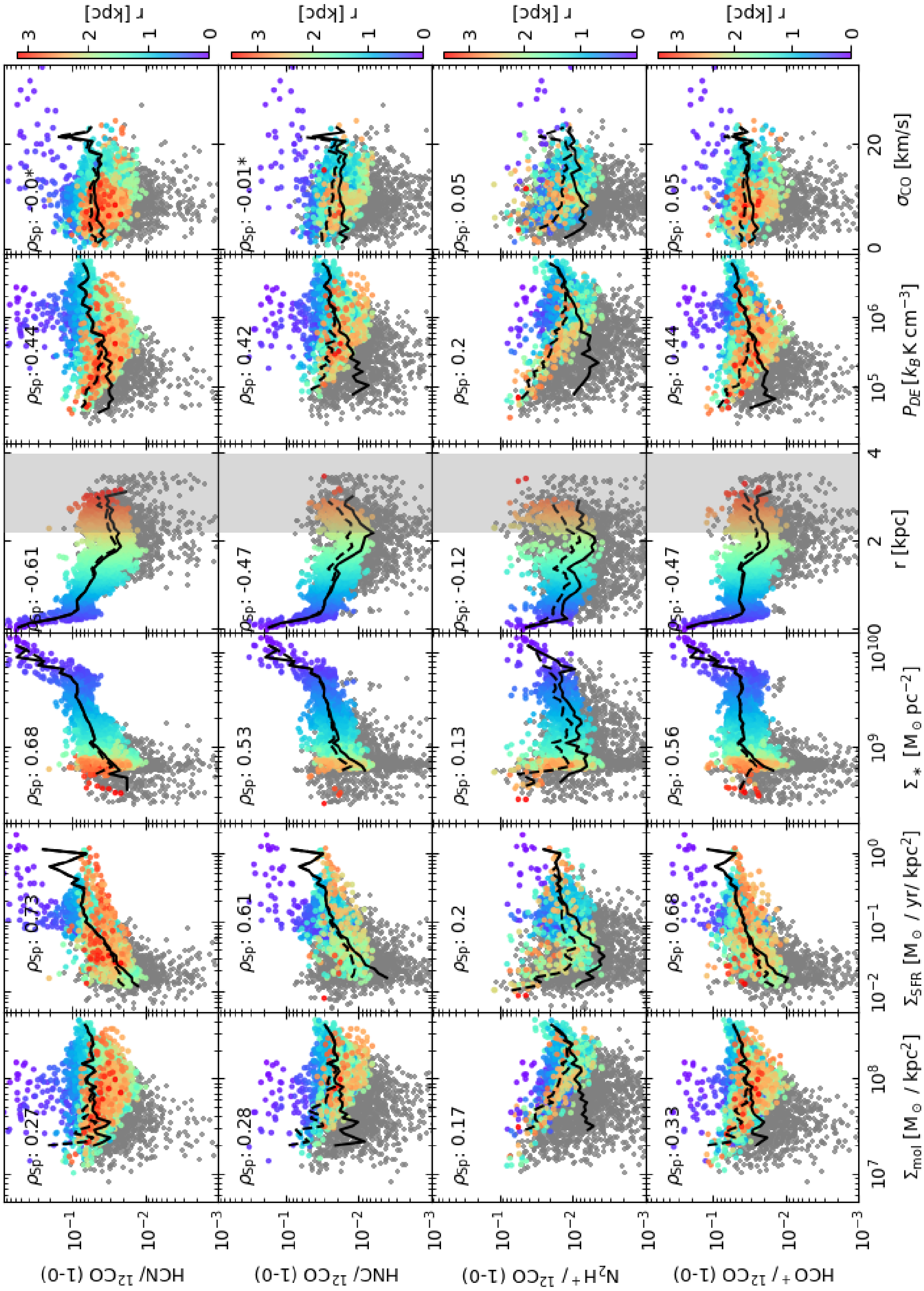

Figure 67: Same as Figure 66 but for ^{12}CO line ratios. We mark spearman correlation coefficients for which the corresponding p-value is below 5% with an asterisk.

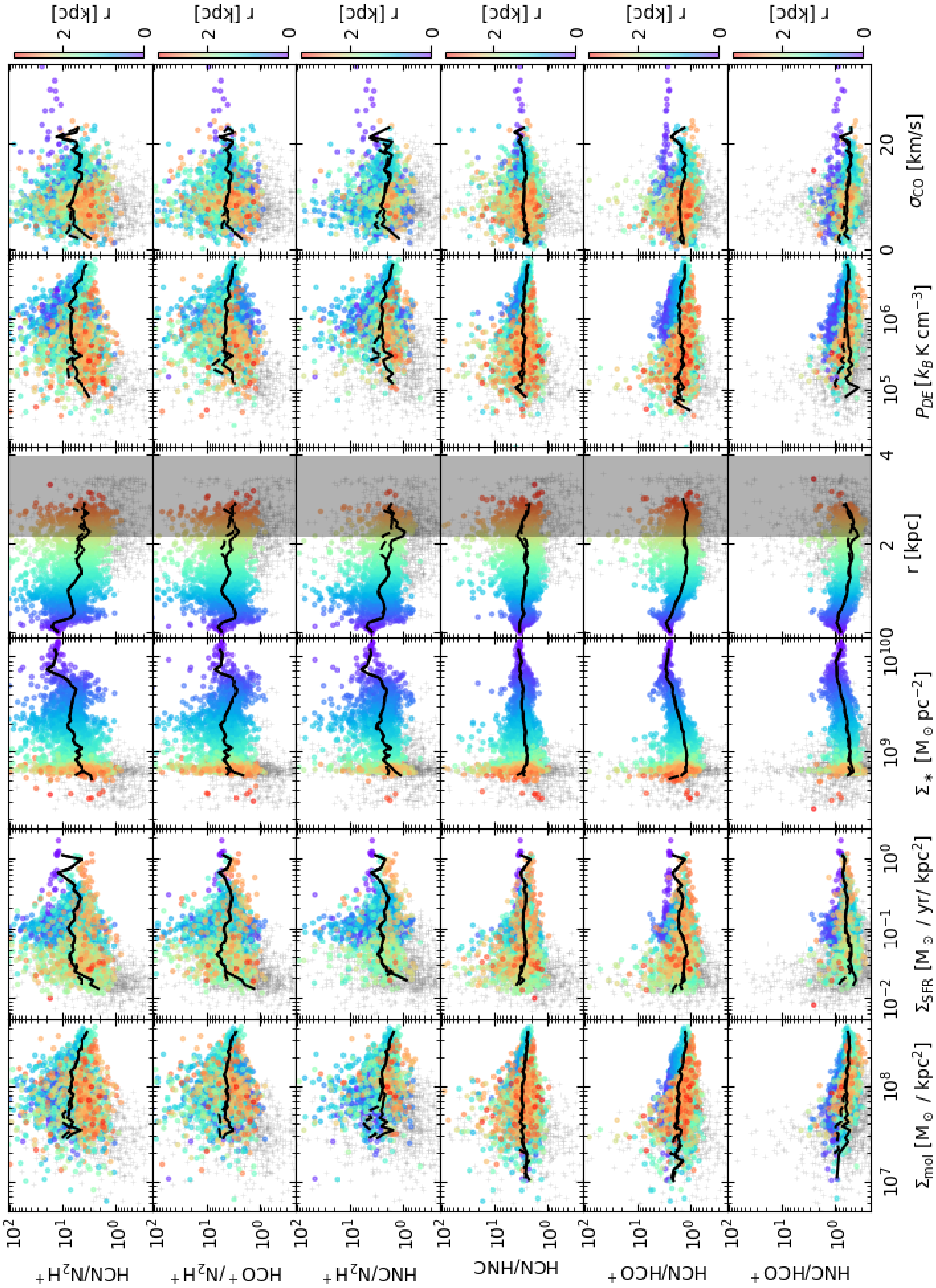

Figure 68: Same as Figure 66 but for line ratios between dense gas tracing lines HCN, HNC, HCO^+ and N_2H^+.

BIBLIOGRAPHY

MY PUBLICATIONS

PEER-REVIEWED FIRST-AUTHOR PUBLICATIONS:

1. **Stuber, S.K.**, Schinnerer, A. Usero, E., Bigiel, den Brok, J., Pety, J., Neumann, L., Jiménez-Donaire, M., Sun, Jiayi, Querejeta M., Barnes, A., Beslic, I., Cao, Y., Dale, D., Eibensteiner, C., Gleis, D., Glover, S., Grasha, K., Klessen, R., Liu, D., Meidt, S., Pan, H., Saito, T., Thorp, M., Williams, T.
   The SWAN view of dense gas in the Whirlpool - A cloud-scale comparison of N_2H^+, HCO^+, HNC and HCN emission in M51
   Submitted to A&A, April 2025

   - Included in Chapter 6

2. **Stuber, S.K.**, Pety, J., Usero, A., Schinnerer, E., Bigiel, F., Jimenez-Donaire, M., den Brok, J., Leroy, A.K., Galic, I., Hughes, A., Thorp, M., Barnes, A., Beslic, I., Eibensteiner, C., Gleis, D., Klessen, R., Liu, D., Pan, H., Saito, T., Sumit, S., Williams, T.
   Surveying the Whirlpool at Arcseconds with NOEMA (SWAN) II: Survey design and observations
   A&A, 696, 182 (2025) DOI:10.1051/0004-6361/202452330

   - Included in Chapter 4

3. **Stuber, S.K.**, Pety, J., Schinnerer, E., Bigiel, Usero, A., Beslic, I., Querejeta, M., F., Jimenez-Donaire, M., Leroy, A., den Brok, J., Neumann, L., Eibensteiner, C., Teng, Y., Barnes, A., Chevance, M., Colombo, D., Dale, D., Glover, S., Liu, D., Pan, H.
   Surveying the Whirlpool at Arcseconds with NOEMA (SWAN). I. Mapping the HCN and N_2H^+ 3mm lines
   A&A, 680, L20 (2023) DOI:10.1051/0004-6361/202348205

   - Included in Chapter 5

4. **Stuber, S.K.**, Schinnerer, E., Williams, T., Querejeta, M., Meidt, S., Emsellem, E., Barnes, A., Klessen, R., Leroy, A., Neumann, J., Sormani, M., Bigiel, F., Chevance, M., Dale, D., Faesi, C., Glover, S., Grasha, K., Kruijssen, D., Liu, D., Pan, H., Pety, J., Pinna, F., Saito, T., Usero, A., Watkins, E.
   The Gas Morphology of Nearby Main Sequence Galaxies
   A&A, 676, 113 (2023) DOI:10.1051/0004-6361/202346318

   - Not included in this thesis

5. **Stuber, S.K.**, Saito, T., Schinnerer, E., Emsellem, E., Querejeta, M., Williams, T., Barnes, A., Bigiel, F., Blanc, G., Dale, D., Grasha, K., Klessen, R., Kruijssen, D., Leroy, A., Meidt, S., Pan, H., Rosolowsky, E., Schruba, A., Sun, J., Usero, A.
   Frequency and nature of central molecular outflows in nearby star-forming disk galaxies
   A&A, 653, 172 (2023) DOI:10.1051/0004-6361/202141093

   - Not included in this thesis

PEER-REVIEWED CO-AUTHOR PUBLICATIONS:

- *Quantitative analysis of the molecular gas morphology in nearby disk galaxies* Yamamoto, Iono, Saito, Kuno, **Stuber, S.K**, Liu, Williams, PASJ 116 (2025)
- *Dense gas scaling relations at kiloparsec scales across nearby galaxies with the ALMA ALMOND and IRAM 30 m EMPIRE surveys* Neumann, Jimenez-Donaire, Leroy, et al., incl. **Stuber**, A&A, 693, L13 (2025)
- *CO Isotopologue-derived Molecular Gas Conditions and CO-to-H2 Conversion Factors in M51* den Brok, Jimenez-Donaire, Leroy, et al., incl. **Stuber**, AJ, 169, 18 (2025)
- *Azimuthal variations of stellar populations in barred galaxies* Neumann, Thomas, Maraston et al., incl. **Stuber**, MNRAS 534, 2438 (2024)
- *Neutral atomic and molecular gas dynamics in the nearby spiral galaxies NGC 1512, NGC 4535, and NGC 7496* Laudage, Eibensteiner, Bigiel et al., incl. **Stuber**, A&A 690, 169L (2024)
- *Do spiral arms enhance star formation efficiency?* Querejeta, Leroy, Meidt et al., incl. **Stuber**, A&A, 687, A293 (2024)
- *PHANGS-JWST: Data-processing Pipeline and First Full Public Data Release* Williams, Lee, Larson et al., incl. **Stuber** ApJS, 273, 13 (2024)
- *A 260 pc resolution ALMA map of HCN(1-0) in the galaxy NGC 4321* Neumann, Bigiel, Barnes et al., incl. **Stuber** accepted for publication in A&A, (2024)
- *Star Formation Efficiency in Nearby Galaxies Revealed with a New CO-to-H2 Conversion Factor Prescription* Teng, Chiang, Sandstrom et al., incl. **Stuber** ApJ, 961, 42 (2024)
- *A constant N2H+ (1-0)-to-HCN (1-0) ratio on kiloparsec scales* Jiménez-Donaire, Usero, Bešlić et al., incl. **Stuber** A&A, 676, L11 (2023)
- *Fuelling the nuclear ring of NGC 1097* Sormani, Barnes, Sun, **Stuber**, et al., MNRAS, 523, 2918 (2023)
- *Kinematic analysis of the super-extended H I disk of the nearby spiral galaxy M 83* Eibensteiner, Bigiel, Leroy et al., incl. **Stuber** A&A, 675, A37 (2023)
- *PHANGS-JWST First Results: Stellar-feedback-driven Excitation and Dissociation of Molecular Gas in the Starburst Ring of NGC 1365?* Liu, Schinnerer, Cao et al., incl. **Stuber** ApJL, 944, L19 (2023)
- *PHANGS-JWST First Results: A Statistical View on Bubble Evolution in NGC 628* Watkins, Barnes, Henny et al., incl. **Stuber** ApJL, 944, L24 (2023)
- *PHANGS-JWST First Results: Multiwavelength View of Feedback-driven Bubbles (the Phantom Voids) across NGC 628* Barnes, Watkins, Meidt et al., incl. **Stuber** ApJL, 944, L22 (2023)
- *The PHANGS-JWST Treasury Survey: Star Formation, Feedback, and Dust Physics at High Angular Resolution in Nearby GalaxieS* Lee, Sandstrom, Leroy et al., incl. **Stuber** ApJL, 944, L17 (2023)

- *PHANGS-JWST First Results: Rapid Evolution of Star Formation in the Central Molecular Gas Ring of NGC 1365* Schinnerer, Emsellem, Henshaw et al., incl. **Stuber** ApJL, 944, L15 (2023)
- *PHANGS-JWST First Results: Spurring on Star Formation: JWST Reveals Localized Star Formation in a Spiral Arm Spur of NGC 628* Williams, Sun, Barnes et al., incl. **Stuber** ApJL, 941, L27 (2022)
- *AGN-driven Cold Gas Outflow of NGC 1068 Characterized by Dissociation-sensitive Molecules* Saito, Takano, Harada et al., incl. **Stuber** ApJ, 935, 155 (2022)
- *The Kiloparsec-scale Neutral Atomic Carbon Outflow in the Nearby Type 2 Seyfert Galaxy NGC 1068: Evidence for Negative AGN Feedback* Saito, Takano, Harada et al., incl. **Stuber** ApJL, 927, L32 (2022)
- *PHANGS-ALMA: Arcsecond CO(2-1) Imaging of Nearby Star-forming Galaxies* Leroy, Schinnerer, Hughes et al., incl. **Stuber** ApJS, 257, 43 (2021)
- *New constraints on the 12CO(2-1)/(1-0) line ratio across nearby disc galaxies* den Brok, Chatzigiannakis, Bigiel et al., incl. **Stuber** MNRAS, 504, 3221 (2021)

BIBLIOGRAPHY

Aalto, S. (2005). In: *Proceedings of the 231st Symposium of the International Astronomical Union*, pp. 261–270.

Aalto, S., N. Falstad, S. Muller, et al. (2020). In: *Astronomy & Astrophysics* 640, A104.

Aalto, S., S. Garcia-Burillo, S. Muller, et al. (2012). In: *Astronomy & Astrophysics* 537, A44.

Aalto, S., S. Garcia-Burillo, S. Muller, et al. (2015). In: *Astronomy & Astrophysics* 574, A85.

Aalto, S., S. Hüttemeister, N. Z. Scoville, et al. (1998). In: *IAU Symposium*. Vol. 184, p. 249.

Aalto, S., A. G. Polatidis, S. Hüttemeister, et al. (2002). In: *Astronomy & Astrophysics* 381.3, pp. 783–794.

Aalto, S., S. J. E. Radford, N. Z. Scoville, et al. (1997). In: *The Astrophysical Journal* 475.2, pp. L107–L110.

Aladro, R., S. Martín, D. Riquelme, et al. (2015). In: *Astronomy & Astrophysics* 579, A101.

Backus, C., T. Velusamy, T. Thompson, et al. (2005). In: *Astronomical Society of the Pacific Conference Series*. Vol. 347, p. 61.

Barnes, A. T., J. Kauffmann, F. Bigiel, et al. (2020). In: *Monthly Notices of the Royal Astronomical Society* 497.2, pp. 1972–2001.

Barnes, A. T., E. J. Watkins, S. E. Meidt, et al. (2023). In: *The Astrophysical Journal Letters* 944.2, p. L22.

Behrens, E., J. G. Mangum, J. Holdship, et al. (2022). In: *The Astrophysical Journal* 939.2, p. 119.

Bemis, A. and C. D. Wilson (2019). In: *Astronomical Journal* 157.3, p. 131.

Bensch, F., J.-F. Panis, J. Stutzki, et al. (1997). In: *Astronomische Gesellschaft Abstract Series*. Vol. 13, p. 205.

Bergin, E. A. and M. Tafalla (2007). In: *Annual Review of Astronomy & Astrophysics* 45.1, pp. 339–396.

Bertin, G., C. C. Lin, S. A. Lowe, et al. (1989a). In: *The Astrophysical Journal* 338, p. 78.

– (1989b). In: *The Astrophysical Journal* 338, p. 104.

Bešlić, I., A. T. Barnes, F. Bigiel, et al. (2021). In: *Monthly Notices of the Royal Astronomical Society* 506.1, pp. 963–988.

Bešlić, I., A. T. Barnes, F. Bigiel, et al. (2024). In: *Astronomy & Astrophysics* 689, A122.

Beuther, H., R. Kuiper, and M. Tafalla (2025). In: arXiv:2501.16866.

Beuther, H., F. Wyrowski, K. M. Menten, et al. (2022). In: *Astronomy & Astrophysics* 665, A63.

Bigiel, F., A. Leroy, F. Walter, et al. (2008). In: *Astronomical Journal* 136.6, pp. 2846–2871.

Bigiel, F., A. K. Leroy, M. J. Jiménez-Donaire, et al. (2016). In: *The Astrophysical Journal* 822.2, p. L26.

Binney, J. and S. Tremaine (2008). Princeton University Press.

Bisbas, T. G., P. P. Papadopoulos, and S. Viti (2015). In: *The Astrophysical Journal* 803.1, p. 37.

Blanc, G. A., A. Heiderman, K. Gebhardt, et al. (2009). In: *The Astrophysical Journal* 704.1, pp. 842–862.

Boger, G. I. and A. Sternberg (2005). In: *The Astrophysical Journal* 632.1, pp. 302–315.

Bolatto, A. D., M. Wolfire, and A. K. Leroy (2013). In: *Annual Review of Astronomy & Astrophysics* 51.1, pp. 207–268.

Bolatto, A. D., T. Wong, D. Utomo, et al. (2017). In: *The Astrophysical Journal* 846.2, p. 159.

Bron, E., C. Daudon, J. Pety, et al. (2018). In: *Astronomy & Astrophysics* 610, A12.

Brouillet, N., S. Muller, F. Herpin, et al. (2005). In: *Astronomy & Astrophysics* 429, pp. 153–159.

Buchbender, C., C. Kramer, M. Gonzalez-Garcia, et al. (2013). In: *Astronomy & Astrophysics* 549, A17.

Buta, R. J. (2013). In: Cambridge University Press, p. 155.

Butterworth, J., S. Viti, P. P. Van der Werf, et al. (2024). In: *Astronomy & Astrophysics* 686, A31.

Calzetti, D., R. C. Kennicutt Jr., L. Bianchi, et al. (2005). In: *The Astrophysical Journal* 633.2, pp. 871–893.

Carroll, B. W. and D. A. Ostlie (2017). Cambridge University Press.

Cecil, G. (1988). In: *The Astrophysical Journal* 329, p. 38.

Cecil, G., M. A. Dopita, B. Groves, et al. (2002). In: *The Astrophysical Journal* 568.2, pp. 627–638.

Chen, H., J. Braine, Y. Gao, et al. (2017). In: *The Astrophysical Journal* 836.1, p. 101.

Chiang, I-D., K. M. Sandstrom, J. Chastenet, et al. (2024). In: *The Astrophysical Journal* 964.1, p. 18.

Colombo, D., A. Hughes, E. Schinnerer, et al. (2014a). In: *The Astrophysical Journal* 784.1, p. 3.

Colombo, D., S. E. Meidt, E. Schinnerer, et al. (2014b). In: *The Astrophysical Journal* 784.1, p. 4.

Cormier, D., F. Bigiel, M. J. Jiménez-Donaire, et al. (2018). In: *Monthly Notices of the Royal Astronomical Society* 475.3, pp. 3909–3933.

Croxall, K. V., Richard W. Pogge, D. A. Berg, et al. (2015). In: *The Astrophysical Journal* 808.1, p. 42.

Cuadrado, S., J. R. Goicoechea, P. Pilleri, et al. (2015). In: *Astronomy & Astrophysics* 575, A82.

Dale, D. A., G. B. Graham, A. T. Barnes, et al. (2025). In: *Astronomical Journal* 169.3, p. 133.

de Vaucouleurs, G., A. de Vaucouleurs, Herold G. Corwin Jr., et al. (1991). Springer, New York.

den Brok, J., M. J. Jiménez-Donaire, A. Leroy, et al. (2025). In: *Astronomical Journal* 169.1, p. 18.

den Brok, J. S., F. Bigiel, K. Sliwa, et al. (2022). In: *Astronomy & Astrophysics* 662, A89.

Dobbs, C. L., M. R. Krumholz, J. Ballesteros-Paredes, et al. (2014). In: *Protostars and Planets VI*. University of Arizona Press, pp. 3–26.

Dobbs, C. L. and J. E. Pringle (2013). In: *Monthly Notices of the Royal Astronomical Society* 432.1, pp. 653–667.

Draine, B. T. (2011). Princeton University Press.

Dumas, G., E. Schinnerer, F. S. Tabatabaei, et al. (2011). In: *Astronomical Journal* 141.2, p. 41.

Egusa, F., J. Koda, and N. Scoville (2011). In: *The Astrophysical Journal* 726.2, p. 85.

Egusa, F., K. Kohno, Y. Sofue, et al. (2009). In: *The Astrophysical Journal* 697.2, pp. 1870–1891.

Egusa, F., E. Mentuch Cooper, J. Koda, et al. (2017). In: *Monthly Notices of the Royal Astronomical Society* 465.1, pp. 460–471.

Eibensteiner, C., A. T. Barnes, F. Bigiel, et al. (2022). In: *Astronomy & Astrophysics* 659, A173.

Einig, L., J. Pety, A. Roueff, et al. (2023). In: *Astronomy & Astrophysics* 677, A158.

Evans II, N. J., A. Heiderman, and N. Vutisalchavakul (2014). In: *The Astrophysical Journal* 782.2, p. 114.

Fabian, A. C. (2012). In: *Annual Review of Astronomy & Astrophysics* 50, pp. 455–489.

Faustino Vieira, H., A. Duarte-Cabral, T. A. Davis, et al. (2024). In: *Monthly Notices of the Royal Astronomical Society* 527.2, pp. 3639–3658.

Ferreras, I., M. Cropper, D. Kawata, et al. (2012). In: *Monthly Notices of the Royal Astronomical Society* 424.3, pp. 1636–1646.

Ferrière, K. M. (2001). In: *Reviews of Modern Physics* 73.4, pp. 1031–1066.

Ford, H. C., P. C. Crane, G. H. Jacoby, et al. (1985). In: *The Astrophysical Journal* 293, pp. 132–147.

Foyle, K., H.-W. Rix, C. L. Dobbs, et al. (2011). In: *The Astrophysical Journal* 735.2, p. 101.

Fraser-McKelvie, A., A. Aragón-Salamanca, M. Merrifield, et al. (2020). In: *Monthly Notices of the Royal Astronomical Society* 495.4, pp. 4158–4169.

Galic et al, I. (submitted). In: *Astronomy & Astrophysics*.

Gallagher, Molly J., A. K. Leroy, F. Bigiel, et al. (2018a). In: *The Astrophysical Journal* 858.2, p. 90.

Gallagher, Molly J., A. K. Leroy, F. Bigiel, et al. (2018b). In: *The Astrophysical Journal* 868.2, p. L38.

Gao, Y. and P. M. Solomon (2004). In: *The Astrophysical Journal* 606.1, pp. 271–290.

Garcia-Burillo, S., M. Guelin, and J. Cernicharo (1993). In: *Astronomy & Astrophysics* 274, pp. 123–147.

García-Burillo, S., F. Combes, A. Usero, et al. (2014). In: *Astronomy & Astrophysics* 567, A125.

Gildas Team (2013). In: *Astrophysics Source Code Library*, ascl:1305.010.

Goldsmith, P. F. and J. Kauffmann (2017). In: *The Astrophysical Journal* 841.1, p. 25.

Gratier, P., E. Bron, M. GE., et al. (2017). In: *Astronomy & Astrophysics* 599, A100.

Hacar, A., A. D. Bosman, and E. F. van Dishoeck (2020). In: *Astronomy & Astrophysics* 635, A4.

Harada, N., D. S. Meier, S. Martín, et al. (2024a). In: *The Astrophysical Journal Supplement Series* 271.2, p. 38.

Harada, N., Y. Nishimura, Y. Watanabe, et al. (2019). In: *The Astrophysical Journal* 871.2, p. 238.

Harada, N., T. Saito, Y. Nishimura, et al. (2024b). In: *The Astrophysical Journal* 969.2, p. 82.

Harada, N., K. Sakamoto, S. Martín, et al. (2018). In: *The Astrophysical Journal* 855.1, p. 49.

Helfer, T. T. and L. Blitz (1993). In: *The Astrophysical Journal* 419, p. 86.

Helfer, T. T., M. D. Thornley, M. W. Regan, et al. (2003). In: *The Astrophysical Journal Supplement Series* 145.2, pp. 259–327.

Henry, A. L., A. C. Quillen, and R. Gutermuth (2003). In: *Astronomical Journal* 126.6, pp. 2831–2839.

Henshaw, J. D., A. T. Barnes, C. Battersby, et al. (2023). In: 534, p. 83.

Heyer, M., B. Gregg, D. Calzetti, et al. (2022). In: *The Astrophysical Journal* 930.2, p. 170.

Heyer, M., Coleman Krawczyk, J. Duval, et al. (2009). In: *The Astrophysical Journal* 699.2, pp. 1092–1103.

Heyer, M. H., J. M. Carpenter, and R. L. Snell (2001). In: *The Astrophysical Journal* 551.2, p. 852.

Ho, L. C., A. V. Filippenko, and W. L. W. Sargent (1997). In: *The Astrophysical Journal Supplement Series* 112.2, p. 315.

Hodge, J. A., I. Smail, F. Walter, et al. (2019). In: *The Astrophysical Journal* 876.2, p. 130.

Hughes, A., S. E. Meidt, D. Colombo, et al. (2013). In: *The Astrophysical Journal* 779, p. 46.

Imanishi, M., S. Baba, K. Nakanishi, et al. (2023). In: *The Astrophysical Journal* 950.1, p. 75.

Indriolo, N. and B. J. McCall (2012). In: *The Astrophysical Journal* 745.1, p. 91.

Indriolo, N., D. A. Neufeld, M. GE., et al. (2015). In: *The Astrophysical Journal* 800.1, p. 40.

Jiménez-Donaire, M. J., F. Bigiel, A. K. Leroy, et al. (2019). In: *The Astrophysical Journal* 880.2, p. 127.

Jiménez-Donaire, M. J., A. Usero, I. Bešlić, et al. (2023). In: *Astronomy & Astrophysics* 676, p. L11.

Jones, G. H., P. C. Clark, S. C. O. Glover, et al. (2023). In: *Monthly Notices of the Royal Astronomical Society* 520.1, pp. 1005–1021.

Jones, P. A., M. G. Burton, M. R. Cunningham, et al. (2012). In: *Monthly Notices of the Royal Astronomical Society* 419.4, pp. 2961–2986.

Jørgensen, J. K., F. L. Schöier, and E. F. van Dishoeck (2004). In: *Astronomy & Astrophysics* 416, pp. 603–622.

Kaneko, H., T. Tosaki, K. Tanaka, et al. (2023). In: *The Astrophysical Journal* 953, p. 139.

Kauffmann, J., P. F. Goldsmith, G. Melnick, et al. (2017). In: *Astronomy & Astrophysics* 605, p. L5.

Kelly, G., S. Viti, S. García-Burillo, et al. (2017). In: *Astronomy & Astrophysics* 597, A11.

Kennicutt, R. C. and N. J. Evans (2012). In: *Annual Review of Astronomy & Astrophysics* 50, pp. 531–608.

Kennicutt Jr., R. C. (1998). In: *Annual Review of Astronomy & Astrophysics* 36, pp. 189–232.

Kennicutt Jr., R. C., D. Calzetti, F. Walter, et al. (2007). In: *The Astrophysical Journal* 671.1, pp. 333–348.

Kessler, S., A. Leroy, M. Querejeta, et al. (Mar. 2020). In: *The Astrophysical Journal* 892.1, p. 23.

Keto, E. R. and P. C. Myers (1986). In: *The Astrophysical Journal* 304, p. 466.

Kim, J., M. Chevance, J. M. D. Kruijssen, et al. (2023). In: *The Astrophysical Journal Letters* 944.2, p. L20.

Kirk, H., Doug Johnstone, and M. Tafalla (2007). In: *The Astrophysical Journal* 668.2, pp. 1042–1063.

Kirsanova, M. S., A. F. Punanova, D. A. Semenov, et al. (2021). In: *Monthly Notices of the Royal Astronomical Society* 507.3, pp. 3810–3829.

Klessen, R. S. and S. C. O. Glover (2015). In: *Lessons from the Local Group*. Springer International Publishing, pp. 137–146.

Koda, J., T. Sawada, M. C. H. Wright, et al. (2011). In: *The Astrophysical Journal Supplement Series* 193.1, p. 19.

Koda, J., N. Scoville, T. Sawada, et al. (2009). In: *The Astrophysical Journal Letters* 700.2, pp. L132–L136.

Kohno, K. (2005). In: *American Institute of Physics Conference Series*. Vol. 783. AIP, pp. 203–208.

Kormendy, J. and L. C. Ho (2013). In: *Annual Review of Astronomy & Astrophysics* 51.1, pp. 511–653.

Kormendy, J. and R. C. Kennicutt Jr. (2004). In: *Annual Review of Astronomy & Astrophysics* 42.1, pp. 603–683.

Kramer, C., J. Peñalver, and A. Greve (2013). In: *IRAM Memo 2017-1*.

Kreckel, K., C. Faesi, J. M. D. Kruijssen, et al. (2018). In: *The Astrophysical Journal Letters* 863.2, p. L21.

Kregel, M., P. C. van der Kruit, and R. de Grijs (2002). In: *Monthly Notices of the Royal Astronomical Society* 334.3, pp. 646–668.

Krieger, N., A. D. Bolatto, A. K. Leroy, et al. (2020). In: *The Astrophysical Journal* 897.2, p. 176.

Krolik, J. H. and T. R. Kallman (1983). In: *The Astrophysical Journal* 267, pp. 610–624.

Kruijssen, J. M. D., A. Schruba, A. P. S. Hygate, et al. (2018). In: *Monthly Notices of the Royal Astronomical Society* 479.2, pp. 1866–1952.

Krumholz, M. R. (2014). In: *Physics Reports* 539, pp. 49–134.

Lada, C. J. and T. M. Dame (2020). In: *The Astrophysical Journal* 898.1, p. 3.

Lada, C. J., J. Forbrich, M. Lombardi, et al. (2012). In: *The Astrophysical Journal* 745.2, p. 190.

Lada, C. J., M. Lombardi, and J. F. Alves (2010). In: *The Astrophysical Journal* 724.1, p. 687.

Lamers, H. J. G. L. M., N. Panagia, S. Scuderi, et al. (2002). In: *The Astrophysical Journal* 566.2, pp. 818–832.

Lang, P., S. E. Meidt, E. Rosolowsky, et al. (2020). In: *The Astrophysical Journal* 897.2, p. 122.

Langer, W. D. and A. A. Penzias (1990). In: *The Astrophysical Journal* 357, p. 477.

Larson, R. B. (1981). In: *Monthly Notices of the Royal Astronomical Society* 194, pp. 809–826.

Ledger, B., T. Saito, D. Iono, et al. (2024). In: *Monthly Notices of the Royal Astronomical Society* 527.2, pp. 2963–2990.

Lee, J. C., K. M. Sandstrom, A. K. Leroy, et al. (2023). In: *The Astrophysical Journal Letters* 944.2, p. L17.

Leroy, A. K., A. Hughes, D. Liu, et al. (2021a). In: *The Astrophysical Journal Supplement Series* 255.1, p. 19.

Leroy, A. K., K. Sandstrom, E. Rosolowsky, et al. (2023). In: *The Astrophysical Journal Letters* 944.2, p. L9.

Leroy, A. K., K. M. Sandstrom, D. Lang, et al. (2019). In: *The Astrophysical Journal Supplement Series* 244.2, p. 24.

Leroy, A. K., E. Schinnerer, A. Hughes, et al. (2017a). In: *The Astrophysical Journal* 846.1, p. 71.

Leroy, A. K., E. Schinnerer, A. Hughes, et al. (2021b). In: *The Astrophysical Journal Supplement Series* 257.2, p. 43.

Leroy, A. K., A. Usero, A. Schruba, et al. (2017b). In: *The Astrophysical Journal* 835.2, p. 217.

Leroy, A. K., F. Walter, P. Martini, et al. (2015). In: *The Astrophysical Journal* 814.2, p. 83.

Leroy, A. K., F. Walter, K. Sandstrom, et al. (2013). In: *Astronomical Journal* 146.2, p. 19.

Lin, C. C. and F. H. Shu (1964). In: *The Astrophysical Journal* 140, p. 646.

Lin, L., H.-A. Pan, S. L. Ellison, et al. (2019). In: *The Astrophysical Journal Letters* 884.2, p. L33.

Liszt, H. and R. Lucas (2001). In: *Astronomy & Astrophysics* 370, pp. 576–585.

Loison, J.-C., V. Wakelam, and K. M. Hickson (2014). In: *Monthly Notices of the Royal Astronomical Society* 443.1, pp. 398–410.

Longmore, S. N., J. Bally, L. Testi, et al. (2013). In: *Monthly Notices of the Royal Astronomical Society* 429.2, pp. 987–1000.

Lord, S. D. and J. S. Young (1990). In: *The Astrophysical Journal* 356, p. 135.

Lundgren, A. A., T. Wiklind, H. Olofsson, et al. (2004). In: *Astronomy & Astrophysics* 413, pp. 505–523.

Luo, G., T. G. Bisbas, M. Padovani, et al. (2024a). In: *Astronomy & Astrophysics* 690, A293.

Luo, G., L. Colzi, Tie Liu, et al. (2024b). In: *Astronomy & Astrophysics* 690, A372.

MacKay, D., M. Thompson, and J. Urquhart (2023). Cambridge University Press.

Maloney, P. R., D. J. Hollenbach, and A. G. G. M. Tielens (1996). In: *The Astrophysical Journal* 466, p. 561.

Maoz, D. (2016). Princeton University Press.

Martín, S., K. Kohno, T. Izumi, et al. (2015). In: *Astronomy & Astrophysics* 573, A116.

Martín, S., J. G. Mangum, N. Harada, et al. (2021). In: *Astronomy & Astrophysics* 656, A46.

Martín, S., M. A. Requena-Torres, J. Martín-Pintado, et al. (2008). In: *The Astrophysical Journal* 678.1, pp. 245–254.

Martínez-García, E. E. and R. A. González-Lópezlira (2013). In: *The Astrophysical Journal* 765.2, p. 105.

Matsushita, S., S. Muller, and J. Lim (2007). In: *Astronomy & Astrophysics* 468.3, pp. L49–L52.

Matsushita, S., D.-V. Trung, F. Boone, et al. (2015). In: *The Astrophysical Journal* 799.1, p. 26.

McQuinn, K. B. W., E. D. Skillman, A. E. Dolphin, et al. (2016). In: *The Astrophysical Journal* 826.1, p. 21.

Meidt, S. E., A. Hughes, C. L. Dobbs, et al. (2015). In: *The Astrophysical Journal* 806.1, p. 72.

Meidt, S. E., E. Schinnerer, S. García-Burillo, et al. (2013). In: *The Astrophysical Journal* 779.1, p. 45.

Meier, D. S. and Jean L. Turner (2005). In: *The Astrophysical Journal* 618.1, pp. 259–280.

Meier, D. S., F. Walter, A. D. Bolatto, et al. (2015). In: *The Astrophysical Journal* 801.1, p. 63.

Meijerink, R., M. Spaans, A. F. Loenen, et al. (2011). In: *Astronomy & Astrophysics* 525, A119.

Michiyama, T., D. Iono, K. Sliwa, et al. (2018). In: *The Astrophysical Journal* 868.2, p. 95.

Mills, E. A. C. and C. Battersby (2017). In: *The Astrophysical Journal* 835.1, p. 76.

Nakai, N., N. Kuno, T. Handa, et al. (1994). In: *Publications of the Astronomical Society of Japan* 46, pp. 527–538.

Nakajima, T., S. Takano, T. Tosaki, et al. (2023). In: *The Astrophysical Journal* 955.1, p. 27.

Neumann, L., F. Bigiel, A. T. Barnes, et al. (2024). In: *Astronomy & Astrophysics* 691, A121.

Neumann, L., J. S. den Brok, F. Bigiel, et al. (2023a). In: *Astronomy & Astrophysics* 675, A104.

Neumann, L., M. J. Gallagher, F. Bigiel, et al. (2023b). In: *Monthly Notices of the Royal Astronomical Society* 521.3, pp. 3348–3383.
Neumann, L., M. J. Jiménez-Donaire, A. K. Leroy, et al. (2025). In: *Astronomy & Astrophysics* 693, p. L13.
Nishimura, Y., T. Shimonishi, Y. Watanabe, et al. (2016a). In: *The Astrophysical Journal* 818.2, p. 161.
– (2016b). In: *The Astrophysical Journal* 829.2, p. 94.
Oka, T., T. R. Geballe, M. Goto, et al. (2019). In: *The Astrophysical Journal* 883.1, p. 54.
Papadopoulos, P. P. (2007). In: *The Astrophysical Journal* 656.2, pp. 792–797.
Patra, S., N. J. Evans II, Kee-Tae Kim, et al. (2025). In: *arXiv e-prints*, arXiv:2503.07931.
Pereira-Santaella, M., L. Colina, S. García-Burillo, et al. (2018). In: *Astronomy & Astrophysics* 616, A171.
Pety, J., V. V. Guzmán, J. H. Orkisz, et al. (2017). In: *Astronomy & Astrophysics* 599, A98.
Pety, J. and N. Rodríguez-Fernández (2010). In: *Astronomy & Astrophysics* 517, A12.
Pety, J., E. Schinnerer, A. K. Leroy, et al. (2013). In: *The Astrophysical Journal* 779.1, p. 43.
Pineda, J. L., W. D. Langer, T. Velusamy, et al. (2013). In: *Astronomy & Astrophysics* 554, A103.
Pirogov, L., I. Zinchenko, P. Caselli, et al. (2003). In: *Astronomy & Astrophysics* 405, pp. 639–654.
Pour-Imani, H., D. Kennefick, J. Kennefick, et al. (2016). In: *The Astrophysical Journal Letters* 827.1, p. L2.
Priestley, F. D., P. C. Clark, S. C. O. Glover, et al. (2023). In: *Monthly Notices of the Royal Astronomical Society* 526.4, pp. 4952–4960.
– (2024). In: *Monthly Notices of the Royal Astronomical Society* 531.4, pp. 4408–4421.
Querejeta, M., A. K. Leroy, S. E. Meidt, et al. (2024). In: *Astronomy & Astrophysics* 687, A293.
Querejeta, M., S. E. Meidt, E. Schinnerer, et al. (2015). In: *The Astrophysical Journal Supplement Series* 219, p. 5.
Querejeta, M., S. E. Meidt, E. Schinnerer, et al. (2016a). In: *Astronomy & Astrophysics* 588, A33.
Querejeta, M., E. Schinnerer, S. García-Burillo, et al. (2016b). In: *Astronomy & Astrophysics* 593, A118.
Querejeta, M., E. Schinnerer, S. García-Burillo, et al. (2017). In: *Astronomy & Astrophysics* 599, p. C1.
Querejeta, M., E. Schinnerer, S. Meidt, et al. (2021). In: *Astronomy & Astrophysics* 656, A133.
Querejeta, M., E. Schinnerer, A. Schruba, et al. (2019). In: *Astronomy & Astrophysics* 625, A19.
Rampadarath, H., R. Soria, R. Urquhart, et al. (2018). In: *Monthly Notices of the Royal Astronomical Society* 476.3, pp. 2876–2889.
Roberts, W. W. (1969). In: *The Astrophysical Journal* 158, p. 123.
Rodrıguez-Fernandez, N. J., J. Pety, and F. Gueth (2008). In: *IRAM-Memos*.
Rosolowsky, E. and A. Leroy (2006). In: *Publications of the Astronomical Society of the Pacific* 118.842, pp. 590–610.
Rybak, M., J. A. Hodge, T. R. Greve, et al. (2022). In: *Astronomy & Astrophysics* 667, A70.
Rydbeck, G., A. Hjalmarson, and O. E. H. Rydbeck (1985). In: *Astronomy & Astrophysics* 144, pp. 282–294.
Sage, L. J. and L. M. Ziurys (1995). In: *The Astrophysical Journal* 447, p. 625.

Saintonge, A., B. Catinella, L. J. Tacconi, et al. (2017). In: *The Astrophysical Journal Supplement Series* 233.2, p. 22.

Saito, T., S. Takano, N. Harada, et al. (2022). In: *The Astrophysical Journal* 935.2, p. 155.

Sandstrom, K. M., A. K. Leroy, F. Walter, et al. (2013). In: *The Astrophysical Journal* 777.1, p. 5.

Santa-Maria, M. G., J. R. Goicoechea, M. Etxaluze, et al. (2021). In: *Astronomy & Astrophysics* 649, A32.

Santa-Maria, M. G., J. R. Goicoechea, J. Pety, et al. (2023). In: *Astronomy & Astrophysics* 679, A4.

Schinnerer, E., E. Emsellem, J. D. Henshaw, et al. (2023). In: *The Astrophysical Journal Letters* 944.2, p. L15.

Schinnerer, E. and A. K. Leroy (2024). In: *Annual Review of Astronomy & Astrophysics* 62.1, pp. 369–436.

Schinnerer, E., S. E. Meidt, D. Colombo, et al. (2017). In: *The Astrophysical Journal* 836.1, p. 62.

Schinnerer, E., S. E. Meidt, J. Pety, et al. (2013). In: *The Astrophysical Journal* 779.1, p. 42.

Schmidt, M. (1959). In: *The Astrophysical Journal* 129, p. 243.

Schober, J., D. R. G. Schleicher, and R. S. Klessen (2015). In: *Monthly Notices of the Royal Astronomical Society* 446.1, pp. 2–17.

Schruba, A., A. K. Leroy, F. Walter, et al. (2011). In: *Astronomical Journal* 142.2, p. 37.

Schuster, K. F., C. Kramer, M. Hitschfeld, et al. (2007). In: *Astronomy & Astrophysics* 461.1, pp. 143–151.

Scoville, N. and J. S. Young (1983). In: *The Astrophysical Journal* 265, pp. 148–165.

Scoville, N. Z., M. S. Yun, L. Armus, et al. (1998). In: *The Astrophysical Journal Letters* 493.2, pp. L63–L66.

Sheth, K., M. Regan, J. L. Hinz, et al. (2010). In: *Publications of the Astronomical Society of the Pacific* 122.898, p. 1397.

Shetty, R., S. N. Vogel, E. C. Ostriker, et al. (2007). In: *The Astrophysical Journal* 665.2, p. 1138.

Shirley, Yancy L. (2015). In: *Publications of the Astronomical Society of the Pacific* 127.949, p. 299.

Silk, Joseph (2013). In: *The Astrophysical Journal* 772.2, p. 112.

Skatrud, D. D., F. C. De Lucia, Geoffrey A. Blake, et al. (1983). In: *Journal of Molecular Spectroscopy* 99.1, pp. 35–46.

Sormani, M. C., A. T. Barnes, J. Sun, et al. (2023). In: *Monthly Notices of the Royal Astronomical Society* 523.2, pp. 2918–2927.

Stuber, S. K., J. Pety, A. Usero, et al. (2025). In: *Astronomy & Astrophysics* 696, A182.

Stuber, S. K., Jerome Pety, E. Schinnerer, et al. (2023a). In: *Astronomy & Astrophysics* 680, p. L20.

Stuber, S. K., T. Saito, E. Schinnerer, et al. (2021). In: *Astronomy & Astrophysics* 653, A172.

Stuber, S. K., E. Schinnerer, T. G. Williams, et al. (2023b). In: *Astronomy & Astrophysics* 676, A113.

Sturm, E., E. González-Alfonso, S. Veilleux, et al. (2011). In: *The Astrophysical Journal Letters* 733.1, p. L16.

Sun, J., A. K. Leroy, E. C. Ostriker, et al. (2020). In: *The Astrophysical Journal* 892.2, p. 148.

Sun, J., A. K. Leroy, E. Rosolowsky, et al. (2022). In: *The Astronomical Journal* 164.2, p. 43.

Sun, J., A. K. Leroy, A. Schruba, et al. (2018). In: *The Astrophysical Journal* 860.2, p. 172.

Sutter, J., K. Sandstrom, J. Chastenet, et al. (2024). In: *The Astrophysical Journal* 971.2, p. 178.
Tafalla, M., J. S.-García, A. Hacar, et al. (2010). In: *Astronomy & Astrophysics* 522, A91.
Tafalla, M., A. Usero, and A. Hacar (2021). In: *Astronomy & Astrophysics* 646, A97.
– (2023). In: *Astronomy & Astrophysics* 679, A112.
Takano, S., T. Nakajima, and K. Kohno (2019). In: *Publications of the Astronomical Society of Japan* 71, S20.
Takano, S., T. Nakajima, K. Kohno, et al. (2014). In: *Publications of the Astronomical Society of Japan* 66.4, p. 75.
Tanaka, K., J. G. Mangum, S. Viti, et al. (2024). In: *The Astrophysical Journal* 961.1, p. 18.
Tang, X. D., C. Henkel, K. M. Menten, et al. (2019). In: *Astronomy & Astrophysics* 629, A6.
Tatematsu, K., R. Kandori, T. Umemoto, et al. (2008). In: *Publications of the Astronomical Society of Japan* 60.3, pp. 407–419.
Teng, Y.-H., I-D. Chiang, K. M. Sandstrom, et al. (2024). In: *The Astrophysical Journal* 961.1, p. 42.
Tielens, A. (2021). Cambridge University Press.
Turner, B. E., L. Pirogov, and Y. C. Minh (1997). In: *The Astrophysical Journal* 483.1, pp. 235–261.
Usero, A., S. García-Burillo, A. Fuente, et al. (2004). In: *Astronomy & Astrophysics* 419, pp. 897–912.
Usero, A., A. K. Leroy, F. Walter, et al. (2015). In: *Astronomical Journal* 150.4, p. 115.
van Breugel, W. J. M. and A. Dey (1993). In: *The Astrophysical Journal* 414, p. 563.
Verley, S., F. Combes, L. Verdes-Montenegro, et al. (2007). In: *Astronomy & Astrophysics* 474.1, pp. 43–53.
Virtanen, P., R. Gommers, T. E. Oliphant, et al. (2020). In: *Nature Methods* 17.3, pp. 261–272.
Vogel, S. N., S. R. Kulkarni, and N. Z. Scoville (1988). In: *Nature* 334.6181, pp. 402–406.
Walter, F., E. Brinks, W. J. G. de Blok, et al. (2008). In: *Astronomical Journal* 136.6, pp. 2563–2647.
Walter, F., R. Decarli, M. Aravena, et al. (Dec. 2016). In: *ApJ* 833.1, p. 67.
Watanabe, Y., N. Sakai, Kazuo Sorai, et al. (2014). In: *The Astrophysical Journal* 788.1, p. 4.
Watkins, E. J., A. T. Barnes, K. Henny, et al. (2023). In: *The Astrophysical Journal Letters* 944.2, p. L24.
Westerhout, G., H. U. Wendlandt, and R. H. Harten (1973). In: *Astronomical Journal* 78, p. 569.
Williams, T. G., J. Sun, A. T. Barnes, et al. (2022). In: *The Astrophysical Journal Letters* 941.2, p. L27.
Wilson, C. D., A. Bemis, B. Ledger, et al. (2023). In: *Monthly Notices of the Royal Astronomical Society* 521.1, pp. 717–736.
Wu, J., N. J. Evans II, Y. Gao, et al. (2005). In: *The Astrophysical Journal Letters* 635.2, pp. L173–L176.
Zhang, C., J. Wang, and T.-W. Cao (2025). In: *The Astrophysical Journal Letters* 978.2, p. L15.

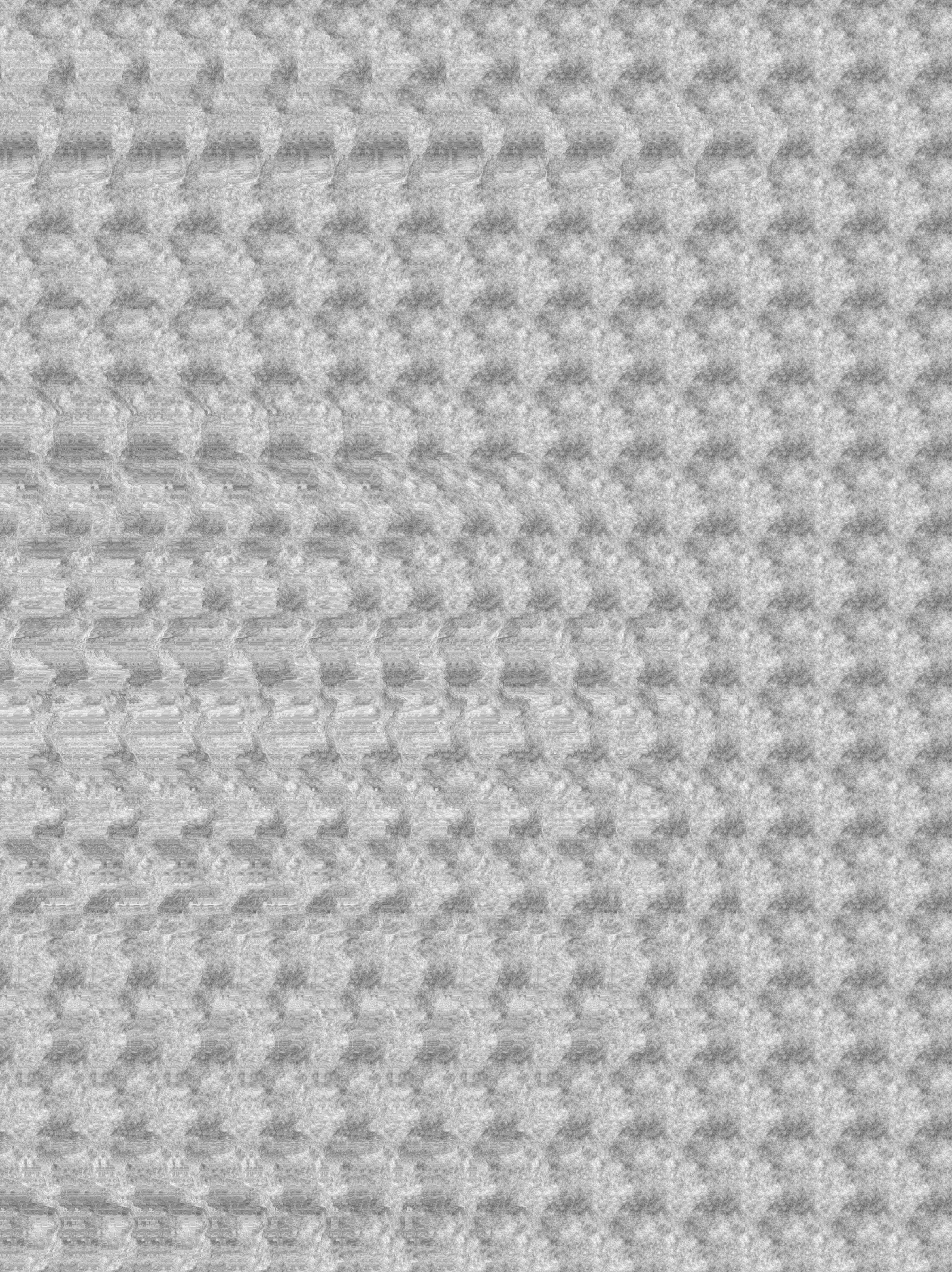

Back cover: Autostereogram of the N_2H^+ mom-0 map, similar to the front cover.

Star formation is fueled by dense molecular gas residing in the dense and cold interiors of molecular clouds. To understand how the large-scale environments within galaxies are able to regulate the properties of star formation within molecular clouds, it is essential to gain a cloud-scale view of this dense molecular gas phase across a range of galactic environments. This thesis provides the first piece in understanding this link, with the most comprehensive analysis of common dense gas tracers on cloud-scales across a diverse set of galactic environments. *"Surveying the Whirlpool galaxy at Arcseconds with NOEMA" (SWAN),* is the largest cloud-scale mapping of 3-4 mm emission in an external galaxy to date. The results of this thesis from the Whirlpool galaxy M51 demonstrate the importance to place the star formation laws into an environmental context.